CHALMERS
UNIVERSITY OF TECHNOLOGY

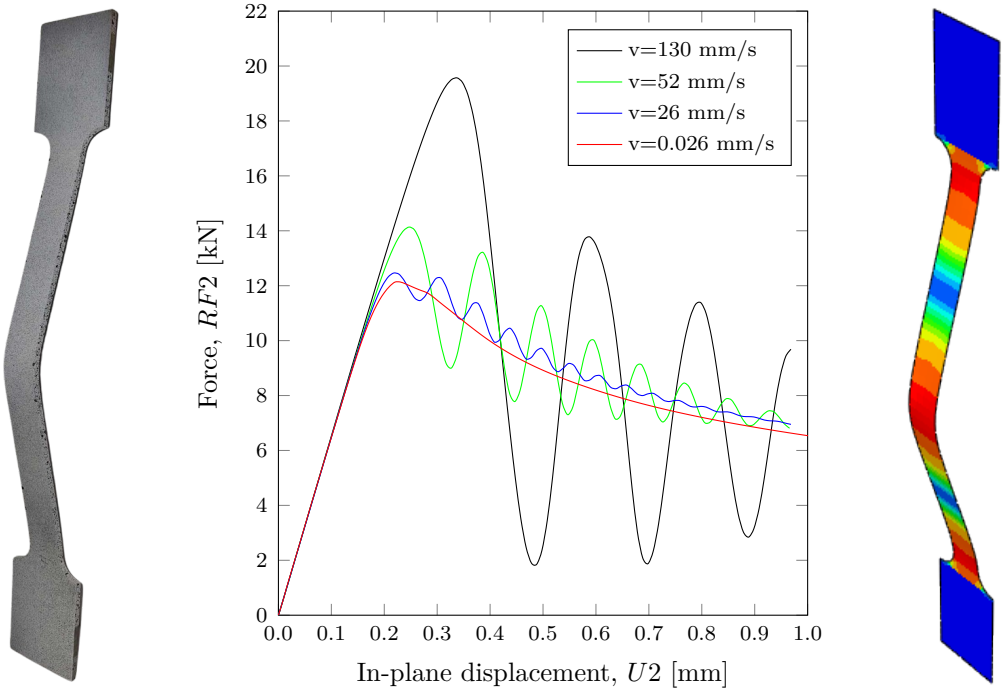

Structural Response in Thin-Walled Steel Structures Subjected to Compressive Axial Dynamic Loading

Master's Thesis in the Master's Program Structural Engineering and Building Technology

HAYK SARGSYAN
NAREK SARGSYAN

Department of Architecture and Civil Engineering
Division of Structural Engineering
CHALMERS UNIVERSITY OF TECHNOLOGY
Master's thesis ACEX30
Gothenburg, Sweden 2024

Master's thesis ACEX30

Structural Response in Thin-Walled Steel Structures Subjected to Compressive Axial Dynamic Loading

Master's Thesis in the Master's Program Structural Engineering and Building Technology

HAYK SARGSYAN
NAREK SARGSYAN

CHALMERS
UNIVERSITY OF TECHNOLOGY

Department of Architecture and Civil Engineering
Division of Structural Engineering
Lightweight Structures
Chalmers University of Technology
Gothenburg, Sweden 2024

Structural Response in Thin-Walled Steel Structures Subjected to Compressive Axial Dynamic Loading

Master's Thesis in the Master's Program Structural Engineering and Building Technology

HAYK SARGSYAN
NAREK SARGSYAN

Supervisor: Morgan Johansson, Norconsult
Examiner: Mohammad Al-Emrani, Chalmers University of Technology

Examensarbete ACEX30
Institutionen för arkitektur och samhällsbyggnadsteknik
Chalmers tekniska högskola, 2024

Department of Architecture and Civil Engineering
Division of Structural Engineering
Lightweight Structures
Chalmers University of Technology
SE-412 96 Gothenburg
Sweden
Telephone +46 31 772 1000

Cover:
Buckled steel rod from experimental testing, structural response under different compressive axial loading rates, and contour plot of rod's deformation derived from FEA.

Department of Architecture and Civil Engineering
Gothenburg, Sweden, 2024

Structural Response in Thin-Walled Steel Structures Subjected to Compressive Axial Dynamic Loading

Master's Thesis in the Master's Program Structural Engineering and Building Technology

HAYK SARGSYAN
NAREK SARGSYAN

Department of Architecture and Civil Engineering
Division of Structural Engineering
Lightweight Structures
Chalmers University of Technology

ABSTRACT

As Swedish cities densify, the proximity between transportation routes and buildings increases, raising concerns about the potential impact of exceptional accidents such as explosions from transportation routes on nearby buildings. In such events, corrugated sheet metal (CSM), frequently used for roofing applications in buildings, becomes susceptible. These thin-walled structures possess limited capabilities in supporting dynamic loads, thus endangering the structural integrity.

This thesis aims to investigate the structural response of a compressed thin-walled steel structure. A simplified model involving thin steel rods subjected to axial loads under both quasi-static and dynamic conditions is employed to understand the fundamentals of dynamic buckling. The employed methodology comprises experimental testing and numerical analyses using the FE software Abaqus CAE. To form the foundation for the experiments, initial numerical analyses are conducted, incorporating the Cowper-Symonds material model for simulation of strain rate effects. In the experimental testing, two different rod configurations are subjected to axial velocities ranging from 0.013 mm/s (10^{-4} s^{-1}) to 195 mm/s (1.5 s^{-1}). Outcomes of these tests are then validated against subsequent numerical analyses.

Findings from experiments and numerical analyses reveal that the structural response of the steel rods is governed by buckling. At increased loading rates, the material exhibits a strengthening effect, manifested through the increase in the critical buckling force. Additionally, inertia effects in the form of dynamic oscillations become apparent at specific strain rates. The initiation of these effects is further accelerated with higher slenderness. Moreover, amplified slenderness and/or initial imperfections cause reduction in load-bearing capacity. Lastly, the amplitude of the dynamic oscillations is damped with increased initial imperfections.

Overall, strong correspondence between the outcomes of the two methods is found. While there are disparities in the predicted axial capacity, the dynamic behavior of the rods simulated in Abaqus CAE closely reflects the dynamic effects observed during experimental testing.

Keywords: Steel rod, Compression, Buckling, Dynamic loading, Quasi-static, Strain rate, Inertia effects, Non-linear finite element analysis, Explosions

Strukturell respons i tunnväggiga stålkonstruktioner utsatta för dynamisk axial belastning i kompression

Examensarbete inom masterprogrammet Konstruktionsteknik och byggnadsteknologi

HAYK SARGSYAN
NAREK SARGSYAN

Institutionen för arkitektur och samhällsbyggnadsteknik
Avdelningen för Konstruktionsteknik
Lättviktskonstruktioner
Chalmers tekniska högskola

SAMMANFATTNING

I takt med att svenska städer förtätas ökar närheten mellan transportrutter och byggnader, vilket väcker oro för potentiella inverkan av exceptionella olyckor såsom explosioner från transportrutter på närliggande byggnader. Vid sådana händelser blir korrugerad plåt (TRP-plåt) som ofta används för takapplikationer på byggnader sårbar. Dessa tunnväggiga strukturer har begränsad förmåga att bära dynamiska laster vilket äventyrar den strukturella integriteten.

Syftet med detta examensarbete är att undersöka den strukturella responsen hos en tryckt tunnväggig stålkonstruktion. En förenklad modell som involverar tunna stålstavar utsatta för både kvasistatiska och dynamiska axiella belastningar används för att förstå grunderna i dynamisk knäckning. Den använda metoden omfattar experimentell provning och numeriska analyser i FE programvaran Abaqus CAE. Till grund för experimenten utförs inledande numeriska analyser som inkorporerar Cowper-Symonds materialmodell för simulering av töjningshastighetseffekter. I den experimentella provningen utsätts två olika stavgeometrier för axiella hastigheter inom intervallet 0.013 mm/s (10^{-4} s^{-1}) till 195 mm/s (1.5 s^{-1}). Resultat från dessa tester valideras sedan mot efterföljande numeriska analyser.

Resultaten från experiment och numeriska analyser avslöjar att den strukturella responsen av stålstavarna styrs av knäckning. Vid ökade belastningshastigheter uppvisar materialet en förstärkningseffekt, vilket manifesteras genom ökningen av den kritiska knäcklasten. Dessutom blir masströghetseffekter i form av dynamiska oscillationer uppenbara vid specifika töjningshastigheter. Initieringen av dessa effekter accelereras också med ökad slankhet. Vidare orsakar ökad slankhet och/eller ökade initial imperfektioner en reduktion av bärförmåga. Slutligen dämpas amplituden av de dynamiska oscillationerna med ökade initial imperfektioner.

Sammantaget finns det en god överensstämmelse mellan resultaten från de två metoderna. Även om det finns skillnader i den predikterade axiella kapaciteten, återspeglar det dynamiska beteendet hos de simulerade stavarna i Abaqus CAE väl med de dynamiska effekter som observerats under experimentell provning.

Nyckelord: Stålstav, Kompression, Knäckning, Dynamisk belastning, Kvasi-statisk belastning, Töjningshastighet, Masströghetseffekter, Icke-linjär finita element analys, Explosioner

Contents

Preface

This thesis investigates the response of thin-walled steel structures subjected to compressive axial dynamic loading. It is part of an ongoing research in the field of impulse-loaded structures within the discipline of structural engineering at Chalmers University of Technology. Collaboratively undertaken by Norconsult and Chalmers University of Technology, the thesis work was conducted from January to June 2024.

Special thanks are extended to our supervisor Morgan Johansson from Norconsult whose profound expertise in explosion loads has offered valuable insights into the topic. His continuous guidance, support and dedication have been pivotal in shaping our research.

It should be noted that experimental testing forms a crucial aspect of this thesis. The testing, performed in the laboratory of the Department of Structural Engineering at Chalmers University of Technology, would not have been feasible without Sebastian Almfeldt, the coordinator of the laboratory.

Finally, we want to express appreciation to our examiner Mohammad Al-Emrani, whose inputs and extensive knowledge concerning steel structures have enhanced the quality of this thesis.

Gothenburg, June 2024
Hayk Sargsyan & Narek Sargsyan

Notations

Roman upper case letters

A	Cross-sectional area/Constant for initial yield strength/Amplitude
A_0	Initial amplitude in smooth step
A_p	Peak amplitude in smooth step
B	Material constant for strain hardening
C	Material constant for strain rate effects
D	Strain rate material parameter
D_{avg}	Material parameter for average dynamic increase factor
D_y	Material parameter for dynamic increase factor for yield strength
E	Modulus of elasticity/Young's modulus
E_k	Kinetic energy
F	Force
F_k	Characteristic pressure load
F_{max}	Maximum force
$F(t)$	External time-dependent force/Impulse load
$F(u)$	External displacement-dependent force
$\triangle F$	Change in force level
${}^tF$	Force at current time increment
${}^{\triangle t}F$	Change in force between two time increments
I	Impulse/Moment of inertia
I_k	Characteristic impulse/Momentum
K_{sec}	Secant stiffness
L	Length
L_c	Parallel length
L_{cr}	Effective buckling length
L_e	Extensometer length

L_k	Length of clamping area
L_o	Gauge length
L_{tot}	Total length of specimen
$\triangle L$	Tensile deformation/Elongation
M	Bending moment
N	Normal force
P	Pressure/Axial load/Axial force
P_0	Atmospheric pressure
P_{cr}	Critical buckling force/Average critical buckling force
$P_{cr.quasi}$	Critical buckling force for quasi-static loading
$P_{cr\#1}$	Critical buckling force for sample 1
$P_{cr\#2}$	Critical buckling force for sample 2
$P_{cr\#3}$	Critical buckling force for sample 3
$\triangle P_{cr}$	Deviation percentage of critical buckling force between two results
$P(t)$	External time-dependent pressure
Q	Equivalent static load
R	Capacity/Resistance force
R_1	Capacity in statics
R_2	Capacity in dynamics
$R(u)$	Internal resisting force
$RF2$	Reaction force in y-direction
T	Test temperature/Time to fracture/Time duration
T^*	Dimensionless temperature
T_m	Melting temperature
T_r	Room temperature
U	Potential energy
$U1$	Degree of freedom for translation in x-direction

$U2$	Degree of freedom for translation in y-direction/In-plane displacement
$U3$	Degree of freedom for translation in z-direction/Out-of-plane displacement
$UR1$	Degree of freedom for rotation about x-axis
$UR2$	Degree of freedom for rotation about y-axis
$UR3$	Degree of freedom for rotation about z-axis
V	Shear force
$V1$	Degree of freedom for velocity in x-direction
$V2$	Degree of freedom for velocity in y-direction
$V3$	Degree of freedom for velocity in z-direction
$VR1$	Degree of freedom for angular velocity about x-axis
$VR2$	Degree of freedom for angular velocity about y-axis
$VR3$	Degree of freedom for angular velocity about z-axis
W	Work
W_i	Internal work
$W_{i,1}$	Internal work under static loading
$W_{i,2}$	Internal work under dynamic loading
W_y	External work

Roman lower case letters

a	Acceleration
a_0	Original thickness of specimen
a_p	Peak acceleration
b	Width
b_0	Original width of parallel length
b_k	Width of clamping area
c	Centre-to-centre distance
e	Initial imperfections
$f_{0.2}$	0.2% offset yield strength

f_u	Ultimate tensile strength/Static ultimate strength
$f_{u,d}$	Dynamic ultimate strength
f_y	Static yield strength/Yield stress
$f_{y,d}$	Dynamic yield strength
$f_{y,d.an}$	Analytical dynamic yield strength
$f_{y,d.num}$	Numerical dynamic yield strength
h	Height
i	Impulse density/Radius of gyration
m	Mass/Exponential constant for thermal softening
n	Exponential constant for strain hardening
p	Strain rate material parameter
p_{avg}	Material parameter for average dynamic increase factor
p_y	Material parameter for dynamic increase factor for yield strength
r	Transition radius
t	Thickness/Time/Simulation time
t_0	Initial time in smooth step
t_1	Initial time/Analysis time for case 1
t_2	Final time/Analysis time for case 2
t_a	Arrival time
t_p	Peak time in smooth step
u	End-shortening/Deformation/Displacement
u_1	Deformation in statics/Small deformations
u_2	Deformation in dynamics/Large deformations
u_{cr}	Average critical end-shortening
$u_{cr\#1}$	Critical end-shortening for sample 1
$u_{cr\#2}$	Critical end-shortening for sample 2
$u_{cr\#3}$	Critical end-shortening for sample 3

$\triangle u_{cr}$	Deviation percentage of critical end-shortening between two results
u_{el}	Elastic deformation
$u_{el,1}$	Deformation limit of elastic response
u_p	Peak displacement
u_{pl}	Plastic deformation
$u_{pl,1}$	Allowable plastic deformation
u_{tot}	Total deformation
${}^{t}u$	Displacement at current time increment
${}^{\triangle t}u$	Change in displacement between two time increments
v	Velocity/Loading rate
v_1	Loading rate for case 1
v_2	Loading rate for case 2
v_p	Peak velocity
w	Deflection
w_{max}	Maximum deflection/Average maximum deflection
$w_{max\#1}$	Maximum deflection for sample 1
$w_{max\#2}$	Maximum deflection for sample 2
$w_{max\#3}$	Maximum deflection for sample 3
$\triangle w_{max}$	Deviation percentage of maximum deflection between two results

Greek letters

α	Corrugation angle
$\dot{\epsilon}$	Strain rate
$\dot{\epsilon}_0$	Reference strain rate
ϵ	Engineering strain
ϵ_3	Plane strain
$\epsilon_{0.2}$	0.2% plastic strain
ϵ_{pl}	Plastic strain

ϵ_{sh}	Strain hardening strain
ϵ_{tot}	Total strain
ϵ_{true}	True strain
$\epsilon_{true,el}$	True elastic strain
$\epsilon_{true,pl}$	True plastic strain
ϵ_u	Ultimate strain
ϵ_y	Yield strain
$\bar{\lambda}$	Relative slenderness ratio
λ	Eigenvalue/Buckling factor/Slenderness
λ_1	Reference relative slenderness
$\lambda_{c.mesh}$	Eigenvalue at current mesh size
$\lambda_{p.mesh}$	Eigenvalue at previous mesh size
$\triangle\lambda$	Deviation percentage of eigenvalues between two mesh sizes
ν	Poisson's ratio
ξ	Dimensionless interpolation parameter in smooth step
ρ	Mass density
σ	Engineering stress
σ_3	Plane stress
σ_{cr}	Critical stress
$\sigma_{i,d}$	Dynamic stress
$\sigma_{i,s}$	Quasi-static stress
σ_{max}	Maximum stress
σ_{true}	True stress
σ_y	Static yield stress
$\sigma_{y,d}$	Dynamic yield stress
χ	Buckling reduction factor
ω	Angular frequency

Abbrevations

BC	Boundary condition
CAD	Computer-aided design
CCD	Charge-coupled device
CS	Cowper-Symond
CSM	Corrugated sheet metal
DIC	Digital image correlation
DIF	Dynamic increase factor
DIF_{avg}	Average dynamic increase factor
$DIF_{0.2}$	Dynamic increase factor at 0.2% offset plastic strain
DIF_i	Dynamic increase factor at specific strain rate
DIF_u	Dynamic increase factor for ultimate strength
DIF_y	Dynamic increase factor for yield strength
DOF	Degrees-of-freedom
FE	Finite element
FEA	Finite element analysis
FEM	Finite element method
GOM	Geometric optical measurement
HSC	High-speed camera
JC	Johnson-Cook
LBA	Linear buckling analysis
NLA	Non-linear analysis
$S4R$	Four-node quadrilateral shell element
$SDOF$	Single-degree-of-freedom
$SHPB$	Split Hopkinson Pressure Bar
TNT	Trinitrotoluene
UTM	Universal testing machine

1 Introduction

This section provides an overview of the thesis topic, emphasizing its significance within the field of structural engineering. Beginning with a brief background on the utilization of corrugated sheet metal (CSM) and discussing the challenges arising from dynamic loads, it outlines the aim and objectives of the thesis, elucidating the research questions addressed. Furthermore, the section delineates the constraints of the research and presents the methodology employed.

1.1 Background

As Swedish cities continue to thrive and expand, there is an increasing need for urban densification within existing urban areas. Densification, a strategic urban planning decision driven by its economic benefits, aims to optimize new land use more efficiently. However, the consequential reduction in distances between buildings and transportation routes, coupled with the close proximity of structures, raises concerns about the potential impact of explosions, such as transportation accidents involving hazardous materials, on nearby buildings. The structural integrity of buildings can be significantly threatened by these exceptional accidents, necessitating a comprehensive understanding of their response to such dynamic events. Structures designed for static loads may not be adequately suited to withstand the dynamic effects of explosions, resulting in substantially different design considerations with energy absorption being more critical than load capacity of these structures.

CSM has nowadays become a prevalent choice for various applications, such as roof structures due to its effectiveness and affordability in supporting static loads. Nevertheless, this conventional roof design exhibits limitations when subjected to dynamic loads caused by explosions. While steel is inherently ductile, due to buckling effects, e.g. compressed flanges under compressive forces, the strong and stiff corrugated sheet metal possesses limited deformation capacity, resulting in low energy absorption capability. Given these limitations, exploring alternative concepts to enhance the effectiveness of CSM roofing under explosion loads could be advantageous, as the conventional design approaches may be overly conservative.

1.2 Aim

The aim of the master's thesis is to investigate and enhance the comprehension of the structural response of thin-walled steel structures subjected to compressive axial dynamic loading.

1.3 Objectives

In this study, a deliberate choice has been made to adopt a simplified approach, focusing on the behavior of a compressed steel rod under various dynamic loading rates. This decision stems from the pursuit of fundamental insights into the influence of different load velocities on the buckling response of the steel rod. To attain the aim of the study, the following objectives are formulated and defined:

- To investigate the structural response of a compressed thin-walled structure, employing a simplified model involving thin steel rods subjected to compressive axial loads under both quasi-static and dynamic conditions.
- To analyze the combination of pivotal parameters influencing the structural behavior of the studied rods, including strain rate and inertia effects (dynamic effects), geometric initial imperfections, and structural slenderness (geometry).
- To compare the obtained results with findings from other studies aiming for validation and an improved understanding of such structures' behavior under dynamic loading conditions.

In alignment with the established objectives, this study addresses key questions concerning the structural performance of a steel rod subjected to compressive axial loading with varying rates:

- What differences arise in the structural response when a steel rod experiences dynamic loading in contrast to quasi-static loading?
- Are there any discernible alterations in the mechanical behavior of the material when considering different loading rates?
- What relationship exists between structural response and the parameters initial imperfections and slenderness, and which impact do these variables have on the axial capacity?
- In what manner does the interplay between strain rate and structural slenderness affect the occurrence of inertia effects during dynamic loading scenarios?
- How effectively do existing strain rate effect models predict the dynamic buckling load?

1.4 Limitations

The primary limitation of the thesis lies in not explicitly studying the static and dynamic structural response of a CSM subjected to transverse loading. To reduce the complexity of the research, the master's thesis focuses on a simplified structure comprising a steel rod supported only at its short ends, subjected to compressive axial forces. This decision is further motivated by the necessity of conducting own experiments.

1.5 Methodology

The research work procedure comprises of three main components: Literature study, numerical non-linear analysis (NLA) and experimental study.

Commencing with the literature study, the aim is to establish a comprehensive understanding of the studied topic. This includes studying impulse-loaded structures and exploring the buckling behavior exhibited by steel structures under quasi-static and dynamic loading. As part of this process, the literature study also entails a thorough examination of previous works in the field, encompassing experimental studies as well as analytical and numerical analyses.

Transitioning from literature study to numerical analyses, Finite Element Method (FEM) using the commercial software Abaqus CAE is employed to investigate the effects of quasi-static and dynamic loading of a steel rod subjected to compressive axial load. In these analyses, both non-linear geometry and non-linear material behavior is considered.

The numerical analyses are performed in two phases, with the first phase serving as the basis for the experimental study. This pre-study is facilitated by utilizing existing constitutive material and strain rate effect models, as well as ISO standard for development of specimen geometry for experimental testing. In parallel, complementary analytical calculations are also carried out to verify the obtained results.

Building upon the numerical analyses, experiments on steel rods of two different geometries subjected to axial load are conducted. These experiments involve material tests in tension and structural tests in compression. To capture high-speed deformations and enable accurate measurements, the testing setup integrates High-speed camera (HSC) and Digital Image Correlation (DIC).

The study culminates with the second phase of numerical analyses, aimed at supporting and validating the experimental findings. Comparative analyses of the outcomes obtained from both methodologies are conducted, accompanied by discussions that elucidate their similarities and discrepancies. Potential causes for discrepancies are also emphasized.

2 Theory

This section delves into important theoretical aspects pertinent for the study. Specifically, it addresses the properties and characteristics of steel, features of CSM, structural stability, explosion and dynamics, and strain rates.

2.1 Characteristics of Steel

Steel is a predominant material for various structures in contemporary construction practices. This material is renowned for having excellent mechanical properties and high strength-to-weight ratio (Dubina et al., 2012). At the market, the common types of steel available include carbon steel, alloy steel, and stainless steel. Among these, carbon steel comprising iron and carbon is the most widely utilized due to its affordability and ease of fabrication. Within the context of steel, a differentiation is made between hot-rolled and cold-rolled steel, each showcasing distinct characteristics stemming from their respective manufacturing processes. Strength classes encompass grades ranging from S235, S275, S355, S420, S460, and beyond. The number in each grade designation, such as 235, signifies the characteristic yield strength of the steel. Notably, S355 emerges as the most extensively used grade in structural engineering applications.

Studying the characteristics and mechanical behavior of steel involves examining the stress-strain curve, which describes how the stress is correlated with strain when a specific steel type is subjected to an applied load. A typical stress-strain curve for carbon steel delineates its mechanical properties, encompassing elastic behavior, yielding, plastic deformation, strain hardening, ultimate strength, necking, and fracture. For a schematic representation with highlighted parameters, see Figure 2.1.

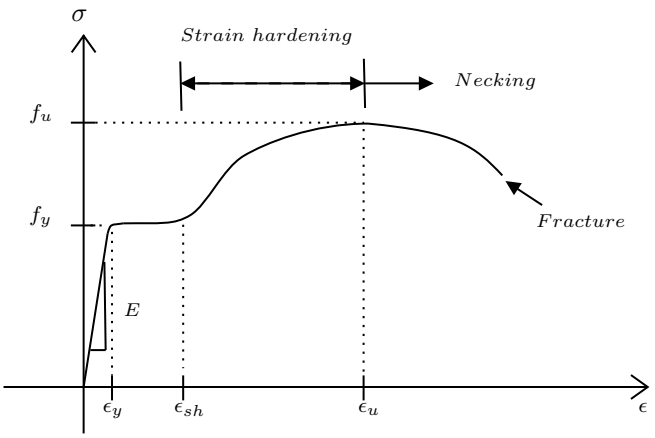

Figure 2.1: Schematic stress-strain relation for hot-rolled carbon steel.

In the initial phase of the stress-strain curve, steel exhibits elastic behavior, meaning that when stress is applied, the material deforms elastically. This phase is reversible,

hence, upon unloading, the steel returns to its original state. The material parameter of interest here is the modulus of elasticity, E, which is described by Hooke's law due to the linear relationship between stress and strain.

With increased stress, the steel eventually reaches the yield stress, f_y, and at this point, plastic deformation ensues, causing permanent changes to e.g. the shape of the material. The corresponding strain is referred to as the yield strain, ϵ_y. It is important to note that pinpointing the specific transition point from elastic to plastic behavior (yield plateau) is challenging to detect when considering cold-worked steel (Al-Emrani et al., 2019). Therefore, the 0.2 % offset method is employed to approximate the transition point, which consequently serves as an equivalence to the yield stress. In this method, an offset yield point is selected and defined as the highest stress the material can withstand without exceeding 0.2 % offset strain, see Figure 2.2 for visualization.

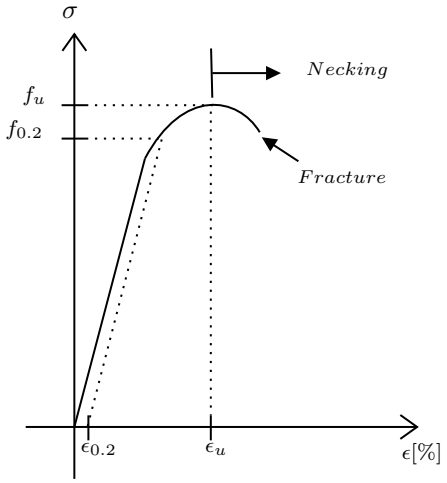

Figure 2.2: Schematic stress-strain relation for cold-formed steel.

As plastic deformation progresses, the material undergoes strain hardening, leading to increased hardness and strength. This, in turn, enhances its resistance to further deformation. The phenomenon, initiated at the strain ϵ_{sh}, is illustrated in Figure 2.1 by an increase in the steepness of the slope in the stress-strain curve.

Ultimately, the stress reaches the ultimate strength, f_u, which represents the maximum stress the material can endure prior to failure. Beyond the ultimate strength, the material experiences necking, a phenomenon characterized by a localized reduction in the material's cross-sectional area (A). As seen in Figure 2.1, the stress diminishes with increased strain, which is attributed to the strain being concentrated in the reduced area. The stress-strain curve reaches its conclusion at the point of fracture, indicating the material's breakage and separation.

2.2 Corrugated Sheet Metal

CSM has become a ubiquitous structure in various engineering applications due to its durability, versatility and other advantages. The utilization of CSM has subsequently emerged as a widespread solution, for instance, in spanning roofs between primary girders. These sheets fall into the category of thin-walled structures (substantially smaller thickness in comparison to its height) and feature pattern of ridges and grooves, forming trapezoidal/corrugated profiles. A schematic illustration of a profile along with an explanation of its parameters is presented in Figure 2.3.

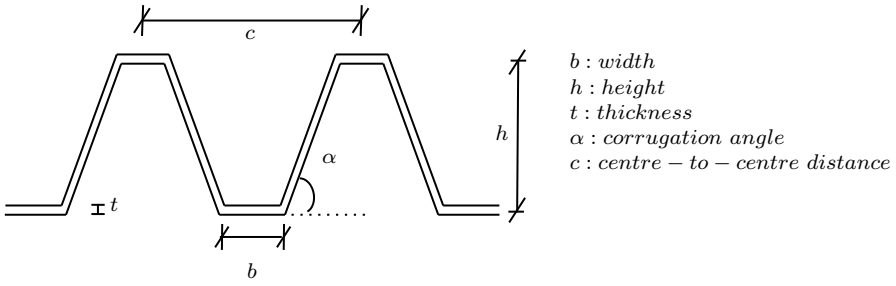

Figure 2.3: Schematic cross-section of CSM profile.

The trapezoidal/corrugated configuration imparts stiffness, strength, and rigidity to the sheet. This design offers excellent strength-to-weight ratio and substantial structural integrity while remaining relatively lightweight (Dubina et al., 2012). The lightweight nature also results in overall reduced load on the roof structure, thereby contributing to the structure's longevity. In the current market, a variety of corrugated sheets with different thicknesses, materials and profiles are available and this versatility enables for customized solutions to meet specific roofing requirements. Typical dimensions for CSM based on the manufacturer Ruukki are provided in Table 2.1.

Table 2.1: Dimensions of CSM based on Ruukki (n.d.).

Parameter	Dimensions [mm]
Thickness	0.6 - 1.5
Height	44 - 153
Width	30 - 117

Thin-walled structures present several challenges due to their inherent nature, demanding careful consideration in the design. One primary concern revolves around buckling (cf. Section 2.3), which can occur under axial compression loading, resulting in instability. This instability phenomenon usually happens at stress levels much lower than the material's yield stress in static conditions (Mallon, 2008). Additionally, geometric imperfections, such as irregularities in the ideal shape of the structural member, may markedly decrease the load-carrying capacity compared to an ideally perfect shaped member. Moreover, given the slender nature, thin-walled

structures are prone to significant deformations when buckling transpires. These deformations introduce geometric nonlinearities (cf. Section 3.1), requiring structural analyses that account for such effects. It is important to note that buckling also hampers the utilization of the steel material's excellent ductility. In other words, maintaining load capacity with increasing deformation becomes unfeasible, which is particularly crucial for structures subjected to explosion loads.

In situations involving static loading, e.g. bending due to self-weight of the structure, where external forces remain relatively constant over time, corrugated sheets are an excellent structural option. This is primarily because of the strength and rigidity conferred by the corrugations, empowering support of significant loads with small deformations. However, under varying loading conditions, such as the impulse or dynamic load from an explosion, thin-walled structures of this type may be susceptible to dynamic phenomena e.g. dynamic buckling. Consequently, they may not serve as suitable option for roofing application. See Section 2.4 for treatment on structures subjected to explosion loads.

2.3 Structural Stability

This section provides an overview of buckling, a structural failure mode observed when slender elements deform/collapse under compression. It differentiates between static and dynamic buckling phenomena and highlights the factors influencing buckling behavior. Moreover, the following section presents pertinent theory and an analytical calculation method for evaluating the critical static buckling load.

2.3.1 Buckling under Static Loading

Buckling or loss of stability is a phenomenon where a system transitions from one equilibrium state to another. This transition is referred to as a bifurcation point, indicating the shift from a stable to an unstable equilibrium path, also termed as the limit path (Kubiak, 2013). The critical load represents the load at which this loss of stability occurs. When a structure experiences a load exceeding the critical load, it exhibits behavior along either a stable post-buckling equilibrium path, characterized by increasing displacement with load or an unstable post-buckling equilibrium path, where the displacement grows as the load decreases, see Figure 2.4.

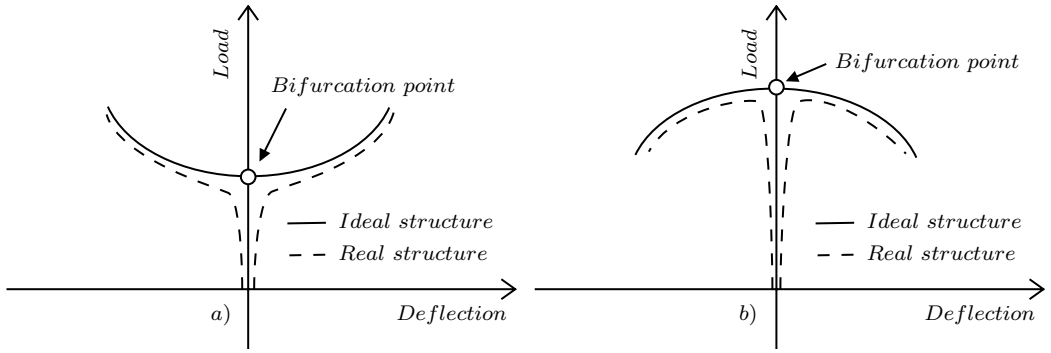

Figure 2.4: Comparison of post-buckling equilibrium paths for ideal and real structures: a) Stable & b) Unstable. Based on Kubiak (2013).

In the case of rods under axial compression, as they transition to a new equilibrium, their post-buckling behavior demonstrates abrupt global buckling at the bifurcation point. An illustration of the behavior of a thin-walled rod in compression is found in Figure 2.5.

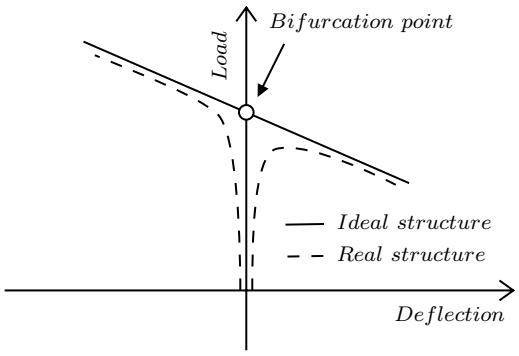

Figure 2.5: Behavior of thin-walled compression rod. Based on Dubina et al. (2012).

When considering only compressive axial loading for very slender/thin members as in the case of CSM, the primary buckling mode that arises is elastic buckling or more commonly known as Euler buckling. This phenomenon takes place within the elastic range of the material. Another type of buckling which can occur under compressive axial loading is inelastic buckling (elastic-plastic), characterized by both elastic and plastic deformation, see also Section 2.4.7. Inelastic buckling occurs when the compressive axial load exceeds the structural element's yield strength. Consequently, resulting in plastic deformation while being in the elastic range of the material. It should be noted that, besides different types of buckling, the buckling phenomenon can occur at different levels, namely local and global. Local buckling encompasses buckling of localized regions within the structural element whereas global buckling pertains to buckling of the entire element.

Sectional buckling, including phenomenon such as local buckling, is identified by a stable post-critical path wherein the structure maintains its structural integrity

but experiences a significant decrease in stiffness. Local buckling may occur before the onset of plastification. Yielding initiates before the structure fails, gradually transitioning from sectional buckling to local plastic mechanism. This transition may coincide closely with the onset of global buckling (Dubina et al., 2012).

2.3.2 Static Buckling Load of Steel Rod under Compression

The analytical calculation approach for determining the static buckling load of a steel rod involves treating it as equivalent to a steel column, owing to their similarities in geometry, shape, and loading configuration. Calculation of a thin steel rod under a static compressive axial load can be centered on the structural model illustrated in Figure 2.6. The rod with arbitrary length, L, is structurally modelled as a fixed-fixed column experiencing compression due to an external axial force, P. The model showcases the induced displacement, u, while also considering the influence of initial imperfections, e.

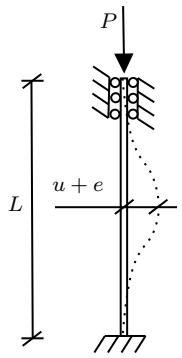

Figure 2.6: Thin steel rod under static compressive axial loading.

The foundation for analysing the depicted structure relies on understanding the fundamentals of the classical Euler buckling theory for columns. Within the static context, the instability problem is defined by linear elastic buckling (Al-Emrani, 2023). This phenomenon is characterized by an abrupt loss of stability and a sudden lateral displacement of slender columns subjected to compressive axial loads, all while remaining within the range of elastic deformation.

Euler buckling theory provides insight into the determination of the elastic critical load at which a structural system becomes unstable and undergoes buckling. The theory considers an idealized scenario with numerous simplifying assumptions (Al-Emrani, 2023). These assumptions include:

- Perfect column without geometrical imperfections
- Linear-elastical material behavior
- Centric loading
- Plane buckling in only one direction
- Absence of residual stresses

The Euler formula for critical buckling load, P_{cr}, for a column is given by Equation 2.1. Alternatively, the load can be expressed in terms of critical stress, σ_{cr}, as outlined in Equation 2.2 where I stands for the moment of inertia and L_{cr} signifies the effective buckling length of the column, taking into account the boundary conditions (BC). In this case, since the column is fixed-fixed, L_{cr} corresponds to 50 % of the entire length of the column ($0.5L$).

$$P_{cr} = \frac{\pi^2 EI}{L_{cr}^2} \tag{2.1}$$

$$\sigma_{cr} = \frac{P_{cr}}{A} = \frac{\pi^2 EI}{AL_{cr}^2} \tag{2.2}$$

By employing the formulation of the radius of gyration, denoted as i through Equation 2.3, the critical buckling stress can be expressed as indicated by Equation 2.4.

$$i = \sqrt{\frac{I}{A}} \tag{2.3}$$

$$\sigma_{cr} = \frac{\pi^2 E}{(\frac{L_{cr}}{i})^2} \tag{2.4}$$

In Equation 2.4, the term $\frac{L_{cr}}{i}$ serves as a parameter representing the slenderness of a column and is commonly assigned to λ. The ensuing substitution results in the rewriting of the expression of the critical buckling stress, as exemplified in Equation 2.5.

$$\sigma_{cr} = \frac{\pi^2 E}{\lambda^2} \tag{2.5}$$

Observation of Equation 2.5 shows that the critical buckling load is solely a function of the material properties of the member and its slenderness. However, structural steel exhibits pronounced non-linear behavior, particularly with the occurrence of yielding, contradicting the earlier assumption of linear-elastic behavior (Al-Emrani, 2023). Consequently, a reference relative slenderness denoted as λ_1 is introduced, accounting for the yield stress/point of the steel. By equating the critical buckling stress to the yield strength of the specific steel, the reference relative slenderness can be solved for, see Equation 2.6. The resulting expression for the reference relative slenderness, denoted as λ_1, is given by Equation 2.7.

$$\sigma_{cr} = \frac{\pi^2 E}{{\lambda_1}^2} = f_y \tag{2.6}$$

$$\lambda_1 = \pi\sqrt{\frac{E}{f_y}} \tag{2.7}$$

This reference relative slenderness serves as a threshold for distinguishing the expected response of the column under compressive load. Below this threshold, the member's capacity is governed by yielding, while beyond it, buckling governs the column's capacity (Al-Emrani, 2023). The relationship between σ_{cr} and λ per classical

buckling theory, considering both linear elastic and elastoplastic material behavior, is further elucidated in Figure 2.7.

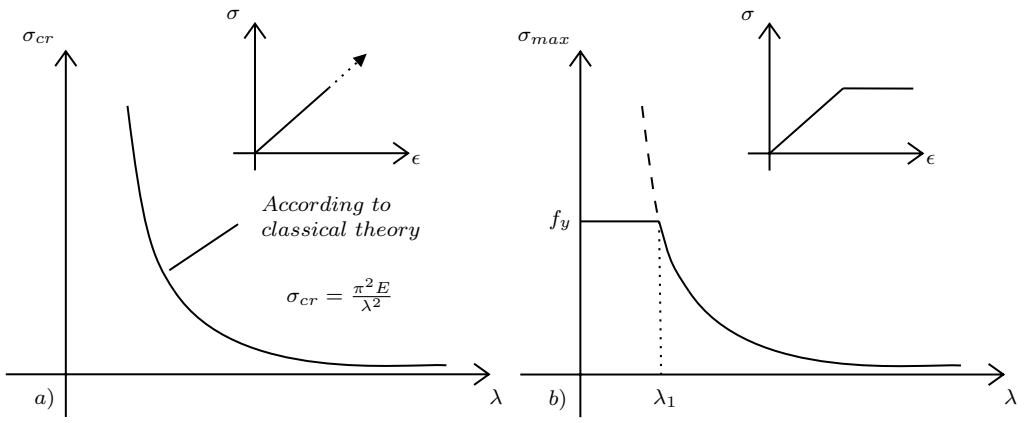

Figure 2.7: Correlation between critical buckling stress and structural slenderness according to classical buckling theory: a) Linear elastic material behavior & b) Elastoplastic material behavior. Based on Al-Emrani (2023).

Al-Emrani (2023) mentions that, for practical reasons in design and analyses, the column strength curve is often represented normalized relative to the yield strength of the steel. Equation 2.8 shows the normalization of the maximum steel stress, σ_{max}, with respect to f_y, where a new parameter, χ, representing the buckling reduction factor is introduced. The normalization of λ with λ_1 is instead defined by the parameter $\bar{\lambda}$, describing the relative slenderness ratio, as seen in Equation 2.9.

$$\chi = \frac{\sigma_{max}}{f_y} \tag{2.8}$$

$$\bar{\lambda} = \frac{\lambda}{\lambda_1} \tag{2.9}$$

The normalized representation of the buckling strength curve of the steel column is illustrated in Figure 2.8.

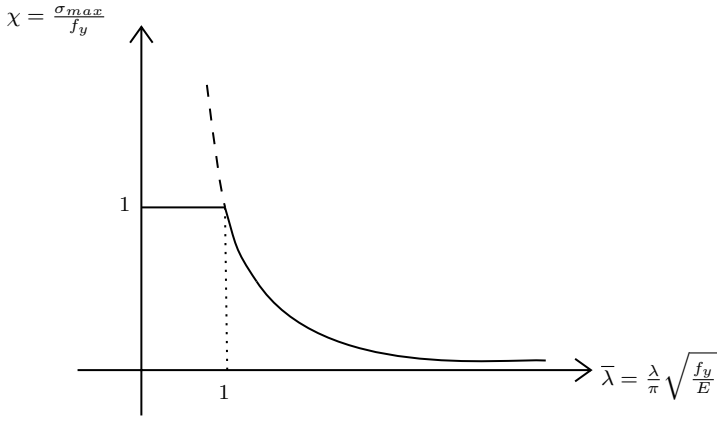

Figure 2.8: Correlation between bucking reduction factor, χ, and relative slenderness, $\bar{\lambda}$. Based on Al-Emrani (2023).

Note that this relation applies exclusively to the classical Euler buckling theory. Test results indicate deviations from the Euler buckling curve in the actual behavior of steel columns with varying slenderness (Al-Emrani, 2023). An illustration of an adopted design buckling curve, derived from these test results, in relation to what is predicted by Euler buckling theory, is seen in Figure 2.9.

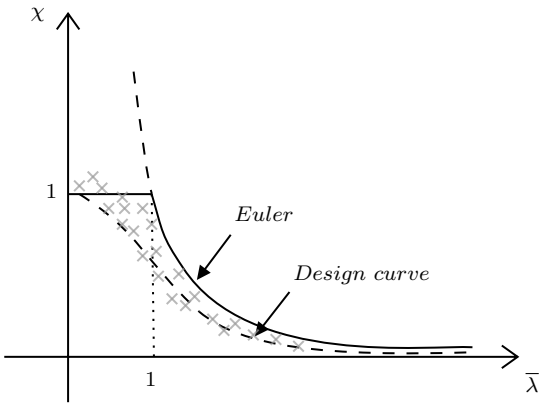

Figure 2.9: Comparison between test results (represented by ×) and the design buckling curve derived from them, alongside the theoretical buckling curve based on Euler theory. Based on Al-Emrani (2023).

A notable observation from Figure 2.9, regarding the thin steel rod under study, is that the ultimate load-bearing capacity of columns with high slenderness closely aligns with predictions derived from Euler buckling theory. This suggests that the capacity of such columns will be primarily governed by elastic instability.

The difference in the buckling curves is mainly associated with initial imperfections and residual stresses. Actual columns typically exhibit deviations from perfect straightness, showcasing geometric variations that have an influence on both their overall behavior and their ultimate load-bearing capacity. Residual stresses, which are inherent internal stresses in steel sections resulting from manufacturing processes, also impact the capacity of columns.

Furthermore, due to initial imperfections, 2nd-order moments are generated upon load application. This 2nd-order effects together with residual stresses are more pronounced for columns with intermediate slenderness, resulting in maximum reduction of the load-bearing capacity (Al-Emrani, 2023). In this scenario, the capacity is governed by inelastic buckling, which arises from the combined effects of yielding (partial plastic deformation) and buckling. For stocky columns, the capacity is determined by yielding, given its insensitivity to both parameters. Conversely, the load-bearing capacity of very slender columns is only marginally affected by residual stresses and initial imperfections, with the ultimate load governed by Euler buckling.

2.3.3 Buckling under Dynamic Loading

It is widely known that aside from static loads, structures may also be subjected to dynamic loads. Dynamic loading refers to the condition in which structures are exposed to external loads that fluctuate over time, e.g. blast loading caused by an explosion. Under dynamic loading, structures experience transient motion, which is a temporary response to dynamic loading events (Mallon, 2008). This movement, defined by its time-dependent behavior, occurs at the onset of dynamic loading and may involve alterations in velocity or deformations. These effects gradually diminish over time as the structure reverts to a state of rest. This stands in contrast to static loading scenarios, where structures remain in equilibrium due to balanced forces, resulting in a stable condition without any net motion.

Given that a structure with some damping is in equilibrium state, the introduction of a dynamic load with small magnitude will generally induce motion of similar scale. Nevertheless, under specific conditions or when various factors such as load magnitude, frequency, etc., come into play, the resulting motion can escalate considerably, leading to notable deformations that signal a "departure" from the structure's initial state. This abrupt and substantial dynamic response to minor alterations in dynamic loading is termed dynamic buckling (Mallon, 2008).

Dynamic buckling in literature, is specifically associated with two distinct phenomena; vibration buckling (parametric resonance) and dynamic pulse buckling. Vibration buckling, akin to resonance, transpires when structures respond to oscillating loads, resulting in an increased lateral vibration by amplification of motion through the interaction of dynamic loads with the system's natural frequencies (Singer et al., 2003). On the other hand, dynamic pulse buckling, as the name suggests, pertains to the behavior and instability of structures when subjected to pulse loads. In this thesis, the focus on dynamic loads will solely be on the latter.

The buckling behavior under dynamic loading is dictated by the amplitude of the pulse load and its duration. When an impulse load characterized by short duration and high amplitude hits a structure, it triggers an impact phenomenon. If the pulse aligns with the natural vibration period of the structure and the load amplitude is moderate, dynamic buckling ensues (Kubiak, 2013). Conversely, for prolonged pulse duration, the load behaves quasi-statically. A crucial point to note is that a shorter pulse may cause the dynamic critical load to surpass the static buckling load. This can be schematically represented as seen in Figure 2.10.

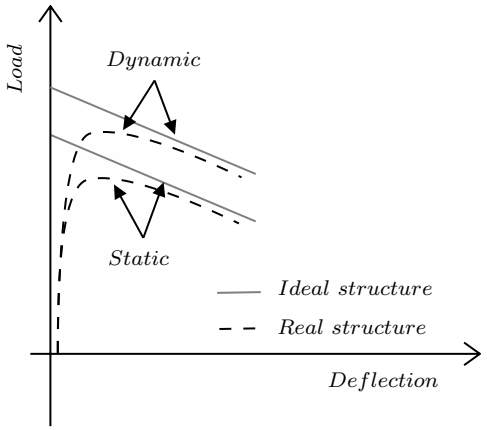

Figure 2.10: Schematic illustration of difference between static and dynamic buckling.

As previously discussed regarding pulse buckling, a fundamental difference between static buckling analysis and pulse buckling analysis emerges. In static buckling analysis, the primary emphasis lies in determining the mode of buckling and subsequently computing the maximum safe load under steady loads. Conversely, in pulse buckling analysis, the load's characteristics (amplitude and duration) directly dictate how the structure will buckle. This implies that identical structures may demonstrate different responses based on the particular attributes of the applied pulse load.

According to Kubiak (2013), damping effects have little impact on the dynamic response, hence, damping is disregarded when dealing with buckling within the elastic range. This is connected to the fact that during elastic deformation, structures absorb significantly more energy than what is dissipated through damping. Furthermore, ideal structures have infinite critical buckling amplitude and hence, dynamic stability loss occurs only in structures with initial imperfections.

Regarding imperfections, Koiter's theory, as discussed in (Mallon, 2008), emphasizes the distinction between stable initial post-buckling load paths (cf. Figure 2.4), which render structures insensitive to imperfections, and unstable secondary post-buckling load paths (cf. Figure 2.5), where imperfections lead to reduced load-bearing capacity. This theory becomes particularly pertinent in scenarios where multiple buckling modes are closely spaced or overlap, thereby amplifying the influence of imperfections.

2.4 Dynamics and Explosions

This section provides a comprehensive overview of explosions, exploring the dynamic principles and load effects linked with them. It covers different types of dynamic loads, wave propagation phenomenon, and the significance of internal work in structural reactions. Furthermore, the readers will gain insights into energy balance and the influence of pivotal parameters such as strength, stiffness, deformation capacity,

and mass. Additionally, deformations under different types of responses are elaborated and the concept of equivalent static load is presented. The following theories draw heavily from the works of Johansson and Laine (2012a–2012c).

2.4.1 Overview of Explosions

Nowadays, particularly within the field of structural engineering, the focus predominantly revolves around static loads. However, it is increasingly recognized as crucial to delve into the analysis of dynamic responses triggered by e.g. explosions. This necessity arises from the fact that explosions induce unique loads, distinct from the static ones typically encountered in conventional scenarios.

An explosion is characterized by an abrupt discharge of energy causing expansion in volume, which in turn leads to increased levels of light and temperature, accompanied by a significant rise in pressure (Johansson & Laine, 2012a). The wave pressure, originating from the explosion, starts to advance, disseminating rapidly across the surrounding area. As the distance from the centre of the explosion increases, the pressure diminishes. In context of explosions, one distinguishes between a positive phase and a negative phase. The positive phase arises when the pressure surpasses the atmospheric pressure, P_0, prompting the pressure wave to force air outward. This movement leaves behind a region of decreased pressure, or a vacuum, resulting in a negative phase where the pressure is below P_0. Figure 2.11 schematically describes the phenomenon of pressure waves with emphasized arrival time (the time it takes for a wave to reach e.g. an object), t_a.

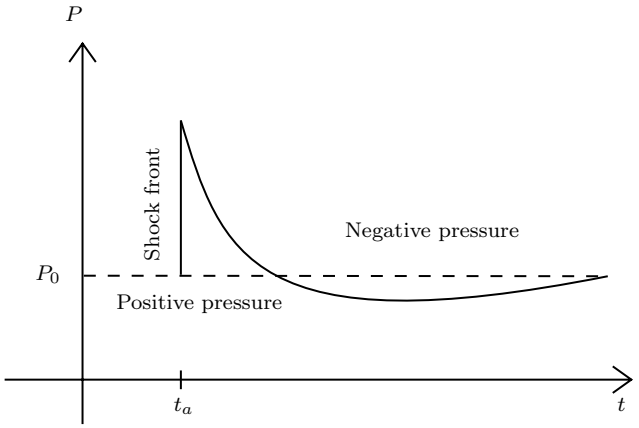

Figure 2.11: Pressure-time representation of pressure wave with positive and negative phase. Based on Johansson and Laine (2012a).

As indicated by Johansson and Laine (2012a), the depiction of Figure 2.11 is frequently simplified to focus solely on the positive phase, which is often linearly represented, as seen in Figure 2.12. The reason for this simplification is that the negative phase generally exerts a minor influence on the overall behavior.

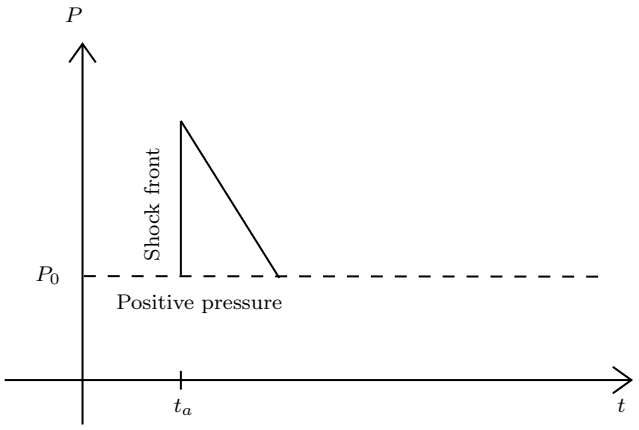

Figure 2.12: Simplified linear representation of pressure wave with solely the positive phase. Based on Johansson and Laine (2012a).

In the context of explosion and wave theory, four fundamental concepts are well-known. These concepts provide insights into the behavior of waves within complex geometric environments (e.g. urban areas). Brief descriptions of these concepts are presented below and further illustrated in Figure 2.13.

- **Diffraction** - Waves bend around obstacles or edges of e.g. buildings.
- **Reflection** - Waves bounce back when encountering surfaces, typically changing their direction.
- **Mirroring** - Phenomenon that occurs when an explosion happens on or near another surface. The effect is that the energy spreading to the surroundings corresponds to the energy from a charge twice as large if it could propagate freely.
- **Confinement** - Buildings hinder propagation of waves, causing energy dissipation to occur at a slower rate than if the waves would travel unimpeded.

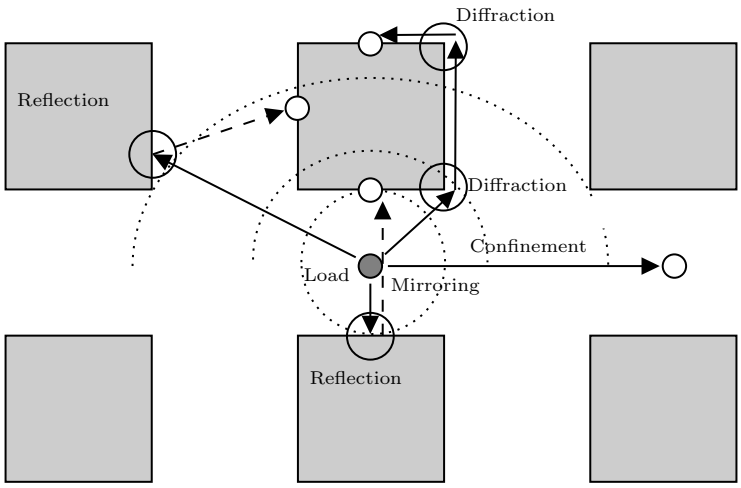

Figure 2.13: Diffraction, reflection, mirroring, and confinement in a complex environment. Based on Johansson and Laine (2012b).

Understanding these phenomena is crucial, as they not only shape the behavior of waves, but also significantly influence how loads are dispersed within complex environments.

2.4.2 Impulse Load and Impulse Density

An impulse load refers to a sudden application of force over a short duration. This type of load is commonly encountered in situations involving shock waves from explosions or collisions between two bodies, leading to a rapid change in momentum (Johansson & Laine, 2012c). Mathematically, impulse is determined as the integral of the applied load and its duration, see Equation 2.10. Impulse density, another term often linked with impulse loading, is instead obtained by multiplying the pressure by the duration of the force application, see Equation 2.11.

$$I = \int_{t_1}^{t_2} F(t)dt \tag{2.10}$$

$$i = \int_{t_1}^{t_2} P(t)dt \tag{2.11}$$

A graphical illustration of the two concepts is found in Figure 2.14.

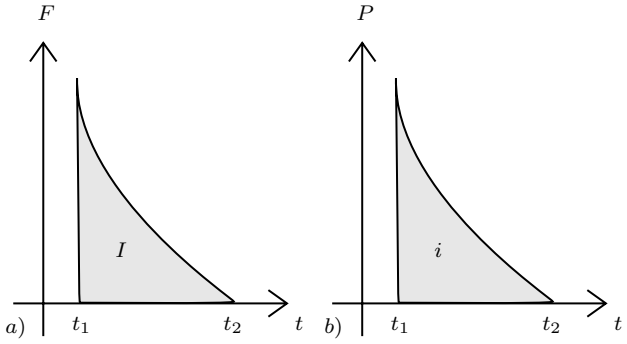

Figure 2.14: The area under the curve represents: a) Impulse & in b) Impulse density. Based on Johansson and Laine (2012c).

Comprehending impulse loads is crucial in various fields, especially in structural engineering, given their potential to induce substantial dynamic effects and structural reactions.

2.4.3 Types of Dynamic Loads

When considering dynamic loading, it is possible to distinguish between two extreme load scenarios: a characteristic impulse load and a characteristic pressure load. Characteristic impulse load, denoted as I_k, is defined as a time-varying load with infinitely high pressure and infinitesimal duration (Johansson & Laine, 2012c). Conversely, for characteristic pressure load, F_k, the load is exerted by an infinitely long shock wave. The two depicted load scenarios are illustrated in Figure 2.15.

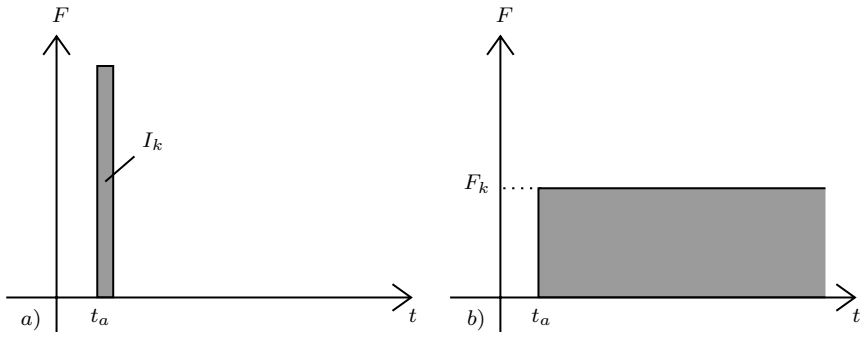

Figure 2.15: Extreme dynamic load scenarios: a) Characteristic impulse load & b) Characteristic pressure load. Based on Johansson and Laine (2012c).

Given that these represent two extreme scenarios, in practice, an arbitrary load with duration represented by $F(t)$ will most likely fall between these two extremes. A prolonged load tends to exhibit characteristics similar to a characteristic pressure load, while a brief load tends to resemble a characteristic impulse load.

2.4.4 Dynamic Concepts

In order to comprehend the effect of the shock-wave from an explosive load on a structure, it is essential to acquaint oneself with fundamental dynamic concepts. The reasoning of the concepts is based on a single-degree-of-freedom (SDOF) system, see Figure 2.16 for visual representation of the system with specified parameters.

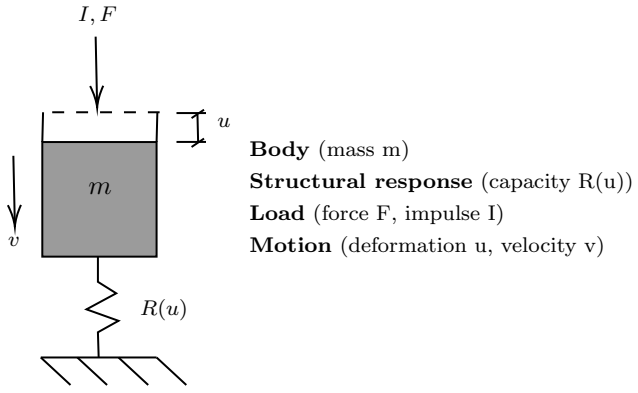

Figure 2.16: SDOF system.

For a body with mass, m, and velocity, v, the impulse (momentum), I_k and the kinetic energy, E_k, can be described by Equation 2.12 and 2.13.

$$I_k = mv \tag{2.12}$$

$$E_k = \frac{mv^2}{2} \tag{2.13}$$

By combining Equation 2.12 and 2.13, a different representation for kinetic energy in relation to momentum is denoted as per Equation 2.14. This alternative expression highlights the connection between kinetic energy and momentum. Furthermore, it is noteworthy that kinetic energy can be viewed as external work, W_y, introducing the possibility of applying Equation 2.15, where W_y corresponds to E_k.

$$E_k = \frac{I_k^2}{2m} \tag{2.14}$$

$$W_y = E_k = \frac{I_k^2}{2m} \tag{2.15}$$

Beyond external work, another pivotal aspect in understanding the dynamic behavior of structures is internal work (W_i), which refers to the energy absorbed by a structure in response to external loads. It can be defined as absorbed energy per deformation, u, as expressed by Equation 2.16, where $R(u)$ corresponds to the resistance force.

$$W_i = \int_0^u R(u)du \tag{2.16}$$

2.4.5 Wave Propagation Phenomenon

When assessing the structural integrity of a construction, it is essential to note that the initial global response of a dynamically loaded structure can significantly diverge from what is observed under equivalent static loading conditions. In both static and dynamic loading situations, an important phenomenon known as wave propagation transpires, highlighting that the transmission of information within a material requires time. This phenomenon becomes particularly evident during impulse loading, characterized by high pressure and short duration. For such loading scenario, certain parts of a structure may fail locally before others are influenced. This occurs due to a delay in the propagation of load information through the material, resulting in time-dependent BC for the structure's initial response (Carlsson & Kristensson, 2012). As an illustration of the concept, consider the response of the frame structure subjected to a leftward load in Figure 2.17.

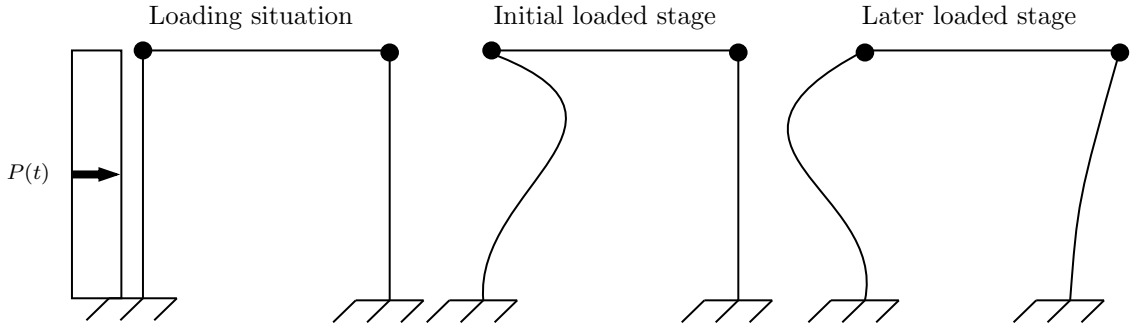

Figure 2.17: Structural response of frame subjected to an impulse load in the initial & the later stages. Based on Johansson and Laine (2012c).

The deformation patterns observed in Figure 2.17 suggests that in the initial stage, only the left member of the frame is influenced by the load, resulting in its deformation. This is because the rear member (right member) has not yet received information about the explosion. With time, the information reaches the rear member, causing it to deform as well. However, as observed, the left member deforms in the opposite direction compared to the initial stage, due to the structure being in oscillation. As previously mentioned, rapid loading can lead to localized failures in parts of a structure before others are affected.

2.4.6 Energy Balance

When a structure is exposed to a dynamic load, kinetic energy is introduced (Johansson & Laine, 2012c). The kinetic energy needs to be counteracted by an internal work which is the response of the structure. A schematic illustration of the phenomenon is depicted in Figure 2.18.

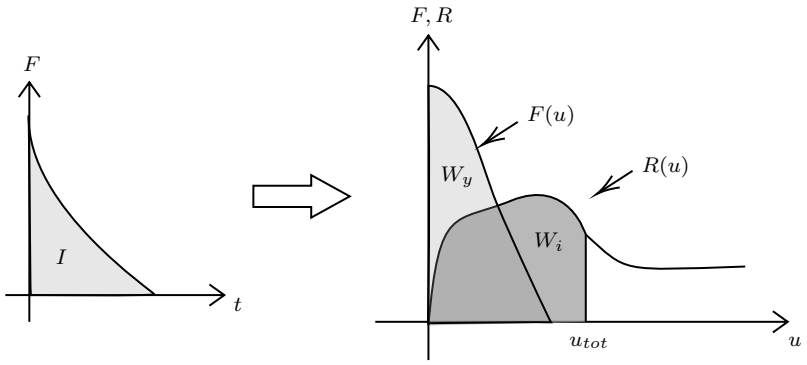

Figure 2.18: Left: Arbitrary impulse load. Right: Interaction between W_e caused by $F(u)$, and W_i induced by $R(u)$. The ultimate deformation, u_{tot}, is determined when equilibrium in energy is reached, i.e., W_i=W_y. Based on Johansson and Laine (2012c).

In Figure 2.18, an arbitrary impulse load ($F(t)$), results in the development of kinetic energy in a body with mass. The external work corresponding to this energy can obtained by integration of the resulting external relationship between load and deformation, $F(u)$, acting on the body. Similarly, with reference to the internally generated resistance force ($R(u)$), within the structure, the internal work can be characterized.

2.4.7 Internal Work as Structural Response

In the examination of structural behaviour, intrinsic characteristics such as strength, stiffness, and deformation capacity become important factors (Johansson & Laine, 2012c). Under diverse loading conditions constructions exhibit distinct reactions. This awareness forms the foundation for examining the three primarily type of responses: elastic, plastic and elastoplastic. A summary of the depicted responses is illustrated in Figure 2.19.

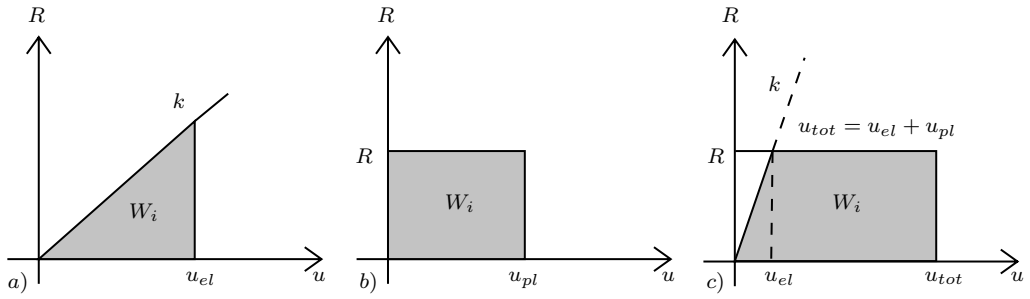

Figure 2.19: Structural responses: a) Elastic b) Plastic & c) Elastoplastic. Based on Johansson and Laine (2012c).

In the case of elastic behavior, which is defined by a constant stiffness, k, the structure exhibits flexibility and does not undergo permanent deformation (Johansson & Laine, 2012c). A plastic response occurs when a structure reaches its capacity limit (R). This results in a plastic deformation, u_{pl}, which upon unloading is irrecoverable. The elastoplastic behaviour has characteristics of both the elastic and the plastic response, in which the structure initially displays elastic behaviour with stiffness k, until the capacity is reached, and beyond this point, plastic behaviour is ensued eventuating in permanent plastic deformation.

2.4.8 Influence of Critical Parameters

In the design and analysis of statically loaded structures, the parameters stiffness and load-bearing capacity are usually critical, since they play an essential role in supporting the designated load while minimizing deformations (Johansson & Laine, 2012c). Conversely, when a structure is exposed to a sudden and strong impulse load, it is often difficult to ascertain that the load in question reaches the level corresponding to its maximum static load-bearing capacity. Hence, in such scenarios, it is preferable and necessary to harness the structure's deformability.

The capacity of a structure to absorb energy is shaped up by an interplay of the applied force and the subsequent deformation (Johansson & Laine, 2012c). If a structure exhibits high deformation capacity and low load-bearing capacity, it results in increased energy absorption. In contrary, a structure with low deformation capacity and high load-bearing capacity yields lower energy absorption, see Figure 2.20. In the context of distinguishing between structures experiencing static and impulse loads, it becomes essential for a structure exposed to dynamic loading to showcase ductile behaviour. This is because optimal deformation capacity leads to increased energy absorption, as opposed to prioritizing high stiffness and load-bearing capacity, which are of greater significance in statically loaded structures.

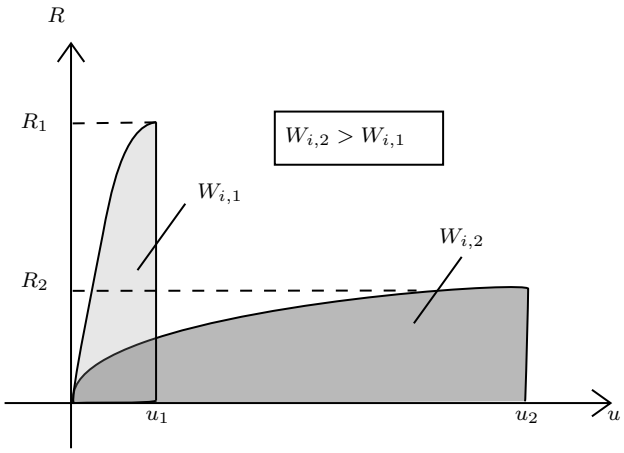

Figure 2.20: Comparison between a structure with high stiffness and low deformation capacity and a structure with low stiffness and high deformation capacity. Based on Johansson and Laine (2012c).

Figure 2.20 suggests that the internal work during static loading is lower than that during dynamic loading. Concurrently, dynamic loading results in higher deformation ($u_2 > u_1$).

Another critical parameter that influences the external work is the mass of the structure. According to Newton's second law (a = F/m), to induce an acceleration, a, in an object with mass, a greater force is required as the mass increases. Similarly, it is evident (cf. Equation 2.15) that an increasing mass leads to an inversely proportional demand for energy absorption capacity in the structure (Johansson & Laine, 2012c).

2.4.9 Deformation under Various Types of Responses

Taking into account the three structural responses (cf. Section 2.4.7) and a characteristic impulse load enables the determination of a structure's deformation (Johansson & Laine, 2012c). The internal work performed in linear elastic response can be expressed according to Equation 2.17.

$$W_i = \frac{k u_{\text{el}}^2}{2} \tag{2.17}$$

With the external work obtained as previously (cf. Equation 2.15), energy equilibrium yields an expression for the elastic deformation, u_{el}, provided in Equation 2.18.

$$u_{el} = \frac{I_k}{\sqrt{mk}} = \frac{I_k}{m\omega} \tag{2.18}$$

The angular frequency in Equation 2.18 can be expressed by Equation 2.19.

$$\omega = \sqrt{\frac{k}{m}} \tag{2.19}$$

By similar reasoning, plastic deformation in plastic response is obtained in accordance with Equation 2.20.

$$u_{pl} = \frac{I_k^2}{2mR} \tag{2.20}$$

In the case of elastoplastic response, the internal work can be expressed as follows.

$$W_i = \frac{R}{2}(u_{\mathrm{el},1} + 2u_{\mathrm{pl},1}) \tag{2.21}$$

Through the application of the external work expression and energy balance, rearrangement of terms provides formula for the plastic deformation, $u_{pl,1}$, see Equation 2.22.

$$u_{pl,1} = u_{\mathrm{pl}} - \frac{u_{\mathrm{el},1}}{2} \tag{2.22}$$

Finally, the total deformation, u_{tot}, is acquired by summation of the elastic and the plastic deformation, see Equation 2.23.

$$u_{tot} = u_{\mathrm{el},1} + u_{\mathrm{pl},1} = u_{\mathrm{pl}} + \frac{u_{\mathrm{el},1}}{2} \tag{2.23}$$

Compilation of aforementioned deformations under various types of responses is illustrated in Figure 2.21.

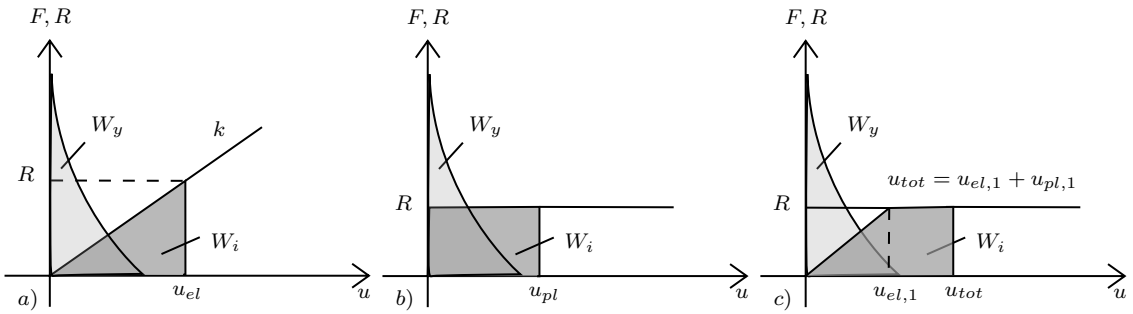

Figure 2.21: Displacements responses under different material behaviors: a) Elastic b) Plastic & c) Elastoplastic. Based on Johansson and Laine (2012c).

2.4.10 Equivalent Static Load

The structural response of a structure subjected to dynamic and static loads can differ greatly, especially with intense but short dynamic impulses. In design, dynamic effects are typically not explicitly considered, instead, simplified static loading models are used. An often employed method, known as equivalent static load, involves determining a static load's magnitude and distribution to match and correspond to the external work of the dynamic load (Johansson & Laine, 2012c).

The differences between a dynamic load and an equivalent static load can be demonstrated by considering a situation where a shelter is exposed to an explosion occurring five meters away with an equivalent pressure wave to that generated by a 125

kg explosive material, trinitrotoluene (TNT). This situation is used as reasoning behind designing against explosion loads in Swedish shelters.

As consequence of the explosion, a pressure peak of 5 MPa is observed, which then decreases to almost zero pressure in about 3 ms, resulting in an impulse of around 2800 Pas (Johansson & Laine, 2012c). Considering now a static load scenario for shelter design with regards to explosion, the load is presumed to exert uniform pressure from all directions, set at a constant 50 Pa. Both scenarios are illustrated as pressure-time relationships in Figure 2.22.

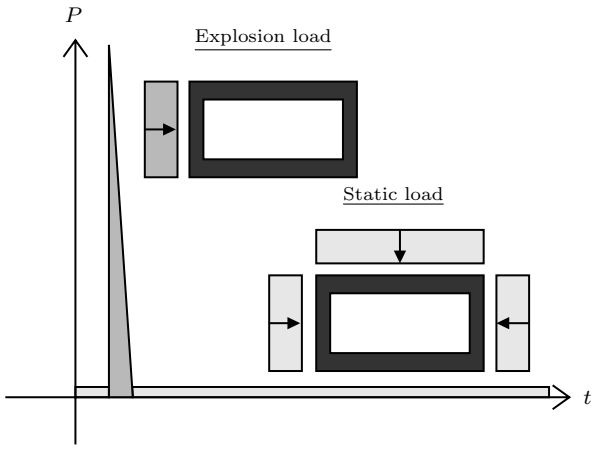

Figure 2.22: Schematic illustration of explosion load and equivalent static load. Based on Johansson and Laine (2012c).

The comparison in Figure 2.22 reveals that the maximum pressure from the dynamic impulse load is approximately 100 times greater than the pressure exerted by the equivalent static load. However, it should be noted that for the explosion load, it is not the magnitude of the pressure that is important, rather the size of the impulse. This load corresponds to a characteristic impulse load.

For structures governed by elastic structural response to impulse loads, the expression for the equivalent static load is determined by the static load that results in the same maximum deformation as the dynamic load, see Equation 2.24.

$$Q = ku_{\text{el}} \tag{2.24}$$

By utilizing the expression for elastic deformation (cf. Equation 2.18), the equivalent static load can be expressed in terms of characteristic impulse load and angular frequency, as shown in Equation 2.25.

$$Q = I_k w \tag{2.25}$$

In the case of plastic response, the expression for the equivalent static load can be obtained as followed. First, the external work is expressed in terms of static load and plastic deformation, see Equation 2.26. By rearranging terms, this expression, along with the equation for external work (cf. Equation 2.15) results in Equation 2.27.

$$W_y = Qu_{\text{pl}} \tag{2.26}$$

$$Q = \frac{I_k^2}{2mu_{\text{pl}}} \tag{2.27}$$

Lastly, with the aid of Equation 2.20 one arrives at a final expression for the equivalent static load, as outlined in Equation 2.28.

$$Q = R \tag{2.28}$$

Further exploring the elastoplastic response, one can in similar manner derive the expression for the equivalent static load, which is identical to Equation 2.28. However, unlike the plastic response where the resistance force is solely influenced and determined by the plastic displacement, in this case, the resistance force is contingent upon both the elastic displacement and the plastic displacement (Johansson & Laine, 2012c).

2.5 Strain Rate

This section centers on strain rate, placing specific emphasis on examining indices associated with strain rate effects. It underscores the significance of inertia and strain rate effects during dynamic loads. Additionally, it discusses various strain rate effect models.

2.5.1 Various Actions and Corresponding Strain Rates

In materials science and civil engineering, there exists a parameter referred to as strain rate, denoted by $\dot{\epsilon}$. It represents the rate at which a material undergoes deformation (change in strain) over time under applied loads. For a general definition of strain rate, see Equation 2.29.

$$\dot{\epsilon} = \frac{\epsilon}{\Delta t} \tag{2.29}$$

Structures experience varying strain rates depending on the nature of the loads applied to them. These strain rates are classified according to their magnitude and the underlying actions (Yang et al., 2022). The contrast between different types of actions and their generated strain rates is illustrated in Figure 2.23.

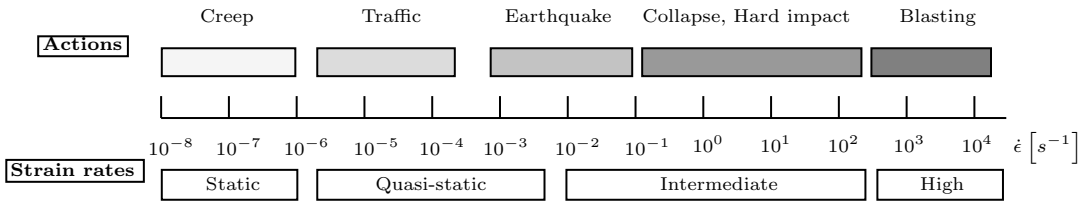

Figure 2.23: Strain rates for different types of actions. Based on Yang et al. (2022).

It can be identified that quasi-static loading is characterized by strain rates ranging from approximately 10^{-5} s^{-1} to 10^{-3} s^{-1}, while strain rates $\leq 10^{-6}$ s^{-1} represent static loading. Conversely, strain rates of 10^{-2} s^{-1} and higher describe dynamic loading conditions.

Furthermore, upon reviewing Figure 2.23, it becomes apparent that blasting often exhibits an exceptionally rapid load rate during a short duration. The typical magnitude of explosion force may result in strain rates approximately 100 million times or more faster than those induced by a static load (Johansson & Laine, 2012c).

2.5.2 Indices of Strain Rate Effects

According to Yang et al. (2022), three different indices are usually employed to assess the effects of strain rate in structural steel. The first index is DIF_y and stands for dynamic increase factor for yield strength. It is the ratio of the dynamic yield strength, $f_{y,d}$, to the static yield strength (f_y), as given by Equation 2.30.

$$DIF_y = \frac{f_{y,d}}{f_y} \tag{2.30}$$

There is also a dynamic increase factor for ultimate tensile strength, abbreviated as DIF_u (Yang et al., 2022). This parameter is expressed as the ratio of the dynamic ultimate tensile strength, $f_{u,d}$, to the static ultimate tensile strength (f_u), as defined by Equation 2.31.

$$DIF_u = \frac{f_{u,d}}{f_u} \tag{2.31}$$

The third index is DIF_{avg}, an average dynamic increase factor for the full dynamic true stress-plastic strain relationship (Yang et al., 2022). To obtain the index of interest, DIF_i is first determined at designated strain intervals from the yielding point. Here, the DIF_i is calculated as the ratio of the dynamic stress, $\sigma_{i,d}$, to the quasi-static stress, $\sigma_{i,s}$, in which the subscript letter i is the count of the defined strain intervals, see Equation 2.32.

$$DIF_i = \frac{\sigma_{i,d}}{\sigma_{i,s}} \tag{2.32}$$

A relationship between DIF_i and true plastic strain, $\epsilon_{\text{true,pl}}$, is then formulated for specific strain rates. Lastly, DIF_{avg} is established by transforming DIF_i into mean values using Equation 2.33. For illustrative definitions of the indices DIF_y, DIF_u and DIF_i, see Figure 2.24.

$$DIF_{avg} = \frac{\sum DIF_i}{i} \tag{2.33}$$

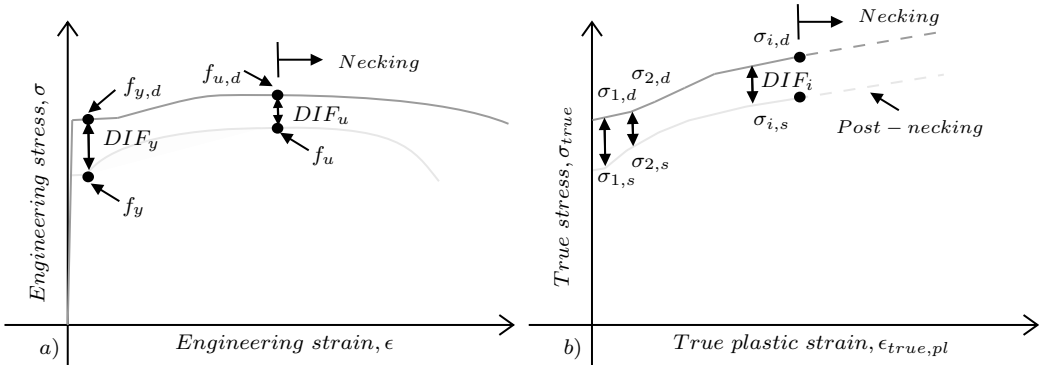

Figure 2.24: Visualization of strain rate effect indices: a) DIF_y and DIF_u & b) DIF_i. Based on Yang et al. (2022).

The material response from the point of yielding is illustrated by the quasi-static and dynamic curves, represented by the light solid grey and the dark lines in Figure 2.24. All pertinent parameters for calculating the indices, along with the indices themselves, are also visually presented in the figure. Additionally, it features the location of necking and the post-necking stage (tension). Observe that the conversion of engineering stress, σ, and strain, ϵ, to true stress, σ_{true} and true strain, ϵ_{true} is obtained through the relations in Equation 2.34 and Equation 2.35, respectively (Yang et al., 2022). The true plastic strain ($\epsilon_{true,pl}$) is then determined by subtracting the true elastic strain, $\epsilon_{true,el}$, from true strain (ϵ_{true}), as seen in Equation 2.36.

$$\sigma_{true} = \sigma(1 + \epsilon) \tag{2.34}$$

$$\epsilon_{true} = \ln(1 + \epsilon) \tag{2.35}$$

$$\epsilon_{true,pl} = \epsilon_{true} - \epsilon_{true,el} = \epsilon_{true} - \frac{\sigma_{\text{true}}}{E} \tag{2.36}$$

It is worth emphasising that the selection between true stress-strain or engineering strain-strain is dictated by the modeling approach and the behavior of the material being simulated. In the context of thin-walled structures, where Finite Element (FE) modeling often relies on shell elements, it is recommended to utilize true stress and true strain. This preference stems from the fact that shell elements accurately incorporate changes in area and dimensions as the material undergoes plastic deformation. As highlighted by Roylance (2001), the material's response during plastic deformation is more accurately described by the utilization of true stress and true strain.

Of the three presented indices, the most commonly utilized index in engineering applications is DIF_y (Yang et al., 2022). However, as Yang et al. (2022) state, applying this approach as a dynamic increase factor (DIF) to the entire quasi-static stress–strain curve may eventuate in predictions of the response that are not completely precise. One reason for the inaccuracy is the propensity of structural steel to undergo significant deformation well beyond its yield point, particularly when exposed to events such as explosions. Secondly, the increase in dynamic yield strength,

when compared to the quasi-static yield strength, usually is greater than the dynamic increment observed at all the other points on the stress–strain curve. Consequently, employing DIF_y tends to overestimate the expected material response. Another aspect is related to the measured values and their sensitivity to errors. In Split Hopkinson Pressure Bar (SHPB) tests, errors in measured values can arise due to non-uniform stress distribution within the elastic range (Yang et al., 2022). The SHPB is a testing machine used for measuring and assessing dynamic mechanical properties of specimens under high strain rates ($\geq 10^2\,\mathrm{s}^{-1}$).

The use of the dynamic amplification factor for DIF_u also introduces several challenges. Firstly, conducting compressive tests using the SHPB method at high strain rates, indicative of explosive or high-speed actions, makes it unachievable to establish DIF_u (Yang et al., 2022). This is due to the continuous increase in compressive stress without reaching a distinct peak, resulting in an insufficiency of data values of DIF_u at the studied strain rates. Furthermore, the approach underestimates the expected constitutive response, as the amplitude of DIF_u is typically less than the amplitude of DIF_y at a certain strain rate.

Given the constrains associated with both DIF_y and DIF_u, a more comprehensive factor for determining a representative model of the dynamic stress-strain relationship is DIF_{avg} (Yang et al., 2022). Among the three indices, this approach is deemed the most suitable for correlating the strain rate dependency with the constitutive response of structural steel after yielding.

2.5.3 Strain Rate and Inertia Effects under Dynamic Loading

In the context of dynamic loading, comprehending the effects of inertia and strain rate is pivotal. When structures are subjected to dynamic loading, the resulting deformations and stresses become strain dependent. During deformation, effects of stress wave propagation and inertia are notably pronounced, thereby altering the material properties, affected by the strain rates (Német & Mihaliková, 2013). The material's response to different strain rates presents a favorable characteristic, as it leads to observed strengthening effects, which can contribute to an enhanced structural safety (Nassr, 2012). In the case of steel columns, a substantial increase in yield strength induced by strain rate has the potential to change the dynamic response of the material.

The significance of inertia resistance becomes crucial when structures are subjected to impulse loads, such as blast loads. This is elucidated through the examination of solution derived for an SDOF system under a triangular impulse load (Hao, 2015). The fundamental underlying theory explaining this importance is the exceptionally brief duration of the load. Under such loading scenarios, the structural response is initially dictated by acceleration, followed by displacement with a phase shift occurring after the acceleration. The application of dynamic load thus involves the induction of initial acceleration, followed by velocity, and ultimately displacement.

It is essential to highlight that, due to the short duration of such events, displacement may not even be initiated (catch up), particularly as the displacement in the elastic phase of the structural response is small (Hao, 2015). For this reason, impulse loads are predominately resisted by the structural inertia. Consequently, increasing the mass of a structure can enhance its resistance against dynamic loads.

Moreover, depending on the loading rate, the governing response and failure mode exhibit disparities when comparing static and low rate loading to high rate loading. Hao (2015) mentions that, for instance, a flexible structure subjected to high-rate loading may experience failure at very small displacements.

The topic of strain rate effects is also significant as these effects influence the structural response of steel structures. Typically, impulse loading is characterized by the generation of high strain rates in the loaded structural elements (Nassr, 2012). Studies employing models developed from data and results, such as those obtained from SHPB tests, show that certain parameters are affected by the loading rates. The findings indicate a noticeable increase in the material's yield strength when subjected to higher loading rates. Additionally, there is an observed rise in the ultimate tensile strength, while the material's modulus of elasticity shows no significant sensitivity to these changes.

2.5.4 Strain Rate Effect Models

To evaluate the influence of strain rate effects on the dynamic characteristics of structural steel, numerous models have been developed, two of which are commonly utilized in the field of impulse-loaded structures. Recognized for their simplicity and high precision, these models are available and can be implemented in FE software such as Abaqus CAE (Yang et al., 2022).

One notable model is the Cowper-Symonds (CS) material model. The model has the advantage that it can be used on a stress-strain curve for steel that features a yield plateau. Describing the influence arising from both strain- and strain rate hardening, the model is characterized by Equation 2.37. Here, p and D are strain rate material parameters (Yang et al., 2022).

$$\frac{\sigma_{y,d}}{\sigma_y} = DIF = 1 + \left(\frac{\dot{\epsilon}}{D}\right)^{\frac{1}{p}} \tag{2.37}$$

Another existing model, the Johnson-Cook (JC) material model, as outlined by Equation 2.38, also takes into account thermal softening effects, wherein the material's strength and hardness decrease with elevated temperature (Yang et al., 2022). Further key feature is the assumption that the material, unlike CS-model, does not exhibit a distinct yield plateau, but instead follows a stress-strain curve akin to that of cold-worked steel.

$$\sigma = \left[A + B{\epsilon_p}^n\right]\left[1 + C\ln\epsilon^*\right]\left[1 - T^{*m}\right] \tag{2.38}$$

Within this context, ϵ^* represents the strain rate at the reference strain rate ($\dot{\epsilon}_0$), expressed by Equation 2.39, while the dimensionless temperature term, T^*, is defined by Equation 2.40, where T, T_m, and T_r denote the test, melting, and room temperatures, respectively.

$$\varepsilon^* = \frac{\dot{\varepsilon}}{\dot{\varepsilon}_0} \tag{2.39}$$

$$T^* = \frac{T - T_r}{T_m - T_r} \tag{2.40}$$

All the other parameters in the JC-model are material constants (cf. Equation 2.38). Here, A represents the initial yield strength of the steel at quasi-static strain rates, B is a strain hardening constant at quasi-static strain rates, and C accounts for the strain rate effects (Nam et al., 2015). The effect of thermal softening is considered through the exponential constant, m, and the exponential strain hardening coefficient, n. Note that the constants A, B, and n can be determined based on the results obtained from e.g. various strain rate tensile tests.

To calculate the DIF for $f_{y,d}$, Equation 2.41 can be employed, where the material parameters D_y and p_y are determined through the application of Equation 2.42 and 2.43, as proposed by Yang et al. (2022).

$$\frac{f_{y,d}}{f_y} = DIF_y = 1 + \left(\frac{\dot{\epsilon}}{D_y}\right)^{\frac{1}{p_y}} \tag{2.41}$$

$$D_y = 1000(\frac{f_y}{235})^{3.8} \tag{2.42}$$

$$p_y = 5(\frac{f_y}{235})^{-0.5} \tag{2.43}$$

Similarly, a model inspired by CS is also established to determine the DIF_{avg} (Yang et al., 2022). The expression is defined by Equation 2.44 with the input parameters D_{avg} and p_{avg} calculated according to Equation 2.45 and 2.46, respectively.

$$DIF_{avg}(\dot{\epsilon}, f_y) = 1 + \left(\frac{\dot{\epsilon}}{D_{avg}}\right)^{\frac{1}{p_{avg}}} \tag{2.44}$$

$$D_{avg} = 1000(\frac{f_y}{235})^{6} \tag{2.45}$$

$$p_{avg} = 3(\frac{f_y}{235})^{0.2} \tag{2.46}$$

To demonstrate the impact of $\dot{\epsilon}$ and f_y on DIF for both cases, DIF_y and DIF_{avg} are determined using the aforementioned approaches for three different structural steel grades: S235, S355 and S460. The results, illustrating the variation in DIF_y and DIF_{avg} values for the studied steel qualities are visualized in Figure 2.25.

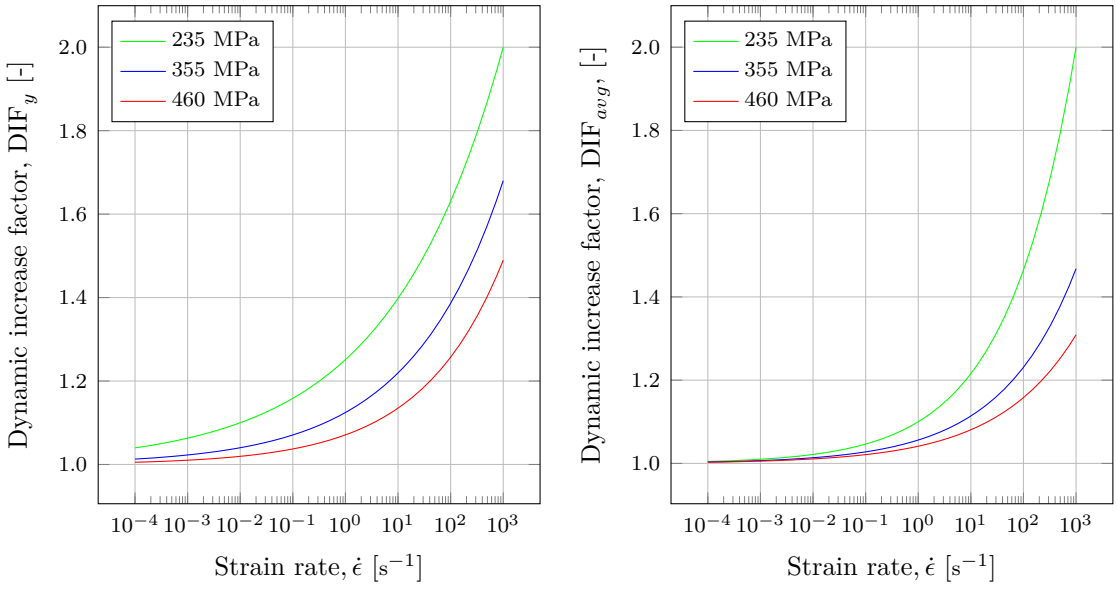

Figure 2.25: DIF as function of strain rate and yield strength for S235, S355 and S460: a) DIF_y & b) DIF_{avg}.

From Figure 2.25, it is evident that the DIF values are strongly dependent on both yield strength and strain rate, with DIF_y being larger than DIF_{avg}, particularly at elevated strain rates.

3 Numerical Analyses

This section provides essential insights into the numerical analyses and the implementation of non-linear finite element analysis (FEA) using the FE software Abaqus CAE. Specifically, the section explores the two main solution methods within FE software for solving a range of static and dynamic problems. Additionally, it delves into techniques for load application and describes the nonlinearities of steel pertinent to the study. Various types of finite elements available in Abaqus CAE and discussions on convergence aspects are also covered.

3.1 Different Types of Nonlinearities

In the assessment of structures using FE software, it is conventional to conduct linear FEA. Such analyses are built upon simplified models, assuming a linear elastic relationship in material response, while simultaneously neglecting potential effects from structural changes, e.g., alterations in geometry. However, those assumptions are not entirely true, given that structural behavior often exhibits nonlinearities stemming from various factors. Two notable examples of such nonlinearities in steel structures involve both non-linear material and geometrical responses. These parameters are of particular interest in the subsequent numerical analyses of the investigated steel rods.

Material nonlinearity is attributed to the non-linear relationship in the stress-strain response of steel. This occurs as the material under applied load undergoes yielding, plastic deformation, and experiences strain hardening, among other factors. **Geometric nonlinearity**, on the other hand, pertains to phenomena such as large deformations and rigid body movement of a structure (Zhang et al., 2023). These effects can lead to changes in the structure's configuration and stiffness, which linear FEA cannot accurately represent. Illustrations of these nonlinearities are presented in Figure 3.1.

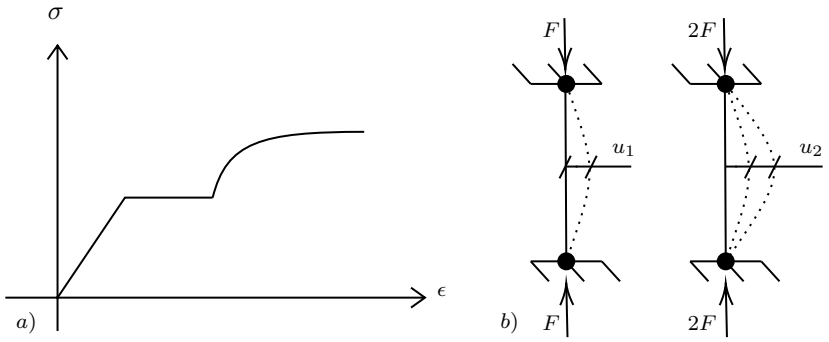

Figure 3.1: Examples of nonlinearities: a) Non-linear material response of steel & b) Non-linear geometric response of a steel member under compression.

From Figure 3.1 a), it is evident that a pronounced non-linear relationship exists between stress and strain for the material. Furthermore, Figure 3.1 b) displays the

substantial increase in deflection of the steel member supported at its short ends as the compressive axial load is doubled.

It is also essential to highlight that the buckling behavior of long and slender steel members subjected to compressive axial forces can be significantly influenced by non-linear geometry. In such cases, the assumption of small deformations may no longer be valid. Moreover, the instability aspect is indirectly affected by initial imperfections, i.e., deviations or irregularities in the ideal geometric element before any load application. Even minor unintended imperfections can magnify the structural member's deformation by introducing second-order moments (Zhang et al., 2023). Consequently, this can lead to buckling failure at load levels much lower than those initially anticipated.

Non-linear FEA is an indispensable tool for accurately depicting the real-world behavior of materials like steel, which exhibit an elastic-plastic nature and, consequently, feature non-linear stress-strain relationship (Zhang et al., 2023). Therefore, it is paramount to employ appropriate material models in numerical analyses to precisely capture variations in stiffness caused by yielding and plasticity. Equally crucial is the consideration of non-linear geometry and initial imperfections in the structural model. This can ensure a more realistic representation of the buckling behavior of the studied steel rods under compressive quasi-static and dynamic loading conditions.

3.2 Solution Methods for Static and Dynamic Analyses

In the context of non-linear FEA a non-linear relationship emerges between displacement and load. The solution of these systems relies on subdividing the load into multiple incremental steps, where the displacement at a particular stage is contingent upon the displacements observed in preceding stages, thereby introducing a historical dependency to the analyses (Plos et al., 2021). As a result, depending on the treatment of load incrementation, two alternative solution methods can be distinguished: the **implicit solution method** and the **explicit solution method**.

3.2.1 Implicit Method

This solution technique, valid and suitable for both dynamic and static analyses, requires equilibrium conditions for each increment and is based on an iterative procedure, as it entails information from both previous and current load increments (Plos et al., 2021).

The implicit solution approach involves establishing an approximate linear stiffness of the system at each step, which relates the load and displacement increments through a linearized representation (Plos et al., 2021). In general, various iterative methods can be employed within the implicit approach to generate a solution.

Although all these methods share a common procedure, distinctions arise in the determination of the stiffness matrix. Due to these differences, the iterative methods are classified into three groups: the tangent stiffness method, the initial stiffness method, and the secant stiffness method.

The foundation of the **tangent stiffness method**, also known as regular Newton-Raphson iteration method lies in the computation and updating of the stiffness matrix in every iteration during the solution process (Plos et al., 2021). Therefore, the stiffness is updated in each iteration. While this method often demands a reduced number of iterations, the individual iterations themselves can be time-intensive, thus impacting the overall computational time for the analysis.

On the contrary, the **initial stiffness method** calculates the stiffness matrix at the onset of every load step, maintaining its consistently application throughout the entire iteration process within the increment (Plos et al., 2021). The stiffness is hence updated only at the beginning of every load step. In comparison to the aforementioned method concerning convergence, the initial stiffness approach necessitates an increased number of iterations. Nevertheless, these iterations are executed more rapidly as each increment employs the same constant stiffness matrix.

The final category of the iterative methods is the **secant stiffness method** which updates the inverse of the stiffness matrix in every iteration, utilizing the information acquired from prior solutions (Plos et al., 2021). This method, sometimes referred to as quasi-Newton iteration method, results in a convergence that falls between the two previously mentioned methods. For schematic illustrations of the three described methods for an SDOF system, see Figure 3.2.

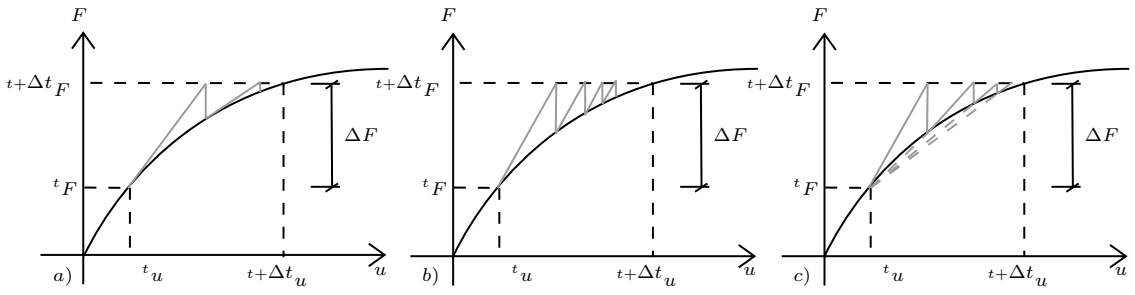

Figure 3.2: Visualization of three iterative methods for a SDOF system: a) tangent stiffness method, b) initial stiffness method & c) secant stiffness method. Based on Plos et al. (2021).

In Figure 3.2, ${}^{t}u$ and ${}^{t+\triangle t}u$ represent the displacement at the current and the next time step (increment), respectively, while ${}^{t}F$ and ${}^{t+\triangle t}F$ symbolize the corresponding load levels (force). In addition, the solid grey lines depict the variation in the stiffness matrix (slope) within each increment, whereas the dashed grey line in Figure 3.2 c) illustrates the secant stiffness.

3.2.2 Explicit Method

In contrast to the implicit method, the equilibrium in each increment in this approach is exclusively derived from information related to earlier load increments (Plos et al., 2021). Moreover, the need for an iterative procedure is eliminated due to the availability of the required information for computation. This technique is commonly used in dynamic analyses, yet it can also simulate the effects arising from static loading.

For this particular solution method, equilibrium is attained without the necessity for iterative procedures (Plos et al., 2021). This is because it focuses on fulfilling dynamic equilibrium rather than static equilibrium, where the displacement in the subsequent increment depends solely on the stiffness and the displacement from former load step.

However, there are also drawbacks to the explicit solution method, with one limitation pertaining to the load incrementation. Specifically, the size of the time steps may become very small due to the requirement for the load increment to adhere to specific conditions (Plos et al., 2021). In quasi-static loading scenarios, this may prompt the exploration of alternative strategies, such as a significant increase in the load rate. Furthermore, the very small step size may extend the duration of the analysis, while the strategies used can introduce additional challenges such as numerical instabilities arising from material nonlinearities and large deformations that may complicate the FEA.

Despite these considerations, the explicit method can aid circumvent numerical issues related to convergence and remain effective in simulating quasi-static loading (Plos et al., 2021). Ultimately, the choice of a suitable solution technique for managing various loading situations is closely linked to the characteristics of the structural model under consideration.

3.3 Load Application Methods

In NLA, the structural response demonstrates a reliance on outcomes derived from previous iterations (cf. Section 3.2). This historical aspect emphasizes the significance of maintaining a chronological record of the order in which loads are applied to a structure (Plos et al., 2021). Fundamentally, numerical analyses allow for the application of loads through three distinct approaches.

The first method, known as **Load-controlled loading method**, is widely used in linear FEA and is also applicable to non-linear FEA (Plos et al., 2021). It follows the principle of gradually increasing the applied forces.

On the other hand, **Displacement-controlled loading method** uses a continuous increase in displacement to describe the load application. Velocities are also frequently exploited, especially in the context of dynamic analyses (Plos et al., 2021).

The **Arc-length method** constitutes the third method of load application, which takes advantage of the aforementioned methods with a specialized technique (Plos et al., 2021). This approach ensures the management of the load vector throughout the iteration process, avoiding the need for monotonically increasing the load. A summary of the load application methods is schematically illustrated in Figure 3.3.

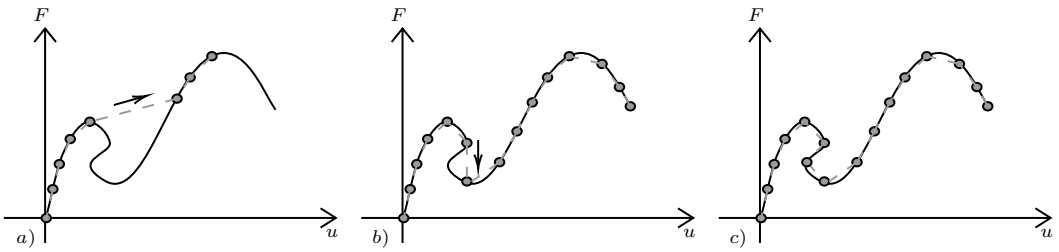

Figure 3.3: True and approximate solutions for various load application approaches: a) Load-controlled method, b) Displacement-controlled method & c) Arc-length method. Based on Plos et al. (2021).

In Figure 3.3, the solid black lines portray the accurate solutions to the problem, while the grey dashed lines with filled grey circles illustrate expected solutions when employing the different methods. Furthermore, the arrows indicate the part of the solution that the given method is unable to capture.

Upon examining the responses in each case individually, it can be noted that the load-controlled method is the most straightforward approach for describing load application. Nonetheless, it is apparent that the successive accrual of force hinders the ability to capture the response in situations where the force diminishes with increased displacement. As a consequence, convergence issues may arise due to the skipping of a specific region in the response, leading to an abrupt transition to a new state where deformations are markedly higher, accompanied by a slight increase in force. In contrast, the displacement-controlled method provides a more refined representation of the majority of the response, only overlooking the "snap-back" portion (see black arrow) characterized by decreased displacement and force. Comparatively, the utilization of the arc-length method in analysis demonstrates a high capability to accurately capture the entire response, including the snap-back segment.

3.4 Type of Finite Elements

To achieve the desired structural response and accurately predict failure modes in numerical analysis, it is crucial to select the appropriate type of finite elements. Certain elements exhibit distinct capabilities in describing specific structural behaviors that other elements may manage less effectively or not at all (Broo et al., 2008). In commercial FE software, such as Abaqus CAE, several types of finite elements with various shapes are available and can be categorized into three main groups: **continuum elements**, **structural elements**, and **special-purpose elements**.

The first element family, referred to as solid (continuum) elements, is applicable to both linear and complex non-linear analyses, encompassing large deformations and plasticity (Dassault Systèmes Simulia Corporation, 2024). Moreover, they are commonly employed for the examination of stresses and strains. These finite elements possess only translational degrees-of-freedom (DOF) and exist in one to three dimensions (Rivai et al., 2013). 3D elements can take the form of bricks, prisms, and tetrahedrons, capable of capturing the volumetric behavior of solid structures. Examples of 2D elements include plane stress ($\sigma_3 = 0$) and strain ($\epsilon_3 = 0$) elements, which are applicable to thin steel plates and thick/long structures (cross-sections). Trusses or cables are typically modeled as 1D elements, appropriate for studying uniaxial deformations. A visual representation of the appearance of continuum elements is illustrated in Figure 3.4.

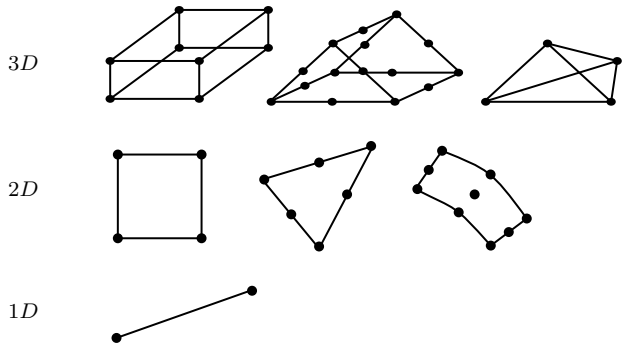

Figure 3.4: Continuum elements of various dimensions. Based on Broo et al. (2008).

Unlike continuum elements, structural elements possess both translational and rotational DOF (Broo et al., 2008). Among the frequently utilized elements in this category for non-linear FEA are truss, beam, and shell elements. These finite elements are suitable for modeling structures under both static and dynamic loading conditions and offer opportunities to study sectional forces (N, V, M) when necessary. Truss elements, characterized by 1D rod elements, are not capable of withstanding bending but are well-suited for modeling trusses or pin-jointed frames since they can resist axial forces (tension/compression).

Beam elements, featuring three translational and three rotational DOF, are utilized in scenarios where the length dimension of a structure significantly exceeds the other two dimensions (Dassault Systèmes Simulia Corporation, 2024). As the name implies, these elements are widely used for modeling structures such as beams or bars/rods, excelling particularly in capturing out-of-plane bending and deformations, which may be crucial for the analysis.

Shell elements are commonly employed to model thin-walled structures like shells or plates, where the thickness dimension is considerably smaller compared to the other two dimensions, and out-of-plane stresses are considered negligible (Dassault Systèmes Simulia Corporation, 2024). Consequently, these finite elements efficiently

capture the in-plane/membrane behavior (shear) of structures and prove to be relevant for engineering problems where bending (out-of-plane) needs consideration in the analysis (Broo et al., 2008). A visual representation of the appearance of structural elements is illustrated in Figure 3.5.

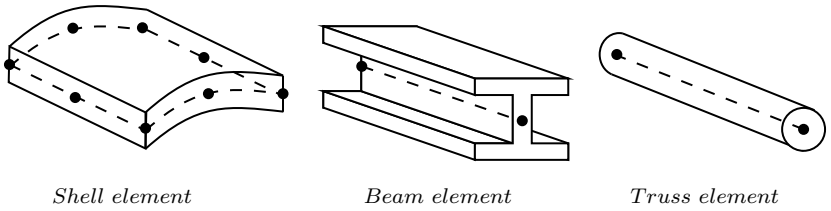

Figure 3.5: Various structural elements. Based on Broo et al. (2008).

Finally, special-purpose elements are utilized in models when specific or unique behaviors need addressing. Typically, these finite elements include springs, interfaces, and contact elements, serving to connect different parts of materials or structures (Broo et al., 2008). For instance, spring elements can be applied for modeling actual springs or restraints, with the latter inhibiting rigid body motion. These elements are also effective in modeling discontinuities or gaps in contacts.

3.5 Convergence

For evaluating equilibrium in the iteration process and ensuring the accuracy of the solution obtained in each increment in nonlinear FEA, it is essential to employ appropriate convergence criteria (Boer et al., 2014). These criteria serve as measures to guarantee efficiency and sufficient accuracy by comparing them with predetermined tolerances. Generally, the criteria include force norm, energy norm, and displacement norm, with the choice of a specific criterion depending on both the nature of the structure and the response to be simulated. A successful combination often involves force and energy norms, while the use of displacement norm is not advisable due to its ineptitude in accurately reflecting non-linear behavior, making it inappropriate for non-linear FEA of steel structures.

Moreover, the convergence of analysis for a specific model heavily depends on the employed iteration methods (cf. Section 3.2.1), the chosen number of iterations, and the determined tolerance types along with their corresponding prescribed values (Plos et al., 2021). In Abaqus CAE, there are several predefined control parameters with carefully determined default values, aiming to provide optimal and sufficiently accurate solutions for non-linear problems.

However, it is worth mentioning that, at times, larger tolerances might need to be chosen to address convergence issues while still enabling the attainment of the same structural response (Plos et al., 2021). Conversely, opting for smaller tolerance values can also lead to a more accurate solution, potentially mitigating challenges related to convergence and resulting in enhanced overall convergence.

4 Pre-Study

Meticulous planning and analysis are essential for achieving meaningful research outcomes. This section serves as a pre-study, emphasizing its pivotal role in validating parameters, predicting anticipated results through analyses, and, most importantly, establishing the foundation for experiments. The pre-study primarily focuses on analyses conducted in Abaqus CAE, supported by simple analytical calculations for verification purposes.

4.1 Orientation

In the pre-study phase, the aim is to foster a deep understanding of the underlying aspects and mechanisms, establishing a solid groundwork for detailed investigations in subsequent stages of the research. The main aspects covered in the pre-study are as follows.

Linear buckling analyses: Examining the buckling deformation pattern under compressive axial load and determining the critical buckling load in the linear elastic range.

Non-linear buckling analyses: Investigating the buckling behaviour with inclusion of material and geometric nonlinearities to understand the structural response beyond the linear elastic range.

Quasi-static analyses: Simulating slow loading conditions to study the structural response when subjected to quasi-static forces.

Dynamic analyses: Exploring the impact of various load rates generating different strain rates in the structure. The analyses are conducted both without and with strain rate effects activated to examine how changes in material properties dictate the response.

Imperfection and slenderness sensitivity analyses: Assessing the influence of these parameters on the structural response under both quasi-static and dynamic loading conditions.

4.2 Theoretical Background

This section introduces essential theories and concepts crucial for laying the groundwork of the pre-study, forming the basis for subsequent experiments and numerical analyses.

4.2.1 Overview of Specimen Geometry for Experiments

To facilitate the execution of material tests on steel rods and ensure proper gripping of the specimens by the testing machine under varying load rates, small "dogbone" shaped steel specimens are employed. These flat tensile specimens are commonly utilized for dynamic testing and are available in standardized sizes (The Swedish Institute for Standards, 2011). The geometrical shape of the specimens used in structural tests reflects this form, with the only difference being that the samples are subjected to compression rather than tension. Figure 4.1 illustrates the standard shape and geometry of a tensile specimen used in quasi-static and dynamic axial testing, along with explanations of its dimensions.

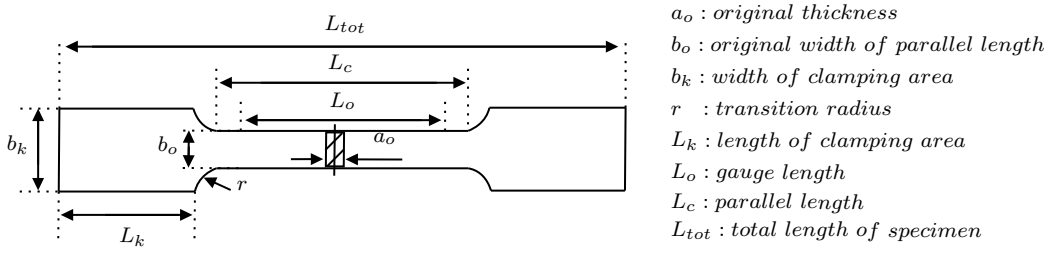

Figure 4.1: Specimen geometry with dimension specifications. Based on The Swedish Institute for Standards (2011).

The relevant dimensions of the flat tensile steel specimens for testing are also determined according to ISO 26203-2:2011, which outlines recommended ratios and sizes for specimen geometry. These guidelines are summarized as follows:

- $\frac{L_o}{b_o} \geq 2$
- $L_c \geq L_o + \frac{b_o}{2}$
- $\frac{b_o}{a_o} \geq 2$
- $\frac{b_o}{b_k} \leq 0.5$
- $r \geq 10\,\text{mm}$

In the context of tensile testing, L_o refers to the length of the main reduced section of the specimen where measurements are taken. During testing, elongation, ΔL, is measured in this region as the applied force (F) gradually increases. The load is recorded by the machine, and after the test is completed, the maximum force, F_{max} is divided by the cross-sectional area (A) to determine the mechanical property f_u.

4.2.2 Constitutive Material Model

The static stress-strain relationship for different steel grades can be established either through experimental material tests or by implementing existing constitutive material models if experimental data are not available. To determine the engineering stress-strain curve for hot-rolled steels, a bi-linear plus non-linear hardening material

model can be utilized (Yun & Gardner, 2017). An illustration of the constitutive model, featuring distinct yield plateau and non-linear strain hardening branch, is presented in Figure 4.2.

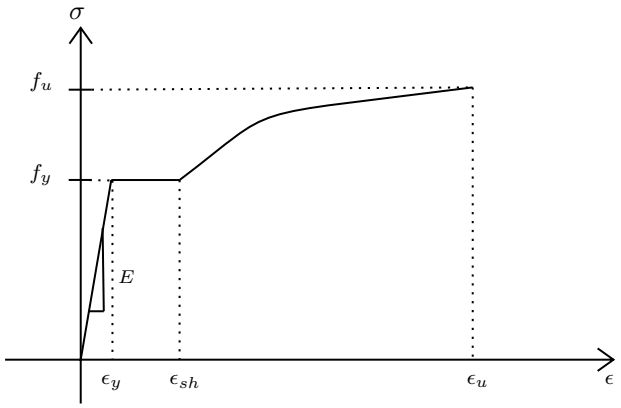

Figure 4.2: Bi-linear plus non-linear hardening stress–strain constitutive model. Based on Yun and Gardner (2017).

Figure 4.2 depicts the thresholds for yield strain (ϵ_y), strain hardening strain (ϵ_{sh}), and ultimate strain (ϵ_u), alongside their corresponding yield strength (f_y) and ultimate strength (f_u). Analytical expressions for calculating ϵ_y, ϵ_{sh}, and ϵ_u are provided in Equations 4.1-4.3.

$$\epsilon_y = \frac{f_y}{E} \tag{4.1}$$

$$\epsilon_{sh} = 0.1\frac{f_y}{f_u} - 0.055, \quad 0.015 \leq \epsilon_{sh} \leq 0.03 \tag{4.2}$$

$$\epsilon_u = 0.6\left(1 - \frac{f_y}{f_u}\right), \quad \epsilon_u \geq 0.06 \tag{4.3}$$

Depending on the range of strain, the stress in the bi-linear plus non-linear hardening model can be calculated through conditional formulations presented in Equation 4.4.

$$\sigma(\epsilon) = \begin{cases} E\epsilon & \text{for} \quad \epsilon \leq \epsilon_y \\ f_y & \text{for} \quad \epsilon_y < \epsilon \leq \epsilon_{sh} \\ f_y + (f_u - f_y)\left[0.4\left(\frac{\epsilon-\epsilon_{sh}}{\epsilon_u-\epsilon_{sh}}\right) + \frac{2\left(\frac{\epsilon-\epsilon_{sh}}{\epsilon_u-\epsilon_{sh}}\right)}{\left[1+400\left(\frac{\epsilon-\epsilon_{sh}}{\epsilon_u-\epsilon_{sh}}\right)^5\right]^{\frac{1}{5}}}\right] & \text{for} \quad \epsilon_{sh} < \epsilon \leq \epsilon_u \end{cases} \tag{4.4}$$

Note that the stress-strain response of hot-rolled steel, as determined by the constitutive model, can be compared with stress-strain curve derived from experiments obtained from tests conducted on hot-rolled steel samples. This comparison can allow for validation and assessment of the model's ability to accurately capture the overall behavior, ensuring alignment with experimental observations.

4.2.3 Determination of Strain Rate

In quasi-static tensile or compressive tests conducted on specimens, the strain rate can be determined by analyzing the strain-time history curve generated during testing. However, when conducting high-speed material or structural testing, the test is completed rapidly, and in such instances, the elongation or deformation of the specimen is assumed to change uniformly with respect to testing speed and elapsed time (Xing et al., 2021). Expressions for strain (ϵ) and the tensile deformation ($\triangle L$) are provided in Equation 4.5 and Equation 4.6, respectively. By applying these equations, the strain rate ($\dot{\epsilon}$) can generally be formulated in both quasi-static and dynamic loading scenarios, as detailed in Equation 4.7.

$$\epsilon = \frac{\triangle L}{L} \tag{4.5}$$

$$\triangle L = vT \tag{4.6}$$

$$\dot{\epsilon} = \frac{\epsilon}{T} = \frac{vT}{LT} = \frac{v}{L} \tag{4.7}$$

In Equations 4.5-4.7, the variable v denotes the loading rate (in mm/s) applied during the test, L represents the original length (in mm) of the specimen, and T signifies the duration of time (in s) from the initiation of the test until the specimen fractures or fails. Consequently, the strain rate ($\dot{\epsilon}$) is expressed in units of s^{-1}. Additionally, in Equation 4.7, L can correspond to either L_c, L_o or the unrestrained length of the specimens (cf. Figure 4.1), depending on the experimental setup and type of loading.

4.2.4 Loading Profiles and Kinematic Relations

After determining the type of load application to implement for FEA, it is necessary to establish how the applied load varies with time during the simulations. Figure 4.3 schematically illustrates a simple configuration for load variations over time in the case of displacement-controlled and velocity-controlled loading, along with their respective relationships.

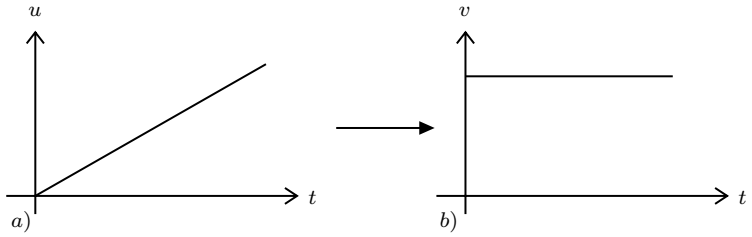

Figure 4.3: Load variation over time: a) Displacement-controlled loading & b) Velocity-controlled loading.

The velocity represents the rate of change of displacement. As displacement linearly increases, velocity becomes constant, describing the slope of the displacement.

When conducting numerical quasi-static or dynamic analyses with low loading rates, the expected dynamic effects are typically small or negligible. During such analyses, it is generally advocated to apply the load as smoothly as possible to avoid abrupt changes that can lead to inaccurate results (Dassault Systèmes Simulia Corporation, 2024). In Abaqus CAE, there is a built-in function called *Smooth step* which enables smooth load application. A schematic illustration of curve of the amplitude, A, for a smooth step definition in the FE-software is visualized in Figure 4.4.

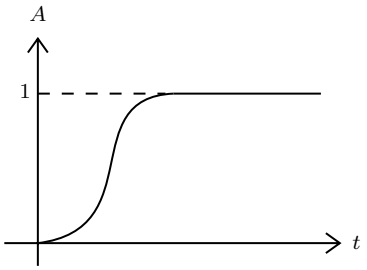

Figure 4.4: Amplitude definition of a smooth step in Abaqus CAE. Based on Dassault Systèmes Simulia Corporation (2024).

Under high loading rates, inertia effects become significant as accelerations arise compared to quasi-static loading. Consideration of the acceleration phase is therefore essential when simulating the response of a structure influenced by a load similar to a characteristic impulse load. A conceptual schematic illustration of the kinematic relation between a, v, and u for an arbitrarily impulse loading with constant peak acceleration, a_p is presented in Figure 4.5.

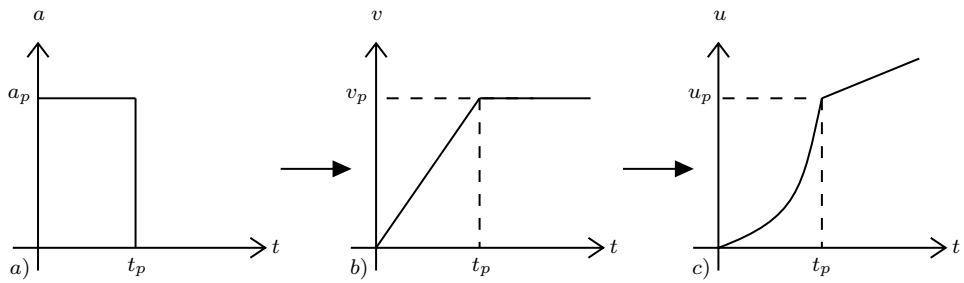

Figure 4.5: Kinematic relation for motion with short duration constant acceleration over time: a) Acceleration & b) Velocity & c) Displacement.

Observations from Figure 4.5 indicate that in dynamic analyses characterized by high loading rates and an acceleration phase, the load needs to be defined either using a linear ramp-up or an exponential amplitude until reaching the point where the peak velocity, v_p, or peak displacement, u_p, is attained at a specific peak time, t_p, in the analysis. After the acceleration phase ends, v_p can remain constant until the end of the simulation.

In scenarios where acceleration (a) linearly increases over a short duration and then ceases, the kinematic relation between a and v can be depicted as schematically

illustrated in Figure 4.6. Here, an arbitrary load with linear acceleration can be understood as being translated into an exponentially increasing velocity function.

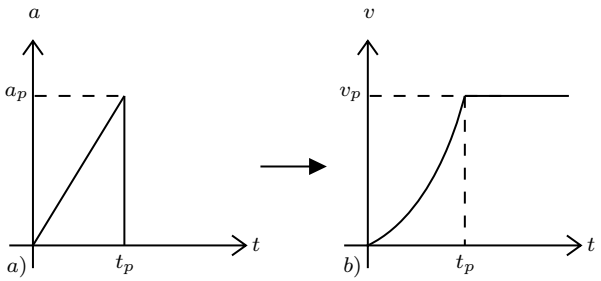

Figure 4.6: Kinematic relation for motion with short duration increasing acceleration over time: a) Acceleration & b) Velocity.

In dynamic analyses with varying loading rates, employing a velocity-controlled approach, defined as a smooth step (cf. Figure 4.4), can provide a more accurate depiction of the applied load. By opting for this combination, the FE-model can directly and more precisely describe how the structural response is influenced by speed variations and also ensure that acceleration at higher loading rates is considered and included in the analyses. Additionally, the use of smooth amplitude curves facilitates a smooth acceleration transition from the initial stage to the peak stage, see also Figure 4.7.

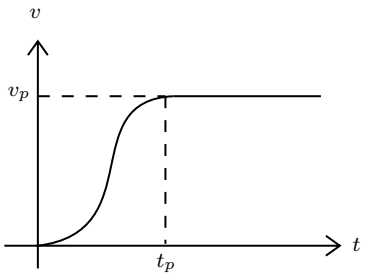

Figure 4.7: Load defined as a smooth velocity step.

It is worth highlighting that the provided velocity-time relation for amplitude definition reflects the major part of the real-world expected acceleration phase. The only difference lies in the smoothing near v_p, which in reality most likely is a more of a sharp edge intersection at the peak value. A comparative illustration of velocity-controlled loading with expected real-world and approximated amplitude curves for linearly increasing short-duration acceleration is presented in Figure 4.8.

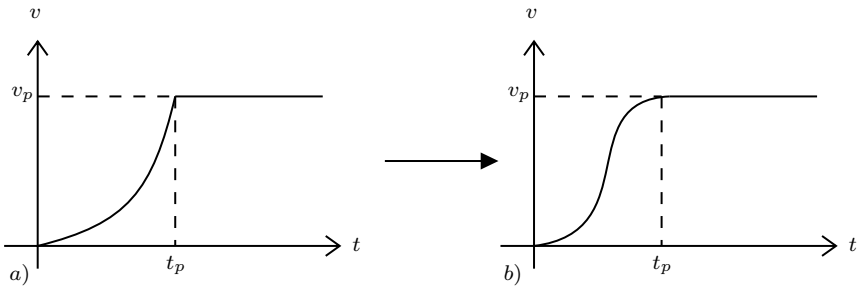

Figure 4.8: Velocity variation over time: a) Exponential amplitude & b) Smooth amplitude.

As observed in Figure 4.8, the definition of the real-acceleration phase closely matches when employing a smoother curve. Therefore, for subsequent quasi-static and dynamic analyses on steel rods, the choice of the built-in smooth step function in Abaqus CAE is considered appropriate for providing a sufficiently accurate definition of acceleration at successively increased loading rates. Furthermore, the smooth definition can also help mitigate and avoid potential convergence issues.

Another aspect worth mentioning is the relationship between loading rate and yielding of the steel material. For an accurate prediction of the dynamic response of a structure, the targeted velocity should be attained before the onset of yielding in the steel. This ensures that the structure reaches its maximum kinetic energy before undergoing plastic deformation, thus reflecting real-world scenarios and minimizing potential errors in numerical analyses. A schematic illustration of the area under the peak velocity-time curve is displayed in Figure 4.9.

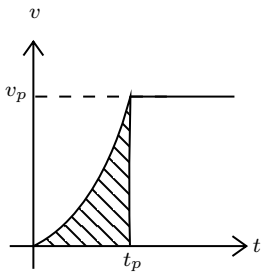

Figure 4.9: Displacement represented as area under the velocity-time curve.

The hatched area under the curve symbolizes the displacement (u) of the structure, which must be less than the displacement at the yield point. Therefore, it should be verified that the defined targeted loading rate (v_p) at at certain peak time (t_p) occurs before yielding. In Abaqus CAE, this verification can be executed by comparing the time step when ϵ_{pl} starts to develop with the specified time step t_p for v_p.

Moreover, to comprehend the implementation of the smooth step amplitude curve, it is important to touch upon the underlying equation as well. The smooth step definition in Abaqus Standard/Abaqus Explicit constructs an amplitude profile using only two data points and is unable to offer a smooth interpolation between multiple

data points (Dassault Systèmes Simulia Corporation, 2024). This approach relies on defining specific data points for the initial and maximum amplitude states, as exemplified in Figure 4.10.

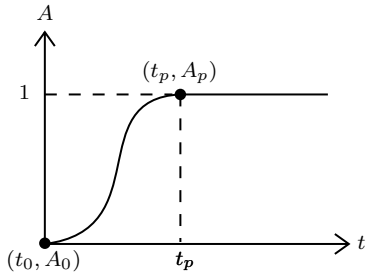

Figure 4.10: Definition of smooth step amplitude based on two data points.

The analytical expression that constructs the smooth shape is presented in Equation 4.8.

$$A = \begin{cases} A_0 & \text{for} \quad t \leq t_0 \\ A_0 + (A_p - A_0)\xi^3(10 - 15\xi + 6\xi^2) & \text{for} \quad t_0 < t \leq t_p \\ A_p & \text{for} \quad t_p \leq t \end{cases} \tag{4.8}$$

$$\text{where} \quad \xi = \frac{t - t_0}{t_p - t_0}$$

In Equation 4.8, the notations A_0 and t_0 represent the initial amplitude and initial time, respectively, while A_p and t_p denote the maximum or peak amplitude and corresponding peak time. To illustrate the application of this, consider dynamic analyses where a specified loading rate is intended to reach its maximum value (v_p) at 0.0025 seconds for a simulation lasting one second. To achieve a smooth loading profile for this scenario, the following input can be defined in the smooth step amplitude dialogue in Abaqus CAE, as shown in Table 4.1.

Table 4.1: Example of input data for smooth step in Abaqus CAE.

Time/frequency [s]	Amplitude [-]
0	0
0.0025	1
1	1

In this context, the initial state before load application is represented by $t_0 = 0$ and $A_0 = 0$. The peak state, reached when v is at its maximum, is specified by $t_p = 0.0025$ and $A_p = 1$. The remaining constant amplitude until the end of the simulation is characterized by the third row in Table 4.1, where $t = 1$ and $A_p = 1$.

4.3 FE-Model for Compressive Axial Loading in Abaqus CAE

This section offers an overview of the fundamental aspects of the developed FE-model of the steel rods. It covers the studied geometries, the defined material model, applied loads and boundary conditions, and also discusses mesh convergence.

4.3.1 Geometry

The initial step in creating the FE-model is to define the geometry of the steel rod structure using a specific type of finite element. Given that the studied steel rods are very thin and slender, they are modeled using *Homogeneous shell element*. These types of elements are suitable for representing thin-walled structures (cf. Section 3.4) and can effectively capture the required structural behavior of the steel rods. Regarding the actual configuration, it bears a resemblance to a tensile member akin to the specimens employed in tension tests (cf. Section 4.2.1). An illustration of the created rod geometry is provided in Figure 4.11.

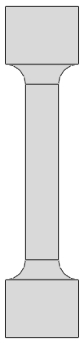

Figure 4.11: 2D visualization of the steel rod's geometry.

In the study, the structural response under compressive axial loading is simulated for two different rod geometries, with specific details such as assigned shell thickness and dimensions provided in Table 4.2.

Table 4.2: Geometry specifications of rod 1 and 2. Based on Figure 4.1.

	a_o [mm]	b_o [mm]	b_k [mm]	r [mm]	L_k [mm]	L_c [mm]	L_{tot} [mm]
Rod 1 (short)	4	20	44	12	35	106	200
Rod 2 (long)	4	20	44	12	35	236	330

Based on the established geometries, the unrestrained or unsupported length of rod 1 is 130 mm, while for rod 2 it is 260 mm. These lengths are determined by subtracting the clamping length (L_k) from both sides of the total specimen length (L_{tot}). Note that these unrestrained lengths are utilized in strain rate calculations (cf. Section 4.2.3).

4.3.2 Material Properties

Given the pronounced non-linear structural behavior of steel, it is crucial to define an appropriate elastic-plastic material model in Abaqus CAE to accurately predict the response of the studied steel rods. As no experimental data from material tests are available at this stage, the pre-study relies on a S355 steel with the material behavior established through the constitutive model presented in Section 4.2.2.

To conduct quasi-static and dynamic non-linear FEA, it is necessary to specify elastic and plastic mechanical properties as well as density for the FE-model. The elastic (linear) material behavior of the steel rods is defined according to Table 4.3

Table 4.3: Elasticity model for FEA.

E [GPa]	ν [-]
210	0.3

In order to characterize the plastic behavior of the rods, the engineering stress-strain curve is initially derived using the constitutive model (cf. Section 4.2.2). Subsequently, this curve is transformed into a true stress-plastic strain relationship (cf. Section 2.5.2). The resulting input data is presented in graphical and tabulated form in Figure 4.12.

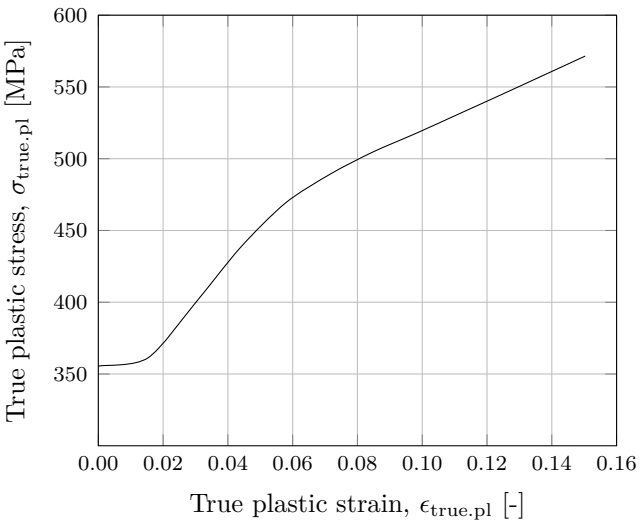

a)

$\sigma_{\text{true,pl}}$ [MPa]	$\epsilon_{\text{true,pl}}$ [-]
355.0	0.0000
355.6	0.0003
361.2	0.0153
399.9	0.0301
438.2	0.0439
469.2	0.0578
489.4	0.0717
504.5	0.0846
518.1	0.0985
531.4	0.1115
544.6	0.1244
558.0	0.1373
571.5	0.1503

b)

Figure 4.12: Plasticity model in Abaqus CAE: a) Graphical presentation & b) Tabulated presentation.

As the material's mass density, ρ, is pivotal in dynamic analyses, it is also incorporated as an input parameter in the FE-model, specified as $\rho = 7.8^{-9}$ t/mm^3. For further details about the analytical calculations for establishing the constitutive material model, see Appendix A.

4.3.3 Boundary Conditions

Ensuring consistency with the experimental setup is essential for accurately comparing numerical results with experimental findings. Therefore, the boundary conditions in the FE-model reflect the end constraints enforced to the specimens in the subsequent experiments. In quasi-static analyses, the steel rods are represented with fixed-fixed boundary conditions, where constraints of type *Displacement/Rotation* are imposed. Specifically, the bottom boundary is restrained from translations and rotations in all directions. This involves prescribing zero movements as well as zero rotations to the associated DOF of the boundary.

The approach for the top boundary adheres to a similar principle, with one notable distinction: the transverse movement is left unconstrained. This deliberate choice enables in-plane deformations of the rods in response to applied loads. A compilation of both constrained and unconstrained degrees of freedom for the bottom and top boundaries for quasi-static analyses is presented in Table 4.4.

Table 4.4: Boundary conditions of the steel rod in quasi-static analyses.

Boundary set	Translations [mm]	Rotations [rad]
Top boundary	$U1 = 0$	$UR1 = 0$
	$U2 =$ unset	$UR2 = 0$
	$U3 = 0$	$UR3 = 0$
Bottom boundary	$U1 = 0$	$UR1 = 0$
	$U2 = 0$	$UR2 = 0$
	$U3 = 0$	$UR3 = 0$

In Table 4.4, *U1*, *U2*, and *U3* represent the DOF for translation in the x, y, and z-directions, respectively. Similarly, *UR1*, *UR2*, and *UR3* denote the DOF for rotation about the x, y, and z-axes, correspondingly. The FE-model of the studied steel rod with the exact locations of the applied fixed-fixed boundary conditions is illustrated in Figure 4.13.

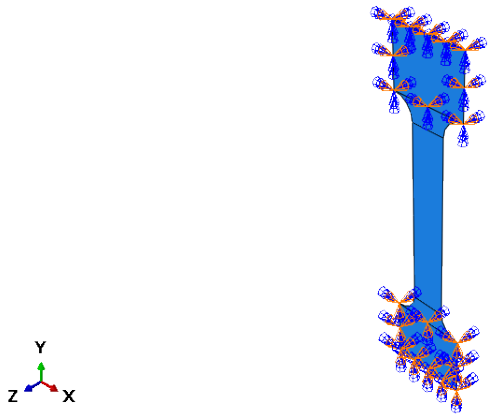

Figure 4.13: Top and bottom boundary conditions of the steel rod in the FE-model.

It is seen from Figure 4.13 that fixed DOF are assigned to the upper and lower rectangular sections of the steel rod, representing the top and bottom boundaries. No additional boundary conditions are defined for the main part of the rod, extending from the transition radius to the central smaller cross-section.

The mentioned displacement boundary conditions are primarily utilized in quasi-static analysis. However, in the case of dynamic analysis, different loading rates are introduced. Thus, the top boundary is subjected to velocities, necessitating a modification to a *Velocity/Angular velocity* boundary condition, as detailed in Table 4.5.

Table 4.5: Boundary conditions of the steel rod in dynamic analyses.

Boundary set	Velocity [mm/s]	Angular velocity [rad/s]
Top boundary	$V1 = 0$	$VR1 = 0$
	$V2 =$ unset	$VR2 = 0$
	$V3 = 0$	$VR3 = 0$
Bottom boundary	$V1 = 0$	$VR1 = 0$
	$V2 = 0$	$VR2 = 0$
	$V3 = 0$	$VR3 = 0$

Observe that the value for $V2$ is unset since the compressive load on the rod structure is applied in this direction.

4.3.4 Load Application

Regarding the application of the external load to the structure, the type of load known as *Shell edge load* in Abaqus CAE is selected, as the steel rod is modeled using thin shell elements (cf. Section 4.3.1). This load type, equivalent to a line load (N/mm), is appropriate for representing both compressive and tensile forces. In the actual FE-model, the compressive load is applied only to the top edge of the rod, see Figure 4.14.

Figure 4.14: Steel rod subjected to compressive axial load.

Note that the following load configuration is applied in the static buckling analyses. In certain cases, the line load is converted to a concentrated force to facilitate easier comparison of numerical results with analytical calculations, such as for P_{cr}. For capturing post-buckling behavior, a displacement-controlled approach is implemented wherein a specific displacement value, e.g., 1 mm, is prescribed for the top boundary (cf. Section 4.3.3) instead of applying a load on the top edge. Specifically, the value of $U2$ for the top boundary in Table 4.4 is revised from "unset" to -1. Similarly, in the dynamic analyses, the value of $V2$ for the top boundary in Table 4.5 is adjusted from "unset" to the actual velocity of interest. These three distinct approaches are consistently applied throughout the study unless specified otherwise.

4.3.5 Mesh Convergence

Regarding the mesh setup in the FEA, a linear geometric order is employed, utilizing a 4-node quadrilateral shell element labeled as $S4R$. This element incorporates reduced integration, hourglass control, and features five specified thickness integration points.

To achieve reliable and accurate numerical results, mesh convergence is conducted. The mesh density is progressively increased from very coarse to very fine sizes. This process ensures that the FE-simulations of specific parameters such as eigenvalues, displacements, and stresses reaches a consistent value. Convergence is considered achieved when the difference in the parameter's value becomes negligible between two successive mesh sizes, indicating that further refinement beyond a specific mesh size will have minimal impact on the accuracy of the solution.

The verification of the convergence is performed for the buckling factor, λ, produced from linear buckling analyses (LBA). To assess convergence, eigenvalues are compared by calculating the deviation between the values obtained from two different meshes, as determined by Equation 4.9.

$$\Delta\lambda = \left| \frac{\lambda_{c.mesh} - \lambda_{p.mesh}}{\lambda_{p.mesh}} \right| \times 100 \quad [\%] \tag{4.9}$$

In Equation 4.9, $\lambda_{c.mesh}$ denotes the eigenvalue at the current mesh size, and $\lambda_{p.mesh}$ represents the eigenvalue at the previous mesh size.

A summary of the studied mesh sizes, along with the corresponding number of generated elements and associated eigenvalues with deviation percentages, is provided in Table 4.6. The data in Table 4.6 pertains to rod 1 (short) under a reference load of 100 N/mm.

Table 4.6: Mesh variation and associated eigenvalues with deviation percentages.

Mesh size [mm]	Number of elements [-]	λ [-]	$\Delta\lambda$ [%]
50	14	40.4	-
10	64	13.4	66.8
7.5	130	13.0	3.0
5	250	12.7	2.3
2	1502	12.6	0.8

Moreover, a graphical illustration of the convergence of the buckling factor with an increased number of elements is displayed in Figure 4.15.

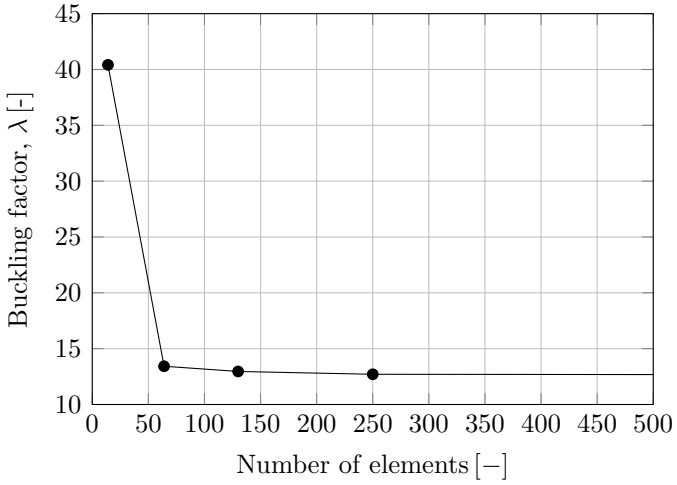

Figure 4.15: Convergence of buckling factor as function of number of elements.

Upon analysis of Figure 4.15, it becomes apparent that convergence of λ occurs at approximately 250 elements, corresponding to a 5 mm mesh size. This is demonstrated by the curve exhibiting a plateau beyond this point, indicating minimal deviation in values between different mesh resolutions. Hence, the mesh size of 5 mm is utilized throughout all the numerical simulations.

4.3.6 Analysis Steps

In the FEA, various steps are utilized to simulate different loading conditions and phenomena. To determine the critical (bifurcation) load, an eigenvalue buckling analysis is conducted using a linear perturbation procedure through the *Buckle* step, employing the subspace iteration method

For non-linear static analyses, the *Static Riks* step is employed with the *Nlgeom* option enabled to accommodate geometric nonlinearity. Within this step, the arc increment is adaptively adjusted to ensure adequate data acquisition, facilitating accurate and efficient capture of non-linear behavior.

In the analysis conducted, a common initial increment size of 0.01 is typically utilized, alongside a maximum increment size set to 0.01, and a maximum number of increments of 10000. Post-buckling behavior is captured by specifying stopping criteria, such as a maximum displacement limit, assigned DOF, and a node region.

For instance, specific parameters such as a maximum displacement of 1 mm, DOF assigned as 2 (y-direction), and a designated node region on the top boundary of the specimen are defined.

Quasi-static and dynamic analyses utilize either the *Dynamic Explicit* or *Dynamic Implicit* step, both activated with the "Nlgeom" option. Time periods are specified based on the analysis duration, with the default time incrementation 'Automatic' used. In implicit analyses, careful attention is given to the incrementation size to prevent convergence issues.

A summary of the Abaqus CAE application across various steps is provided below:

- **Step module: Linear perturbation: Buckle: Eigensolver: Subspace**
- **Step module: General: Static, Riks:**
- **Step module: General: Dynamic, Explicit:**
- **Step module: Dynamic, Implicit:**

To account for strain rate dependency, the strain rate material parameters p (exponent) and D (multiplier) in the CS-model are specified. This is achieved by the following Abaqus CAE usage.

- **Property module: Material editor: Suboptions: Rate Dependent: Hardening: Power Law**

Imperfections are accounted for using keyword commands. The buckled shape from the linear buckling analysis is saved by including the following lines under "FIELD OUTPUT":

```
*NODE FILE, GLOBAL=YES, LAST MODE=1
U
```

The geometric imperfections are then introduced into the model by adding the following lines directly after the "STEP" section:

```
*IMPERFECTION, FILE=LBA, STEP=LBA
1, 0.4
```

In this context, 1 refers to the buckling mode number, and 0.4 denotes the magnitude of the initial imperfection in mm.

4.3.7 Post-Processing Setup

In the post-processing stage, it is crucial to focus on analyzing output variables in specific regions, parts, or exact positions of the steel rod structure that are critical and of most interest for the study. Therefore, this section provides a brief description of extraction of simulation results pertinent to the studied parameters. An overview of the established node sets in Abaqus CAE for post-processing of outputs such as reaction force, $RF2$, in-plane displacement, $U2$, and out-of-plane displacement, $U3$ is presented next.

The initial step involves establishing a node set along the bottom boundary of the geometry, which is relevant for retrieving reaction forces resulting from applied loads, displacements, or velocities on the top boundary. Subsequently, a node set is created to evaluate in-plane displacements at the top edge of the top boundary, while another node set is designated to assess out-of-plane displacements in the middle section of the steel rods. An illustration of the assigned set locations in the FE-model, depicting the steel rod structure's behavior in terms of reaction force, in-plane displacement, and out-of-plane displacement, is presented in Figure 4.16.

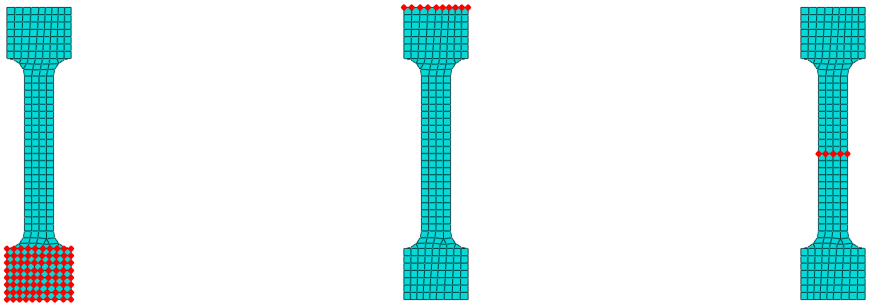

Figure 4.16: Post-processing node sets: a) Reaction force, b) In-plane displacement, c) Out-of-place displacement.

It is worth mentioning that the evaluation of reaction forces is based on summation, whereas displacements (both in-plane and out-of-plane) are determined as the average across all nodes. In a displacement-controlled approach, all nodes associated with the set for in-plane displacement will have identical displacement values, making the average calculation unnecessary. However, in a load-controlled scenario, nodes exhibit varying values, thus requiring the average calculation.

4.4 Results

This section presents the initial findings from the pre-study analyses, involving a thorough examination of various parameters such as imperfections. The investigation focuses on the structural behavior of the two previously mentioned rod geometries (cf. Section 4.3.1) under quasi-static and dynamic compressive axial loading condi-

tions. Additionally, a sub-study verifying the Power Law model in Abaqus CAE for describing strain rate effects are included.

4.4.1 Buckling Analyses

The comparison between critical buckling loads (P_{cr}) derived from analytical calculations based on linear theory and those obtained from numerical simulations through both linear and non-linear buckling analyses is provided in Table 4.7. It is important to note that the numerical simulations account for a member with a negligible imperfection of 0.01 mm.

Table 4.7: Comparison of critical buckling loads for rod 1 and 2.

	Analytical [kN]	Linear FEA [kN]	Nonlinear FEA [kN]
Rod 1 (200 mm)	52.3	55.9	28.1
Rod 2 (330 mm)	13.1	13.5	13.5

As observed in Table 4.7, the analytical and linear buckling loads from FEA yield similar results. It is noteworthy that in the analytical calculation, only the narrow section (b_o) of the "dogbone" specimen is considered for calculating the moment of inertia, neglecting the contribution from the radius section. This eventuates in a minor underestimation of the calculated buckling load. For details on the analytical buckling load calculation and the process of converting eigenvalues from LBA in Abaqus CAE to actual buckling loads (linear FEA), see Appendix B. For input files (Python scripts) of the static analyses of both rod geometries in Abaqus CAE, see Appendices I-J.

Concerning the buckling load in the non-linear scenario, it is evident that the more slender rod (rod 2) exhibits a critical buckling load close to that predicted by linear analysis. This phenomenon is attributed to the dominance of Euler buckling in highly slender members, resulting in closely aligned outcomes. On the other hand, the stockier rod (rod 1), with intermediate slenderness, shows a significant reduction in critical buckling load (cf. Section 2.3.2).

4.4.2 Static Analyses

The static analyses focus on the correlation between force and in-plane, as well as force and out-of-plane displacements, pertaining to both rod geometries. In addition, the investigation also explores how various initial imperfections influence these correlations.

Schematic representations delineating the relationship between force and in-plane displacement, as well as force and out-of-plane displacement for rod 1 and 2, are shown in Figure 4.17 and 4.18, respectively. These figures offer insights into the

critical load levels and corresponding displacements, highlighting points of instability and post-buckling behavior.

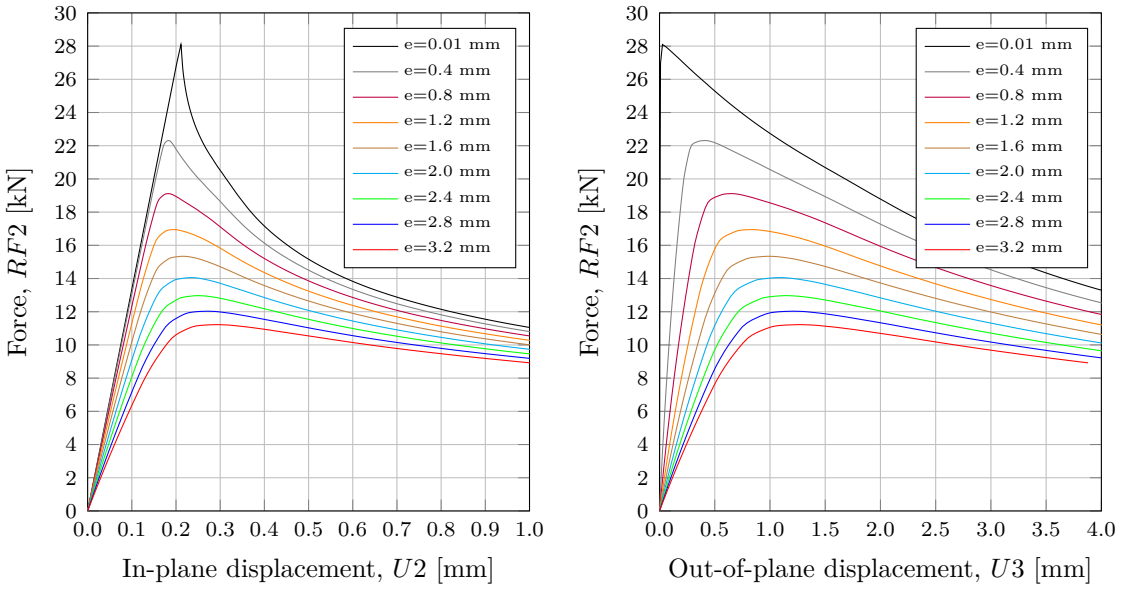

Figure 4.17: Relationship between compressive axial force and displacement for rod 1: a) In-plane & b) Out-of-plane.

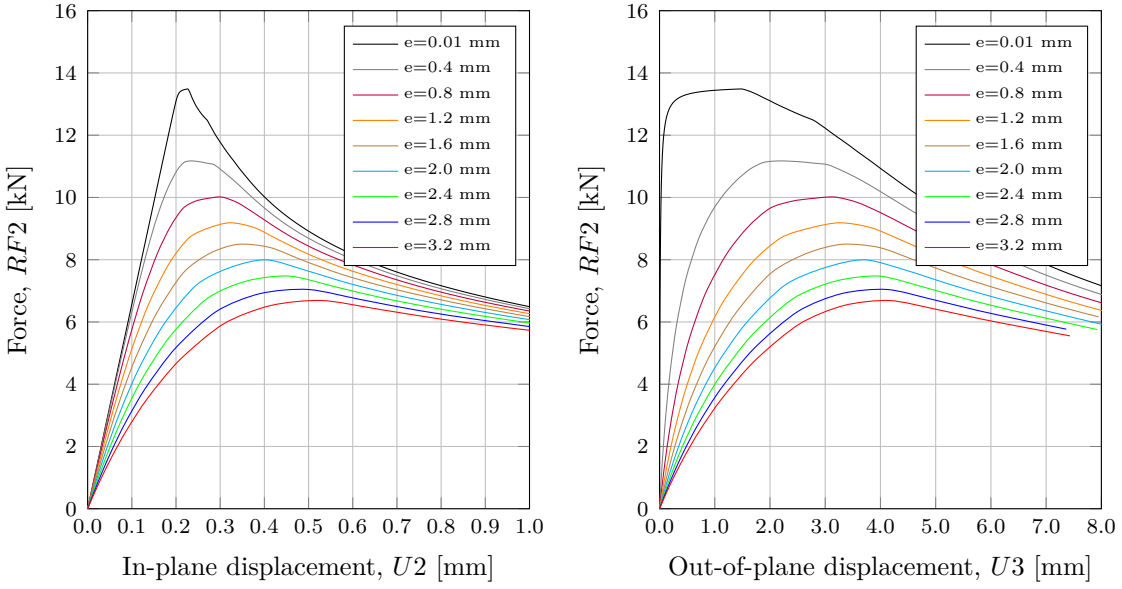

Figure 4.18: Relationship between compressive axial force and displacement for rod 2: a) In-plane & b) Out-of-plane.

Based on Figure 4.17 and 4.18, it may be observed that buckling occurs at approximate in-plane displacements ranging between 0.2 mm to 0.3 mm, as highlighted by discernible peaks in the graphs. Notably, as imperfections increase, these peaks become less pronounced and shift towards higher in-plane displacements. Furthermore, it is apparent that the magnitude of out-of-plane displacements for rod 2 is larger than that for rod 1. This is reasonable since rod 2 is more slender than rod 1.

4.4.3 Validation of Dynamic Model

Transitioning to dynamic analyses, an important aspect involves validating the dynamic model by comparing it to the static model under slow loading conditions. This verification ensures that the dynamic model operates as anticipated, thereby producing trustworthy results.

Verification of both rod geometries for an initial imperfection of 0.4 mm and loading rates of 0.013 mm/s for rod 1 and 0.026 mm/s for rod 2 is presented in Figure 4.19. These velocities correspond to an approximate strain rate of 10^{-4} s^{-1} indicative of quasi-static loading condition. Both Dynamic Implicit and Dynamic Explicit techniques were utilized for verification, and they produced the same results. Consequently, only the outcomes from the Dynamic Implicit analyses are showcased in Figure 4.19. The congruence of the curves, demonstrated by their identical alignment in Figure 4.19, validates that the dynamic model behaves as expected.

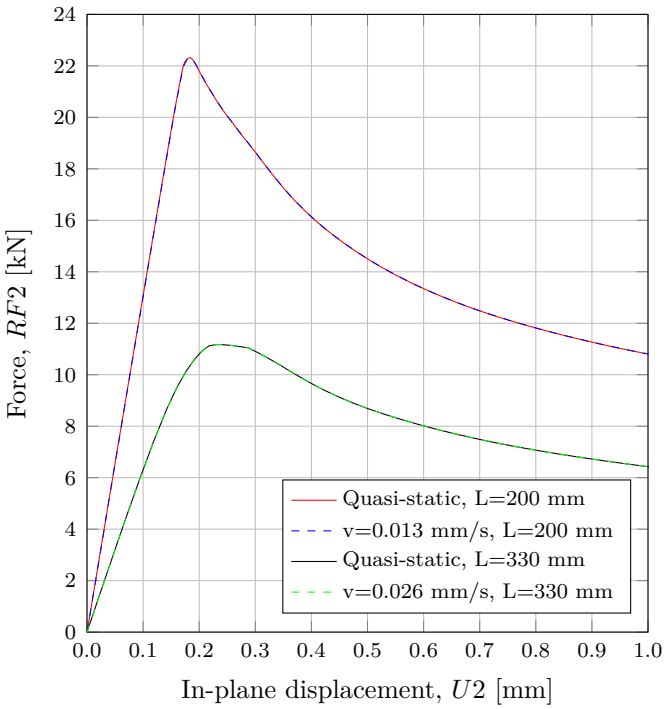

Figure 4.19: Comparison of dynamic and static models under slow loading conditions for both rod geometries, considering an initial imperfection of 0.4 mm.

4.4.4 Single Tensile Member under Varying Loading Rates

Prior to analyzing the steel rod structure under dynamic compressive loading with consideration of strain rate effects, an initial investigation is conducted on a single tensile element. This examination involves subjecting the element to loading rates spanning both quasi-static and dynamic ranges. The primary objective of this preliminary study is to confirm and validate the functionality of the CS-model (cf. Section 2.5.4) in Abaqus CAE for rate-dependent plasticity, while also ensuring that the numerical analyses accurately represent the material behavior under dynamic conditions.

4.4.4.1 FE-Model in Abaqus CAE

For this sub-study, the FE-model consists of a single steel shell element with dimensions of $100 \times 100 \times 4$ mm, and a mesh size of 100 mm is assigned. At the bottom boundary, a constraint of type *Symmetry/Antisymmetry/Encastre* is applied to ensure complete restraint in all DOF (U1=U2=U3=0 and UR1=UR2=UR3=0). Conversely, at the top boundary, a *Velocity/Angular velocity* BC is prescribed. An axial tensile force is applied as a velocity in the in-plane direction (V2), while all other DOF are restrained (V1=V3=0 and VR1=VR2=VR3=0). The FE-model allows only in-plane elongation of the element, where $V2 \neq 0$ describes various loading rates (mm/s). An illustrative depiction of the studied configuration in Abaqus CAE is shown in Figure 4.20.

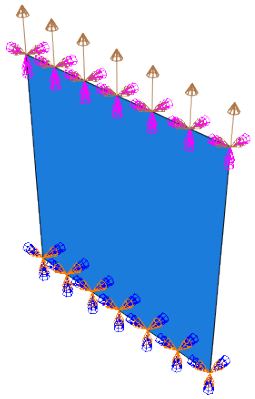

Figure 4.20: Single shell element with boundary conditions and applied velocity.

The material behavior of the tensile element mirrors the material properties of S355 specified for the analyses of the steel rod structure under compressive loading (cf. Section 4.3.2). To investigate strain rate effects and their influence on the dynamic characteristics of the single element under study, *Rate Dependent* behavior (CS-model) is introduced in addition to the previously defined behaviors. This involves specifying a multiplier (D) and an exponent (p) in the FE-model (cf. Equation 2.37). For the analytical model describing the increase in yield strength, DIF_y is utilized. The hardening parameters are calculated using Equations 2.42-2.43, resulting in the values $D_y = 4795.23$ and $p_y = 4.07$, which are input into Abaqus CAE.

For the solution technique, the Dynamic Implicit step is employed, as the Dynamic Explicit method requires considerably more computational time for simulations in the quasi-static range. As discussed previously, both methods yield similar results (cf. Section 4.4.3), and by appropriately selecting simulation time (t) and incrementation, as well as ensuring a sufficient number of data outputs, no convergence issues are encountered. As a consequence, achieving consistent simulation results for both increased and decreased loading rates is facilitated by utilizing a simple v-t relation outlined in Equation 4.10.

$$v_1 t_1 = v_2 t_2 \tag{4.10}$$

In the given relation, v_1 and t_1 represent the loading rate and analysis time for case 1 (reference), while v_2 and t_2 are the parameters for case 2. The unknown t_2 is then determined by rewriting of Equation 4.10 as shown in Equation 4.11.

$$t_2 = \frac{v_1 t_1}{v_2} \tag{4.11}$$

To validate the Power law in Abaqus CAE and to encompass both quasi-static and dynamic loading scenarios, the behavior of the tensile element is simulated under eight different loading rates, each differing by a factor of 10. A summary of the studied loading rates and their corresponding strain rates is provided in Table 4.8. Note that the strain rates are obtained through the application of Equation 4.7.

Table 4.8: Loading rates and corresponding strain rates.

Loading rates [mm/s]	0.001	0.01	0.1	1	10	100	1000	10000
Strain rates [s^{-1}]	10^{-5}	10^{-4}	10^{-3}	10^{-2}	10^{-1}	10^{0}	10^{1}	10^{2}

Further, the loading rates are implemented using smooth amplitude curves (cf. Figure 4.10). To maintain consistency, another simple relation is formulated to define t_p, as shown in Equation 4.12.

$$t_p = \frac{t}{40} \tag{4.12}$$

This relationship ensures that yielding occurs after the targeted loading rate (v_p) is reached.

4.4.4.2 Simulation Outcomes

For verification purposes, the results of the numerical analyses for all the studied cases are presented as stress-strain relationships in a single figure. This allows for examination of the material behavior and facilitates assessment of whether an increase in f_y is achieved at higher loading rates (cf. Section 2.5.3). The influence of loading rates, ranging from quasi-static to dynamic states, on the overall structural behavior of the studied element is illustrated in Figure 4.21. Observe that Figure 4.21 displays the average von Mises stress against the average logarithmic strain LE22 of the element.

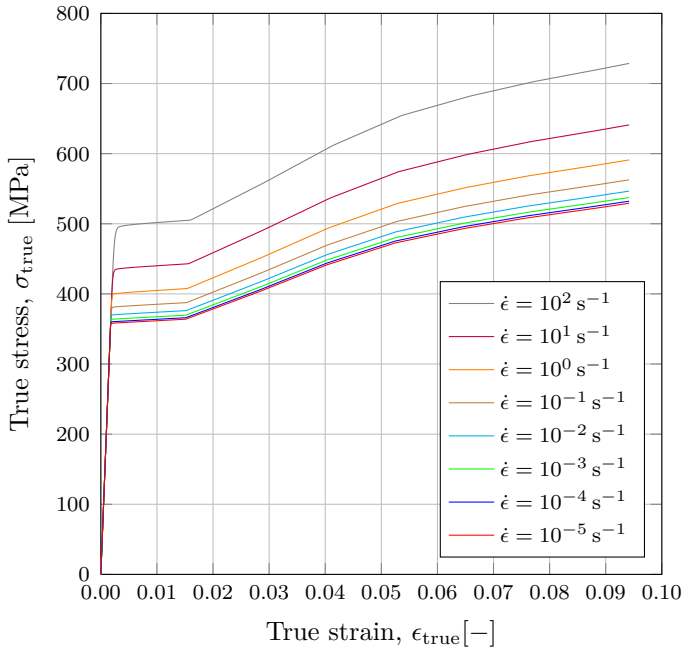

Figure 4.21: Material behavior of a single tensile element under varying loading rates.

As observed in Figure 4.21, the shape of the curves reflects the defined material behavior, with a noticeable rise in f_y (plateau) as the loading rates increase to dynamic conditions. It can be noted that the yield strength of the material under the dynamic loading (10^2 s^{-1}) is significantly higher than the yield strength at the lowest strain rate (10^{-5} s^{-1}) characterizing the quasi-static loading condition. Upon examining Figure 4.21, it is also evident that the strain rate effects are less pronounced among the quasi-static cases, as indicated by the minor differences in f_y.

Complementing Figure 4.21, Table 4.9 provides a summary of the numerical values of yield strength extracted at $\epsilon = 0.00295$ for all the cases, alongside the analytically calculated f_y. It is important to note that the numerical values, denoted as $f_{y.d.num}$, are extracted from the plateaus at the specified strain (ϵ), whereas the analytical values, $f_{y.d.an}$, calculated based on Equation 2.41, theoretically represent the exact yield point. Therefore, while the presented $f_{y.d.num}$ values may not precisely represent the onset of yielding, they are adequate for comparison and verification purposes.

Table 4.9: Variation of yield strength with different strain rates.

$\dot{\epsilon}$ [s^{-1}]	10^{-5}	10^{-4}	10^{-3}	10^{-2}	10^{-1}	10^{0}	10^{1}	10^{2}
$f_{y.d.an}$ [MPa]	357	360	363	369	380	399	433	492
$f_{y.d.num}$ [MPa]	359	361	364	371	382	401	436	493

To further elucidate and quantify the difference between $f_{y.d}$ (dynamic) and f_y (static) at the studied strain rates, DIF_y is determined for both numerical and

analytical values from Table 4.9. Subsequently, the variation of DIF_y with strain rates, spanning from quasi-static to dynamic states, is visualized in Figure 4.22.

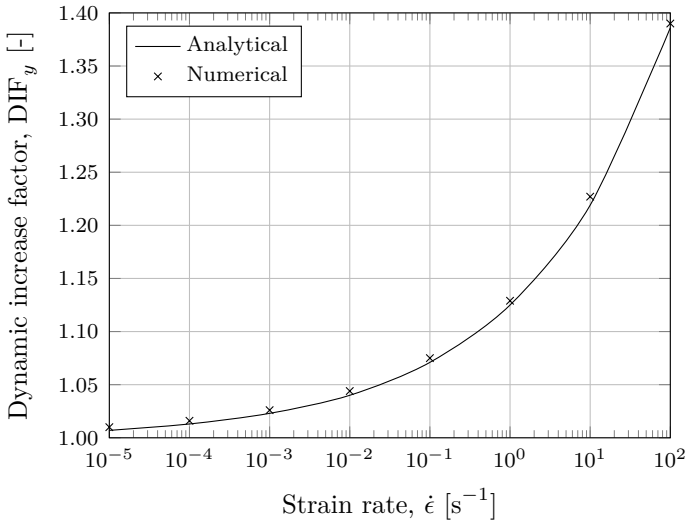

Figure 4.22: DIF_y as function of strain rates for numerically and analytically calculated yield strengths.

Upon studying Figure 4.22, it becomes clear that the DIF_y values obtained from numerical analyses closely align with those derived from the analytical solution. This demonstrates also the effectiveness of the specified strain rate parameters in yielding reasonable results.

Lastly, based on the observations from Figure 4.21 and Figure 4.22, it can be concluded that the Power Law in Abaqus CAE is functioning as intended. Pronounced strain rate effects, leading to increased yield strength, are evident at higher loading rates, particularly conspicuous under dynamic loading conditions. For further details on the analytical calculations and the input file in Abaqus CAE, see Appendix C and Appendix K, respectively.

4.4.5 Quasi-Static and Dynamic Analyses

The outcomes of the quasi-static and dynamic analyses focus on three specific initial imperfection levels: e = 0.2 mm, e = 0.4 mm, and e = 0.8 mm. To ensure alignment with experimental conditions, velocities chosen for analyses match those used in subsequent experiments. Specifically, for rod 1, the loading rates of [0.013, 13, 26, 65, 195] mm/s are considered, resulting in approximate strain rates of [10^{-4}, 0.1, 0.2, 0.5, 1.5] s^{-1}. Similarly, for rod 2, the selected loading rates are [0.026, 26, 52, 130] mm/s, corresponding to strain rates of [10^{-4}, 0.1, 0.2, 0.5] s^{-1}.

Figure 4.23 illustrates the structural behavior of rod 1 at different velocities and imperfection levels, without accounting for strain rate effects.

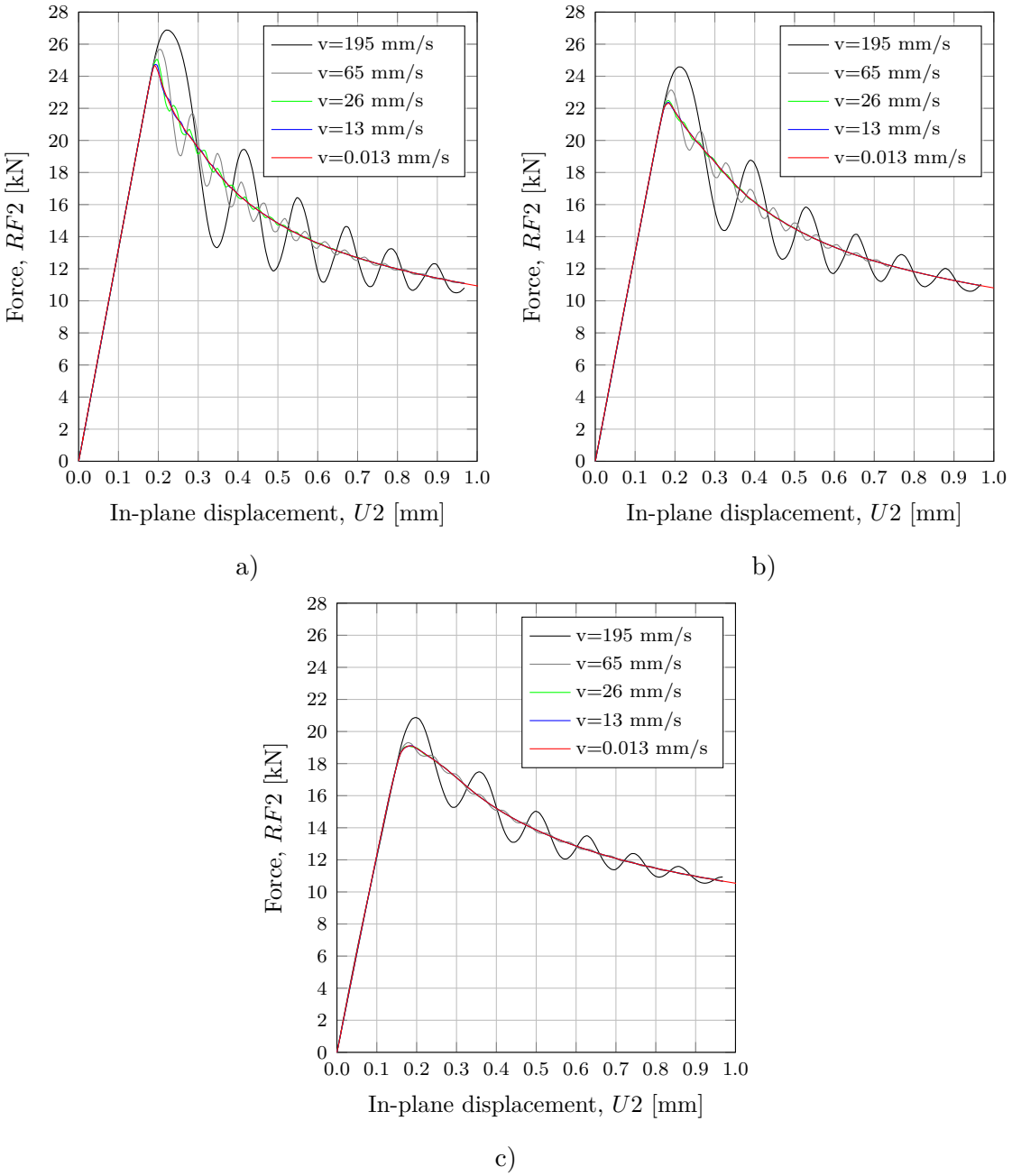

Figure 4.23: Relationship between compressive axial force and in-plane displacement for rod 1 across different velocities and imperfection levels without consideration of strain rate effects: a) e=0.2 mm, b) e=0.4 mm & c) e=0.8 mm.

Similarly, the results for rod 2 without considering the strain rate effects is shown in Figure 4.24.

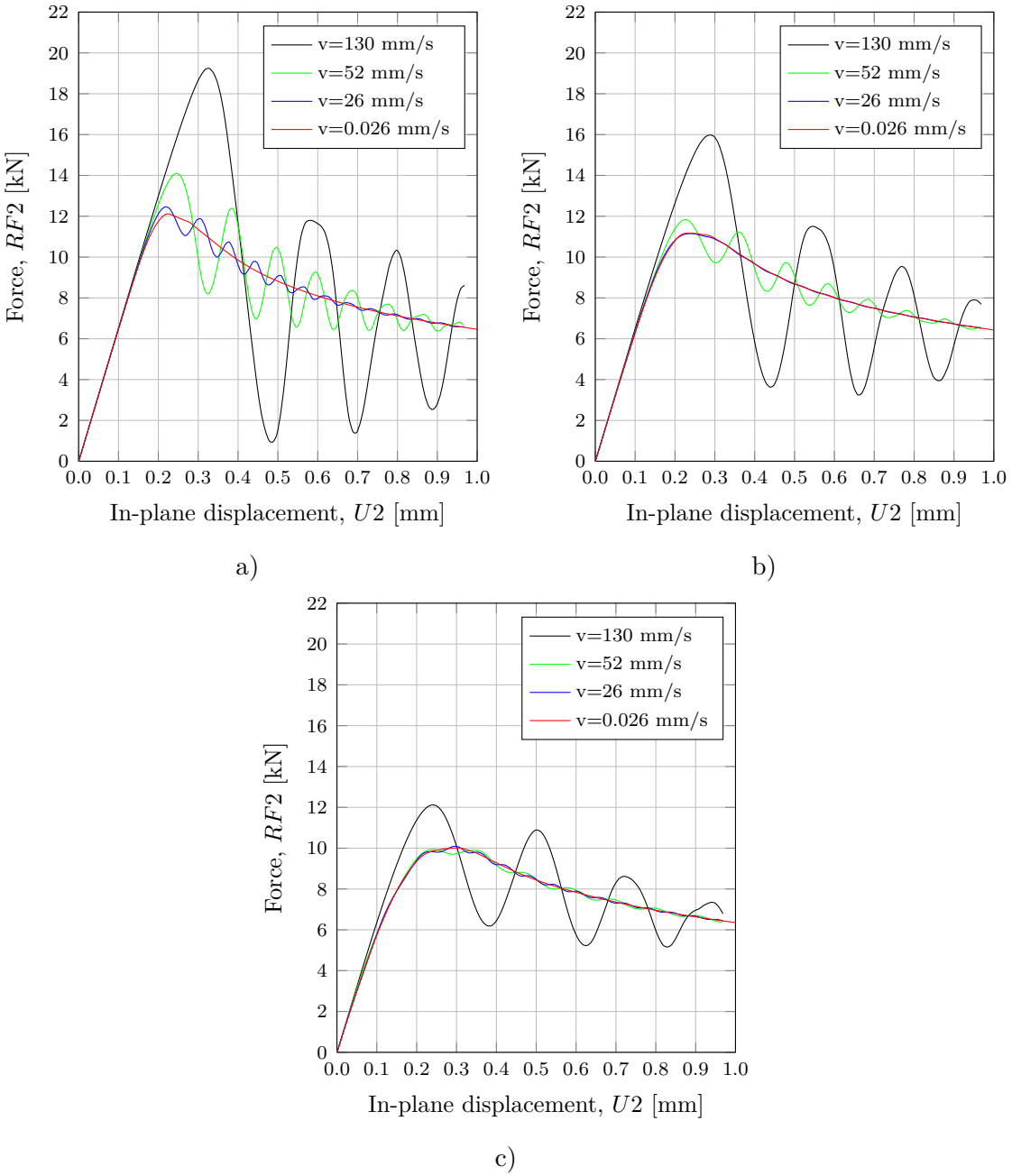

Figure 4.24: Relationship between compressive axial force and in-plane displacement for rod 2 across different velocities and imperfection levels without consideration of strain rate effects: a) e=0.2 mm, b) e=0.4 mm & c) e=0.8 mm.

Transitioning to the analyses incorporating strain rate effect considerations, Figure 4.25 elucidates the observed outcomes for rod 1, while Figure 4.26 displays the corresponding findings for rod 2.

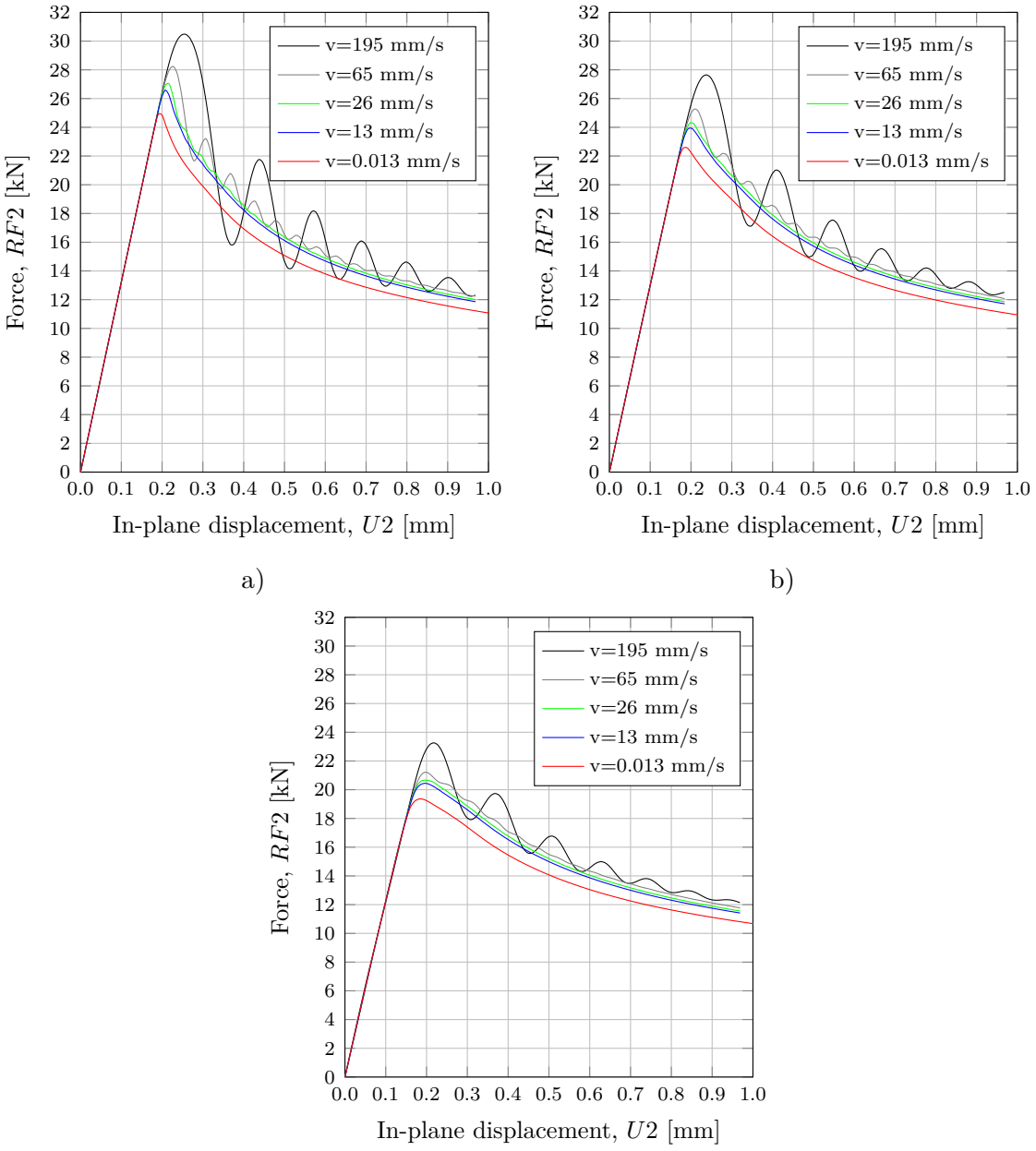

Figure 4.25: Relationship between compressive axial force and in-plane displacement for rod 1 across different velocities and imperfection levels with consideration of strain rate effects: a) e=0.2 mm, b) e=0.4 mm & c) e=0.8 mm.

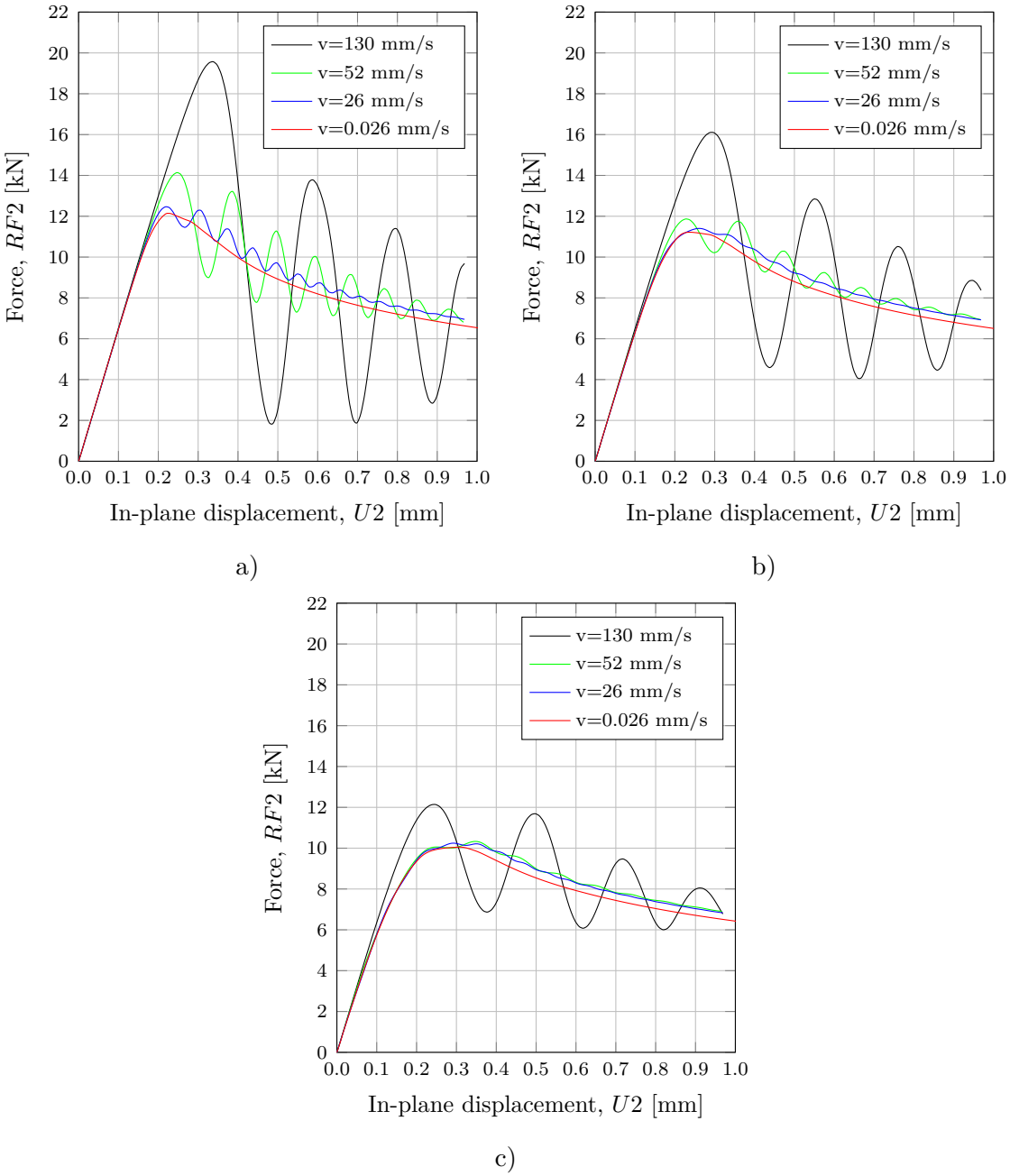

Figure 4.26: Relationship between compressive axial force and in-plane displacement for rod 2 across different velocities and imperfection levels with consideration of strain rate effects: a) e=0.2 mm, b) e=0.4 mm & c) e=0.8 mm.

Through comprehensive analyses based on Figures 4.23-4.26, several key insights emerge regarding the dynamic behavior of the rod geometries under scrutiny. The charts illustrate noticeable oscillations, indicating the onset of inertia effects and a critical transition in material response. These dynamic oscillations become more pronounced with increased strain rates, emphasizing heightened dynamic behavior. Notably, higher strain rates lead to increased load-carrying capacity, particularly

when considering strain rate dependency. This highlights the intricate relationship between strain rate and material strength under dynamic loading conditions.

Furthermore, it can be observed that dynamical effects intensify with higher slenderness. Additionally, higher initial imperfections diminish the load-carrying capacity of the rods, aligning with observations from the quasi-static analyses. The results also suggest a correlation between dynamic oscillations and imperfections, as the amplitudes of the oscillations appear to be damped with larger initial imperfections.

5 Experimental Study

This section outlines the conducted experimental investigation aimed at bolstering and validating the numerical analyses. The experimental study delves into both the material behavior in tension and the structural response in compression of the rods through a sequence of experiments. It covers descriptions of the test specimens and their preparations, presents the experimental setup and instrumentation, and discusses details about the tests themselves. Additionally, DIC is briefly introduced. The section also covers data acquisition, analyses and results of the material tests.

5.1 Digital Image Correlation

Digital image correlation (DIC) is a widely employed optical technique across engineering and material mechanics fields for measuring strain and displacements in materials/structures. Comprising three fundamental components - Digital, Image and Correlation, the technique leverages digital technology such as charge-coupled device camera (CCD) to capture series of images of a specimen at different states of motion/deformation (McCormick & Lord, 2010). Initially, images of the object are taken in its undeformed state. After load application, as the specimen progressively deforms, subsequent images are taken. By means of software algorithms, the images (deformed) are then correlated and compared with reference images (undeformed) to track the deformation.

This technique, through advanced software algorithms enables the acquisition of precise and accurate quantitative displacement data (Xiufeng et al., 2020). Such data can be effectively utilized to validate numerical analyses, among other applications. An additional advantage of this method is its non-destructive nature, meaning that the measurement process does not damage the specimen under study. Moreover, DIC enables "real-time" monitoring of specimen behavior during testing, enhancing the understanding of the structural response. In the experiments, the commercial DIC code Aramis is utilized.

5.2 Experimental Method and Procedures

This section provides an overview of the methodology employed for the physical experiments utilizing a 4 mm thick steel sheet of grade S355.

5.2.1 Overview of Test Specimens

The test specimen utilized in the experiments adheres to the two rod geometries outlined in Section 4.3.1, with adjustments made to the clamping area of the specimens to align their dimensions with those of the grips in the testing machine. Specifically, the clamping length (L_k) is extended from 35 to 60 mm, and the clamping width (w_k) widened from 44 mm to 44.44 mm to ensure easy and secure fixation within the

testing machine grips, see also Section 5.2.3. Schematic visualization of the geometries with specified dimensions is found in Figure 5.1, while the physical specimens are shown in Figure 5.2.

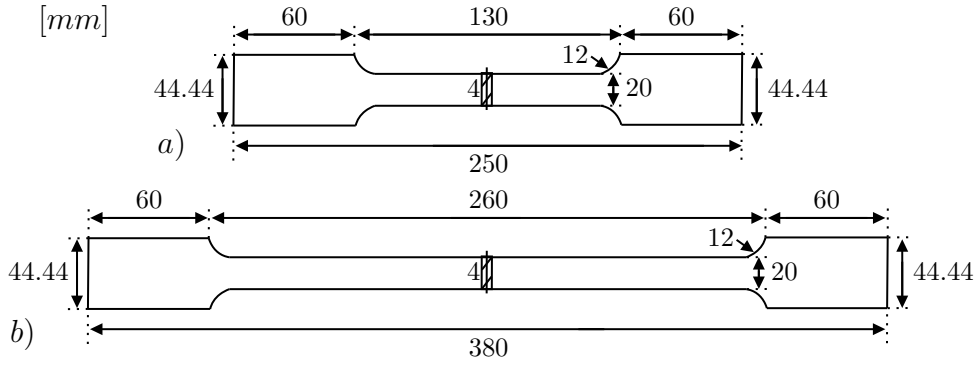

Figure 5.1: Schematic models of test specimens: a) Rod 1 & b) Rod 2.

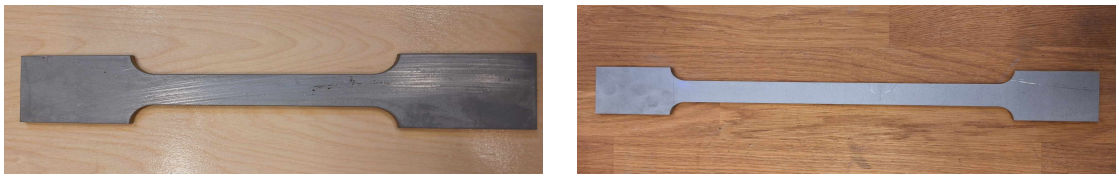

a) b)

Figure 5.2: Physical models of test specimens: a) Rod 1 & b) Rod 2.

For more details about the process of producing the individual test specimens, see Section 5.2.2.

5.2.2 Sample Measurements and Preparations

Initially, specimens are cut from the S355 steel sheet metal using a water jet system, with the cutting process meticulously guided by Computer-Aided Design (CAD) geometries. This process results in the creation of the desired sample shapes, each representing an individual coupon of the sheet metal. An illustration of the sheet metal after water jet cutting of the specimen geometries is shown in Figure 5.3.

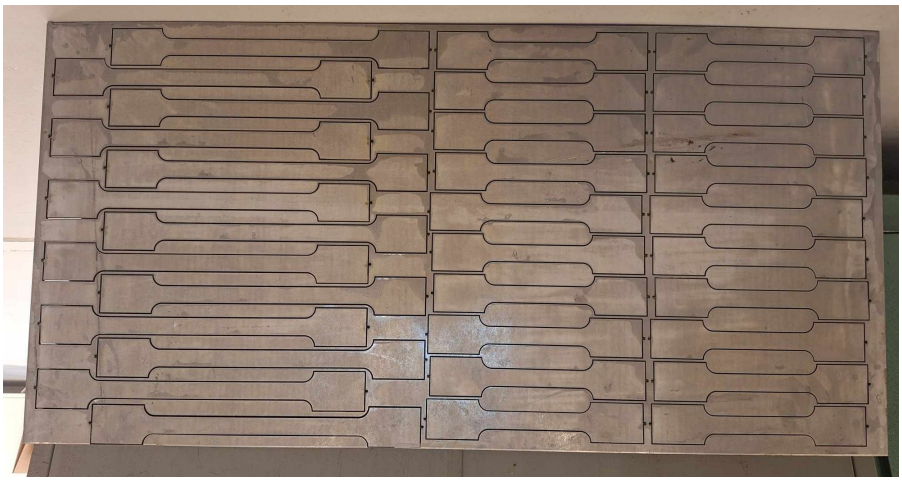

Figure 5.3: Sheet metal after completed water jet cutting.

The specimens are then detached from the sheet metal, and control measurements are conducted on single samples. Using a micrometer, the thickness of several coupons is measured. The results reveal that the actual through-thickness of both rod 1 and 2 ranges from 3.85 to 3.95 mm across the various studied cases, deviating from the intended 4 mm thickness. Consequently, an average thickness of 3.90 mm is assumed for subsequent post-processing of the experimental data and analyses.

Discrepancies in dimensions also become evident when measuring the unrestrained top and bottom widths of the specimens using the same equipment. While the width on the top face of the specimens measures 20 mm as intended, the width on the bottom face ranges from 19.70 mm to 19.80 mm, with a mean width of 19.75 mm. This suggests a reduction in the original cross-sectional area, transitioning from a rectangular to a trapezoidal shape. Note that the decrease in width at the bottom side is potentially a repercussion of the cutting process, due to the oblique angle of the water jet. The upper face is expected to remain unaffected upon contact, while the lower face can be affected as the jet penetrates at an angle through the thickness of the sheet metal. A schematic illustration of the changes in dimensions relative to the original cross-section, is presented in Figure 5.4.

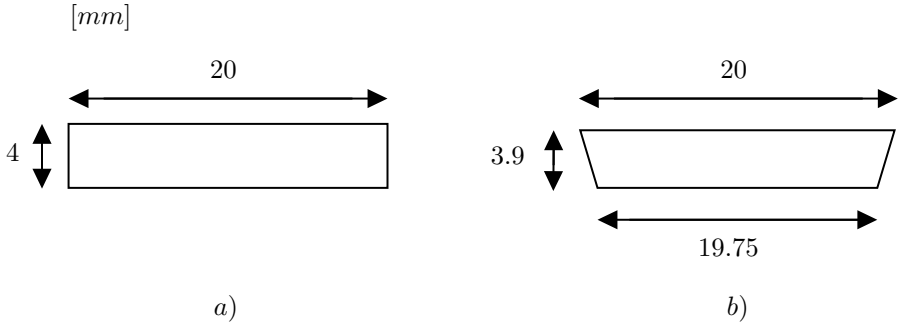

Figure 5.4: Cross-sectional area of the unrestrained part of the specimens: a) Intended & b) Achieved.

Furthermore, due to manufacturing process, the sheet metal, and consequently the coupons, are anticipated to have certain initial geometric imperfections that need consideration in the analyses. To evaluate the magnitude of these imperfections, manual measurements are performed on five arbitrary samples from both rod 1 and 2. This procedure involves placing the coupon specimen on a completely flat surface and using a micrometer attached to it. By moving the micrometer along the specimen, variations in its initial shape are observed, and eccentricities in the middle of the unrestrained length of the specimens noted. Through this approach, approximate maximum initial imperfections are determined for both rod geometries, which can be implemented in the FE-model in Abaqus CAE. A visual representation of the adopted technique is also provided in Figure 5.5.

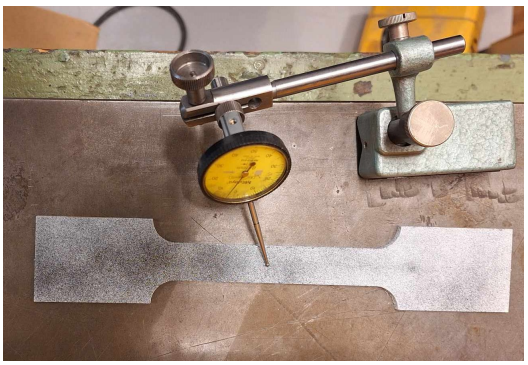

Figure 5.5: Manual measurement of initial imperfections.

A summary of the measured initial imperfections for the studied samples of both rod geometries is presented in Table 5.1. It is worth highlighting that the more slender specimens (rod 2) exhibit higher initial imperfections compared to the shorter specimens (rod 1).

Table 5.1: Approximate values of initial imperfections for both rod geometries.

	Initial Imperfections [mm]				
	Sample 1	Sample 2	Sample 3	Sample 4	Sample 5
Rod 1 (250 mm)	0.05	0.04	0.05	0.06	0.05
Rod 2 (380 mm)	0.30	0.28	0.29	0.28	0.30

Once the measurements are completed, the specimens undergo preparation prior to testing. This sample preparation involves painting the specimens white and applying a black speckle pattern (dots or lines) to one face for measurement with DIC. For an illustration of the painted sheet metal, see Figure 5.6.

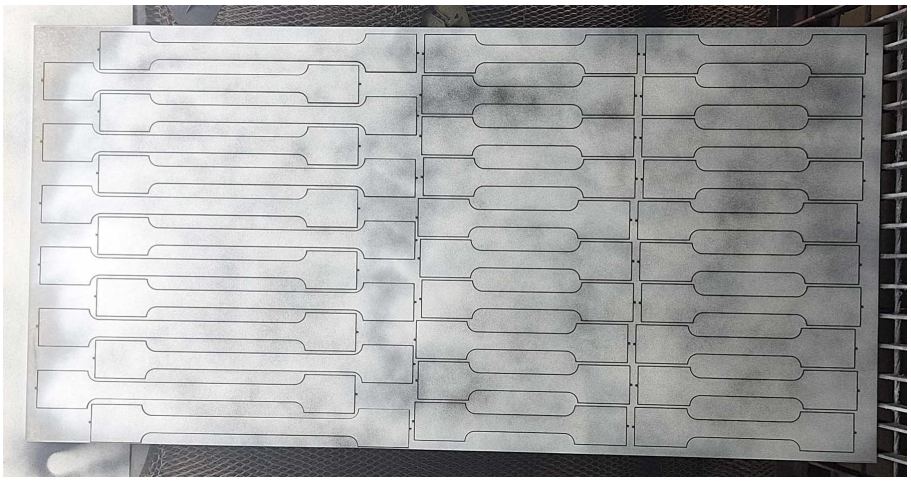

Figure 5.6: Spray painting of steel sheet metal for DIC measurement.

In order to facilitate through-thickness measurements, the specimens are also painted on the thickness side in the same manner, but with a coarser speckle pattern. Illustrations of the prepared specimens for DIC measurements are shown in Figure 5.7.

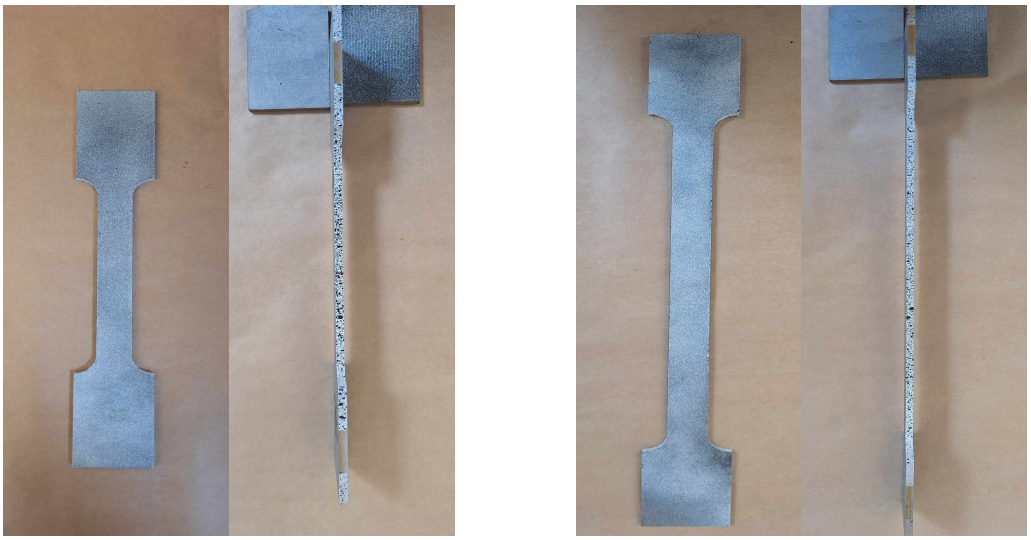

a) b)

Figure 5.7: Top and side perspectives of painted specimens for DIC measurement: a) Rod 1 & b) Rod 2.

This preparation enhances the contrast between the features of the specimen's surface and aids the measuring systems in effectively tracking deformations during testing.

5.2.3 Experimental Setup and Instrumentation

To conduct material and structural tests and obtain reliable results, appropriate equipment and experimental setup are necessary. The testing of specimens is enabled

by the use of a servo-hydraulic universal testing machine (UTM) with an axial capacity of approximately 100 kN. This equipment includes two grips, each equipped with clamping devices measuring 44.44 mm in width (w_k) and 60 mm in length (L_k).

Alongside the UTM, the instrumentation integrates two static DIC cameras (Aramis) and one high-speed camera. Specifically, the DIC systems capture images of the entire surface of one side of the specimen, enabling measurements of deformations in both in-plane and out-of-plane directions. Simultaneously, the HSC records the thickness side of the specimen, facilitating measurements of out-of-plane deformations. Given its capability to capture rapid motion at high frame rates, the HSC emerges as a crucial component in the setup, especially since the experiments involve testing specimens at high loading rates, in both tension and compression.

Furthermore, LED lighting is employed to ensure optimal conditions for photography and capturing of clear, high-quality images, as subsequent analysis and post-processing heavily rely on studying them. To provide shielding and reduce exposure to strong lighting, a light cover is also incorporated in the setup. Note that the second light source is positioned behind this light cover, directed towards the thickness side of the test specimens. An illustration depicting the experimental setup and instrumentation, with different components highlighted by arrows, is shown in Figure 5.8.

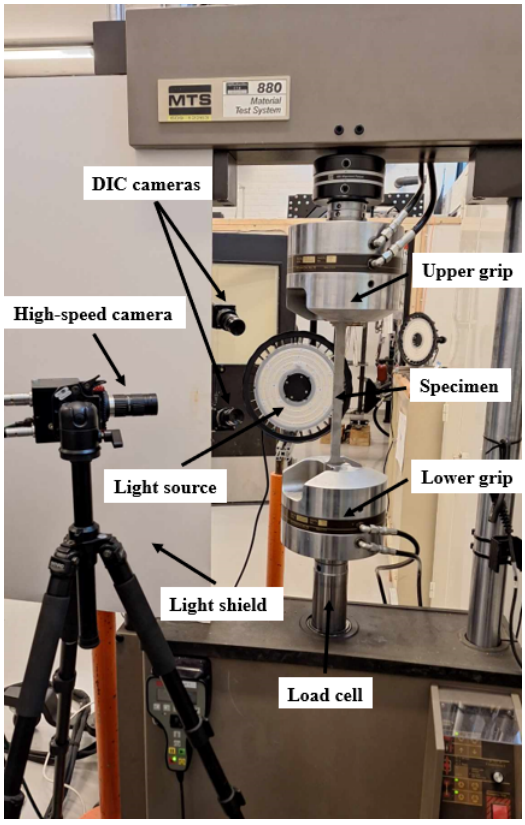

Figure 5.8: Experimental setup for material and structural testing.

It is worth noting that while the fixed parts of the specimens have the same dimensions as the clamping devices, they are secured marginally higher to prevent any risk of the specimens' bottom edge getting trapped during movement of the lower grip. Specifically, the specimens are secured with an offset of approximately 5 mm from both the top and bottom clamping devices. As a result, the unrestrained length of rod 1 becomes 140 mm, and for rod 2, 270 mm. A close-up perspective illustrating the secure fixation of the specimens within the clamping devices is portrayed in Figure 5.9.

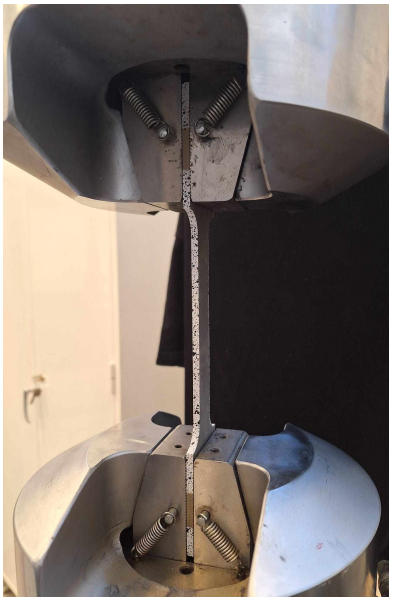

Figure 5.9: Specimen secured within the clamping devices of the UTM.

With all preparations completed and the experimental setup organized, the material and structural tests are initiated.

5.2.4 Material Tests

The material testing involves conducting tensile tests on rod 1 to determine key mechanical properties such as f_y, f_u, and ϵ_u. By utilizing the stress-strain relationships derived from the tests, the material behavior of the steel rods can then be defined within the FE-model for subsequent numerical analyses. Note that material tests are not carried out on rod 2, as the characterization achieved through the tensile testing of rod 1 suffices for the intended purposes.

In evaluating potential material strain rate effects, the specimens are subjected to tensile loading with four different velocities ranging from quasi-static to more rapid rates. Furthermore, to ensure a credible and sufficient dataset, three specimens are tested at each loading rate. A compilation of the pertinent experimental parameters for the material tests is found in Table 5.2.

Table 5.2: Experiment specifications for material tests.

Parameters	**Details**
Steel grade of sheet metal	S355
Thickness of sheet metal	3.9 [mm]
Main dimensions of specimens	250 x 44.44 x 3.9 [mm]
Approximate loading rates	0.013, 1.3, 13, 130 [mm/s]
Number of specimens / loading rate	3
Total number of specimens	$3 \times 4 = 12$

Using the velocities specified in Table 5.2, approximate strain rates of [10^{-4}, 10^{-2}, 10^{-1}, 1] s^{-1} can be attained. These strain rates encompass both quasi-static loading (10^{-4} s^{-1}) and moderately rapid loading (1 s^{-1}), which should be sufficient to elucidate how varying strain rates influence the material response of the studied steel rods. Notice that the strain rates are determined using Equation 4.7, taking into account the unrestrained length (130 mm) of the specimens.

For applying axial force, displacement-controlled loading is used (cf. Section 3.3). Throughout the entire testing procedure, the specimens undergo gradual elongation, with necking forming after the ultimate strength is reached. To determine when the test is concluded, a failure criterion is specified. In this case, the test concludes when the force drops to 75 % of the maximum force reached during the test. This predetermined threshold ensures that the specimens remain intact, while also enabling clear observation of the failure mode.

5.2.5 Structural Tests

Structural testing, unlike material testing, involves subjecting both rod geometries to compressive axial loads at varying rates. The primary objective is to assess the structural performance of the test specimens, focusing on analyzing and evaluating their deformation behavior. Additionally, the examination of two different rod geometries with distinct slenderness ratios can provide insights into how quasi-static and dynamic buckling are influenced by the slenderness.

The procedure for the compression tests follows the same consistent methodology as the tensile tests. Each type of rod geometry is studied at four different loading rates, with three trials conducted for each rate. It is worth noting that the selected velocities are determined by the findings of the numerical analyses conducted in the pre-study (cf. Section 4.4.5). A summary of the experimental parameters for the structural tests of rod 1 and 2 is presented in Table 5.3 and 5.4, respectively.

Table 5.3: Experiment specifications for structural tests of rod 1.

Parameters	**Details**
Steel grade of sheet metal	S355
Thickness of sheet metal	3.9 [mm]
Main dimensions of specimens	250 x 44.44 x 3.9 [mm]
Approximate loading rates	0.013, 13, 65, 195 [mm/s]
Number of specimens / loading rate	3
Total number of specimens	$3 \times 4 = 12$

Table 5.4: Experiment specifications for structural tests of rod 2.

Parameters	**Details**
Steel grade of sheet metal	S355
Thickness of sheet metal	3.9 [mm]
Main dimensions of specimens	380 x 44.44 x 3.9 [mm]
Approximate loading rates	0.026, 26, 52, 130 [mm/s]
Number of specimens / loading rate	3
Total number of specimens	$3 \times 4 = 12$

In the case of rod 1, the selected loading rates correspond to strain rates of [10^{-4}, 10^{-1}, 0.5, 1.5] s^{-1}. Conversely, for rod 2, the specified loading rates correspond to strain rates of [10^{-4}, 10^{-1}, 0.2, 0.5] s^{-1}. Notably, the highest strain rate achieved for rod 1 is 1.5 s^{-1}, correlating with a velocity of 195 mm/s, while for rod 2, the highest strain rate obtained is 0.5 s^{-1}, correlating with a velocity of 130 mm/s.

The structural tests also utilize displacement-controlled loading for load application. As the load increases during testing, the specimens are compressed until they reach a critical load level, resulting in global buckling. To ensure adequate out-of-plane deformations, a criterion of 10 mm relative end-shortening is applied to both geometries. This pre-set value serves as a command parameter for concluding the tests, while also enabling clear observation of the buckled specimens.

5.3 Data Acquisition and Analyses

This section describes the post-processing and analyses of the experimental data, concluding with the outcomes of the material tests.

5.3.1 Inspection of Specimens from Material Tests in GOM

Following the completion of experiments, acquired data and images from both the DIC cameras (Aramis) and the HSC undergo analysis. The data obtained from the material tests are evaluated to establish the mechanical properties of the tested specimens and to generate stress-strain relationships. Simultaneously, information gathered from structural tests is utilized to construct force-deformation curves, illustrating the global response of the steel rods.

To enable post-processing of data obtained from the different measuring systems used during testing, the software "GOM Correlate Professional 2018" (GOM) is employed. GOM facilitates the inspection of deformation patterns in DIC and HSC images, serving as a pivotal tool for measurements of parameters such as in-plane and out-of-plane displacements.

For the inspection of surfaces of specimens subjected to quasi-static loading rates, e.g., v = 0.013 mm/s and intermediate loading rates, e.g., v = 1.3 mm/s, only images from DIC are utilized. However, for specimens subjected to more rapid loading, e.g., v = 130 mm/s, measurements are carried out on imported images from HSC, while imported data from the UTM is used for studying the applied force.

It is important to note that ensuring proper synchronization between the results derived from the HSC images and the UTM force data is essential for accurate inspection and analysis. This involves aligning the time in the UTM file precisely with the simulation time recorded by the HSC.

The process of determining the material behavior of rod 1 at various loading rates involves converting force to engineering stress and elongation to engineering strain. Due to the absence of strain gauges or extensometers during material testing to directly measure the elongation (strain) of the specimens, analysis is conducted using GOM to obtain this property. Initially, two points along the unrestrained length of the specimens, positioned far apart from each other, are defined. A virtual extensometer is then constructed by measuring the distance between the points. Depending on the loading rate, the points are created, and the extensometer length is measured either on the 2D speckled top surface (DIC) or on the 2D through-thickness surface (HSC) of the specimens. Illustrative depictions of the surface inspections for elongation measurements in GOM using DIC and HSC images of the specimens, are visualized in Figure 5.10 and 5.11, respectively.

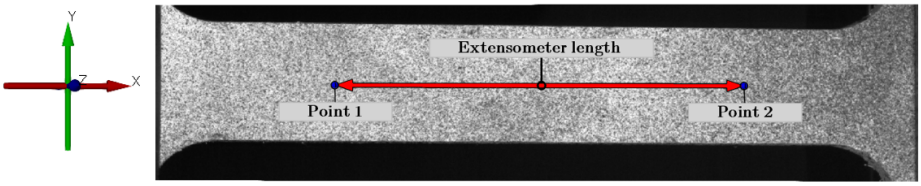

Figure 5.10: Surface inspection setup for determining elongation using DIC imaging.

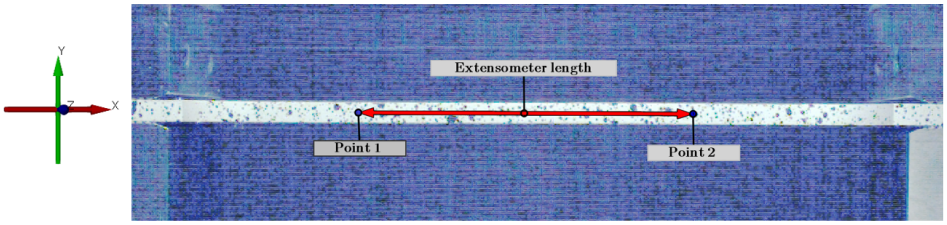

Figure 5.11: Surface inspection setup for determining elongation using HSC imaging.

In accordance with the inspection setups presented in Figure 5.10 and 5.11, the elongation (ΔL) is defined as the increase in length in the x-direction between two points from the reference (undeformed) stage up to the final deformed stage. Furthermore, the initial distance between these points corresponds to the extensometer length, L_e, which ranges from approximately 70 to 80 mm. Apart from this, data of the force values are exported either from GOM or directly retrieved from the UTM.

By leveraging the information obtained from the analysis performed in GOM, engineering strain is calculated by dividing the elongation at any time during testing with the original extensometer length, as detailed in Equation 5.1. Meanwhile, engineering stress is determined by dividing the applied axial force with the original cross-sectional area of the specimens, as outlined in Equation 5.2.

$$\epsilon = \frac{\triangle L}{L_{ext}} \tag{5.1}$$

$$\sigma = \frac{P}{A} \tag{5.2}$$

The subsequent phase of post-processing the experimental data from the material tests entails deriving stress-strain relationships for rod 1 at each loading rate. Additionally, a graphical representation highlighting the disparities in material behavior under different loading scenarios is compiled. For more detailed information about the different stress-strain curves, see Section 5.3.3.

5.3.2 Inspection of Specimens from Structural Tests in GOM

In contrast to deriving the stress-strain relationship in GOM based on material tests, structural tests focus on analyzing both in-plane (in x-direction) and out-of-plane displacements (in z-direction). This involves studying specific points and sections that are critical or of most interest, defined either on DIC images or HSC images.

The initial setup involves creating two sections: one along the x-direction of the specimens to measure in-plane displacement, and another along the y-direction for out-of-plane displacement. The position of the latter section is determined by the magnitude of the highest out-of-plane displacements. To extract values from this section, two points are defined: one at the midpoint and the other at the edge of the section. This allows for the evaluation of potential variations in the out-of-plane displacements along the width direction of the compressed specimen. Conversely, in-plane displacements are inspected at a point along the first section adjacent to the left lower grip, i.e., the moving part. This method ensures a realistic representation of end-shortening of the specimens. Notice that these points are analyzed against the reference stage, i.e., the undeformed geometry. Illustrative descriptions of the inspection setups in GOM for both the top and through-thickness surfaces are visualized in Figure 5.12 and 5.13, respectively.

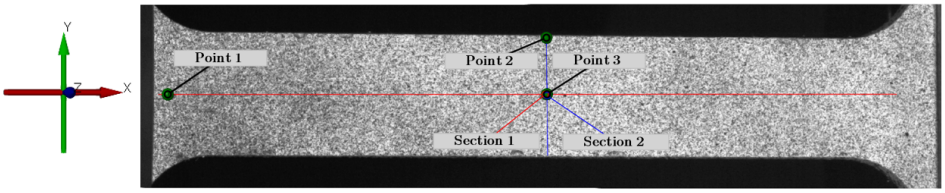

Figure 5.12: Surface inspection setup for determining in-plane and out-of-plane displacements using DIC imaging.

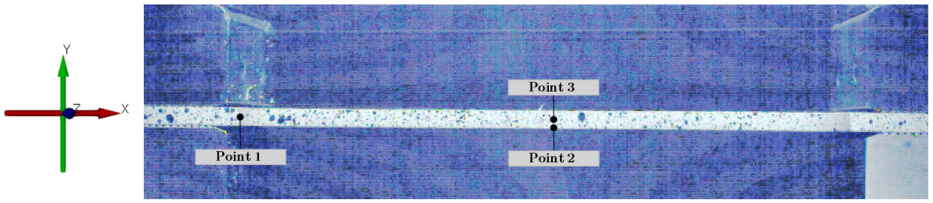

Figure 5.13: Surface inspection setup for determining in-plane and out-of-plane displacements using HSC imaging.

By integrating the available data of applied force from UTM or GOM with the evaluated in-plane displacements, the structural response for both geometries can be depicted through force-end-shortening curves for respective loading rates.

5.3.3 Outcomes of Material Tests

Figure 5.14 illustrates the obtained engineering stress-strain relationships at velocities ranging from 0.013 m/s to 130 m/s. The consistency observed across repeated specimens indicate a reliable outcome from the material tests. Consequently, a processed curve is generated by averaging the stress-strain relationships of the three specimens for further analysis. A summary of the processed curves is presented in Figure 5.15.

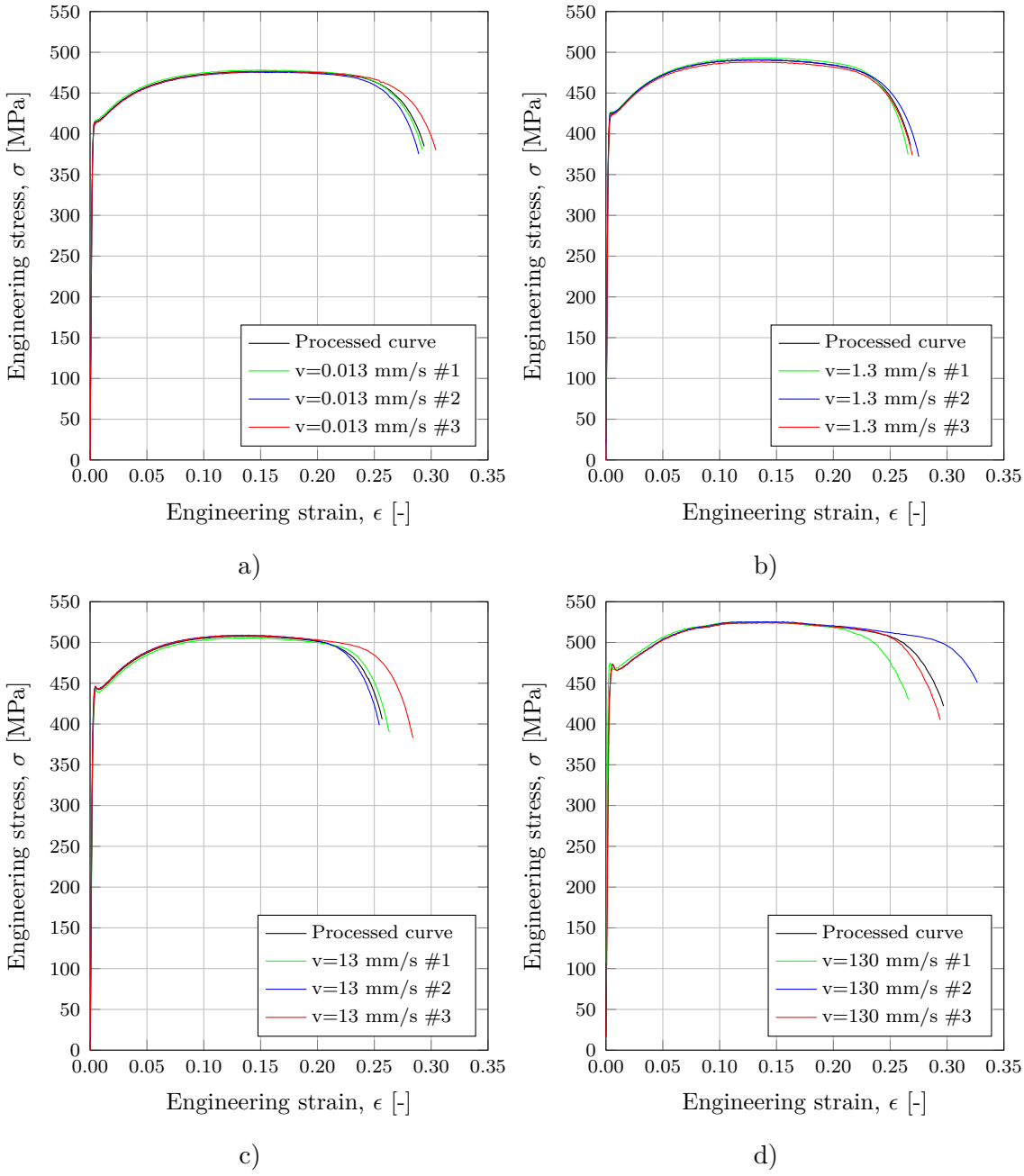

Figure 5.14: Engineering stress-strain curves at different loading rates: a) v=0.013 mm/s, b) v=1.3 mm/s, c) v=13 mm/s & d) v=130 mm/s.

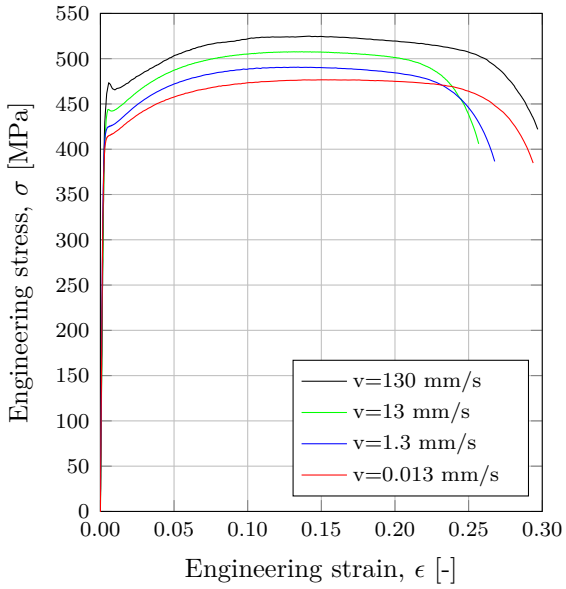

Figure 5.15: Processed engineering stress-strain curves at the different velocities.

From these curves, the Young's modulus and the yield strengths are then evaluated. Notably, the linear parts of the curves, derived from various velocities, exhibit consistent alignment and reflect the theory that the Young's modulus remains relatively insensitive to changes in strain rate (cf. Section 2.5.3). The material's stiffness is determined based on the quasi-static curve obtained at loading rate of 0.013 mm/s. The initial determination of the yield strengths is based on the 0.2 % offset method. In the engineering stress-strain curves, a linear curve representing the 0.2 % offset strain is added, see Figure 5.16.

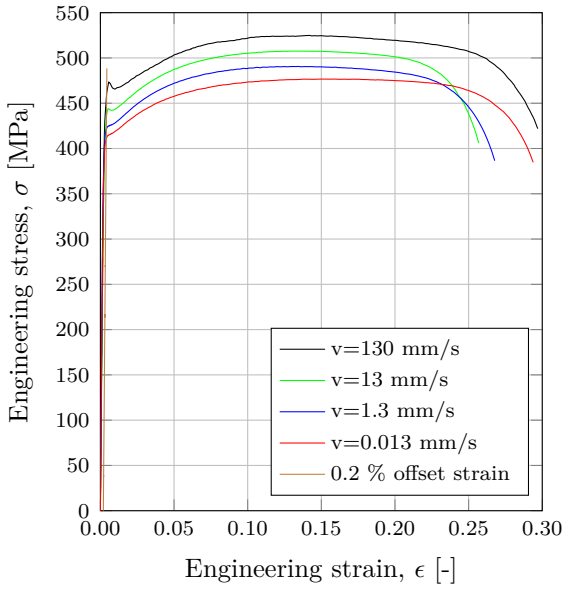

Figure 5.16: Processed engineering stress-strain curves at the different velocities with addition of 0.2 % offset strain.

A magnified view of Figure 5.16, focusing on the intersections between the 0.2 % offset strain curve and the original curves, is shown in Figure 5.17. These intersections represent the 0.2 % offset yield strengths. Moreover, the peaks within the linear range of each curve are pinpointed for comparison purposes. This approach is employed to ascertain the yield strengths by considering the highest values within the linear region of each curve.

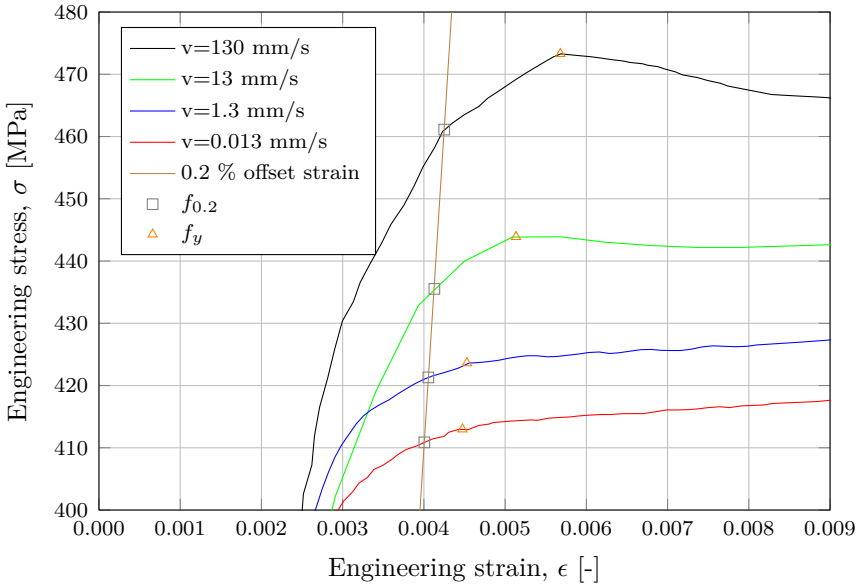

Figure 5.17: Magnified view of yield strength region across the different velocities.

As observed in Figure 5.17, it is evident that the difference between the yield strengths obtained from the 0.2 % offset method and those obtained from the highest value approach becomes more noticeable at higher velocities. Given that the steel's behavior resembles that of cold-formed steel, which lacks a distinct yield plateau, emphasis is placed on the 0.2 % offset yield strength. The mechanical properties derived from the quasi-static load case are outlined in Table 5.5.

Table 5.5: Mechanical properties of steel derived from the material test considering the quasi-static load case.

Steel Grade	E [GPa]	$f_{0.2}$ [MPa]	f_u [MPa]	$\epsilon_{0.2}$ [%]	ϵ_u [%]
S355	205	411	477	0.40	15.03

Note that the value of Young's modulus is derived from the slope of the stress-strain curve in the elastic region, specifically up to 300 MPa. Further compilation of parameters and determined strain rate indices are shown in Table 5.6.

Table 5.6: Compilation of parameters and strain rate indices derived from the processed curves.

v [mm/s]	$\dot{\epsilon}$ [s^{-1}]	$f_{0.2}$ [MPa]	f_y [MPa]	f_u [MPa]	$\epsilon_{0.2}$ [%]	ϵ_y [%]	ϵ_u [%]	$DIF_{0.2}$ [-]	DIF_y [-]	DIF_u [-]
0.013	10^{-4}	411	413	477	0.40	0.45	15.03	1	1	1
1.3	10^{-2}	421	424	491	0.41	0.45	13.42	1.025	1.026	1.029
13	10^{-1}	436	444	508	0.41	0.51	13.70	1.060	1.075	1.065
130	1	461	473	525	0.43	0.57	14.21	1.122	1.146	1.101

Observations from Table 5.6 suggest that as the velocity increases, both yield strength and ultimate strength also increase, resulting in larger DIF values. It is essential to recognize that these DIF values are computed relative to the strength values obtained at the strain rate of 10^{-4} s^{-1}, even though this strain rate does not reflect static condition. Another noteworthy observation is that the magnitude of DIF_u is lower than that of DIF_y at the highest strain rate (1 s^{-1}), but higher at the lower strain rates.

To summarize the material response of rod 1, the engineering stress-strain curve is contextualized by displaying images of the physical elongation pattern of the specimen at specific stages during testing. The correlation between those parameters, for an arbitrary specimen (#3) subjected to a velocity of 130 mm/s is illustrated in Figure 5.18.

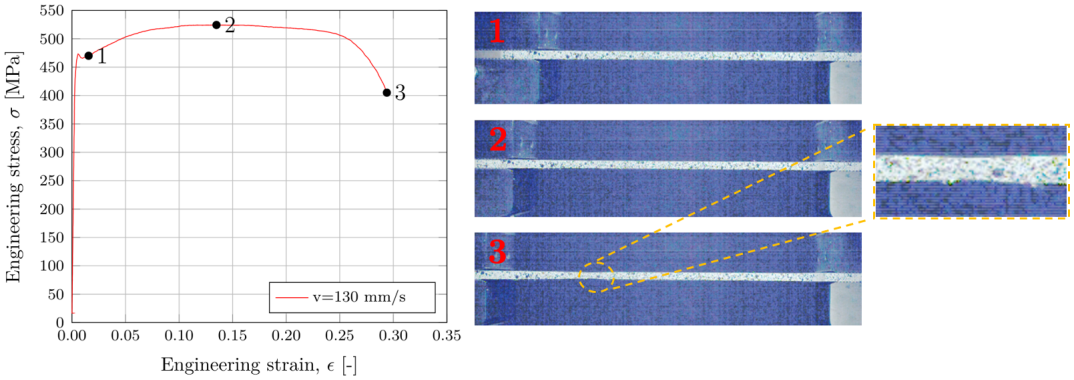

Figure 5.18: Material behavior of a sample loaded at v=130 mm/s: Left) Engineering stress-strain curve with highlighted instances marked by numbered dots & Right) HSC images of the elongated specimen at corresponding stages of testing.

With the derived stress-strain curve and the physical response interconnected, it can be observed how the elongation of the material increases during testing. A closer inspection of the magnified region depicted in Figure 5.18 also reveals the formation of necking. For physical visualization of all the elongated specimens from the material testing of rod 1, see Appendix D.

5.3.4 Development of Constitutive Model

The evaluation of S355 steel's mechanical behavior concerning its strain rate dependency involves analyzing the CS-model, particularly focusing on the yield stress (cf. Equation 2.37). By considering the different yield strengths corresponding to their respective strain rates, a curve fitting approach using a nonlinear power curve ($y = ax^b$) is employed to determine the strain rate material parameters D and p. The curve fitting process, based on the evaluation of DIF_y, uses experimental data spanning from a strain rate of 10^{-4} s^{-1} to 1 s^{-1}. Furthermore, an extrapolation technique is utilized to ascertain the static yield strength at a strain rate of 10^{-6} s^{-1}. This extrapolated approximate static yield strength, corresponding to $DIF_y = 1$, acts as the reference point for calculating DIF_y across the studied strain rates. Figure 5.19 displays the experimental data points, the extrapolated static yield strength, and the curve representing the fitted model. For comparison purposes, the evaluation of the existing material model proposed by Yang et al. (2022), based on the extrapolated approximate static yield and the Equations 2.41-2.43, is further highlighted in Figure 5.19.

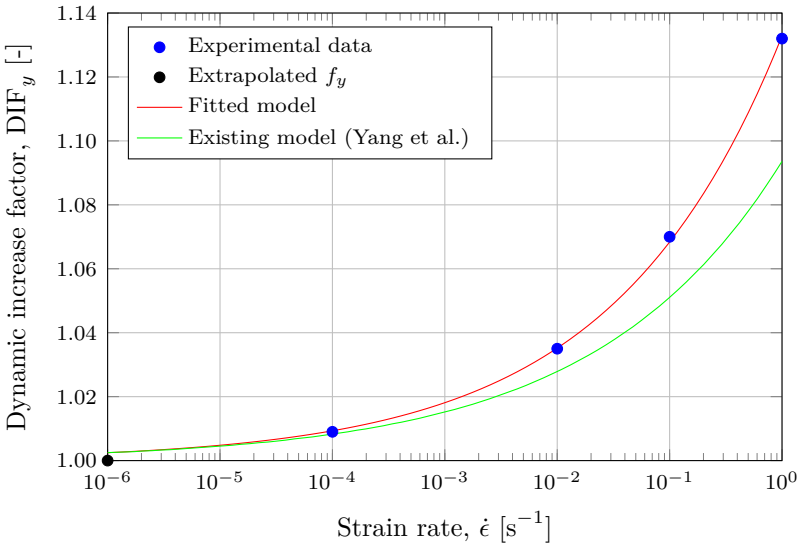

Figure 5.19: Illustration of DIF_y values with curve fitting across varying strain rates.

Finalization of the fitting renders the CS-model as expressed in Equation 5.3, with parameters D = 1094 and p = 3.47. As seen in Figure 5.19, the fitted curve slightly differs from the existing model, resulting in higher DIF_y values. See also Appendix E for details of the curve fitting procedure.

$$DIF_y = 1 + \left(\frac{\dot{\epsilon}}{1094}\right)^{\frac{1}{3.47}} \tag{5.3}$$

For conducting numerical buckling analyses, the acquired strain rate dependent parameters are utilized alongside true stress-strain data. This data, as presented in graphical and tabulated form in Figure 5.20, is derived from the engineering stress-strain curve (until necking), considering the quasi-static load case.

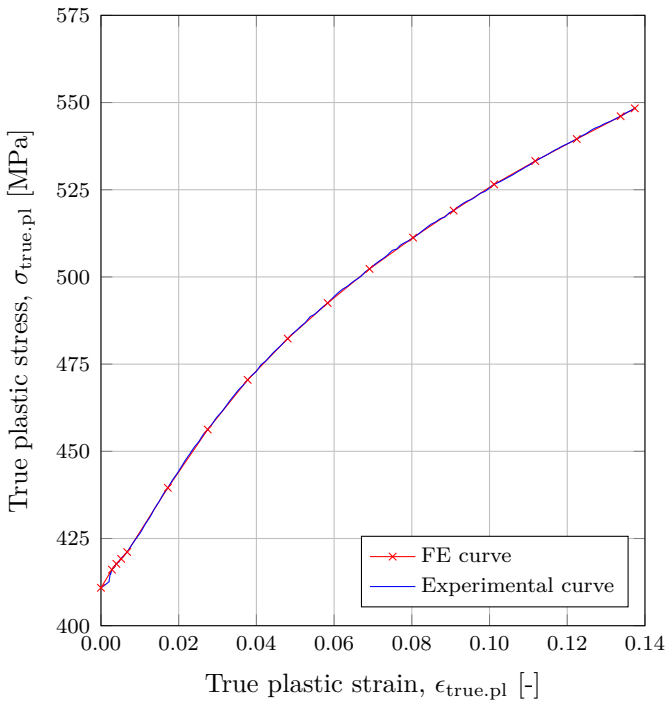

a)

$\sigma_{true,pl}$ [MPa]	$\epsilon_{true,pl}$ [-]
410.9	0.0000
416.1	0.0028
417.7	0.0040
419.2	0.0052
421.1	0.0068
439.5	0.0172
456.3	0.0275
470.5	0.0378
482.3	0.0481
492.5	0.0584
502.3	0.0691
511.3	0.0803
519.0	0.0908
526.5	0.1012
533.2	0.1118
539.5	0.1224
546.1	0.1337
548.3	0.1374

b)

Figure 5.20: Plasticity model in Abaqus CAE derived from material testing: a) Graphical presentation & b) Tabulated presentation.

The plasticity model depicted in Figure 5.20 utilizes a subset of data points from the experimental curve. As seen, the chosen number of points provide a satisfactory representation of the experimental curve.

6 Results

This section delineates the key findings derived from structural tests and numerical analyses conducted on both rod geometries, leveraging the material behavior established through the material tests. Additionally, it presents a comparative evaluation of FEA outcomes and experimental findings, aimed at validating the results or assessing any disparities between these two approaches.

6.1 Outcomes of Structural Tests

The structural response of the experimentally tested steel rods is investigated by analyzing their axial capacity against both in-plane and out-of-plane displacements. Specifically, the critical forces leading to global buckling of the compressed rods are identified at various loading rates, along with associated critical end-shortenings and maximum deflections. A comparison is made between rod 1 and 2 to investigate how slenderness and initial imperfections affect their structural behavior. This comparison also aims to identify any differences in dynamic effects observed between the two rod geometries.

6.1.1 Structural Response of Rod 1

After post-processing the experimental data and inspecting rod 1 (cf. Section 5.3.1), the structural response is established, characterized by force-end-shortening and force-deflection relationships. Following the methodology employed in material testing, force-end-shortening curves integrate data from all three samples tested at each loading rate, accompanied by a processed curve. This curve represents the average response of the samples and serves as a basis for subsequent comparisons.

The variation in axial capacity for rod 1 with end-shortening under applied loading rates of 0.013 mm/s, 13 mm/s, 65 mm/s, and 195 mm/s, is illustrated in Figure 6.1.

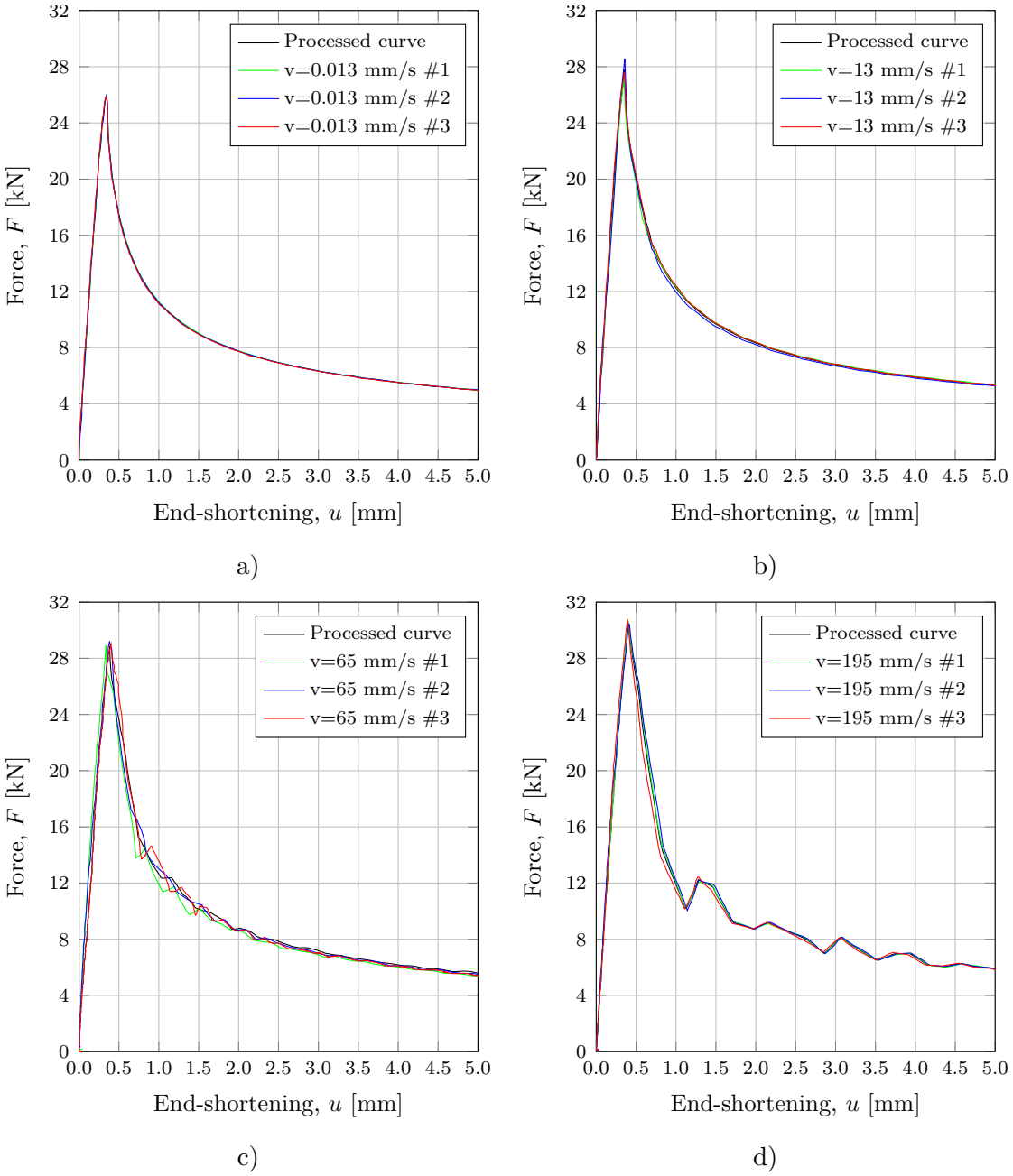

Figure 6.1: Relationship between compressive axial force and end-shortening for rod 1, featuring experimental data and a processed curve obtained at the different velocities: a) v=0.013 mm/s, b) v=13 mm/s, c) v=65 mm/s & d) v=195 mm/s.

Observations from Figure 6.1 suggest a similar structural behavior among the three samples, indicating strong overall agreement. However, small deviations in the critical buckling force is apparent, particularly noticeable at loading beyond the quasi-static range, such as at v = 13 mm/s. Further analysis of Figure 6.1 c) reveals the emergence of inertia effects around v = 65 mm/s, evident from distinct sharp dynamic oscillations or fluctuations in the force-end-shortening curve. In contrast, Figure 6.1 b) does not exhibit such effects. It is worth noting that, since no inter-

mediate loading rates between 13 mm/s and 65 mm/s have been studied, it cannot be definitively ascertained that inertia effects manifest precisely at 65 mm/s. These dynamic oscillations are likely to occur at an earlier loading rate.

Comparison of Figure 6.1 d) with Figure 6.1 a) also demonstrates that the critical buckling forces observed under more rapid loading are tangibly higher than those under quasi-static loading, highlighting the influence of strain rate and inertia effects. To elucidate the structural behavior across the studied loading rates and their interrelation, processed curves from the various cases are compiled together in Figure 6.2. This compilation serves as an illustrative summary of the experimental findings regarding the structural behavior of rod 1 under different compressive axial loading conditions.

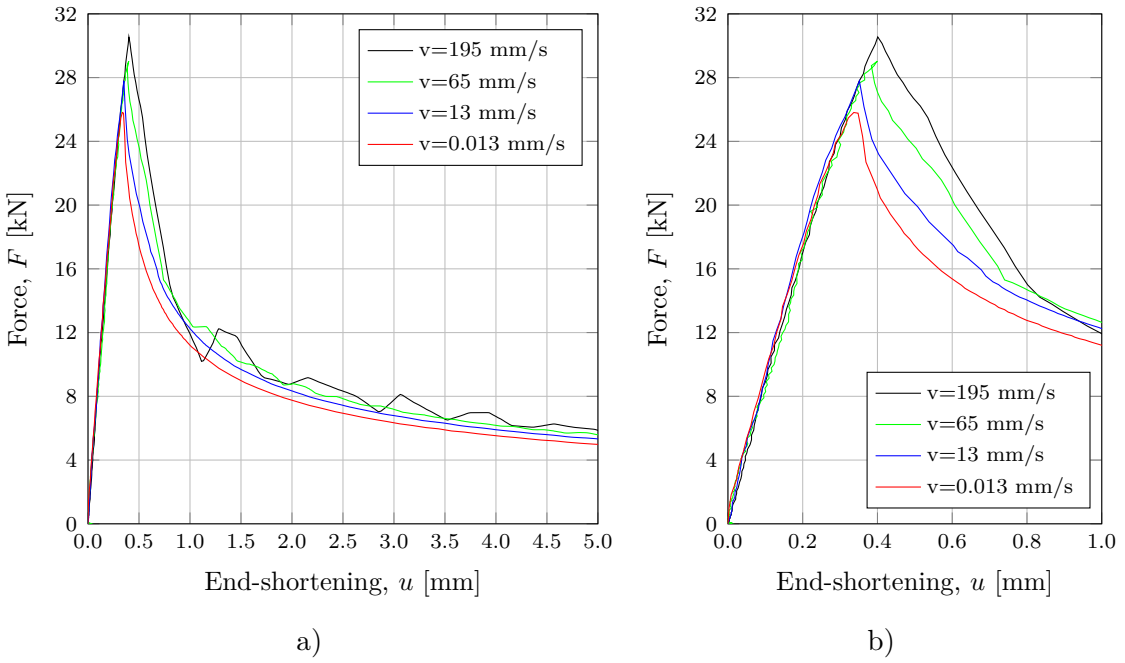

Figure 6.2: a) Relationship between compressive axial force and end-shortening for rod 1, featuring processed curves obtained at the different velocities & b) Magnified view of the response for 1 mm end-shortening.

Upon careful examination of Figure 6.2, the dynamic effects become conspicuous when contrasting the structural responses of rod 1 at higher loading stages with the reference quasi-static loading stage. A notable increase in the critical buckling force is evident with escalated strain rates, accompanied by the appearance of inertia effects. Furthermore, the results suggest that the stiffness of the rod remains largely unaffected by dynamic loading.

To supplement the visual representations, experimental data extracted from Figures 6.1-6.2 is provided to aid in quantifying the critical buckling force and the associated end-shortening at which the instability occurs. Table 6.1 offers numerical values of the critical buckling force for the three samples ($P_{cr\#1-3}$) tested at each

loading rate, along with their corresponding critical end-shortening ($u_{cr\#1-3}$). Additionally, an average of the critical buckling force (P_{cr}) and end-shortening (u_{cr}) is also presented.

Table 6.1: Variations in critical buckling force and end-shortening for rod 1 across the different loading rates.

Rod 1		Individual specimens						Average of specimens	
v [mm/s]	$\dot{\epsilon}$ [s^{-1}]	$P_{\text{cr}\#1}$	$P_{\text{cr}\#2}$ [kN]	$P_{\text{cr}\#3}$	$u_{\text{cr}\#1}$	$u_{\text{cr}\#2}$ [mm/s]	$u_{\text{cr}\#3}$	P_{cr} [kN]	u_{cr} [mm/s]
0.013	10^{-4}	25.86	25.95	25.88	0.341	0.342	0.338	**25.90**	**0.340**
13	10^{-1}	27.19	28.59	27.61	0.351	0.358	0.355	**27.80**	**0.355**
65	0.5	28.93	29.16	29.03	0.337	0.381	0.391	**29.04**	**0.370**
195	1.5	30.55	30.41	30.69	0.400	0.418	0.390	**30.55**	**0.403**

Table 6.1 illustrates that as rod 1 experiences higher strain rates, its load-bearing capacity increases. Concurrently, it necessitates greater critical end-shortening to induce global buckling. The increase in capacity relative to the critical buckling force for quasi-static loading, $P_{\text{cr.quasi}}$, is further elucidated in Table 6.2.

Table 6.2: Increase in critical buckling load for rod 1 at elevated loading rates.

v [mm/s]	$\dot{\epsilon}$ [s^{-1}]	P_{cr} [kN]	$\frac{P_{\text{cr}}}{P_{\text{cr.quasi}}}$ [-]
0.013	10^{-4}	25.90	1.00
13	10^{-1}	27.80	1.07
65	0.5	29.04	1.12
195	1.5	30.55	1.18

Utilizing the critical force in conjunction with its corresponding end-shortening allows computation of the secant stiffness, K_{sec}. This stiffness, as defined by Equation 6.1, provides insight into potential variations in material stiffness under different loading rates. The outcomes of this computation are summarized in Table 6.3.

$$K_{sec} = \frac{P_{cr}}{u_{cr}} \tag{6.1}$$

Table 6.3: Secant stiffness for rod 1 across varying loading rates.

v [mm/s]	$\dot{\epsilon}$ [s^{-1}]	P_{cr} [kN]	u_{cr} [mm]	K_{sec} [kN/mm]
0.013	10^{-4}	25.90	0.340	76
13	10^{-1}	27.80	0.355	78
65	0.5	29.04	0.370	78
195	1.5	30.55	0.403	76

As indicated by Table 6.3, secant stiffness values show little to no variation across the different loading rates. This consistency suggests that the material's stiffness exhibits limited sensitivity to changes in loading rates.

Transitioning the focus from the structural response concerning the force-end-shortening relationship, Figure 6.3 illustrates the force-deflection curves for rod 1 across various loading rates, considering an in-plane compression of 10 mm.

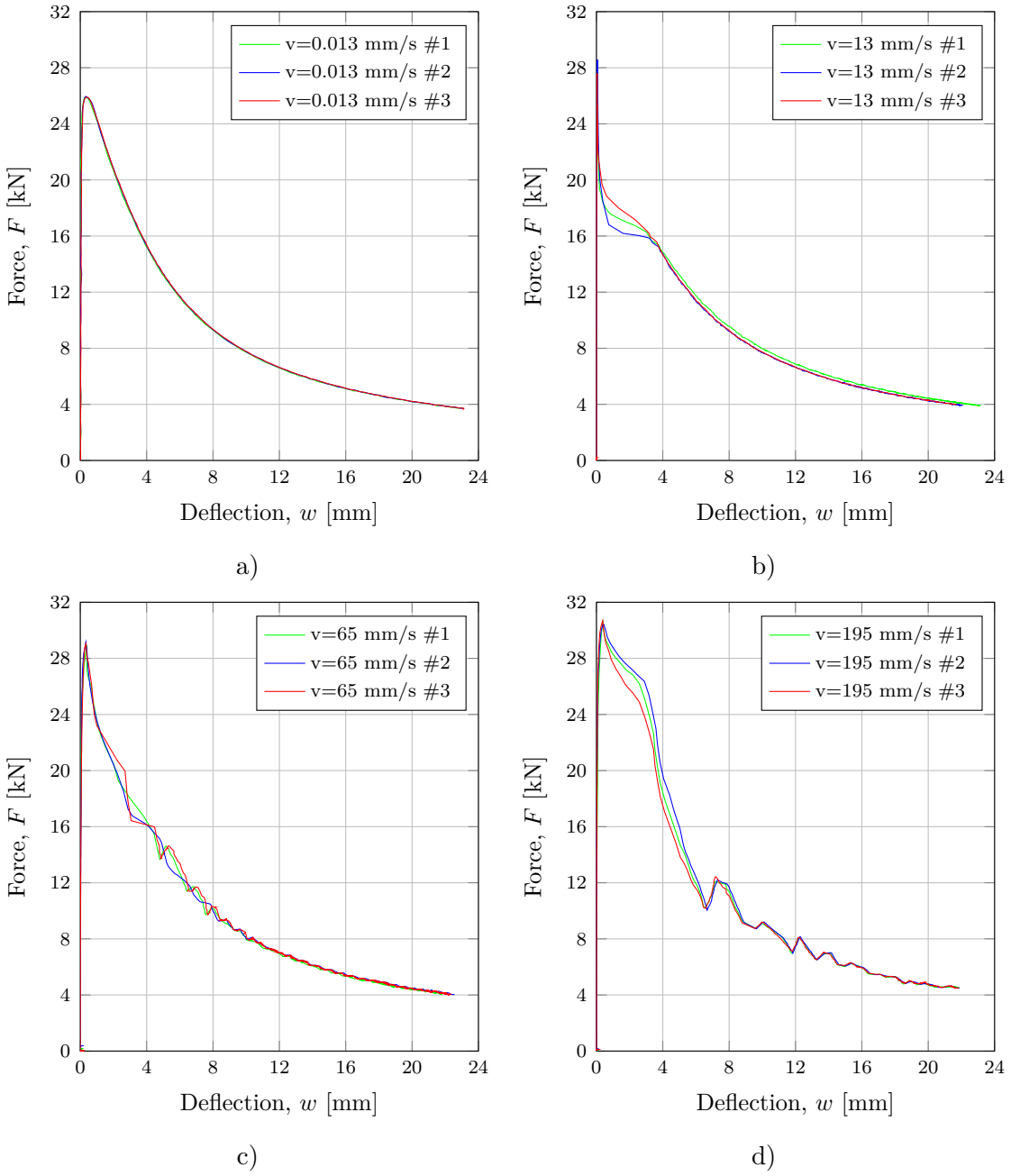

Figure 6.3: Relationship between compressive axial force and deflection for rod 1, featuring experimental data obtained at the different velocities: a) v=0.013 mm/s, b) v=13 mm/s, c) v=65 mm/s & d) v=195 mm/s.

After examining Figure 6.3, it is apparent that the global structural response bears a resemblance to the characteristics observed in the force-end-shortening curves. Initially, the axial capacity of the rod exhibits a linear increase until it reaches the critical buckling force. Subsequently, the capacity decreases as the rod transitions into post-buckling behavior. Additionally, at a loading rate of 65 mm/s, inertia effects become apparent in the structural response. However, it is important to note that the deflection corresponding to the onset of buckling varies significantly across the different loading rates. For instance, in Figure 6.3 b), the critical buckling load is observed to occur at a deflection close to 0 mm, whereas in Figure 6.3 a), the deflection for the onset of buckling is larger. This is in contrast to the obtained force-end-shortening relations, where the end-shortening corresponding to the onset of buckling increases with higher loading rates.

When comparing the force-deflection relationships obtained at the different loading rates, noticeable changes in the overall shape of the curves are observed. These discrepancies could stem from limitations in the ability of the HSC to accurately track movements perpendicular to the rod's plane, especially at loading rates of 13 mm/s and higher. Factors such as low resolution, dust interference, sensor noise, and the nature of 2D images could all contribute to inaccuracies in the measurements. Consequently, these inaccuracies might then lead to large variations in each measurement point and result in different behaviors in the force-deflection curves.

For the purpose of comparison, Figure 6.4 presents a summary of the structural behavior of specimen #3 across the different loading rates.

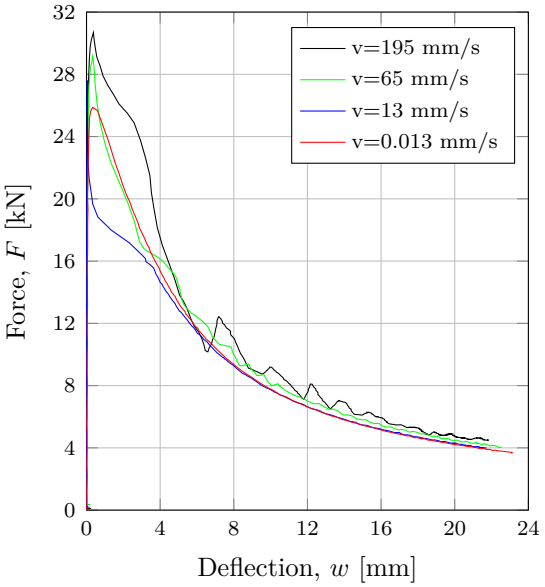

Figure 6.4: Relationship between compressive axial force and deflection for rod 1, featuring the curves for specimen #3 obtained at the various velocities.

In Table 6.4, the deflection values for a 10 mm in-plane compression obtained from the analyzed points (cf. Figures 5.12-5.13) are compiled for each individual specimen.

Table 6.4: Variations in maximum deflection for rod 1 across the different loading rates.

Rod 1		Individual specimens			Average of specimens
v [mm/s]	$\dot{\epsilon}$ [s^{-1}]	$w_{max\#1}$	$w_{max\#2}$ [mm]	$w_{max\#3}$	w_{max} [mm]
0.013	10^{-4}	23.08	23.11	23.12	**23.10**
13	10^{-1}	23.11	22.03	21.74	**22.29**
65	0.5	21.82	22.55	22.33	**22.23**
195	1.5	21.88	21.84	21.84	**21.85**

The recorded deflection values, ranging from approximately 22 to 23 mm, illustrate a marginal decrease as the loading rate increases. Physically measured deflections also fall within this range. It is noteworthy that the magnitude of the deflection is more than twice the magnitude of the end-shortening (10 mm).

To summarize the structural response of rod 1, the force-end-shortening curve is contextualized by displaying images of the physical deflection pattern of the specimen at specific stages during testing. The correlation between applied compressive force, end-shortening, and deflection for an arbitrary specimen (#2) subjected to a velocity of 195 mm/s is illustrated in Figure 6.5.

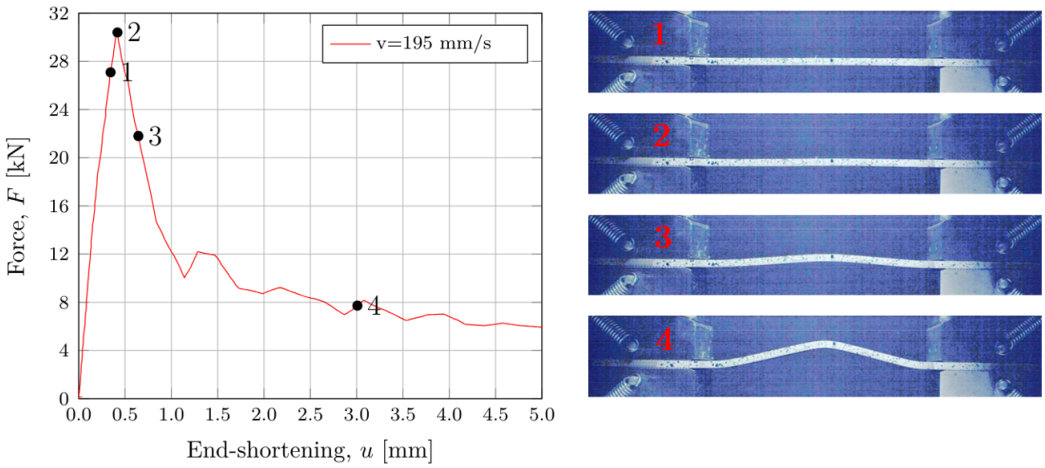

Figure 6.5: Structural behavior of a sample from rod 1 loaded at v=195 mm/s: Left) Force-end-shortening curve with highlighted instances marked by numbered dots & Right) HSC images of the out-of-plane displacements of the specimen at corresponding stages of testing.

As noticed, there is no pronounced deflection prior to the onset of buckling. With increased compression, the rod's structural response transitions to a post-buckling behavior and distinct buckling mode corresponding to fixed-fixed BC emerges. For physical visualization of all the buckled specimens from the structural testing of rod 1, see Appendix F.

6.1.2 Structural Response of Rod 2

Following the same methodology as for rod 1, the structural behavior of rod 2 exhibited at loading rates of 0.026 mm/s, 26 mm/s, 52 mm/s, and 130 mm/s, is presented in terms of force-end-shortening relationships, as illustrated in Figure 6.6.

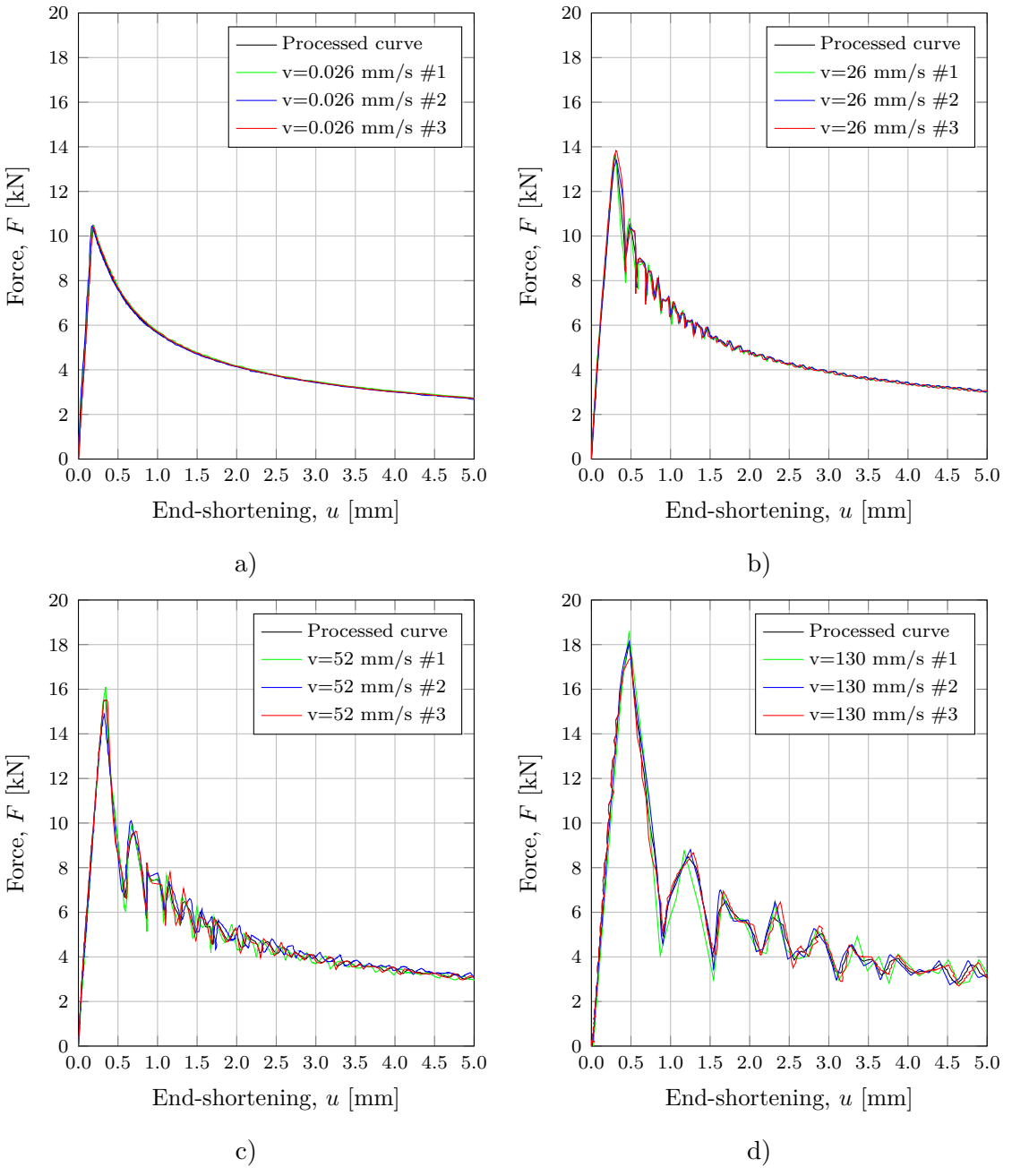

Figure 6.6: Relationship between compressive axial force and end-shortening for rod 2, featuring experimental data and a processed curve obtained at the different velocities: a) v=0.026 mm/s, b) v=26 mm/s, c) v=52 mm/s & d) v=130 mm/s.

In general, Figure 6.6 illustrates that the different samples demonstrate similar responses across all the examined loading rates. However, as the loading rate increases, noticeable discrepancies in axial capacity emerge among the three samples, as shown in Figure 6.6 b)-d). The disparities in the critical buckling force values may stem from limitations in the sampling frequency of the UTM. During rapid loading, the buckling onset occurs almost immediately, making it more challenging to measure and obtain sufficient force data around the instability stage. Consequently, deviations in critical force values between cases may arise due to inadequate data. Furthermore, analyses of force-time data from UTM reveals a significant increase in force magnitude between the time step instantly preceding buckling and the time step at which buckling occurs.

Concerning dynamic effects, Figure 6.6 b) illustrates that inertia effects for rod 2 become apparent initially at v = 26 mm/s. These dynamic oscillations then intensify, characterized by larger amplitudes with increased loading rate. Additionally, a comparison between the responses depicted in Figure 6.6 a) and d) also reveals the emergence of strain rate effects. These effects are evident as there is a distinct rise in axial capacity when relating the structural response from rapid loading to quasi-static loading. Furthermore, the processed responses of rod 1 from the various loading scenarios are also consolidated in Figure 6.7.

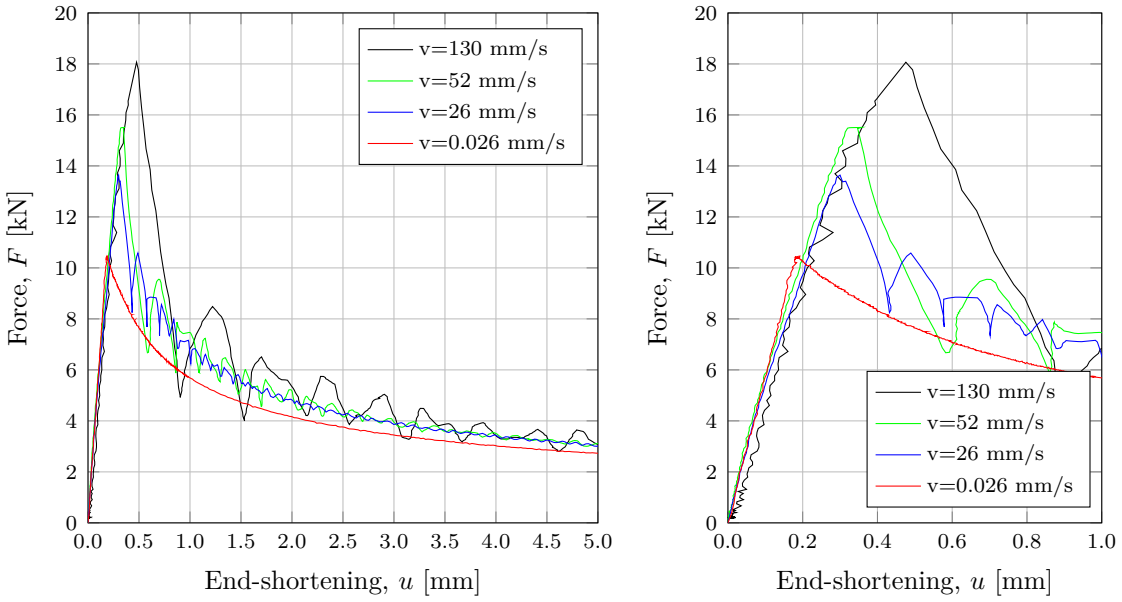

Figure 6.7: a) Relationship between compressive axial force and end-shortening for rod 2, featuring processed curves obtained at the different velocities & b) Magnified view of the response for 1 mm end-shortening.

When analyzing the responses in Figure 6.7 a), the manifestation of inertia and strain rate effects becomes clear. It is worth noting that the results suggest some deviation in the stiffness of the rods among the four cases of loading, see Figure 6.7 b). The

numerical values of the critical buckling force and associated end-shortening, as visually observed in Figures 6.6-6.7, are compiled in Table 6.5.

Table 6.5: Variations in critical buckling force and end-shortening of rod 2 across the different loading rates.

Rod 2		Individual specimens						Average of specimens	
v [mm/s]	$\dot{\epsilon}$ [s^{-1}]	$P_{\text{cr}\#1}$	$P_{\text{cr}\#2}$ [kN]	$P_{\text{cr}\#3}$	$u_{\text{cr}\#1}$	$u_{\text{cr}\#2}$ [mm/s]	$u_{\text{cr}\#3}$	P_{cr} [kN]	u_{cr} [mm/s]
0.026	10^{-4}	10.45	10.44	10.40	0.195	0.168	0.185	**10.43**	**0.183**
26	10^{-1}	13.62	13.37	13.84	0.290	0.317	0.311	**13.61**	**0.306**
52	0.2	16.10	14.91	15.51	0.345	0.328	0.358	**15.51**	**0.344**
130	0.5	18.52	18.12	17.42	0.475	0.477	0.511	**18.02**	**0.488**

Table 6.5 shows that when rod 2 is subjected to quasi-static loading (0.026 mm/s), buckling occurs with minimal induced end-shortening. Conversely, under dynamic loading condition (130 mm/s), a significantly greater amount of compression is required to induce instability in the rod. To quantify the effects of strain rate on rod 2, the increase in axial capacity relative to the reference quasi-static loading state is elucidated in Table 6.6.

Table 6.6: Increase in critical buckling load of rod 2 at elevated loading rates.

v [mm/s]	$\dot{\epsilon}$ [s^{-1}]	P_{cr} [kN]	$\frac{P_{\text{cr}}}{P_{\text{cr.quasi}}}$ [-]
0.026	10^{-4}	10.43	1.00
26	10^{-1}	13.61	1.30
52	0.2	15.51	1.49
130	0.5	18.02	1.73

The results suggest that the resistance of rod 2 increases by approximately 30 % to 73 % as it undergoes loading within the dynamic range. However, while this increase in capacity is evident, a 73 % rise in relation to the quasi-static condition may seem somewhat unreasonable. Additionally, the secant stiffness of rod 2 across the studied loading rates is determined and presented in Table 6.7.

Table 6.7: Secant stiffness for rod 2 across varying loading rates.

v [mm/s]	$\dot{\epsilon}$ [s^{-1}]	P_{cr} [kN]	u_{cr} [mm]	K_{sec} [kN/mm]
0.026	10^{-4}	10.43	0.183	57
26	10^{-1}	13.61	0.306	44
52	0.2	15.51	0.344	45
130	0.5	18.02	0.488	37

Upon examination of Table 6.7, variations in stiffness K_{sec} are observed between the different loading conditions, as also noted earlier in Figure 6.7 b). These deviations

are unexpected, and potential explanations for this sensitivity to strain rates are likely connected to the force and end-shortening data.

Shifting the focus, Figure 6.8 illustrates the force-deflection curves for rod 2 at the various loading rates, considering an in-plane compression of 10 mm.

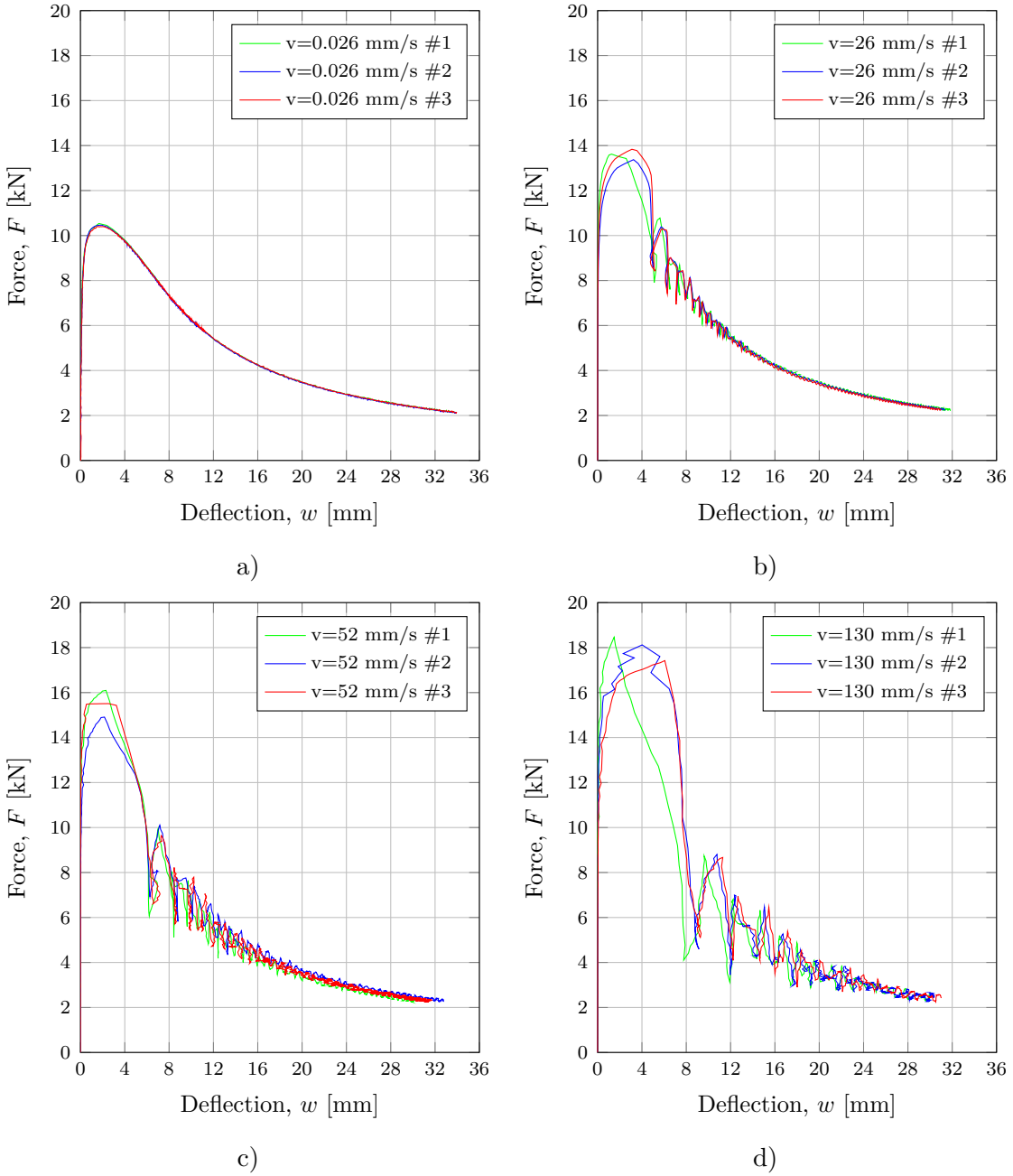

Figure 6.8: Relationship between compressive axial force and deflection for rod 2, featuring experimental data obtained at the different velocities: a) v=0.026 mm/s, b) v=26 mm/s, c) v=52 mm/s & d) v=130 mm/s.

In Figures 6.8 b)-d), analogous dynamic effects to those observed in the force-end-shortening responses are visible. However, the response around the critical loading

stage differs among the three samples. In particular, Figure 6.8 d) exhibits irregular variations and jumps in the curves, complicating the reading of the deflection value at buckling. These irregularities may stem from the limitations of the HSC. Furthermore, there is a certain decrease in maximum deflection values between quasi-static and dynamic loading conditions. The force-deflection behavior of a representative sample across the different loading rates is illustrated in Figure 6.9.

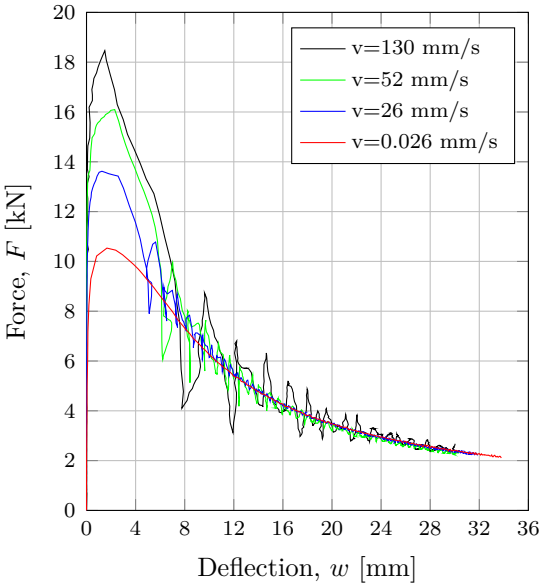

Figure 6.9: Relationship between compressive axial force and deflection for rod 2, featuring the curves for specimen #1 obtained at the various velocities.

To complement the visual illustrations of the structural responses, Table 6.8 presents the deflection values for each individual specimen, along with an average representation at corresponding strain rates for a 10 mm in-plane compression.

Table 6.8: Variations in maximum deflection for rod 2 across different loading rates.

Rod 2		Individual specimens			Average of specimens
v [mm/s]	$\dot{\epsilon}$ [s^{-1}]	$w_{max\#1}$	$w_{max\#2}$ [mm]	$w_{max\#3}$	w_{max} [mm]
0.026	10^{-4}	33.78	33.94	33.88	**33.87**
26	10^{-1}	31.84	31.36	30.98	**31.39**
52	0.2	30.32	32.77	31.72	**31.60**
130	0.5	30.04	30.38	31.01	**30.48**

The deflection variation, as seen in Table 6.8, ranges from approximately 34 to 30.5 mm, which is approximately three times the magnitude of the in-plane compression. These values diminish with escalated strain rates, reflecting the anticipated material strengthening under rapid loading conditions.

Interestingly, the average deflection at a velocity of 52 mm/s exceeds that observed at 26 mm/s, contrary to the expected trend of reduced out-of-plane deformation. This deviation can be attributed to notable fluctuations among individual sample values. Furthermore, it is noteworthy that the physical measurements of the specimens closely correspond to the range obtained from the analyses.

In a similar manner to rod 1, the force-end-shortening curve is contextualized by displaying images of the physical deflection pattern of the specimen at specific stages during testing. Figure 6.10 provides a summarized illustration of the structural behavior of an arbitrary specimen (#1) subjected to a velocity of 130 mm/s.

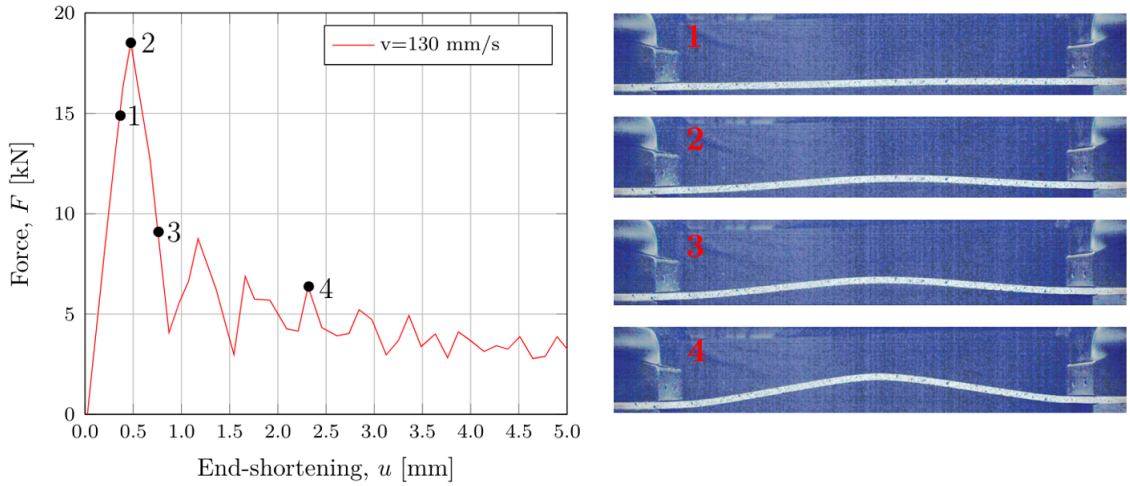

Figure 6.10: Structural behavior of a sample from rod 2 loaded at v=130 mm/s: Left) Force-end shortening curve with highlighted instances marked by numbered dots, & Right) HSC images of the out-of-plane displacements of the specimen at corresponding stages of testing.

Upon careful examination, Figure 6.10 divulges that this slender rod exhibits certain deformation in the out-of-plane direction when experiencing global instability. The post-buckling behavior is further characterized by a distinct buckled shape, which becomes greater in magnitude as the compression increases. For physical visualizations of all the buckled specimens from the structural testing of rod 2, see Appendix G.

6.1.3 Summary of Responses of Rod 1 & 2

A comprehensive overview of the findings derived from the examination of the two rod geometries concerning important parameters such as critical buckling force, end-shortening, deflection, and stiffness reveals significant insights into their comparative performance. Table 6.9 provides a comparison of the axial capacities of both rod geometries at various loading rates.

Table 6.9: Comparison of load-bearing capacities between rod 1 and 2 across various loading rates.

Rod 1				Rod 2			
v [mm/s]	$\dot{\epsilon}$ [s^{-1}]	P_{cr} [kN]	$\frac{P_{cr}}{P_{cr.quasi}}$ [-]	v [mm/s]	$\dot{\epsilon}$ [s^{-1}]	P_{cr} [kN]	$\frac{P_{cr}}{P_{cr.quasi}}$ [-]
0.013	10^{-4}	25.90	1.00	0.026	10^{-4}	10.43	1.00
13	10^{-1}	27.80	1.07	26	10^{-1}	13.61	1.30
65	0.5	29.04	1.12	52	0.2	15.51	1.49
195	1.5	30.55	1.18	130	0.5	18.02	1.73

The comparison clearly shows a significant difference in axial capacity between rod 1 and 2, with the former displaying higher axial capacity. What stands out is the stark contrast in the increase of critical buckling force under the same loading rates. Specifically, at a strain rate of 0.5 s^{-1}, rod 1 demonstrates an increase of about 12 %, while rod 2 shows a substantial rise of approximately 73 %. Referring to the pre-study (cf. Figure 4.26), which involved FEA on rod 2 with imperfections of 0.2 and 0.4 mm, the anticipated rise in critical buckling force relative to the quasi-static case was approximately 45 % to 60 %. Given that the imperfection (0.30 mm) in the tested geometry falls within this specified range, the observed increase of 73 % appears somewhat higher than expected.

Additional summarized data on critical end-shortening and final deflection values for respective rod geometries is found in Table 6.10.

Table 6.10: Comparison of critical end-shortening and deflection between rod 1 and 2 across various loading rates.

Rod 1				Rod 2			
v [mm/s]	$\dot{\epsilon}$ [s^{-1}]	u_{cr} [mm]	w_{max} [mm]	v [mm/s]	$\dot{\epsilon}$ [s^{-1}]	u_{cr} [mm]	w_{max} [mm]
0.013	10^{-4}	0.340	23.10	0.026	10^{-4}	0.183	33.87
13	10^{-1}	0.355	22.29	26	10^{-1}	0.306	31.39
65	0.5	0.370	22.23	52	0.2	0.344	31.60
195	1.5	0.403	21.85	130	0.5	0.488	30.48

Table 6.10 indicates a significant disparity in deflection between rod 1 and 2, with rod 2 exhibiting larger deflection. Notably, the deflection diminishes as the loading rate increases. Furthermore, while both rod geometries show an increase in critical end-shortening with higher loading rates, the increase in end-shortening for rod 2 is more erratic across consecutive strain rates. The observed erratic pattern can be attributed to the critical buckling force potentially being higher than anticipated. Final comparison of data between both rod geometries is conducted regarding secant stiffness, see Table 6.11.

Table 6.11: Comparison of secant stiffness between rod 1 and 2 across various loading rates.

Rod 1			Rod 2		
v [mm/s]	$\dot{\epsilon}$ [s^{-1}]	K_{sec} [kN/mm]	v [mm/s]	$\dot{\epsilon}$ [s^{-1}]	K_{sec} [kN/mm]
0.013	10^{-4}	76	0.026	10^{-4}	57
13	10^{-1}	78	26	10^{-1}	44
65	0.5	78	52	0.2	45
195	1.5	76	130	0.5	37

The data presented in Table 6.11 confirms that rod 1 is stiffer than rod 2. Additionally, while the stiffness of rod 1 remains consistent across different loading rates, there is notable variability in the stiffness of rod 2. However, considering the findings from the material testing, particularly the observation that the Young's modulus is relatively unaffected by changes in loading rates, it is reasonable to conclude that the material's stiffness is generally insensitive to varying loading rates. Therefore, the unexpected differences in stiffness, especially those observed for rod 2, are likely due to inaccurately estimated critical buckling forces and associated end-shortening from the UTM.

6.1.4 Velocity-End-Shortening Relations for Rod 1 & 2

In order to gain a deeper understanding of the velocities experienced by the specimens during testing and verify whether the targeted loading rates in the UTM have been achieved, additional study is conducted. This study involves deriving velocity-end-shortening relationships for both rod geometries by analyzing point 1 in GOM (cf. Figures 5.12-5.13). Analyzing this point ensures that the extracted values are most representative, as it is closest to where the load is applied. Figure 6.11 demonstrates how the velocity of rod 1 varies with increasing end-shortening across all samples under different loading rates.

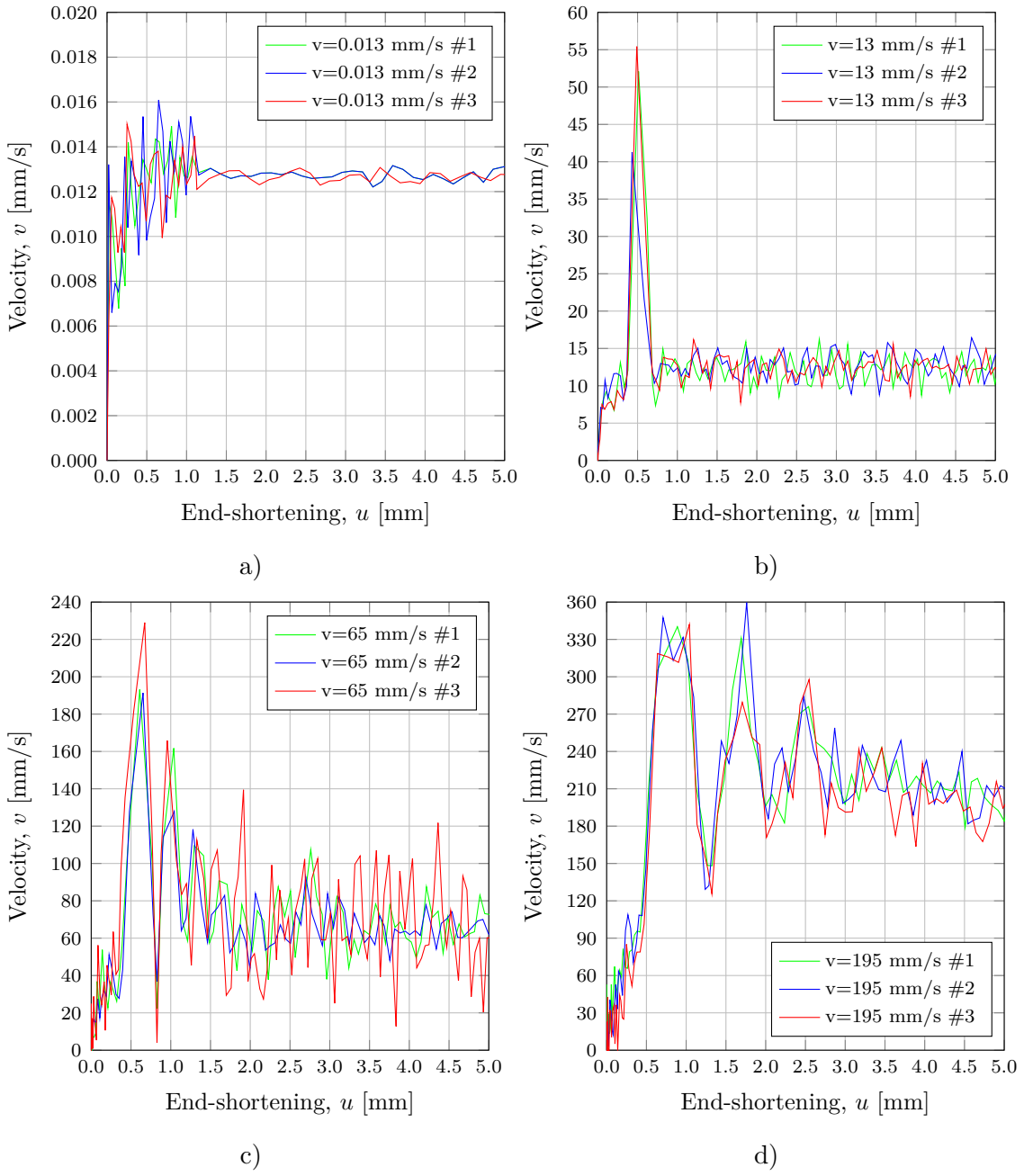

Figure 6.11: Relationship between velocity and end-shortening for rod 1: a) v=0.013 mm/s, b) v=13 mm/s, c) v=65 mm/s & d) v=195 mm/s.

Figure 6.11 shows that the targeted velocities have been fairly successfully achieved. The applied velocities closely match those experienced by rod 1 across various loading rates. It should be noted that a certain amount of time, and consequently end-shortening is required to reach the desired velocity. This observation is likely linked to the UTM and its operational system. Preparatory testing, conducted without any specimens, revealed that the target velocity was not reached until a specific duration of time (ms) had elapsed. This effect is seen in Figure 6.11, as immediately after the compression is initiated, the samples experience markedly lower velocities.

Further examination of the figure reveals consistent behavior among the three samples, with only minor deviations in maximum velocities. For the majority of the tests, the desired velocities remain stable, especially tangible in Figure 6.11 a). However, under more rapid loading, distinct fluctuations are observed. Furthermore, a conspicuous rise in velocity is noticeable in Figure 6.11 b)-d), possibly indicating the occurrence of buckling at that time instant. Transitioning from rod 1, the velocity experienced by rod 2 under different loading conditions is visualized in Figure 6.12.

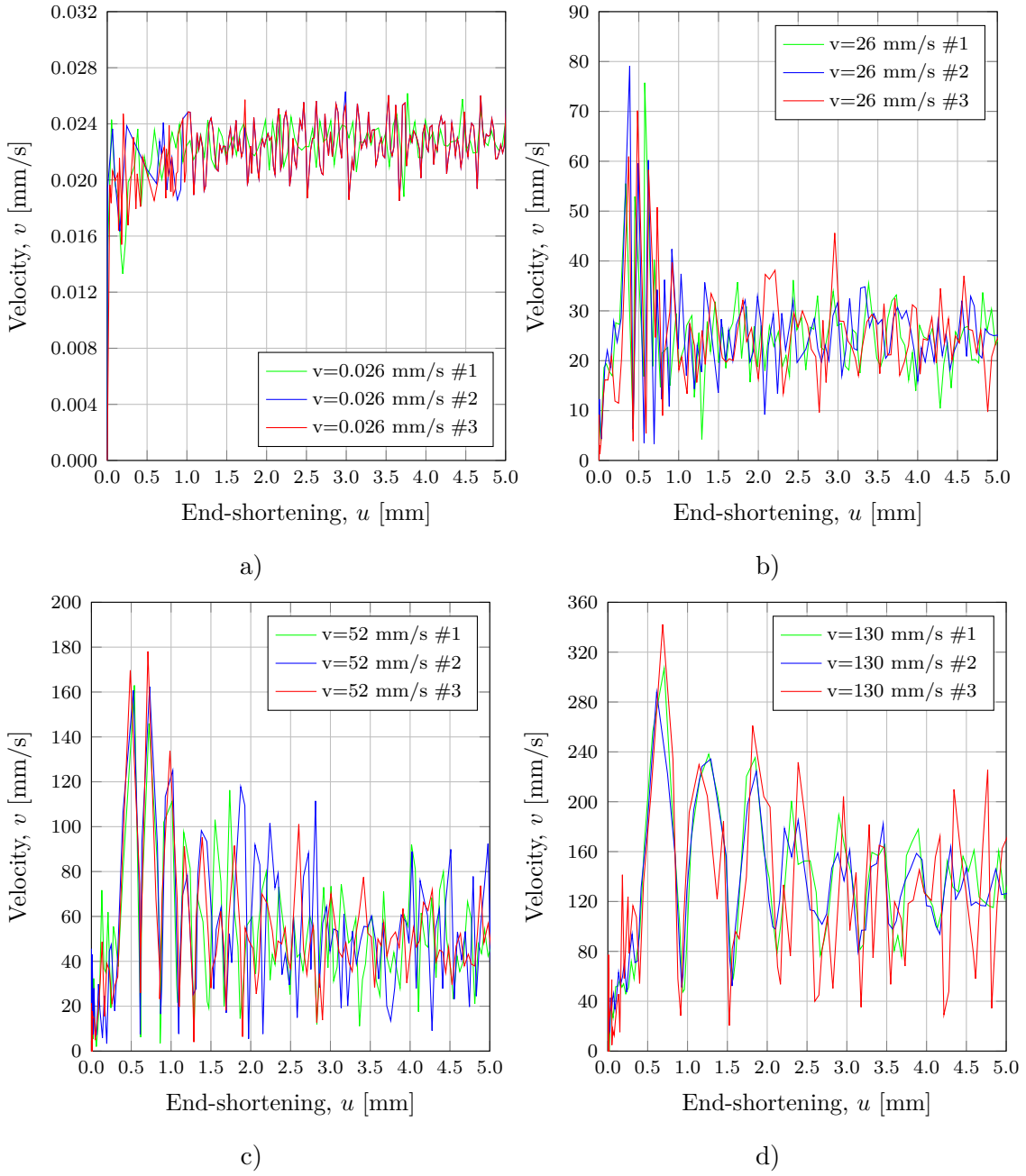

Figure 6.12: Relationship between velocity and end-shortening for rod 2: a) v=0.026 mm/s, b) v=26 mm/s, c) v=52 mm/s & d) v=130 mm/s.

Similarly to rod 1, it can be verified that rod 2 has experienced the targeted velocities. Although larger fluctuations are observed in Figure 6.12, a mean amplitude or a trend line in the post-buckling stage of the velocity-end-shortening curve suggests that the velocities reflect the applied loading rates from the UTM.

6.2 FEA

This section presents the numerical results of both rod geometries derived from the FEA, serving as a basis for validation and comparison with experimental results. Additionally, a brief description of the employed FE-model for the analyses is provided.

6.2.1 Updated FE-model

To ensure accurate simulation results and alignment with the experimental testing conditions, modifications are implemented on the existing FE-models for the two rod geometries outlined in Section 4.3.1. These modifications involve extending the clamping length from its original 35 mm to 60 mm, reducing the thickness from 4 mm to 3.9 mm, and updating the mechanical properties based on the material testing data (cf. Section 5.3.3 and 5.3.4). The updated mechanical properties include modified Young's modulus, a new plasticity model, and revised strain rate material parameters in the CS-model. Additionally, imperfection values are adjusted to reflect an average of manually measured imperfections, specifically 0.05 mm for rod 1 and 0.30 mm for rod 2.

In Section 5.2.2, it was mentioned that the actual cross-sectional area of the unrestrained part of the specimens takes on a trapezoidal shape. However, accurately representing this shape using shell elements in the FE-modeling is impractical. To address this challenge, a simplified approach is adopted, which is based on the width of the top face (20 mm) and the attained thickness (3.9 mm). An alternative approach is to model the specimens based on an average width between the top and bottom faces. Nonetheless, this will lead to undesired modifications to the transition radius. Consequently, this alternative approach is not further investigated. It is also worth noting that although the clamping width of the physical specimens measured 44.44 mm, the FE-models maintain the original width of 44 mm. This decision stems from the realization that the clamping widths, being the clamped parts, exert no influence on the overall structural response.

6.2.2 Outcomes of Simulations

The outcomes of the FEA, conducted using the dynamic explicit step, encompass the depiction of force-end-shortening and force-deflection relationships. In Figures 6.13-6.14 the force-end-shortening relationship for rod 1 and 2 is illustrated respectively.

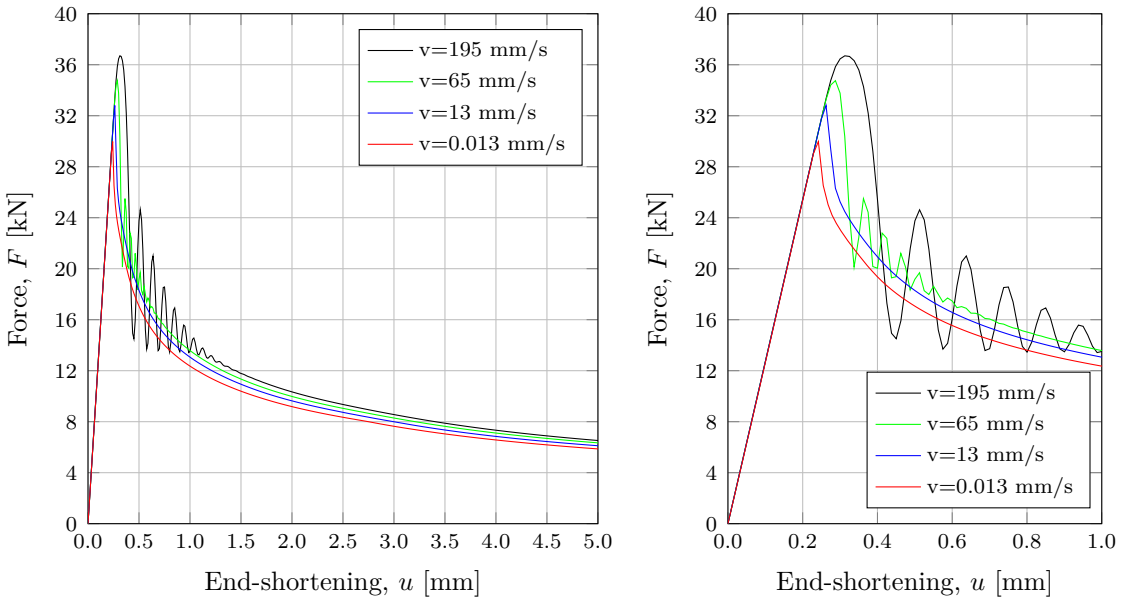

Figure 6.13: a) Relationship between compressive axial force and end-shortening for rod 1, featuring FEA results obtained at the different velocities, considering an initial imperfection of 0.05 mm & b) Magnified view of the response for 1 mm end-shortening.

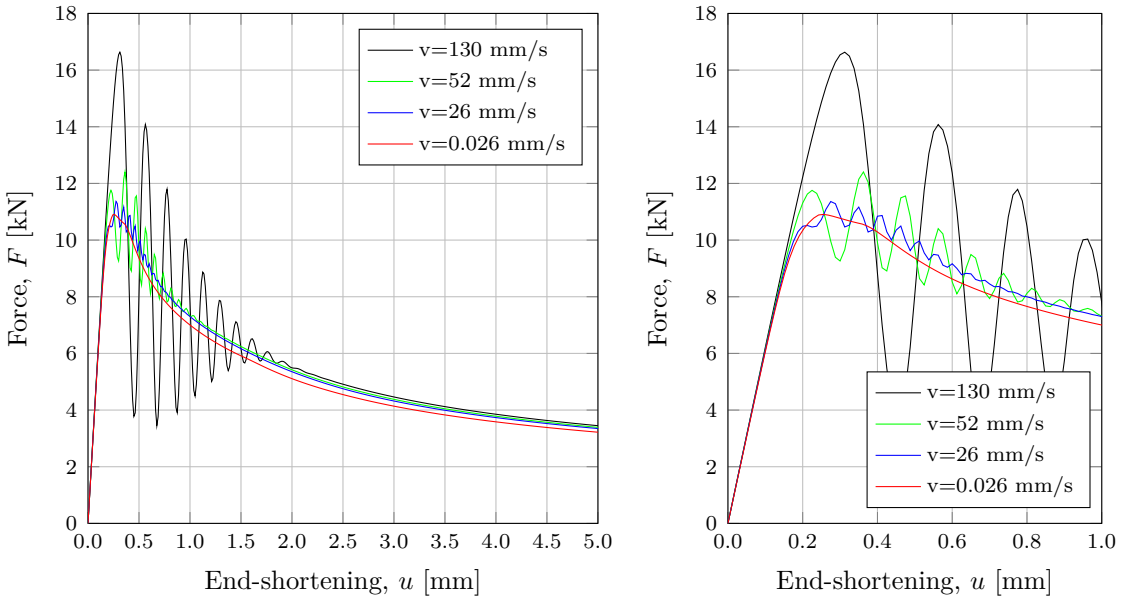

Figure 6.14: a) Relationship between compressive axial force and end-shortening for rod 2, featuring FEA results obtained at the different velocities, considering an initial imperfection of 0.30 mm & b) Magnified view of the response for 1 mm end-shortening.

Upon analysis and comparison of the figures, it is evident that rod 1 exhibits significantly higher axial capacity than rod 2. Inertia effects manifest at a loading rate of 26 mm/s for rod 2, while for rod 1, they become apparent at 65 mm/s. Further illustrations of the obtained force-deflection relationships for both rod geometries is provided in Figure 6.15.

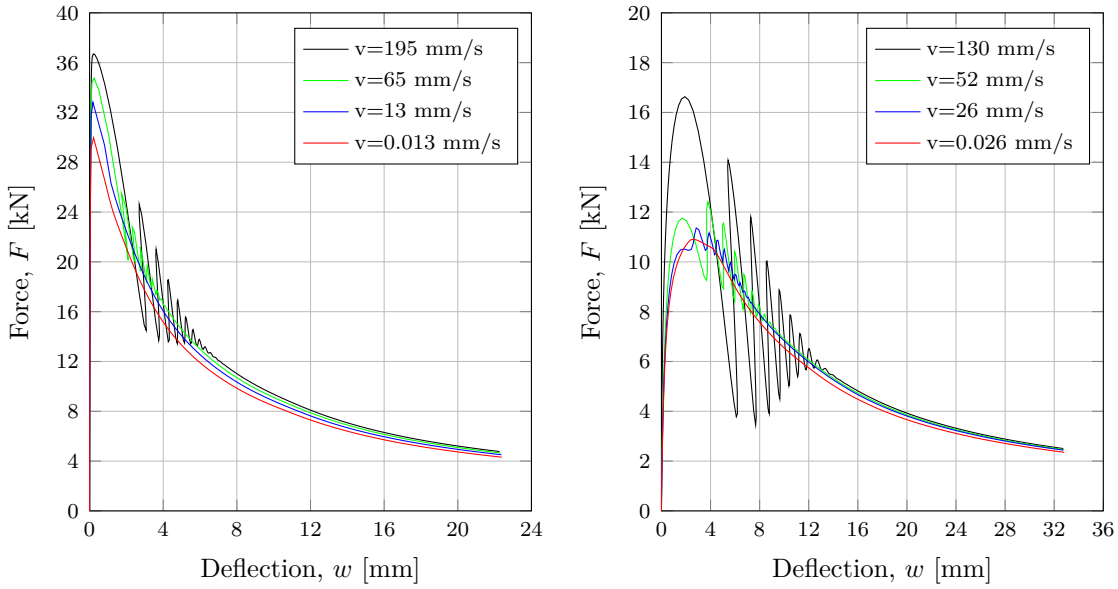

a) b)

Figure 6.15: Relationship between compressive axial force and deflection, featuring FEA results for both rod geometries: a) Rod 1 & b) Rod 2.

A summary of the critical buckling force, critical end-shortening, and deflection at various strain rates for rod 1 is presented in Table 6.12. Similarly, Table 6.13 provides an overview of these parameters for rod 2.

Table 6.12: Compilation of FEA results for rod 1 across various loading rates.

v [mm/s]	$\dot{\epsilon}$ [s^{-1}]	P_{cr} [kN]	$\frac{P_{\text{cr}}}{P_{\text{cr.quasi}}}$ [-]	u_{cr} [mm]	w_{max} [mm]
0.013	10^{-4}	29.98	1.00	0.215	22.39
13	10^{-1}	32.81	1.09	0.263	22.37
65	0.5	34.75	1.16	0.288	22.32
195	1.5	36.70	1.22	0.313	22.27

Table 6.13: Compilation of FEA results for rod 2 across various loading rates.

v [mm/s]	$\dot{\epsilon}$ [s^{-1}]	P_{cr} [kN]	$\frac{P_{\text{cr}}}{P_{\text{cr.quasi}}}$ [-]	u_{cr} [mm]	w_{max} [mm]
0.026	10^{-4}	10.91	1.00	0.256	32.81
26	10^{-1}	11.36	1.04	0.275	32.76
52	0.2	12.41	1.14	0.362	32.75
130	0.5	16.63	1.52	0.313	32.74

Based on the data provided in both tables, it can be ascertained that the critical end-shortening necessary to initiate buckling falls within the range of 0.2 - 0.4 mm compression for both rod geometries across the studied velocities. Another observation is that the deflection for rod 1 is approximately 2.2 magnitudes larger than the final end-shortening of 10 mm, while for rod 2, it is approximately 3.3. Furthermore, there is a higher increase in critical buckling force for rod 2 compared to rod 1. Specifically, at a strain rate of 0.5 s^{-1}, the increase for rod 1 is 12 %, whereas for rod 2, it is 52 %. For input files of the quasi-static and dynamic analyses of rod 1 and 2 in Abaqus CAE, see Appendices L-M.

6.3 Comparison of Experimental and Numerical Results for Rod 1 & 2

The comparative analysis between the results obtained from structural tests and those acquired from FE-simulations for both rod geometries reveals both similarities and disparities. Table 6.14 presents a summary comparison of key parameters for both evaluation methods for rod 1. Further contextualization in terms of percentage differences is provided in Table 6.15.

Table 6.14: Comparison of experimental and numerical results for rod 1.

		Experimental				Numerical			
v [mm/s]	$\dot{\epsilon}$ [s^{-1}]	u_{cr} [mm]	w_{max} [mm]	P_{cr} [kN]	$\frac{P_{\text{cr}}}{P_{\text{cr.quasi}}}$ [-]	u_{cr} [mm]	w_{max} [mm]	P_{cr} [kN]	$\frac{P_{\text{cr}}}{P_{\text{cr.quasi}}}$ [-]
0.013	10^{-4}	0.340	23.10	25.90	1.00	0.215	22.39	29.98	1.00
13	10^{-1}	0.355	22.29	27.80	1.07	0.263	22.37	32.81	1.09
65	0.5	0.370	22.23	29.04	1.12	0.288	22.32	34.75	1.16
195	1.5	0.403	21.85	30.55	1.18	0.313	22.27	36.70	1.22

Table 6.15: Deviation percentages between experimental and numerical results for rod 1.

v [mm/s]	$\dot{\epsilon}$ [s^{-1}]	$\triangle u_{\text{cr}}$ [%]	$\triangle w_{\text{max}}$ [%]	$\triangle P_{\text{cr}}$ [%]	$\triangle \frac{P_{\text{cr}}}{P_{\text{cr.quasi}}}$ [%]
0.013	10^{-4}	36.8	3.1	15.8	-
13	10^{-1}	25.9	0.4	18.0	1.9
65	0.5	22.2	0.4	19.7	3.6
195	1.5	22.3	1.9	20.1	3.4

The most prominent difference in the results emerges with the critical buckling force. Numerical simulations produce values approximately 20 % higher than those obtained from structural testing. Moreover, significant deviations arise in the measurements of critical end-shortening. In contrast to these disparities, the deflection values show good similarity between the two methods. Additionally, minimal deviation in the increase of the critical buckling force is observed. This suggests that the adopted CS-model effectively predicts the increase factor for critical buckling force across varying strain rates. Furthermore, an intriguing observation emerges regarding the strong correlation between structural testing and FE-simulations, particularly evident in the identification of inertia effects at a loading rate of 65 mm/s (cf. Figure 6.1 and 6.13). Transitioning the focus to rod 2, the comparison of parameters between the two methods is detailed in Table 6.16 and 6.17.

Table 6.16: Comparison of experimental and numerical results for rod 2.

		Experimental				Numerical			
v [mm/s]	$\dot{\epsilon}$ [s^{-1}]	u_{cr} [mm]	w_{max} [mm]	P_{cr} [kN]	$\frac{P_{\text{cr}}}{P_{\text{cr.quasi}}}$ [-]	u_{cr} [mm]	w_{max} [mm]	P_{cr} [kN]	$\frac{P_{\text{cr}}}{P_{\text{cr.quasi}}}$ [-]
0.026	10^{-4}	0.183	33.87	10.43	1.00	0.256	32.81	10.91	1.00
26	10^{-1}	0.306	31.39	13.61	1.30	0.275	32.76	11.36	1.04
52	0.2	0.344	31.60	15.51	1.49	0.362	32.75	12.41	1.14
130	0.5	0.488	30.48	18.02	1.73	0.313	32.74	16.63	1.52

Table 6.17: Deviation percentages between experimental and numerical results for rod 2.

v [mm/s]	$\dot{\epsilon}$ [s^{-1}]	$\triangle u_{\text{cr}}$ [%]	$\triangle w_{\text{max}}$ [%]	$\triangle P_{\text{cr}}$ [%]	$\triangle \frac{P_{\text{cr}}}{P_{\text{cr.quasi}}}$ [%]
0.026	10^{-4}	39.9	3.1	4.6	-
26	10^{-1}	10.1	4.4	16.5	20.0
52	0.2	5.2	3.6	20.0	23.5
130	0.5	35.9	7.4	7.7	12.1

When comparing rod 2 to 1, the critical buckling force values show a greater degree of similarity between the methods despite obvious deviations. Notably, both methods exhibit a close alignment of critical buckling force under quasi-static loading

scenario, with a deviation of approximately 5 %. Similarly to rod 1, considerable dissimilarities are apparent in the critical end-shortening measurements, while deflections demonstrate good correlation. However, unlike rod 1, significant disparities are noted in the increase factor of the critical buckling force. Regarding the appearance of inertia effects, they manifest at a loading rate of 26 mm/s in both methods (cf. Figure 6.1 and 6.13). This alignment implies that the model used in the numerical analyses adequately captures the dynamic response of the structure under the given loading conditions. For verification of the governing failure mode for both rod geometries and the calculation of the percentage deviation in critical buckling force for the quasi-static case between the two methods, see Appendix H.

6.4 Sensitivity Analyses

During structural testing, the clamping areas on both the top and bottom surfaces of the specimens were not fully secured, resulting in an unclamped length of approximately 6.5 mm (cf. Figure 5.9). Consequently, a comprehensive analysis is conducted to evaluate the potential impact of the unclamped region on the structural response. This analysis entails numerical simulations utilizing the FE-model, wherein the clamping length is partitioned to represent the unclamped area, see Figure 6.16.

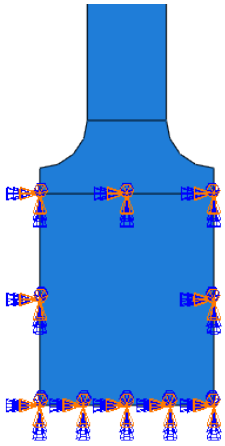

Figure 6.16: Partitioned clamping in FE-model.

Given the significant disparity between the FEA and experimental results for rod 1, particularly regarding its critical buckling force, the analysis is performed exclusively for this rod. The aim is to identify and eliminate any possible factors contributing to this notable difference. The outcomes of this comparison analysis, focusing on force-end-shortening and force-deflection relationships are visualised in Figures 6.17-6.18.

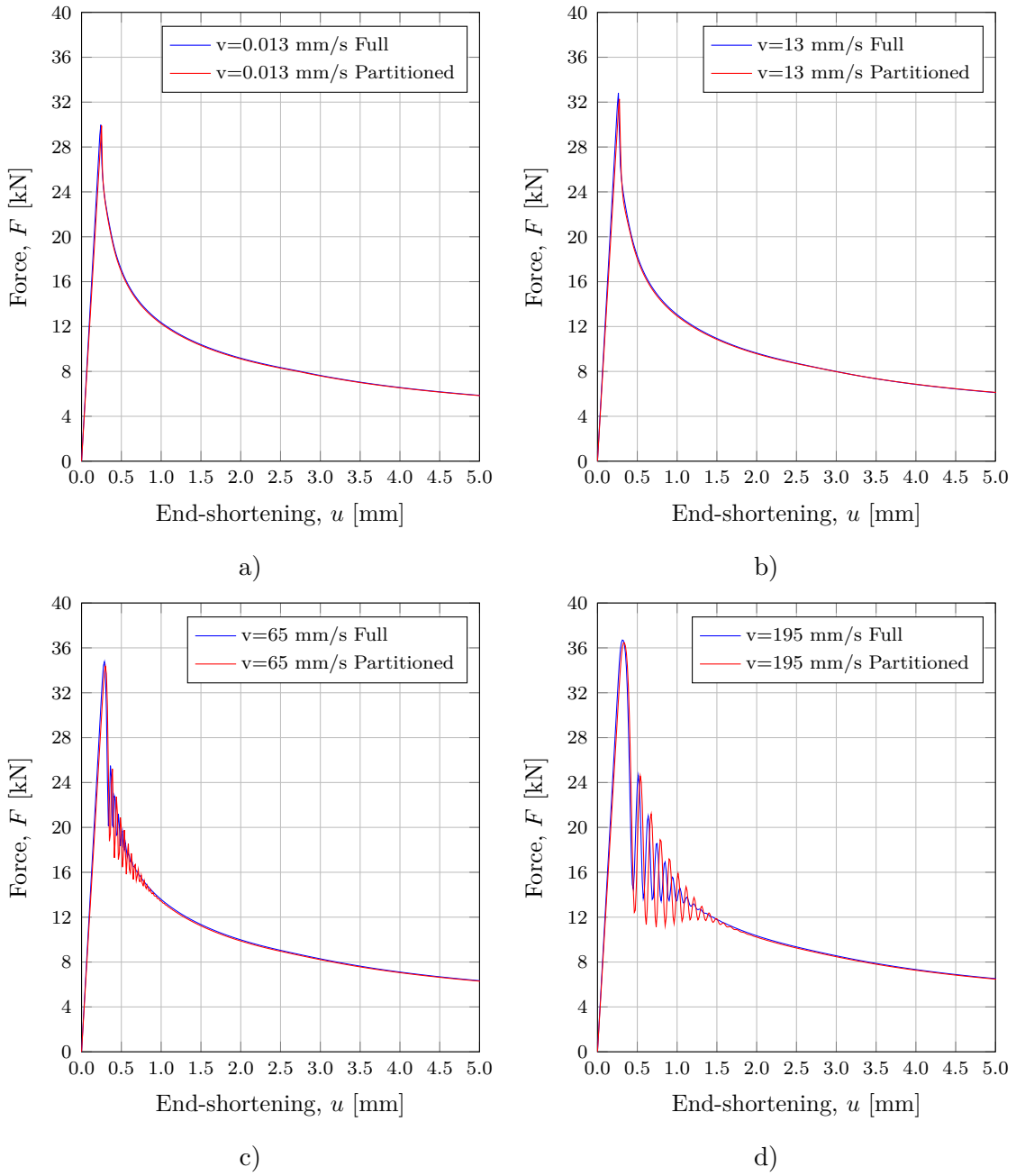

Figure 6.17: Relationship between compressive axial force and end-shortening for rod 1, featuring FEA results under full and partitioned clamping conditions: a) v=0.013 mm/s, b) v=13 mm/s, c) v=65 mm/s & d) v=195 mm/s.

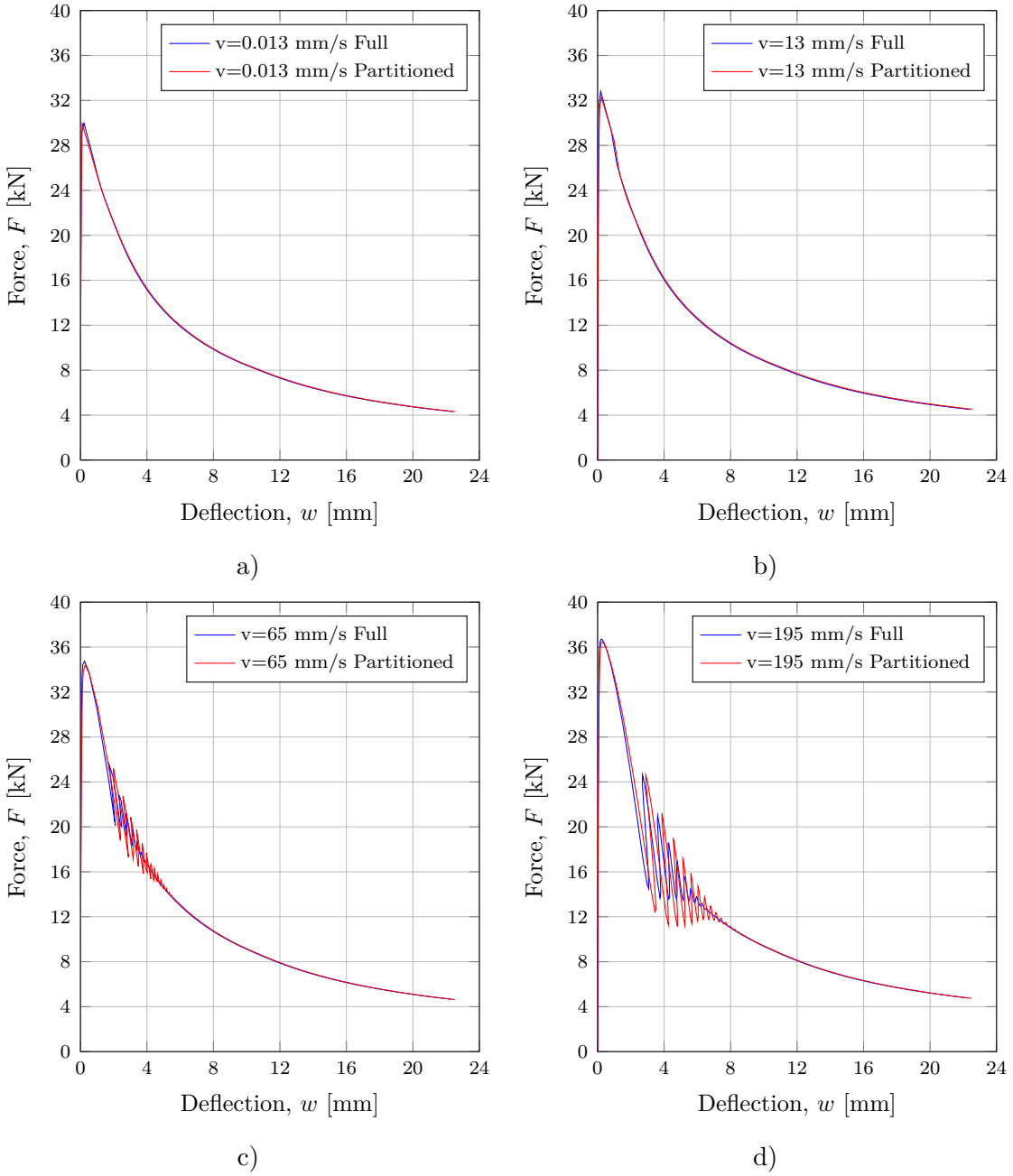

Figure 6.18: Relationship between compressive axial force and deflection for rod 1, featuring FEA results under full and partitioned clamping conditions: a) v=0.013 mm/s, b) v=13 mm/s, c) v=65 mm/s & d) v=195 mm/s.

The comparison between the two clamping conditions in Figures 6.17-6.18 suggests negligible influence of the modified clamping on the structural response. It is clearly visible that the curves for both clamping conditions closely align with each other. However, subtle difference in terms of higher amplitude of dynamic oscillations in the case of partitioned clamping is noted. To better accentuate the distinctions between the two cases, the numerical values of key parameters for each case are provided in Table 6.18. For deviation percentages between the two cases, see Table 6.19.

Table 6.18: Comparison of results for rod 1 between full and partitioned clamping conditions.

Full clamping					Partitioned clamping				
v [mm/s]	$\dot{\epsilon}$ [s^{-1}]	P_{cr} [kN]	u_{cr} [mm]	w_{max} [mm]	v [mm/s]	$\dot{\epsilon}$ [s^{-1}]	P_{cr} [kN]	u_{cr} [mm]	w_{max} [mm]
0.013	10^{-4}	29.98	0.215	22.39	0.013	10^{-4}	29.90	0.251	22.56
13	10^{-1}	32.81	0.263	22.37	13	10^{-1}	32.28	0.275	22.55
65	0.5	34.75	0.288	22.32	65	0.5	34.36	0.300	22.53
195	1.5	36.70	0.313	22.27	195	1.5	36.46	0.338	22.49

Table 6.19: Deviation percentages of the results of rod 1 between the two clamped conditions.

v [mm/s]	$\dot{\epsilon}$ [s^{-1}]	$\triangle P_{cr}$ [%]	$\triangle u_{cr}$ [%]	$\triangle w_{max}$ [%]
0.013	10^{-4}	0.3	16.7	0.8
13	10^{-1}	1.6	4.6	0.8
65	0.5	1.1	4.2	0.9
195	1.5	0.7	8.0	1.0

The data from both tables corroborate that the specific clamping condition employed during experimental testing have a marginal effect on the structural response. A discrepancy of approximately 1-2 % is attained for critical buckling force and deflection, with the most significant deviation observed in the critical end-shortening.

Another pivotal aspect of structural testing involves assessing the geometric imperfections inherent in the specimens. As detailed in Section 5.2.2, the imperfections of the specimens were measured manually. Given the susceptibility of manual measurements to limitations such as subjective interpretation and challenges associated with accuracy, it is important to approach the interpretation of structural testing results with caution. To address and verify the possible inaccuracies stemming from manual measurements, imperfection sensitivity analysis is performed. This analysis, akin to the methodology employed in the pre-study, aims to determine how the magnitude of imperfections affects the critical buckling force of rod 1. The findings of the analysis, focusing on the quasi-static loading scenario, are visualized in Figure 6.19, depicting the relationship between force and end-shortening. For more detailed insights into the critical buckling force associated with each imperfection, see Table 6.20.

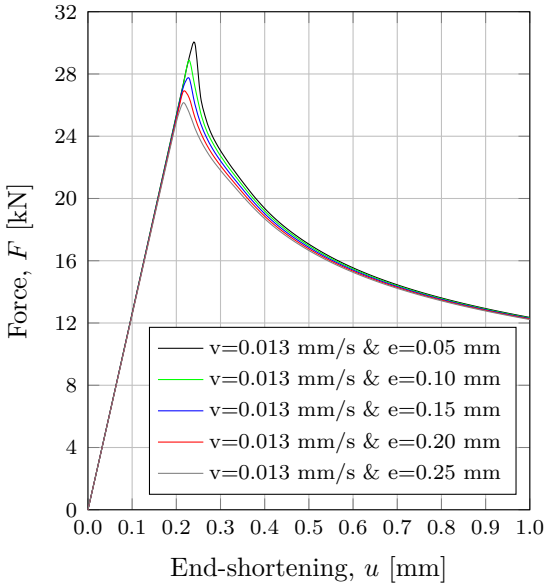

Figure 6.19: Relationship between compressive axial force and end-shortening for rod 1 across different initial imperfection magnitudes.

Table 6.20: Reduction in critical buckling force for rod 1 due to increased initial imperfections.

e [mm]	P_{cr} [kN]	$\triangle P_{\text{cr}}$ [kN]
0.05	30.0	-
0.10	28.9	-1.1
0.15	27.7	-1.2
0.20	26.9	-0.8
0.25	26.2	-0.7
		Σ -3.8

The data presented in Table 6.20 underscores the rod's heightened sensitivity to imperfections. Even a small increase of 0.20 mm in imperfection correlates with a significant reduction in axial capacity, approximately 4 kN. Considering that the manually measured imperfections of 0.05 mm may not accurately reflect the true imperfections, it becomes evident that such discrepancies will substantially impact the interpretation of the structural tests. It should also be mentioned that FE-simulation considering imperfections based on the buckling mode for a simply supported loading scenario has been implemented. The outcome reveals negligible difference when compared to fixed-fixed loading scenario.

Finally, an additional study is conducted on the loading profile, focusing specifically on the velocity-time relationship applied to the rod structure in Abaqus CAE. As previously observed, the critical buckling force for rod 2, at a velocity of 26 mm/s, shows a deviation of 16.5 % between the two methods (cf. Table 6.17). This deviation is associated with the second peak in the amplitude profile reaching a higher

magnitude than the first peak (cf. Figure 6.14). To assess whether this deviation is influenced by the loading profile, the velocity-time data from UTM for an arbitrary sample (#1) of rod 2 loaded at v = 26 mm/s is implemented into the FEA, see Figure 6.20. Figure 6.21 shows a comparison of the structural response between the original smooth step amplitude and the velocity-time data from the UTM.

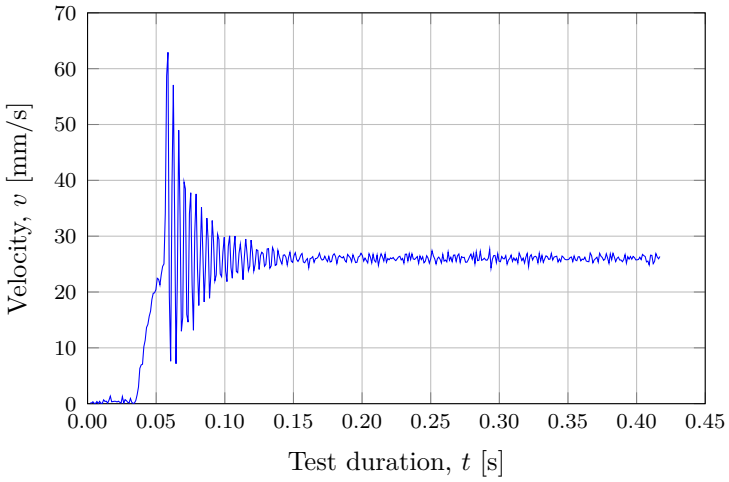

Figure 6.20: Velocity-time data from UTM for sample #1, loaded at v=26 mm/s.

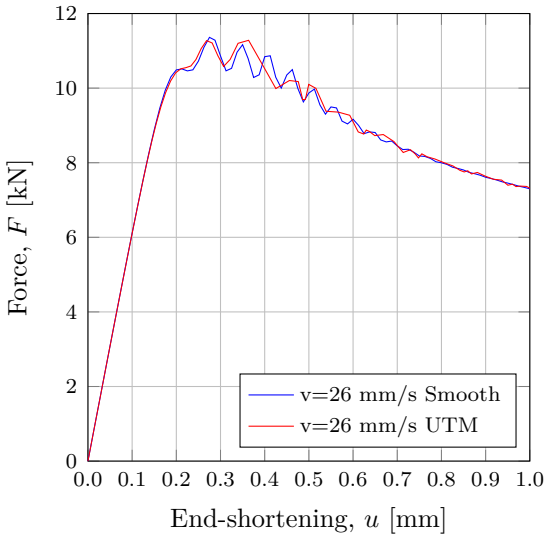

Figure 6.21: Comparison of structural response using original smooth step amplitude and UTM velocity-time data.

Based on the outcome depicted in Figure 6.21, it is concluded that the loading profile has minimal influence on the amplitude profile and the phase shift, as only marginal effects are observed. Furthermore, there is negligible difference in the critical buckling force between the two scenarios. This sensitivity analysis further bolsters that the discrepancies are most likely connected to the geometric properties of the steel rods rather than the kinematic relationships employed.

7 Discussion

This section presents a summary and discussion of the pertinent observations and findings encountered throughout the study. Furthermore, possible sources of uncertainties and errors influencing the results are delineated.

7.1 General

The aim of this thesis was to analyze and deepen the understanding of the structural response of thin-walled steel structures under compressive axial dynamic loads. Through a combination of numerical simulations and experimental investigations focusing on simplified fixed-fixed rod structures subjected to varying loading rates, this study has successfully achieved its goal.

Overall, the results from the pre-study, experiments, and final FEA exhibit relatively strong correlation. Initial observations from the numerical analyses align closely with the findings of the experiments. However, discrepancies emerge when the final FEA outcomes are compared with the structural responses obtained from the experiments.

It is also worth mentioning that centering the study on two distinct geometries provides several advantages. Primarily, it offers a comprehensive understanding of structural behavior by revealing sensitivity to geometry changes. Secondly, utilizing results attained from two different geometries facilitates the generalization of conclusions. Lastly, by incorporating two rod geometries, enhanced robustness of the analyses or experimental testing is achieved as the impact of potential errors that may arise when relying solely on one geometry is excluded.

7.2 Key Findings and Objective Interconnections

Through rigorous examination of the outcomes from the various methodologies employed, several interesting aspects emerge. Both experimental and numerical investigations presented in this study highlight the intricate relationship between material behavior, structural response and loading conditions.

One key finding is the material's sensitivity to strain rate variations. This phenomenon is clearly demonstrated during material testing, where an increase in both yield strength and ultimate tensile strength is observed with elevated loading rates. However, Young's modulus remains rather insensitive to changes in strain rates. It is worth noting that these aspects have been extensively studied, with numerous research efforts dedicated to evaluating the tensile behavior of metals across a wide range of strain rates. For instance, studies by Cadoni et al. (2018) on S355 mild steel and N. K. Singh and Gupta (2014) on CP800 steel have provided comprehensive insights into these occurrences, corroborating the observations from the material testing conducted in this study.

The phenomenon of strain rate sensitivity is further substantiated by the observed increase in critical buckling loads and associated end-shortening values. This aligns with the findings of Paik and Thayamballi (2003), who investigated the dynamic behavior of ship plating under compressive axial loading at strain rates similar to those in this study.

In contrasting the two rod geometries, a strong correlation between structural response and slenderness emerges. As demonstrated throughout all phases of the study, the critical buckling force for rod 1 is significantly higher than that of rod 2. This indicates that greater slenderness leads to reduced axial capacity. Furthermore, thorough imperfection sensitivity analyses, especially those conducted during the pre-study, reveal a similar impact on the structural response, i.e., decreased axial capacity with increased geometric initial imperfections. These insights highlight that the structural response is significantly influenced by the geometric properties of the studied rods.

When analyzing the dynamic behavior of the two rod geometries through FEA using the CS-model and comparing it with the outcomes of the structural testing, varying levels of correlation are observed. While the critical buckling force values from the FEA for rod 1 across the different strain rates exhibit a discrepancy of approximately 4-5 kN in comparison to the structural testing results, strong alignment in the increase factor for force is demonstrated (cf. Table 6.14). Conversely, a reverse scenario is observed for rod 2, where the critical buckling force values are more in line with the experimental results while the increase factors differ (cf. Table 6.16). The verification of the CS-model during the pre-study showed good correlation with the outcomes of the study by Yang et al. (2022). Moreover, based on the observed correspondence in material behavior between FEA and the results from the structural testing of rod 1, it can be inferred that the CS-model provides reasonable predictions of the dynamic behavior of the material.

Another important discovery from this study concerns the presence of inertia effects during dynamic loading. Structural testing disclose these effects at loading rate of 65 mm/s for rod 1 (cf. Figure 6.2) and at 26 mm/s for rod 2 (cf. Figure 6.7). Furthermore, the identical observations in the FEA reinforce the reliability of the FE-model, indicating a strong correlation in the dynamic behavior captured by both methods for the studied geometries.

Interestingly, the interplay between strain rate and structural slenderness influences the initiation of inertia effects. As mentioned above, rod 2 demonstrates dynamic oscillations at an applied velocity of 26 mm/s, equivalent to a strain rate of 10^{-1} s^{-1}. In contrast, rod 1 shows no such effects at the same strain rate (13 mm/s). This emphasizes the significant influence of structural geometry on dynamic behavior, where higher slenderness accelerates the onset of inertia effects. Building upon the examination of dynamic oscillations, the pre-study investigations further illuminate that rods with heightened geometric perfection, exhibit larger oscillation amplitudes, suggesting a more pronounced dynamic response.

In conclusion, the findings successfully address the research questions posed in this study. Through the utilization of various methodologies, valuable insights into the dynamic buckling behavior of a simplified thin-walled structure have been attained.

7.3 DIC and Post-Processing in GOM

Utilizing DIC for experimental testing and GOM for post-processing and evaluation of the test results has proven effective and reliable. With the aid of these tools, detailed information about the surface of the studied specimens was captured, enabling the identification and analysis of critical sections/points of interest for evaluating the structural response. However, it is essential to acknowledge the inherent challenge of consistently measuring identical critical points across all specimens. Despite their nominal geometric similarity, the speckled pattern resulting from painting, made it challenging to accurately pinpoint and measure these points. Therefore, small deviations may be expected when comparing measurements between different samples.

Prior to the commencement of testing, the accuracy of the speckled pattern for each specimen was verified using GOM. However, during post-processing, missing data were observed when measuring relevant parameters at critical points. These data gaps occurred at various stages throughout the testing duration, particularly noticeable in the structural tests involving rapid loading. One plausible explanation for this observation could be attributed to limitations of the HSC utilized during testing. The rapid loading conditions may have posed challenges for the HSC's capabilities. Additionally, factors such as low resolution, dust interference, and sensor noise could have exacerbated the situation.

Another essential aspect of post-processing involved the integration of data from the UTS and HSC, specifically crucial for analyzing results under rapid loading conditions. Nevertheless, aligning data from these disparate systems posed challenges. The UTS and HSC operated with different sampling frequencies, with the HSC running for a longer duration than the UTS. This necessitated precise synchronization to establish correspondence between specific time instances in UTS data and the captured HSC images. Unfortunately, explicit information regarding this synchronization was missing, complicating the procedure.

To address this, analytical calculations were performed to determine synchronization times based on the respective sampling frequencies, assuming that the HSC was triggered simultaneously with the UTS. However, this approach proved sensitive, resulting in phase shifts, particularly noticeable in the measurements of critical buckling force and associated end-shortening. For instance, different synchronization times resulted in shifts in critical end-shortening values, leading to either higher or lower deformation levels. Given the significance of these insights, the sensitivity of this method underscores the need for precise synchronization techniques to ensure accurate measurements in structural testing scenarios.

7.4 Causes for Deviations and Uncertainties from Experiments

Following the completion of multiple analyses and comparisons between experimental and numerical studies, it is essential to discuss the potential causes of deviations observed among the results. Upon reflection of the experiments, certain aspects remain unproven and unresolved, necessitating further investigation.

Firstly, specimen dimensions were determined through manual measurements utilizing micrometers and other equipment, thereby increasing the likelihood of inaccuracies in the recorded values. Measurements conducted on a selection of specimens from both road geometries revealed a deviation in thickness, ranging from 3.85 mm to 3.95 mm, instead of the intended 4 mm (cf. Section 5.2.2). Furthermore, discrepancies were noted in the width of the parallel length across faces, with the top side measuring 20 mm, while the bottom ranged from 19.70 mm to 19.80 mm.

This information prompted an approximation of the cross-sectional area using reduced dimensions and a modified geometric shape (cf. Figure 5.4). However, in the final FEA, a decision was made to retain a rectangular section instead of transitioning to a trapezoidal one, resulting in a 0.63 % difference in the cross-sectional area. Consequently, minor deviations are anticipated, as the moment of inertia is affected by the sectional dimensions. Despite indications of dimensions deviating from the desired values ($a_o = 4$ mm and $b_o = 20$ mm) obtained from manual measurements, the precise cross-section of the specimens remains highly uncertain, lacking verification and validation from alternative measurement approaches.

Another crucial parameter pertains to initial geometric imperfections. Similar to the method used for determining cross-sectional area, manual technique was employed to assess the initial imperfections of a few samples for both rod geometries. Readings suggested that rod 1 had an average initial imperfection of 0.05 mm, whereas rod 2 had 0.30 mm (cf. Section 5.2.2). Nonetheless, it is noteworthy that the measured values for these samples may not necessarily be representative of other non-measured coupons of same dimensions.

The adopted technique, which involves moving the micrometer pointer along the specimen's surface, raises uncertainties about whether the recorded values accurately represent the critical section with the highest imperfection magnitude. Moreover, these values are sensitive to the pressure exerted by the pointer on the specimens. Measuring initial deviations with the specimens secured in the testing machine and fixed in the grips would also be pertinent, as clamping pressure might introduce additional, uncontrolled imperfections that have not been verified during the experiments.

Based on the outcomes of the experiments and FEA, it is challenging to determine whether the utilized imperfection magnitudes are accurate. On one hand, the comparison of the critical buckling force for rod 2 under quasi-static loading reveals a

difference of only 4.6 % (cf. Table 6.17), suggesting that the imperfections for this slender rod are relatively close to reality. However, for rod 1, there is a lack of agreement for the corresponding case. The capacity from the experiments is distinctly lower, with a deviation of about 15.8 % against the numerically obtained capacity (cf. Table 6.17). This is highly likely connected to these imperfections among other factors. Sensitivity analysis in Abaqus CAE also revealed that the axial capacity of rod 2 decreases by approximately 3.8 kN as a result of increased initial imperfections by 0.20 mm (cf. Table 6.20).

To address uncertainties regarding the measured cross-sectional areas and initial geometric imperfections of the specimens, it is necessary to employ more precise and sophisticated measuring techniques. For instance, utilizing 2D or 3D scanning would enable accurate measurements of the entire specimen's geometry, providing detailed information about its dimensions. Additionally, generating a mesh directly from this scan data and importing it into Abaqus CAE can further enhance accuracy. Implementing these measures will lead to a more realistic representation of the specimen's geometry in the FE-model, thereby eliminating uncertainties and potential errors related to rod geometry.

Shifting the focus, the acquired experimental data and the UTM should also be discussed. The testing machine had limitations regarding sampling frequency, which became noticeable when the rods were compressed more rapidly. Under quasi-static loading, the recorded data contained a sufficient number of values, ensuring that the derived structural responses at this loading rate are reliable and representative. Conversely, when the tests lasted for a very short time, only a limited number of data points could be retrieved. This limitation was particularly significant under dynamic loading, as only a few data points were recorded around the critical stage of the test.

A significant and abrupt increase in force was observed between two consecutive time steps at the onset of buckling due to the lack of data points. This absence of smooth transitions introduces a risk of inaccurately predicting the capacity of the rods. This limitation is potentially exemplified by deviations in the experimentally predicted critical buckling force of rod 2 under escalated strain rates compared to the numerically determined values. Except for the quasi-static case, deviations around 20 % can be observed between the two approaches (cf. Table 6.17).

Furthermore, while the deviation in buckling load from loading with a velocity of 130 mm/s is only 7.7 %, the substantial increase in capacity by 73 % relative to the quasi-static capacity is unexpectedly high (cf. Table 6.16). In conclusion, having more data points around the buckling stage would have been advantageous to reduce the uncertainty of possible inaccurate predictions of force values.

8 Final Remarks

This section presents the conclusions drawn from the study, summarizing key findings and outlining potential areas for further research.

8.1 Conclusions

This thesis investigates the dynamic behavior of two S355 steel rod structures under compressive axial loading, exploring strain rates ranging from 10^{-4} s^{-1} to 1.5 s^{-1}. The examined rod structures are shaped like "dogbone" with a thickness of 4 mm and unsupported length of 130 mm (rod 1) or 260 mm (rod 2). The study employs a combination of experimental testing, including both structural tests (compression) and material tests (tension), and numerical simulations conducted in Abaqus CAE. Material testing is performed to establish the material behavior of the rods and to determine the strain rate parameters for the CS-model. Based on the results obtained, the following conclusions can be drawn:

1. Both experimental and numerical findings highlight the material's sensitivity to strain rate, revealing an increase in strength under higher loading rates (decreased load duration). This correlation is substantiated by the observed augmentation in critical buckling load and associated end-shortening value, indicative of instability onset. Notably, in material testing, this phenomenon is manifested by the increase in yield strength and ultimate tensile strength.

2. The derived strain rate material parameters (D = 1094 and p = 3.47) for the CS-model show good agreement with experimental findings from structural tests involving rod 1. Tensile simulations utilizing derived parameters from other studies also show strong correlation between analytical and numerical predictions of strain rate effects.

3. There is a notable correlation between structural response and the parameters imperfection and slenderness. As initial imperfections and/or slenderness of the rods increase, their axial capacity decreases.

4. The structural response influenced by inertia effects manifests at lower strain rates as the slenderness increases. Dynamic oscillations are observed for rod 2 at a strain rate of 10^{-1} s^{-1} (v = 26 mm/s), whereas no such oscillations are seen for rod 1 at the same strain rate (v = 13 mm/s). For rod 1, these dynamic oscillations are first observed at a strain rate of 0.5 s^{-1} (v = 65 mm/s).

5. The stiffness (Young's modulus and/or secant stiffness) of the material in the linear elastic range remains relatively insensitive to strain rates, a finding corroborated by both material and structural testing of rod 1.

6. For steel rods with increased geometric perfection, dynamic oscillations exhibit greater prominence, evidenced by higher amplitudes. This implies that reduced geometric initial imperfections result in heightened dynamic behavior, particularly noticeable when comparing various imperfection levels under identical strain rates for rod 2.

7. Increased slenderness of a structure results in higher strain rate sensitivity. This is evident in the critical buckling load, where the more slender rod (rod 2) experiences a significantly larger increase compared to the less slender rod (rod 1) at the same strain rate.

8.2 Further Studies

Having established a fundamental understanding through the examination of a simple structure, a compressed steel rod, exploring more advanced structures for future studies can be contemplated. One possible path forward is to consider evaluating the structural response of a thin-walled steel plate, supported on four sides, subjected to compressive axial dynamic loading. Then, attention can be directed towards investigating a CSM subjected to dynamic load acting perpendicular to its plane. These studies would provide a deeper insight into the structural response of more complex structures and enable the application of fundamental knowledge to more realistic scenarios.

Another alternative for future study could be to investigate a drop-weight impact experiment, simulating a rapid pressure load on a test specimen. Such experiment could entail conducting tests on a steel rod with a hinged connection and uniform width (i.e., no broad fixtures like dogbone specimens) while employing a drop-weight apparatus to simulate the impact.

It should be noted that throughout this study, extensive research has been conducted to determine the dynamic buckling load through analytical means. However, challenges have been encountered in attempts to utilize existing papers presenting analytical models for predicting the dynamic buckling load. Reproducing the findings from those papers has proven difficult due to insufficient details, especially concerning input parameters and model assumptions. Consequently, this aspect has been omitted from this study due to the inability to produce satisfactory results or obtain adequate clarity on the methodologies employed in those papers.

To address this gap, a further study could leverage both existing experimental data from dynamic loading, particularly compressive axial loads applied to simple structures like columns and rods, and analytical models from previous literature. By integrating these two sources of information, a new analytical framework could be developed. This framework would aim to accurately predict dynamic buckling loads by considering critical parameters such as mass, slenderness, initial imperfections, and loading rate.

Bibliography

Al-Emrani, M. (2023). *Steel structures : Course literature - VSM 191* (Vol. Report ACE 2023:1). Chalmers University of Technology.

Al-Emrani, M., Engström, B., Johansson, M., & Johansson, P. (2019). *Bärande konstruktioner : Del 1* (Vol. Report ACE 2019:2). Chalmers University of Technology.

Boer, A., Hendriks, M., den Uijl, J., Belletti, B., & Damoni, C. (2014). Nonlinear fea guideline for modelling of concrete infrastructure objects. *Computational Modelling of Concrete Structures - Proceedings of EURO-C 2014*, *2*, 977–985. https://doi.org/10.1201/b16645-109

Broo, H., Lundgren, K., & Plos, M. (2008). *A guide to non-linear finite element modelling of shear and torsion in concrete bridges*. Chalmers University of Technology.

Cadoni, E., Forni, D., Gieleta, R., & Kruszka, L. (2018). Tensile and compressive behaviour of s355 mild steel in a wide range of strain rates. *The European Physical Journal Special Topics*, *227*, 29–43. https://doi.org/10.1140/epjst/e2018-00113-4

Carlsson, M., & Kristensson, R. (2012). *Structural response with regard to explosions : Mode superposition, damping and curtailment*. Structural Mechanics, Lund University.

Dassault Systèmes Simulia Corporation. (2024). *Abaqus analysis user's manual*. Dassault Systèmes Simulia Corporation. https://help.3ds.com/2024/English/DSSIMULIA_Established/SIMACAEELMRefMap/simaelm-c-solidcont.htm?contextscope=all

Dubina, D., Ungureanu, V., & Landolfo, R. (2012). *Design of cold-formed steel structures : Eurocode 3: Design of steel structures. part 1-3 design of cold-formed steel structures* (1.ed.). Ernst & Sohn.

Hao, H. (2015). Predictions of structural response to dynamic loads of different loading rates. *International Journal of Protective Structures*, *6*, 585–606. https://doi.org/10.1260/2041-4196.6.4.585

Johansson, M., & Laine, L. (2012a). *Bebyggelsens motståndsförmåga mot extrem dynamisk belastning del 1: Last av luftstötvåg*.

Johansson, M., & Laine, L. (2012b). *Bebyggelsens motståndsförmåga mot extrem dynamisk belastning del 2: Explosion i gatukorsning*.

Johansson, M., & Laine, L. (2012c). *Bebyggelsens motståndsförmåga mot extrem dynamisk belastning del 3: Kapacitet hos byggnader*.

Kubiak, T. (2013). *Static and dynamic buckling of thin-walled plate structures*. https://doi.org/10.1007/978-3-319-00654-3

Mallon, N. (2008). *Dynamic stability of thin-walled structures : A semi-analytical and experimental approach* [Phd Thesis 1 (Research TU/e / Graduation TU/e)]. Mechanical Engineering. Technische Universiteit Eindhoven. https://doi.org/10.6100/IR637287

McCormick, N., & Lord, J. (2010). Digital image correlation. *Materials Today*, *13*, 52–54. https://doi.org/10.1016/S1369-7021(10)70235-2

N. K. Singh, M. K. S., E. Cadoni, & Gupta, N. K. (2014). Quasi-static and dynamic tensile behavior of cp800 steel. *Mechanics of Advanced Materials and Structures*, *21*(7), 531–537. https://doi.org/10.1080/15376494.2012.699594

Nam, H., Kim, J., Han, J., Kim, J., & Kim, Y. (2015). *Ductile fracture simulation for a106 gr. b carbon steel under high strain rate loading condition*.

Nassr, A. A. (2012). *Experimental and analytical study of the dynamic response of steel beams and columns to blast loading* [Doctoral dissertation].

Német, M., & Mihaliková, M. (2013). The effect of strain rate on the mechanical properties of automotive steel sheets. *Acta Polytechnica*, *53*, 384–387. https://doi.org/10.14311/1839

Paik, J., & Thayamballi, A. (2003). An experimental investigation on the dynamic ultimate compressive strength of ship plating. *International Journal of Impact Engineering - INT J IMPACT ENG*, *28*, 803–811. https://doi.org/10.1016/S0734-743X(02)00154-9

Plos, M., Johansson, M., Zandi, K., & Shu, J. (2021). Recommendations for assessment of reinforced concrete slabs. *Division of Structural Engineering, Chalmers University of Technology, Report ACE*, *3*.

Rivai, A., Bapokutty, O., & Wai, C. (2013). Modelling optimization involving different types of elements in finite element analysis. *IOP Conference Series: Materials Science and Engineering*, *50*. https://doi.org/10.1088/1757-899X/50/1/012036

Roylance, D. (2001). Stress-strain curves. *Massachusetts Institute of Technology study, Cambridge*.

Ruukki. (n.d.). *Load-bearing sheets*. https://www.ruukki.com/gbr/building-envelopes/products/roof-structure/load-bearing-sheets#load-bearing

Singer, J., Arbocz, J., Weller, T., & Cheney, J. (2003). Buckling experiments: Experimental methods in buckling of thin-walled structures. shells, built-up structures, composites and additional topics, volume 2. *Applied Mechanics Reviews - APPL MECH REV*, *56*. https://doi.org/10.1115/1.1523358

The Swedish Institute for Standards. (2011). *Metallic materials – Tensile testing at high strain rates – Part 2: Servo-hydraulic and other test systems* (ISO 26203-2:2011). https://www-sis-se.proxy.lib.chalmers.se/api/document/get/82022

Xing, X., Linri, L., & Qin, H. (2021). Dynamic tensile behavior of steel strands at different strain rates. *Structures*, *33*. https://doi.org/10.1016/j.istruc.2021.04.012

Xiufeng, H., Jihang, W., & Zhenhua, Z. (2020). Research on application of digital image correlation method, 838–840. https://doi.org/10.1109/ICAICA50127.2020.9182584

Yang, X., Yang, H., Gardner, L., & Wang, Y. (2022). A continuous dynamic constitutive model for normal- and high-strength structural steels. *Journal of Constructional Steel Research*, *192*, 107254. https://doi.org/https://doi.org/10.1016/j.jcsr.2022.107254

Yun, X., & Gardner, L. (2017). Stress-strain curves for hot-rolled steels. *Journal of Constructional Steel Research*, *133*, 36–46. https://doi.org/10.1016/j.jcsr.2017.01.024

Zhang, Z.-J., Chen, B.-S., Bai, R., & Liu, Y.-P. (2023). Non-linear behavior and design of steel structures: Review and outlook. *Buildings*, *13*, 2111. https://doi.org/10.3390/buildings13082111

Appendices

A Pre-Study: Stress-Strain Constitutive Model

Analytical stress–strain relationship

Establishment of material behaviour for structural steel S355 based on constitutive model.

Input data

Young's modulus of structural steel: $E := 210\ \textit{GPa}$

Yield strength of steel grade S355: $f_y := 355\ \textit{MPa}$

Ultimate tensile strength of S355: $f_u := 490\ \textit{MPa}$

Bi–linear plus nonlinear hardening stress–strain model

Yield strain: $\varepsilon_y := \frac{f_y}{E} = 0.0017 \quad (\sigma_y := f_y) \quad \varepsilon_y = 0.17\%$

Strain hardening strain: $\varepsilon_{sh} := 0.1 \cdot \frac{f_y}{f_u} - 0.055 = 0.0174 \quad \varepsilon_{sh} = 1.74\%$

$0.015 \le \varepsilon_{sh} \le 0.03 = 1$ OK! (Condition)

Ultimate strain: $\varepsilon_u := 0.6 \cdot \left(1 - \frac{f_y}{f_u}\right) = 0.1653 \quad \varepsilon_u = 16.53\%$

$\varepsilon_u \ge 0.06 = 1$ OK! (Condition for hot–rolled steels)

Different strain values between ε_{sh} and ε_u for capturing the nonlinear response:

$$\varepsilon_{sh.u1} := \varepsilon_{sh} + \frac{\varepsilon_u - \varepsilon_{sh}}{10} \quad \varepsilon_{sh.u2} := \varepsilon_{sh} + 2 \cdot \frac{\varepsilon_u - \varepsilon_{sh}}{10} \quad \varepsilon_{sh.u3} := \varepsilon_{sh} + 3 \cdot \frac{\varepsilon_u - \varepsilon_{sh}}{10}$$

$$\varepsilon_{sh.u4} := \varepsilon_{sh} + 4 \cdot \frac{\varepsilon_u - \varepsilon_{sh}}{10} \quad \varepsilon_{sh.u5} := \varepsilon_{sh} + 5 \cdot \frac{\varepsilon_u - \varepsilon_{sh}}{10} \quad \varepsilon_{sh.u6} := \varepsilon_{sh} + 6 \cdot \frac{\varepsilon_u - \varepsilon_{sh}}{10}$$

$$\varepsilon_{sh.u7} := \varepsilon_{sh} + 7 \cdot \frac{\varepsilon_u - \varepsilon_{sh}}{10} \quad \varepsilon_{sh.u8} := \varepsilon_{sh} + 8 \cdot \frac{\varepsilon_u - \varepsilon_{sh}}{10} \quad \varepsilon_{sh.u9} := \varepsilon_{sh} + 9 \cdot \frac{\varepsilon_u - \varepsilon_{sh}}{10}$$

Initiation av loop variable for stress–calculation: $i := 0, 1 .. 12$

Strain: $\varepsilon := \left[0 \ \varepsilon_y \ \varepsilon_{sh} \ \varepsilon_{sh.u1} \ \varepsilon_{sh.u2} \ \varepsilon_{sh.u3} \ \varepsilon_{sh.u4} \ \varepsilon_{sh.u5} \ \varepsilon_{sh.u6} \ \varepsilon_{sh.u7} \ \varepsilon_{sh.u8} \ \varepsilon_{sh.u9} \ \varepsilon_u\right]^T$

Stress:

$$\sigma_i := \left\| \begin{array}{l} \text{if } \varepsilon_i \le \varepsilon_y \\ \quad \left\| \sigma \leftarrow E \cdot \varepsilon_i \right. \\ \text{else if } \varepsilon_y < \varepsilon_i \le \varepsilon_{sh} \\ \quad \left\| \sigma \leftarrow f_y \right. \\ \text{else if } \varepsilon_{sh} < \varepsilon_i \le \varepsilon_u \\ \quad \left\| \sigma \leftarrow f_y + \left(f_u - f_y\right) \cdot \left(0.4 \left(\frac{\varepsilon_i - \varepsilon_{sh}}{\varepsilon_u - \varepsilon_{sh}} \right) + \frac{2 \cdot \left(\frac{\varepsilon_i - \varepsilon_{sh}}{\varepsilon_u - \varepsilon_{sh}} \right)}{\left(1 + 400 \cdot \left(\frac{\varepsilon_i - \varepsilon_{sh}}{\varepsilon_u - \varepsilon_{sh}} \right)^5 \right)^{\left(\frac{1}{5}\right)}} \right) \right. \end{array} \right.$$

Engineering stress–strain curve for S355:

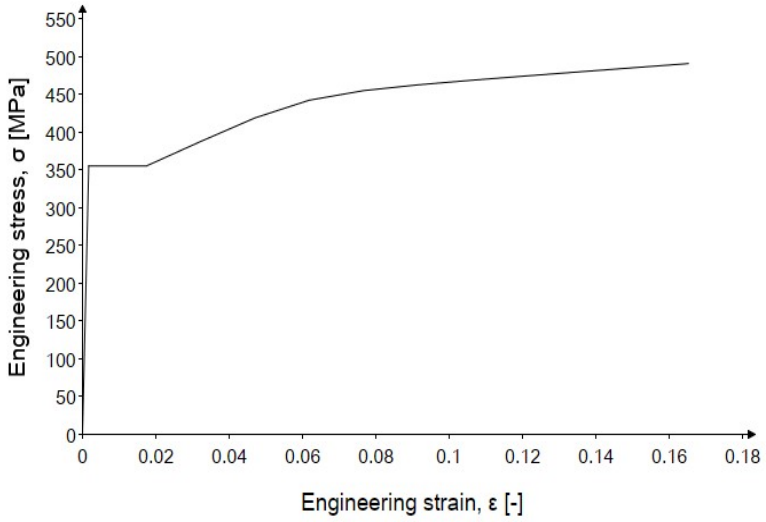

Conversion of engineering stress & strain to true stress & strain for defining the material behavior in Abaqus CAE (after yielding).

True strain: $\varepsilon_{true} := \ln\left(1 + \varepsilon\right)$

True stress: $\sigma_{true} := \overrightarrow{\sigma \cdot \left(1 + \varepsilon\right)}$

True stress–strain curve for S355:

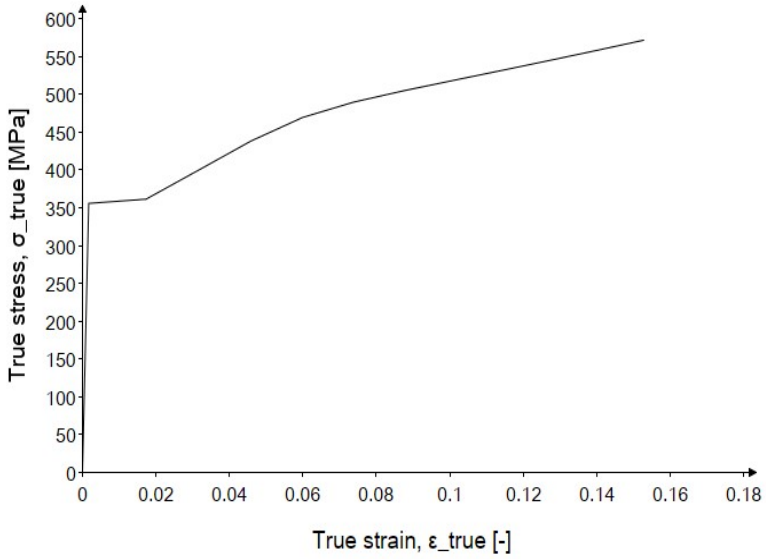

Comparisons of Engineering stress–strain curve vs True stress–strain curve:

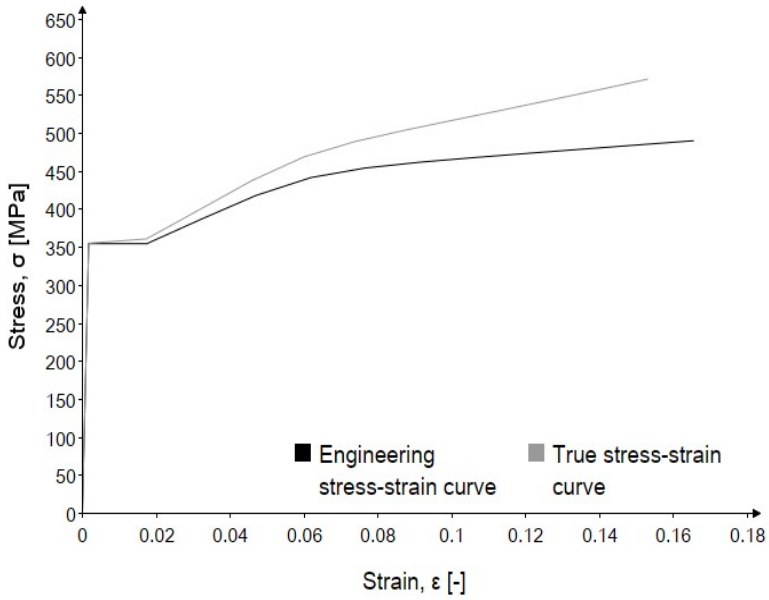

Plasticity data defintion in Abaqus CAE:

Generating vectors representing true stress and true strain, specifically for the plastic region of the material's reponse from the onset of yielding to the point of necking. The parameters are converted (unitless) to match the unit definition in Abaqus (MPa).

$$\sigma_{true.region} := \frac{\left[\sigma_{true_1}\ \sigma_{true_2}\ \sigma_{true_3}\ \sigma_{true_4}\ \sigma_{true_5}\ \sigma_{true_6}\ \sigma_{true_7}\ \sigma_{true_8}\ \sigma_{true_9}\ \sigma_{true_{10}}\ \sigma_{true_{11}}\ \sigma_{true_{12}}\right]^T}{MPa}$$

$$\varepsilon_{true.region} := \left[\varepsilon_{true_1}\ \varepsilon_{true_2}\ \varepsilon_{true_3}\ \varepsilon_{true_4}\ \varepsilon_{true_5}\ \varepsilon_{true_6}\ \varepsilon_{true_7}\ \varepsilon_{true_8}\ \varepsilon_{true_9}\ \varepsilon_{true_{10}}\ \varepsilon_{true_{11}}\ \varepsilon_{true_{12}}\right]^T$$

Young's modulus definition in Abaqus: $E_{Abaqus} := \frac{E}{MPa} = 210000$

Plastic true strain: $\varepsilon_{true.pl.region} := \varepsilon_{true.region} - \frac{\sigma_{true.region}}{E_{Abaqus}}$ $\left(\varepsilon_{plastic} := \varepsilon_{tot} - \varepsilon_{elastic}\right)$

∴ The input data for the plasticty in Abaqus is hence:

$$\sigma_{true.Abaqus} := \begin{bmatrix} 355 \\ 355.6 \\ 361.2 \\ 399.9 \\ 438.2 \\ 469.2 \\ 489.4 \\ 504.5 \\ 518.1 \\ 531.4 \\ 544.6 \\ 558 \\ 571.5 \end{bmatrix} \qquad \varepsilon_{true.pl.Abaqus} := \begin{bmatrix} 0.0000 \\ 0.0003 \\ 0.0153 \\ 0.0301 \\ 0.0439 \\ 0.0578 \\ 0.0717 \\ 0.0846 \\ 0.0985 \\ 0.1115 \\ 0.1244 \\ 0.1373 \\ 0.1503 \end{bmatrix}$$ (Direct input in Abaqus)

Resulting True stress–plastic strain curve for the model in Abaqus:

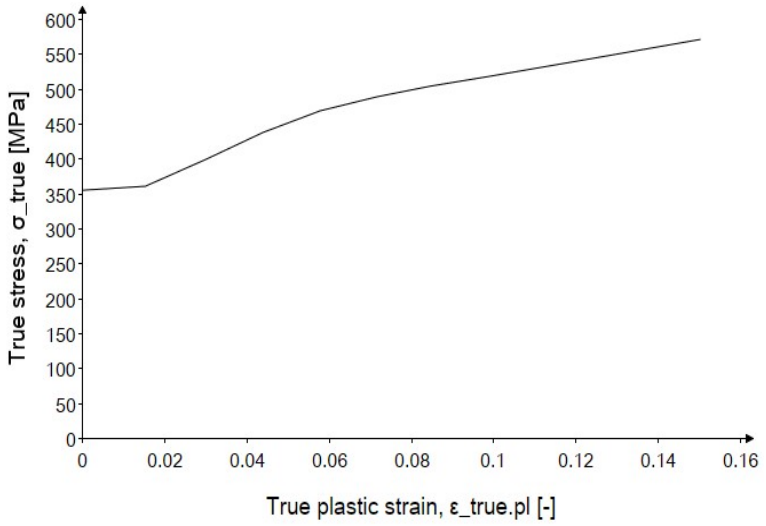

B Pre-study: Critical Buckling Load of Rod 1&2

Analytical calculation of buckling load

Rod geometry 1

Geometric properties

Total length of the rod: $L_{tot} := 200\ mm$
Clamping length: $L_k := 35\ mm$
Clamping width: $b_k := 44\ mm$
Shell thickness: $a_o := 4\ mm$
Transition radius: $r := 12\ mm$
Width of parallel length: $b_o := 20\ mm$
Parallel length: $L_c := L_{tot} - 2 \cdot L_k - 2 \cdot r = 106\ mm$
Unrestrained length: $L := L_{tot} - 2 \cdot L_k = 130\ mm$ (for buckling)

Buckling length

Effective length factor for fixed–fixed BC: $k := 0.5$
Buckling length for the rod: $L_{cr} := k \cdot L = 65\ mm$

Sectional constants

Cross–sectional area: $A := b_o \cdot a_o = 80\ mm^2$
Second moment of area: $I := \frac{b_o \cdot a_o^3}{12} = 106.7\ mm^4$ (around weak axis)
Radius of gyration: $i := \sqrt{\frac{I}{A}} = 1.2\ mm$

Material properties

Young's modulus of structural steel: $E := 210\ GPa$
Yield strength of steel grade S355: $f_y := 355\ MPa$

Slenderness of the rod

Slenderness: $\lambda := \frac{L_{cr}}{i} = 56.3$
Relative slenderness: $\lambda_1 := \pi \cdot \sqrt{\frac{E}{f_y}} = 76.4$
Relative slenderness ratio: $\lambda_{bar} := \frac{\lambda}{\lambda_1} = 0.74$ (ideal geometry)

Euler buckling

Critical buckling load (elastic): $P_{cr} := \frac{\pi^2 \cdot E \cdot I}{L_{cr}^2} = 52.3\ kN$

Yielding

Yielding load: $P_y := f_y \cdot A = 28.4\ kN$

Rod geometry 2

Geometric properties

Total length of the rod: $L_{tot} := 330\ mm$
Clamping length: $L_k := 35\ mm$
Clamping width: $b_k := 44\ mm$
Shell thickness: $a_o := 4\ mm$
Transition radius: $r := 12\ mm$
Width of parallel length: $b_o := 20\ mm$
Parallel length: $L_c := L_{tot} - 2 \cdot L_k - 2 \cdot r = 236\ mm$
Unrestrained length: $L := L_{tot} - 2 \cdot L_k = 260\ mm$

Buckling length

Effective length factor for fixed–fixed BC: $k := 0.5$
Buckling length for the rod: $L_{cr} := k \cdot L = 130\ mm$

Sectional constants

Cross–sectional area: $A := b_o \cdot a_o = 80\ mm^2$

Second moment of area: $I := \frac{b_o \cdot a_o^{\,3}}{12} = 106.7\ mm^4$

Radius of gyration: $i := \sqrt{\frac{I}{A}} = 1.2\ mm$

Slenderness of the rod

Slenderness: $\lambda := \frac{L_{cr}}{i} = 112.6$

Relative slenderness: $\lambda_1 := \pi \cdot \sqrt{\frac{E}{f_y}} = 76.4$

Relative slenderness ratio: $\lambda_{bar} := \frac{\lambda}{\lambda_1} = 1.47$

Euler buckling

Critical buckling load (elastic): $P_{cr} := \frac{\pi^2 \cdot E \cdot I}{L_{cr}^{\,2}} = 13.1\ kN$

Yielding

Yielding load: $P_y := f_y \cdot A = 28.4\ kN$

Conversion of eigenvalue in FEA to buckling load

Reference load in Abaqus

Shell edge line load: $q := 100 \ \frac{N}{mm}$

Conversion to concentrated load: $P := q \cdot b_k = 4.4 \ kN$

Rod geometry 1

Eigenvalue: $\lambda_{eig} := 12.706$

Critical buckling load : $P_{cr} := \lambda_{eig} \cdot P = 55.9 \ kN$

Rod geometry 2

Eigenvalue: $\lambda_{eig} := 3.0749$

Critical buckling load : $P_{cr} := \lambda_{eig} \cdot P = 13.5 \ kN$

C Pre-study: DIF for a Single Tensile Element

Strain–rate effects

Establishment of dynamic yield stress, $\sigma_{y.d}$ for a single tensile element across a range of applied velocities, spanning from quasi–static to dynamic loading states, based on dynamic simulations in Abaqus CAE with rate–dependent plasticity.

Determination of strain–rate

Length of tensile element: $L := 100\ mm$ (from Abaqus)

Loading rates: $v := [0.001\ \ 0.01\ \ 0.1\ \ 1\ \ 10\ \ 100\ \ 1000\ \ 10000]\ \frac{mm}{s}$ (from Abaqus)

Strain rates: $\varepsilon' := \frac{v}{L} = [1 \cdot 10^{-5}\ \ 1 \cdot 10^{-4}\ \ 1 \cdot 10^{-3}\ \ 1 \cdot 10^{-2}\ \ 1 \cdot 10^{-1}\ \ 1\ \ 1 \cdot 10\ \ 1 \cdot 10^{2}]\ \frac{1}{s}$

Strain–rate effect model

Static y ield strength : $f_y := 355\ MPa$

Exponent in power law (CS model): $p_y := 5 \cdot \left(\frac{f_y}{235\ MPa}\right)^{-0.5} = 4.07$

Multiplier in power law (CS model): $D_y := 1000 \cdot \left(\frac{f_y}{235\ MPa}\right)^{3.8} = 4795.23$

Initiation av loop variable for DIF–calculation: $i := 0, 1 .. 7$

Dynamic increase factor for yield strength: $DIF_{y.an_i} := \left\| DIF \leftarrow 1 + \left(\frac{\left(\left(\varepsilon'\right)^{\mathrm{T}}\right)_i}{D_y \cdot \frac{1}{s}} \right)^{\frac{1}{p_y}} \right| = \begin{bmatrix} 1.007 \\ 1.013 \\ 1.023 \\ 1.04 \\ 1.071 \\ 1.125 \\ 1.219 \\ 1.386 \end{bmatrix}$

Dynamic y ield strength : $f_{y.d.an} := DIF_{y.an} \cdot f_y = \begin{bmatrix} 357.61 \\ 359.59 \\ 363.09 \\ 369.25 \\ 380.1 \\ 399.2 \\ 432.85 \\ 492.11 \end{bmatrix} MPa$ (Analytical)

Numerical results (Abaqus CAE)

The yield plateu−values from Abaqus simulations for the different ε' are extracted at approximately $\varepsilon := 0.00295$ (based on 1000 datapoints). At this strain level the material has reached yielding for all cases, though, not neccessarily corresponding to the exact yielding point for all loading rates. These values are divided by the static yield strength, $f_y = 355$ ***MPa*** for comparison of DIF_y−values between the results obtained from the numerical analyses with the results obtained from the analytical method.

Dynamic yield strength : $f_{y.d.num} := \begin{bmatrix} 358.67 \\ 360.71 \\ 364.30 \\ 370.63 \\ 381.75 \\ 400.78 \\ 435.52 \\ 493.34 \end{bmatrix}$ ***MPa***

Dynamic increase factor for yield strength: $DIF_{y.num} := \frac{f_{y.d.num}}{f_y} = \begin{bmatrix} 1.01 \\ 1.016 \\ 1.026 \\ 1.044 \\ 1.075 \\ 1.129 \\ 1.227 \\ 1.39 \end{bmatrix}$

Comparison of DIF_y as function of ε' for numerical and analytical calculations

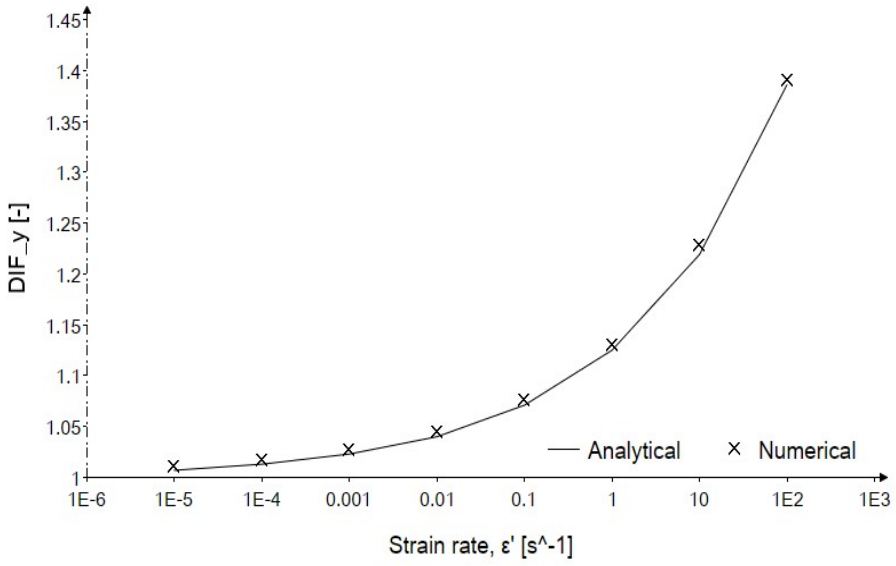

D Experimental Study: Material Tests of Rod 1

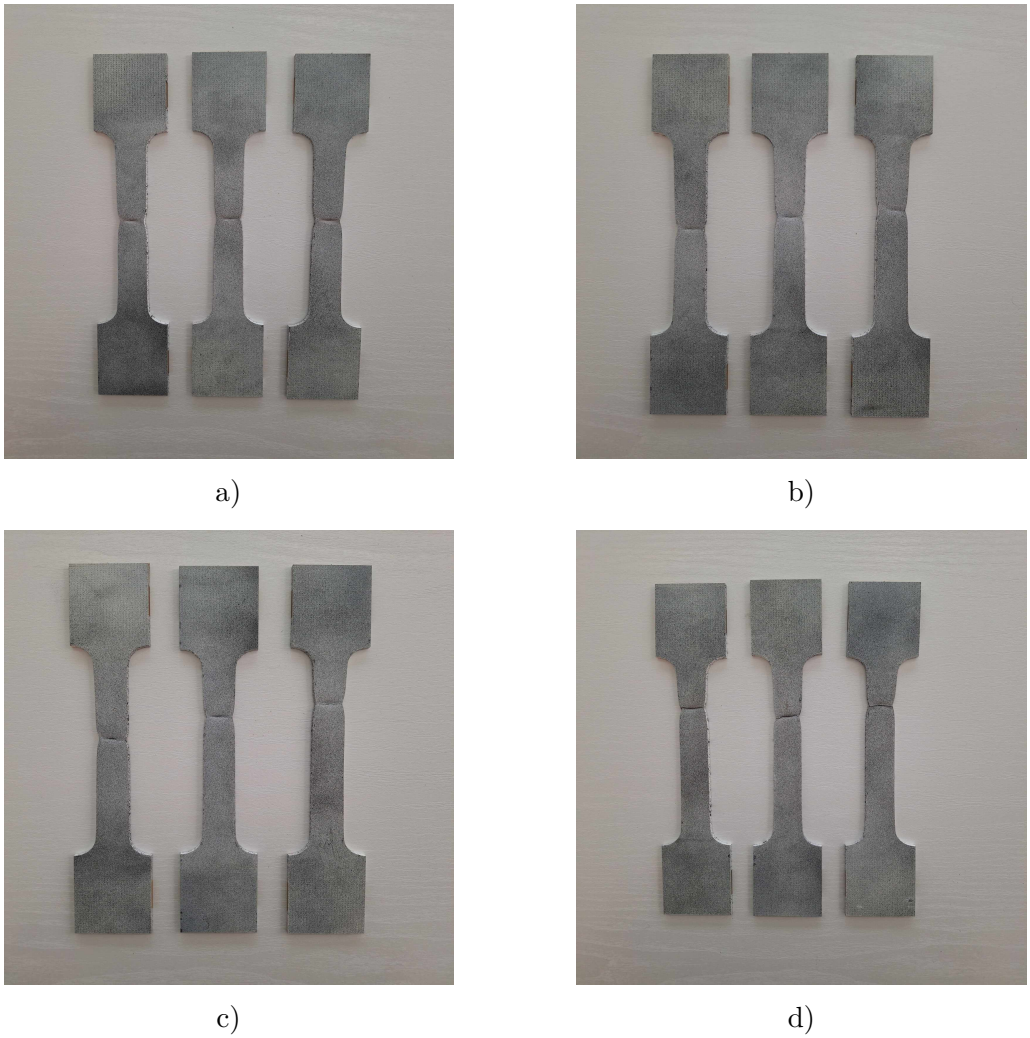

a) b) c) d)

Figure D.1: Necking of rod 1 for three samples observed at different velocities: a) v = 0.013 mm/s, b) v = 1.3 mm/s, c) v = 13 mm/s & d) v = 130 mm/s.

E Experimental Study: Development of Constitutive Model

Cowper - Symonds material model

$$\frac{\sigma_{y,d}}{\sigma_y} = DIF = 1 + (\frac{\dot{e}}{D})^{\frac{1}{p}} \rightarrow DIF - 1 = (\frac{\dot{e}}{D})^{\frac{1}{p}}$$

Summary from material testing + extrapolated f_y

Strain rate, $\dot{\epsilon}$ [1/s]	Yield strength, σ_y [MPa]	Stress ratio, DIF_y [-]	DIF_y - 1 [-]
1.0E - 6	407.19	1.000	0.000
1.0E - 4	410.87	1.009	0.009
1.0E - 2	421.31	1.035	0.035
1.0E - 1	435.53	1.070	0.070
1.0E+0	461.11	1.132	0.132

Power curve fitting approach

Equation	↔	$y=ax^b$
y	↔	$DIF_y - 1$
x	↔	$\dot{\epsilon}$
b	↔	1/p
a	↔	(1/D)^b

Comparison of experimental data with fitted curve

a	0.13
b	0.29

DIF_y - 1 [-]	$y=ax^b$	Res^2
0.000	0.002	6.10E - 06
0.009	0.009	8.33E - 08
0.035	0.035	2.67E - 07
0.070	0.068	1.50E - 06
0.132	0.133	1.82E - 07
	Sum	8.13E - 06

The values of variables a and b are determined based on the result yielding the lowest sum of squared residuals, Res^2. These residuals (Res) represent the differences between the experimental data including the extrapolated f_y and the data predicted by the fitted curve.

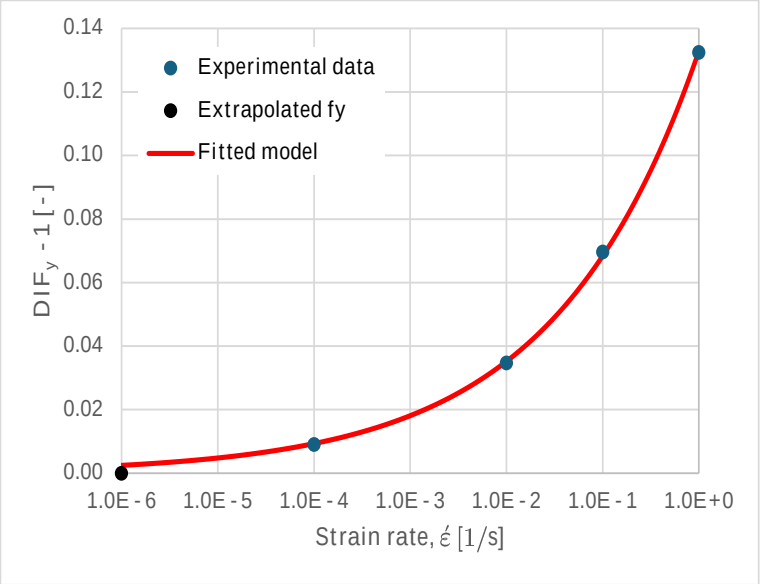

Determination of parameters

p	**3.47**
D	**1094.02**

DIF$_y$ variation with strain rate

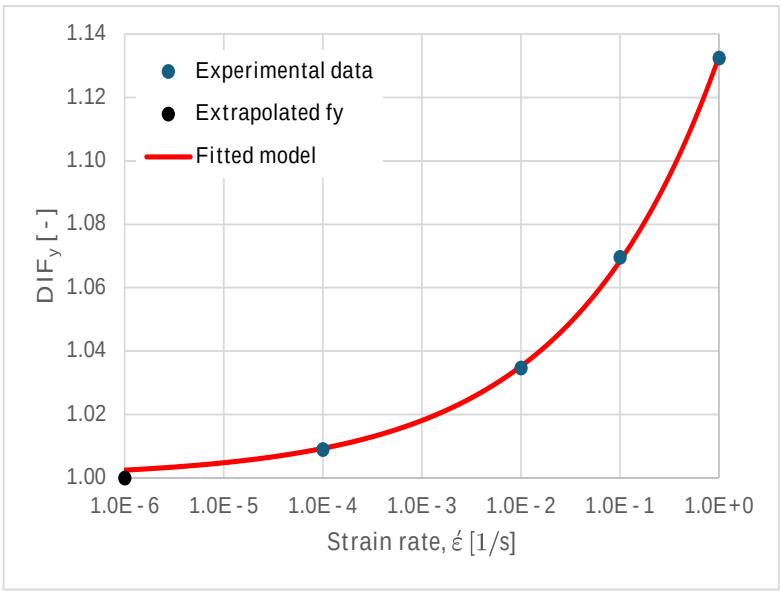

F Experimental Study: Structural Tests of Rod 1

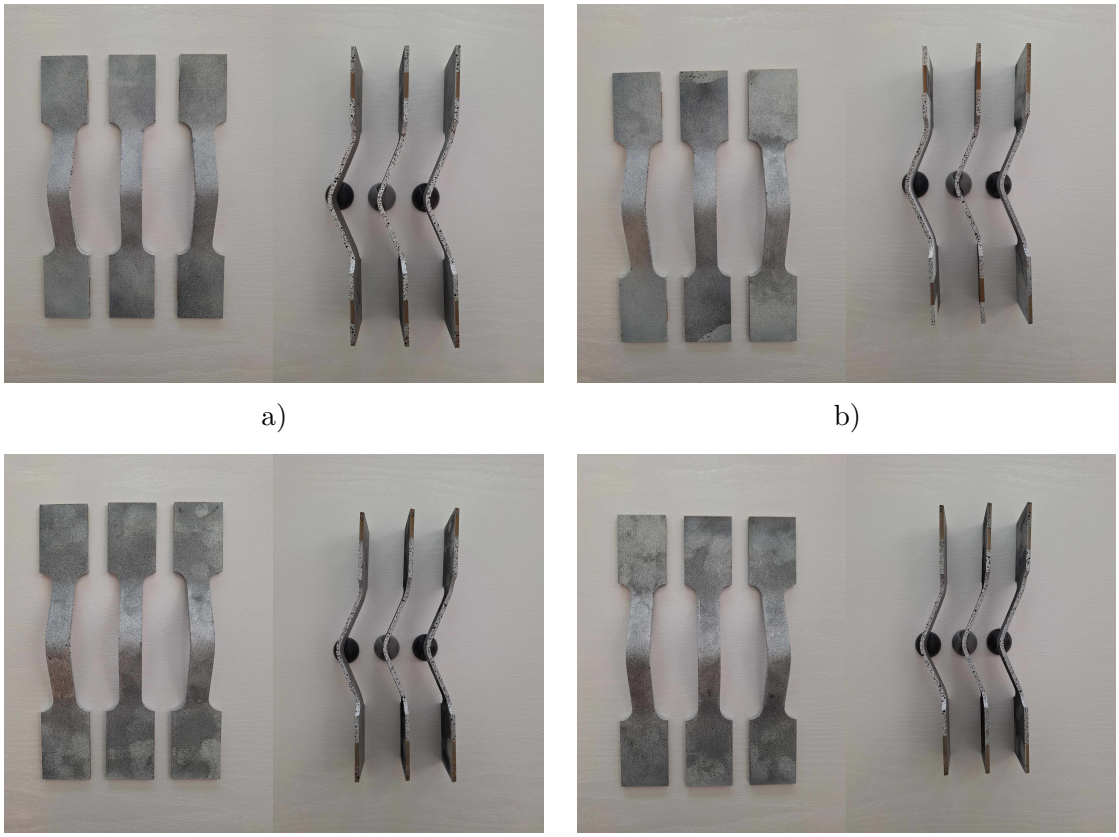

a) b)

c) d)

Figure F.1: Front and side perspectives of the buckled shape of rod 1 for three samples observed at different velocities: a) v = 0.013 mm/s, b) v = 13 mm/s, c) v = 65 mm/s & d) v = 195 mm/s.

G Experimental Study: Structural Tests of Rod 2

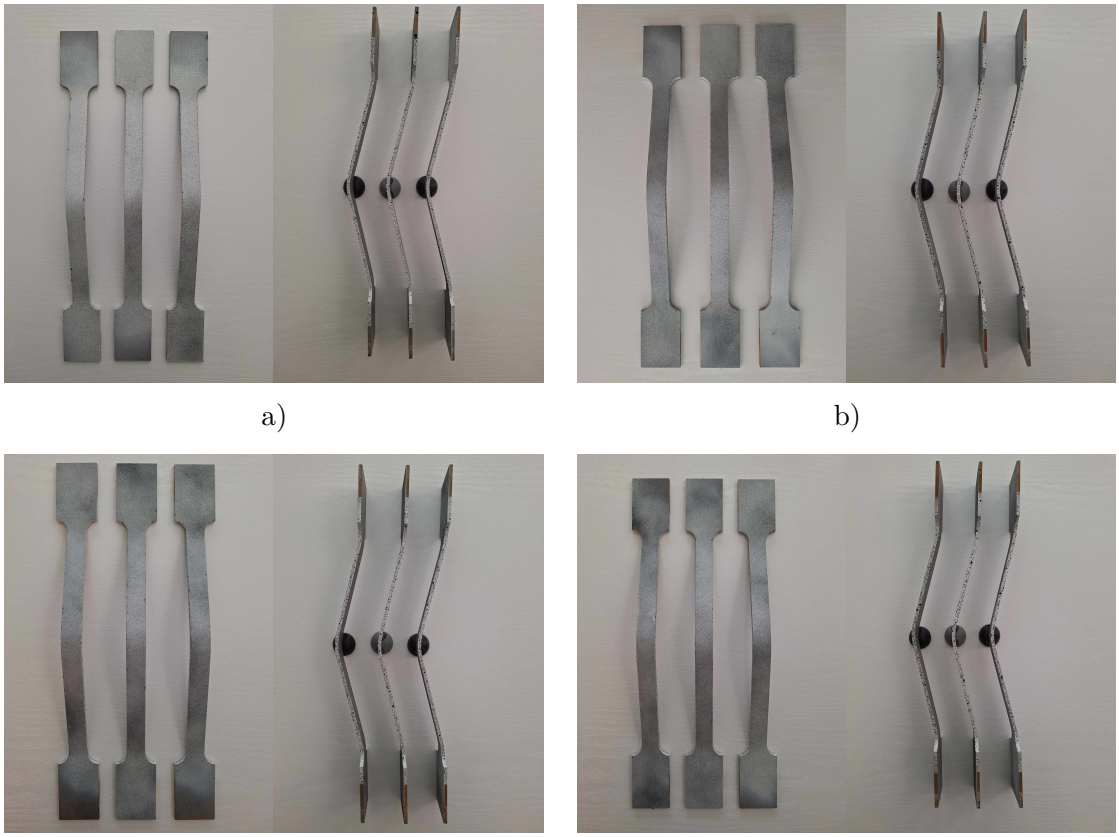

a) b)

c) d)

Figure G.1: Front and side perspectives of the buckled shape of rod 2 for three samples observed at different velocities: a) v = 0.026 mm/s, b) v = 26 mm/s, c) v = 52 mm/s & d) v = 130 mm/s.

H FEA & Experiments: Failure Mode Verification

Critical buckling load from experiments & FEA

Rod 1

Geometric properties

Total length of the rod: $L_{tot} := 250\ mm$
Clamping length: $L_k := 60\ mm$
Clamping width: $b_k := 44.44\ mm$
Transition radius: $r := 12\ mm$
Average thickness: $a_o := 3.9\ mm$ (experimental measurement)
Top width of parallel length: $b_{o.t} := 20\ mm$ (experimental measurement)
Bottom width of parallel length: $b_{o.b} := 19.75\ mm$ (experimental measurement)

Average width of parallel length: $b_o := \frac{b_{o.t} + b_{o.b}}{2} = 19.88\ mm$

Parallel length: $L_c := L_{tot} - 2 \cdot L_k - 2 \cdot r = 106\ mm$
Unrestrained length: $L := L_{tot} - 2 \cdot L_k = 130\ mm$
Initial imperfections: $e := 0.05\ mm$ (experimental measurement)

Buckling length

Effective length factor for fixed–fixed BC: $k := 0.5$
Buckling length for the rod: $L_{cr} := k \cdot L = 65\ mm$

Sectional constants

Approximated cross–sectional area: $A := b_o \cdot a_o = 77.51\ mm^2$

Second moment of area: $I := \frac{b_o \cdot {a_o}^3}{12} = 98.2\ mm^4$

Radius of gyration: $i := \sqrt{\frac{I}{A}} = 1.1\ mm$

Mechanical properties

0.2 % offset yield strength of the S355 (quasi–static): $f_{0.2} := 411\ MPa$ (material tests)
Young's modulus of the steel (quasi–static): $E := 205\ GPa$ (material tests)

Slenderness of the rod

Slenderness: $\lambda := \frac{L_{cr}}{i} = 57.7$

Relative slenderness: $\lambda_1 := \pi \cdot \sqrt{\frac{E}{f_{0.2}}} = 70.2$

Relative slenderness ratio: $\lambda_{bar} := \frac{\lambda}{\lambda_1} = 0.82$

Euler buckling (Linear response)

Critical buckling load (elastic): $P_{cr} := \frac{\pi^2 \cdot E \cdot I}{L_{cr}^2} = 47\ kN$ (ideal)

Yielding

Yielding load: $P_y := f_{0.2} \cdot A = 31.9\ kN$

Findings (Non–linear response)

Experimental critical buckling load (quasi–static): $P_{cr.exp} := 25.90\ kN$ (structural tests)
Numerical critical buckling load (quasi–static): $P_{cr.num} := 29.98\ kN$

Deviation between results: $\Delta P_{cr} := \frac{|P_{cr.exp} - P_{cr.num}|}{P_{cr.exp}} = 15.8\%$

Verification of governing failure mode

$P_{cr.exp} < P_y = 1$ OK !
$P_{cr.num} < P_y = 1$ OK !

Rod 2

Geometric properties

Total length of the rod:	$L_{tot} := 380\ mm$
Clamping length:	$L_k := 60\ mm$
Clamping width:	$b_k := 44.44\ mm$
Transition radius:	$r := 12\ mm$
Average thickness:	$a_o := 3.9\ mm$
Top width of parallel length:	$b_{o.t} := 20\ mm$
Bottom width of parallel length:	$b_{o.b} := 19.75\ mm$
Average width of parallel length:	$b_o := \frac{b_{o.t} + b_{o.b}}{2} = 19.88\ mm$
Parallel length:	$L_c := L_{tot} - 2 \cdot L_k - 2 \cdot r = 236\ mm$
Unrestrained length:	$L := L_{tot} - 2 \cdot L_k = 260\ mm$
Initial imperfections:	$e := 0.30\ mm$ (experimental measurement)

Buckling length

Effective length factor for fixed–fixed BC:	$k := 0.5$
Buckling length for the rod:	$L_{cr} := k \cdot L = 130\ mm$

Sectional constants

Approximated cross–sectional area: $A := b_o \cdot a_o = 77.51\ mm^2$

Second moment of area: $I := \frac{b_o \cdot a_o^3}{12} = 98.2\ mm^4$

Radius of gyration: $i := \sqrt{\frac{I}{A}} = 1.1\ mm$

Mechanical properties

0.2 % offset yield strength of the S355 sheet metal: $f_{0.2} := 411\ MPa$
Young's modulus of the steel: $E := 205\ GPa$

Slenderness of the rod

Slenderness: $\lambda := \frac{L_{cr}}{i} = 115.5$

Relative slenderness: $\lambda_1 := \pi \cdot \sqrt{\frac{E}{f_{0.2}}} = 70.2$

Relative slenderness ratio: $\lambda_{bar} := \frac{\lambda}{\lambda_1} = 1.65$

Euler buckling (Linear response)

Critical buckling load (elastic): $P_{cr} := \frac{\pi^2 \cdot E \cdot I}{L_{cr}^2} = 11.8\ kN$

Yielding

Yielding load: $P_y := f_{0.2} \cdot A = 31.9\ kN$

Findings (Non–linear response)

Experimental critical buckling load (quasi–static): $P_{cr.exp} := 10.43\ kN$
Numerical critical buckling load (quasi–static): $P_{cr.num} := 10.91\ kN$

Deviation between results: $\Delta P_{cr} := \frac{|P_{cr.exp} - P_{cr.num}|}{P_{cr.exp}} = 4.6\%$

Verification of governing failure mode

$P_{cr.exp} < P_y = 1$ OK !
$P_{cr.num} < P_y = 1$ OK !

I Input File: Static Analysis of Rod 1

```
from part import *
from material import *
from section import *
from assembly import *
from step import *
from load import *
from mesh import *
from job import *
from sketch import *
from visualization import *

# Rename model
mdb.models.changeKey(fromName='Model-1', toName='Linear model')

# Specimen properties
ao=4.0          # original thickness
bk=44.0         # width of the clamping area
bo=20.0         # original width of the parallel length
Lcl=35.0        # length of clamped area
Ltot=200.0      # total length of specimen
r=12.0          # transition radius
force=100.0     # reference load value

# Create a geometry
s = mdb.models['Linear model'].ConstrainedSketch(name='__profile__',
    sheetSize=200.0)
g, v, d, c = s.geometry, s.vertices, s.dimensions, s.constraints
s.setPrimaryObject(option=STANDALONE)
s.Line(point1=(0.0, 0.0), point2=(bk/2, 0.0))
s.HorizontalConstraint(entity=g[2], addUndoState=False)
s.Line(point1=(bk/2, 0.0), point2=(bk/2, -Lcl))
s.VerticalConstraint(entity=g[3], addUndoState=False)
s.Line(point1=(bk/2, -Lcl), point2=(bo/2, -Lcl))
s.HorizontalConstraint(entity=g[4], addUndoState=False)
s.Line(point1=(bo/2, -Lcl), point2=(bo/2, -Ltot/2))
s.VerticalConstraint(entity=g[5], addUndoState=False)
s.FilletByRadius(radius=r, curve1=g[4], nearPoint1=(bk/2-0.1,
    -Lcl-0.1), curve2=g[5], nearPoint2=(bo/2+0.1,
    -Lcl-0.1))
s.Line(point1=(bo/2, -Ltot/2), point2=(0.0, -Ltot/2))
s.HorizontalConstraint(entity=g[7], addUndoState=False)
s.Line(point1=(0.0, -Ltot/2), point2=(0.0, 0.0))
s.VerticalConstraint(entity=g[8], addUndoState=False)
s.setAsConstruction(objectList=(g[8], ))
s.setAsConstruction(objectList=(g[7], ))
s.copyMirror(mirrorLine=g[8], objectList=(g[2], g[3], g[4], g[5], g[6]))
s.copyMirror(mirrorLine=g[7], objectList=(g[5], g[6], g[4], g[3], g[2], g[9],
    g[10], g[11], g[13], g[12]))
p = mdb.models['Linear model'].Part(name='Tensile member', dimensionality=THREE_D,
    type=DEFORMABLE_BODY)
p = mdb.models['Linear model'].parts['Tensile member']
p.BaseShell(sketch=s)
s.unsetPrimaryObject()

# Create partition
f, e, d = p.faces, p.edges, p.datums
t = p.MakeSketchTransform(sketchPlane=f[0], sketchUpEdge=e[12],
    sketchPlaneSide=SIDE1, origin=(0.0, -Ltot/2, 0.0))
```

```
s = mdb.models['Linear model'].ConstrainedSketch(name='__profile__',
    sheetSize=500, gridSpacing=10, transform=t)
g, v, d1, c = s.geometry, s.vertices, s.dimensions, s.constraints
s.setPrimaryObject(option=SUPERIMPOSE)
p.projectReferencesOntoSketch(sketch=s, filter=COPLANAR_EDGES)
s.Line(point1=(-bk/2, Ltot/2-Lcl), point2=(bk/2, Ltot/2-Lcl))
s.HorizontalConstraint(entity=g[18], addUndoState=False)
s.PerpendicularConstraint(entity1=g[3], entity2=g[18], addUndoState=False)
s.Line(point1=(-bo/2, (Ltot/2-Lcl-r)), point2=(bo/2, (Ltot/2-Lcl-r)))
s.HorizontalConstraint(entity=g[19], addUndoState=False)
s.PerpendicularConstraint(entity1=g[4], entity2=g[19], addUndoState=False)
s.Line(point1=(-bo/2, -(Ltot/2-Lcl-r)), point2=(bo/2, -(Ltot/2-Lcl-r)))
s.HorizontalConstraint(entity=g[20], addUndoState=False)
s.PerpendicularConstraint(entity1=g[6], entity2=g[20], addUndoState=False)
s.Line(point1=(-bk/2, -(Ltot/2-Lcl)), point2=(bk/2, -(Ltot/2-Lcl)))
s.HorizontalConstraint(entity=g[21], addUndoState=False)
s.TangentConstraint(entity1=g[7], entity2=g[21], addUndoState=False)
f = p.faces
pickedFaces = f.getSequenceFromMask(mask=('[#1 ]', ), )
e, d1 = p.edges, p.datums
p.PartitionFaceBySketch(sketchUpEdge=e[12], faces=pickedFaces, sketch=s)
s.unsetPrimaryObject()

# Define material properties
mdb.models['Linear model'].Material(name='Steel')
mdb.models['Linear model'].materials['Steel'].Density(table=((7.8e-9, ), ))
mdb.models['Linear model'].materials['Steel'].Elastic(table=((210000.0, 0.3), ))
mdb.models['Linear model'].materials['Steel'].Plastic(scaleStress=None, table=(
    (355.0, 0.0), (355.6, 0.0003), (361.2, 0.0153), (399.9, 0.0301), (438.2,
    0.0439), (469.2, 0.0578), (489.4, 0.0717), (504.5, 0.0846), (518.1, 0.0985), (
    531.4, 0.1115), (544.6, 0.1244), (558.0, 0.1373), (571.5, 0.1503)))

# Create a shell section
mdb.models['Linear model'].HomogeneousShellSection(name='Steel', preIntegrate=OFF,
    material='Steel', thicknessType=UNIFORM, thickness=ao, thicknessField='',
    nodalThicknessField='', idealization=NO_IDEALIZATION,
    poissonDefinition=DEFAULT, thicknessModulus=None, temperature=GRADIENT,
    useDensity=OFF, integrationRule=SIMPSON, numIntPts=5)

# Assign section to the part
faces = f.getSequenceFromMask(mask=('[#1f ]', ), )
region = p.Set(faces=faces, name='Set-1')
p.SectionAssignment(region=region, sectionName='Steel', offset=0.0,
    offsetType=MIDDLE_SURFACE, offsetField='',
    thicknessAssignment=FROM_SECTION)

# Create a root assembly
a = mdb.models['Linear model'].rootAssembly
a.DatumCsysByDefault(CARTESIAN)
a.Instance(name='Tensile member-1', part=p, dependent=ON)
# Create a buckling step
mdb.models['Linear model'].BuckleStep(name='LBA', previous='Initial', numEigen=6, vectors=12)

# Apply loads and boundary conditions
f1 = a.instances['Tensile member-1'].faces
faces1 = f1.getSequenceFromMask(mask=('[#2 ]', ), )
region = a.Set(faces=faces1, name='Set-1')
mdb.models['Linear model'].DisplacementBC(name='Bottom boundary',
    createStepName='LBA', region=region, u1=0.0, u2=0.0, u3=0.0, ur1=0.0,
    ur2=0.0, ur3=0.0, amplitude=UNSET, buckleCase=PERTURBATION_AND_BUCKLING,
```

```
    fixed=OFF, distributionType=UNIFORM, fieldName='', localCsys=None)
faces1 = f1.getSequenceFromMask(mask=('[#1 ]', ), )
region = a.Set(faces=faces1, name='Set-2')
mdb.models['Linear model'].DisplacementBC(name='Top boundary',
    createStepName='LBA', region=region, u1=0.0, u2=UNSET, u3=0.0, ur1=0.0,
    ur2=0.0, ur3=0.0, amplitude=UNSET, buckleCase=PERTURBATION_AND_BUCKLING,
    fixed=OFF, distributionType=UNIFORM, fieldName='', localCsys=None)
s1 = a.instances['Tensile member-1'].edges
side1Edges1 = s1.getSequenceFromMask(mask=('[#c ]', ), )
region = a.Surface(side1Edges=side1Edges1, name='Surf-1')
mdb.models['Linear model'].ShellEdgeLoad(name='Load', createStepName='LBA',
    region=region, magnitude=force, distributionType=UNIFORM, field='',
    localCsys=None)

# Generate mesh
p.seedPart(size=5.0, deviationFactor=0.1, minSizeFactor=0.1)
p.generateMesh()

# Adding keyword for buckling shape
mdb.models['Linear model'].keywordBlock.synchVersions(storeNodesAndElements=False)
mdb.models['Linear model'].keywordBlock.insert(41, """
*NODE FILE, GLOBAL=YES, LAST MODE=1
U""")

# Create different sets for post-processing
n = p.nodes
nodes = n.getSequenceFromMask(mask=('[#8 ]', ), )
p.Set(nodes=nodes, name='RF')
nodes = n.getSequenceFromMask(mask=('[#c000001c #1f ]', ), )
p.Set(nodes=nodes, name='Set-2')
nodes = n.getSequenceFromMask(mask=('[#5000 #0:6 #c0000000 #1 ]', ), )
p.Set(nodes=nodes, name='Set-3')

# Create and submit job for linear buckling
mdb.Job(name='LBA', model='Linear model', description='', type=ANALYSIS, atTime=None,
        waitMinutes=0, waitHours=0, queue=None, memory=90, memoryUnits=PERCENTAGE,
        getMemoryFromAnalysis=True, explicitPrecision=SINGLE, nodalOutputPrecision=SINGLE,
        echoPrint=OFF, modelPrint=OFF, contactPrint=OFF, historyPrint=OFF, userSubroutine='',
        scratch='', resultsFormat=ODB, numThreadsPerMpiProcess=1, multiprocessingMode=DEFAULT,
        numCpus=1, numGPUs=0).submit(consistencyChecking=OFF)
mdb.jobs['LBA'].waitForCompletion()

# Linear static analysis for verification of reaction force (RF2)
mdb.Model(name='Linear static', objectToCopy=mdb.models['Linear model'])
p = mdb.models['Linear static'].parts['Tensile member']
a = mdb.models['Linear static'].rootAssembly
mdb.models['Linear static'].StaticStep(name='LBA', previous='Initial',
    maintainAttributes=True)
mdb.models['Linear static'].keywordBlock.setValues(edited = 0)
mdb.models['Linear static'].keywordBlock.synchVersions(
    storeNodesAndElements=False)
mdb.models['Linear static'].steps.changeKey(fromName='LBA', toName='LSA')
mdb.Job(name='LSA', model='Linear static', description='', type=ANALYSIS,
    atTime=None, waitMinutes=0, waitHours=0, queue=None, memory=90,
    memoryUnits=PERCENTAGE, getMemoryFromAnalysis=True,
    explicitPrecision=SINGLE, nodalOutputPrecision=SINGLE, echoPrint=OFF,
    modelPrint=OFF, contactPrint=OFF, historyPrint=OFF, userSubroutine='',
    scratch='', resultsFormat=ODB, numThreadsPerMpiProcess=1,
    multiprocessingMode=DEFAULT, numCpus=1, numGPUs=0)
mdb.jobs['LSA'].submit(consistencyChecking=OFF)
```

```
mdb.jobs['LSA'].waitForCompletion()

# Create a new model for non-linear analysis
mdb.Model(name='Non-linear model', objectToCopy=mdb.models['Linear model'])

# Delete load and modify boundary condition for post-buckling
del mdb.models['Non-linear model'].loads['Load']
mdb.models['Non-linear model'].boundaryConditions['Top boundary'].setValues(
    u2=-1.0, buckleCase=PERTURBATION_AND_BUCKLING)

# Create a non-linear step
regionDef=mdb.models['Non-linear model'].rootAssembly.allInstances['Tensile member-1'].sets['RF']
mdb.models['Non-linear model'].StaticRiksStep(name='LBA', previous='Initial',
    maintainAttributes=True, nodeOn=ON, maximumDisplacement=-1.0,
    region=regionDef, dof=2, maxNumInc=100000, initialArcInc=0.01,
    minArcInc=1e-15, maxArcInc=0.01, nlgeom=ON)
mdb.models['Non-linear model'].steps.changeKey(fromName='LBA', toName='NBA')

# Specify history outputs
regionDef=mdb.models['Non-linear model'].rootAssembly.sets['Set-1']
mdb.models['Non-linear model'].HistoryOutputRequest(name='H-Output-1',
    createStepName='NBA', variables=('RF2', ), region=regionDef,
    sectionPoints=DEFAULT, rebar=EXCLUDE)
regionDef=mdb.models['Non-linear model'].rootAssembly.allInstances['Tensile member-1'].sets['RF']
mdb.models['Non-linear model'].HistoryOutputRequest(name='H-Output-2',
    createStepName='NBA', variables=('U2', ), region=regionDef,
    sectionPoints=DEFAULT, rebar=EXCLUDE)
regionDef=mdb.models['Non-linear model'].rootAssembly.allInstances['Tensile member-1'].sets['Set-2']
mdb.models['Non-linear model'].HistoryOutputRequest(name='H-Output-3',
    createStepName='NBA', variables=('U2', ), region=regionDef,
    sectionPoints=DEFAULT, rebar=EXCLUDE)
regionDef=mdb.models['Non-linear model'].rootAssembly.allInstances['Tensile member-1'].sets['Set-3']
mdb.models['Non-linear model'].HistoryOutputRequest(name='H-Output-4',
    createStepName='NBA', variables=('U3', ), region=regionDef,
    sectionPoints=DEFAULT, rebar=EXCLUDE)

# Introducing imperfections
mdb.models['Non-linear model'].keywordBlock.setValues(edited = 0)
mdb.models['Non-linear model'].keywordBlock.synchVersions(
    storeNodesAndElements=False)
mdb.models['Non-linear model'].keywordBlock.replace(31, """
** ----------------------------------------------------------------
**
** STEP: NBA
**
*IMPERFECTION, FILE= LBA, STEP=1
1, 0.4""")

# Create and submit job for non-linear analysis
mdb.Job(name='NBA', model='Non-linear model', description='', type=ANALYSIS,
    atTime=None, waitMinutes=0, waitHours=0, queue=None, memory=90,
    memoryUnits=PERCENTAGE, getMemoryFromAnalysis=True,
    explicitPrecision=SINGLE, nodalOutputPrecision=SINGLE, echoPrint=OFF,
    modelPrint=OFF, contactPrint=OFF, historyPrint=OFF, userSubroutine='',
    scratch='', resultsFormat=ODB, numThreadsPerMpiProcess=1,
    multiprocessingMode=DEFAULT, numCpus=1, numGPUs=0)
mdb.jobs['NBA'].submit(consistencyChecking=OFF)
```

J Input File: Static Analysis of Rod 2

```
from part import *
from material import *
from section import *
from assembly import *
from step import *
from load import *
from mesh import *
from job import *
from sketch import *
from visualization import *

# Rename model
mdb.models.changeKey(fromName='Model-1', toName='Linear model')

# Specimen properties
ao=4.0          # original thickness
bk=44.0         # width of the clamping area
bo=20.0         # original width of the parallel length
Lcl=35.0        # length of clamped area
Ltot=330.0      # total length of specimen
r=12.0          # transition radius
force=100.0     # reference load value

# Create a geometry
s = mdb.models['Linear model'].ConstrainedSketch(name='__profile__',
    sheetSize=200.0)
g, v, d, c = s.geometry, s.vertices, s.dimensions, s.constraints
s.setPrimaryObject(option=STANDALONE)
s.Line(point1=(0.0, 0.0), point2=(bk/2, 0.0))
s.HorizontalConstraint(entity=g[2], addUndoState=False)
s.Line(point1=(bk/2, 0.0), point2=(bk/2, -Lcl))
s.VerticalConstraint(entity=g[3], addUndoState=False)
s.Line(point1=(bk/2, -Lcl), point2=(bo/2, -Lcl))
s.HorizontalConstraint(entity=g[4], addUndoState=False)
s.Line(point1=(bo/2, -Lcl), point2=(bo/2, -Ltot/2))
s.VerticalConstraint(entity=g[5], addUndoState=False)
s.FilletByRadius(radius=r, curve1=g[4], nearPoint1=(bk/2-0.1,
    -Lcl-0.1), curve2=g[5], nearPoint2=(bo/2+0.1,
    -Lcl-0.1))
s.Line(point1=(bo/2, -Ltot/2), point2=(0.0, -Ltot/2))
s.HorizontalConstraint(entity=g[7], addUndoState=False)
s.Line(point1=(0.0, -Ltot/2), point2=(0.0, 0.0))
s.VerticalConstraint(entity=g[8], addUndoState=False)
s.setAsConstruction(objectList=(g[8], ))
s.setAsConstruction(objectList=(g[7], ))
s.copyMirror(mirrorLine=g[8], objectList=(g[2], g[3], g[4], g[5], g[6]))
s.copyMirror(mirrorLine=g[7], objectList=(g[5], g[6], g[4], g[3], g[2], g[9],
    g[10], g[11], g[13], g[12]))
p = mdb.models['Linear model'].Part(name='Tensile member', dimensionality=THREE_D,
    type=DEFORMABLE_BODY)
p = mdb.models['Linear model'].parts['Tensile member']
p.BaseShell(sketch=s)
s.unsetPrimaryObject()

# Create partition
f, e, d = p.faces, p.edges, p.datums
t = p.MakeSketchTransform(sketchPlane=f[0], sketchUpEdge=e[12],
    sketchPlaneSide=SIDE1, origin=(0.0, -Ltot/2, 0.0))
```

```
s = mdb.models['Linear model'].ConstrainedSketch(name='__profile__',
    sheetSize=500, gridSpacing=10, transform=t)
g, v, d1, c = s.geometry, s.vertices, s.dimensions, s.constraints
s.setPrimaryObject(option=SUPERIMPOSE)
p.projectReferencesOntoSketch(sketch=s, filter=COPLANAR_EDGES)
s.Line(point1=(-bk/2, Ltot/2-Lcl), point2=(bk/2, Ltot/2-Lcl))
s.HorizontalConstraint(entity=g[18], addUndoState=False)
s.PerpendicularConstraint(entity1=g[3], entity2=g[18], addUndoState=False)
s.Line(point1=(-bo/2, (Ltot/2-Lcl-r)), point2=(bo/2, (Ltot/2-Lcl-r)))
s.HorizontalConstraint(entity=g[19], addUndoState=False)
s.PerpendicularConstraint(entity1=g[4], entity2=g[19], addUndoState=False)
s.Line(point1=(-bo/2, -(Ltot/2-Lcl-r)), point2=(bo/2, -(Ltot/2-Lcl-r)))
s.HorizontalConstraint(entity=g[20], addUndoState=False)
s.PerpendicularConstraint(entity1=g[6], entity2=g[20], addUndoState=False)
s.Line(point1=(-bk/2, -(Ltot/2-Lcl)), point2=(bk/2, -(Ltot/2-Lcl)))
s.HorizontalConstraint(entity=g[21], addUndoState=False)
s.TangentConstraint(entity1=g[7], entity2=g[21], addUndoState=False)
f = p.faces
pickedFaces = f.getSequenceFromMask(mask=('[#1 ]', ), )
e, d1 = p.edges, p.datums
p.PartitionFaceBySketch(sketchUpEdge=e[12], faces=pickedFaces, sketch=s)
s.unsetPrimaryObject()

# Define material properties
mdb.models['Linear model'].Material(name='Steel')
mdb.models['Linear model'].materials['Steel'].Density(table=((7.8e-9, ), ))
mdb.models['Linear model'].materials['Steel'].Elastic(table=((210000.0, 0.3), ))
mdb.models['Linear model'].materials['Steel'].Plastic(scaleStress=None, table=(
    (355.0, 0.0), (355.6, 0.0003), (361.2, 0.0153), (399.9, 0.0301), (438.2,
    0.0439), (469.2, 0.0578), (489.4, 0.0717), (504.5, 0.0846), (518.1, 0.0985), (
    531.4, 0.1115), (544.6, 0.1244), (558.0, 0.1373), (571.5, 0.1503)))

# Create a shell section
mdb.models['Linear model'].HomogeneousShellSection(name='Steel', preIntegrate=OFF,
    material='Steel', thicknessType=UNIFORM, thickness=ao, thicknessField='',
    nodalThicknessField='', idealization=NO_IDEALIZATION,
    poissonDefinition=DEFAULT, thicknessModulus=None, temperature=GRADIENT,
    useDensity=OFF, integrationRule=SIMPSON, numIntPts=5)

# Assign section to the part
faces = f.getSequenceFromMask(mask=('[#1f ]', ), )
region = p.Set(faces=faces, name='Set-1')
p.SectionAssignment(region=region, sectionName='Steel', offset=0.0,
    offsetType=MIDDLE_SURFACE, offsetField='',
    thicknessAssignment=FROM_SECTION)

# Create a root assembly
a = mdb.models['Linear model'].rootAssembly
a.DatumCsysByDefault(CARTESIAN)
a.Instance(name='Tensile member-1', part=p, dependent=ON)

# Create a buckling step
mdb.models['Linear model'].BuckleStep(name='LBA', previous='Initial', numEigen=6, vectors=12)

# Apply loads and boundary conditions
f1 = a.instances['Tensile member-1'].faces
faces1 = f1.getSequenceFromMask(mask=('[#2 ]', ), )
region = a.Set(faces=faces1, name='Set-1')
mdb.models['Linear model'].DisplacementBC(name='Bottom boundary',
    createStepName='LBA', region=region, u1=0.0, u2=0.0, u3=0.0, ur1=0.0,
```

```
    ur2=0.0, ur3=0.0, amplitude=UNSET, buckleCase=PERTURBATION_AND_BUCKLING,
    fixed=OFF, distributionType=UNIFORM, fieldName='', localCsys=None)
faces1 = f1.getSequenceFromMask(mask=('[#1 ]', ), )
region = a.Set(faces=faces1, name='Set-2')
mdb.models['Linear model'].DisplacementBC(name='Top boundary',
    createStepName='LBA', region=region, u1=0.0, u2=UNSET, u3=0.0, ur1=0.0,
    ur2=0.0, ur3=0.0, amplitude=UNSET, buckleCase=PERTURBATION_AND_BUCKLING,
    fixed=OFF, distributionType=UNIFORM, fieldName='', localCsys=None)
s1 = a.instances['Tensile member-1'].edges
side1Edges1 = s1.getSequenceFromMask(mask=('[#c ]', ), )
region = a.Surface(side1Edges=side1Edges1, name='Surf-1')
mdb.models['Linear model'].ShellEdgeLoad(name='Load', createStepName='LBA',
    region=region, magnitude=force, distributionType=UNIFORM, field='',
    localCsys=None)

# Generate mesh
p.seedPart(size=5.0, deviationFactor=0.1, minSizeFactor=0.1)
p.generateMesh()

# Adding keyword for buckling shape
mdb.models['Linear model'].keywordBlock.synchVersions(storeNodesAndElements=False)
mdb.models['Linear model'].keywordBlock.insert(41, """
*NODE FILE, GLOBAL=YES, LAST MODE=1
U""")

# Create different sets for post-processing
n = p.nodes
nodes = n.getSequenceFromMask(mask=('[#8 ]', ), )
p.Set(nodes=nodes, name='RF')
nodes = n.getSequenceFromMask(mask=('[#c000001c #1f ]', ), )
p.Set(nodes=nodes, name='Set-2')
nodes = n.getSequenceFromMask(mask=('[#5000 #0:9 #e000000 ]', ), )
p.Set(nodes=nodes, name='Set-3')

# Create and submit job for linear buckling
mdb.Job(name='LBA', model='Linear model', description='', type=ANALYSIS, atTime=None,
        waitMinutes=0, waitHours=0, queue=None, memory=90, memoryUnits=PERCENTAGE,
        getMemoryFromAnalysis=True, explicitPrecision=SINGLE, nodalOutputPrecision=SINGLE,
        echoPrint=OFF, modelPrint=OFF, contactPrint=OFF, historyPrint=OFF, userSubroutine='',
        scratch='', resultsFormat=ODB, numThreadsPerMpiProcess=1, multiprocessingMode=DEFAULT,
        numCpus=1, numGPUs=0).submit(consistencyChecking=OFF)
mdb.jobs['LBA'].waitForCompletion()

# Linear static analysis for verification of reaction force (RF2)
mdb.Model(name='Linear static', objectToCopy=mdb.models['Linear model'])
p = mdb.models['Linear static'].parts['Tensile member']
a = mdb.models['Linear static'].rootAssembly
mdb.models['Linear static'].StaticStep(name='LBA', previous='Initial',
    maintainAttributes=True)
mdb.models['Linear static'].keywordBlock.setValues(edited = 0)
mdb.models['Linear static'].keywordBlock.synchVersions(
    storeNodesAndElements=False)
mdb.models['Linear static'].steps.changeKey(fromName='LBA', toName='LSA')
mdb.Job(name='LSA', model='Linear static', description='', type=ANALYSIS,
    atTime=None, waitMinutes=0, waitHours=0, queue=None, memory=90,
    memoryUnits=PERCENTAGE, getMemoryFromAnalysis=True,
    explicitPrecision=SINGLE, nodalOutputPrecision=SINGLE, echoPrint=OFF,
    modelPrint=OFF, contactPrint=OFF, historyPrint=OFF, userSubroutine='',
    scratch='', resultsFormat=ODB, numThreadsPerMpiProcess=1,
    multiprocessingMode=DEFAULT, numCpus=1, numGPUs=0)
```

```
mdb.jobs['LSA'].submit(consistencyChecking=OFF)
mdb.jobs['LSA'].waitForCompletion()

# Create a new model for non-linear analysis
mdb.Model(name='Non-linear model', objectToCopy=mdb.models['Linear model'])

# Delete load and modify boundary conditions for post-buckling
del mdb.models['Non-linear model'].loads['Load']
mdb.models['Non-linear model'].boundaryConditions['Top boundary'].setValues(
    u2=-1.0, buckleCase=PERTURBATION_AND_BUCKLING)

# Create a non-linear step
regionDef=mdb.models['Non-linear model'].rootAssembly.allInstances['Tensile member-1'].sets['RF']
mdb.models['Non-linear model'].StaticRiksStep(name='LBA', previous='Initial',
    maintainAttributes=True, nodeOn=ON, maximumDisplacement=-1.0,
    region=regionDef, dof=2, maxNumInc=100000, initialArcInc=0.01,
    minArcInc=1e-15, maxArcInc=0.01, nlgeom=ON)
mdb.models['Non-linear model'].steps.changeKey(fromName='LBA', toName='NBA')

# Specify history outputs
regionDef=mdb.models['Non-linear model'].rootAssembly.sets['Set-1']
mdb.models['Non-linear model'].HistoryOutputRequest(name='H-Output-1',
    createStepName='NBA', variables=('RF2', ), region=regionDef,
    sectionPoints=DEFAULT, rebar=EXCLUDE)
regionDef=mdb.models['Non-linear model'].rootAssembly.allInstances['Tensile member-1'].sets['RF']
mdb.models['Non-linear model'].HistoryOutputRequest(name='H-Output-2',
    createStepName='NBA', variables=('U2', ), region=regionDef,
    sectionPoints=DEFAULT, rebar=EXCLUDE)
regionDef=mdb.models['Non-linear model'].rootAssembly.allInstances['Tensile member-1'].sets['Set-2']
mdb.models['Non-linear model'].HistoryOutputRequest(name='H-Output-3',
    createStepName='NBA', variables=('U2', ), region=regionDef,
    sectionPoints=DEFAULT, rebar=EXCLUDE)
regionDef=mdb.models['Non-linear model'].rootAssembly.allInstances['Tensile member-1'].sets['Set-3']
mdb.models['Non-linear model'].HistoryOutputRequest(name='H-Output-4',
    createStepName='NBA', variables=('U3', ), region=regionDef,
    sectionPoints=DEFAULT, rebar=EXCLUDE)

# Introducing imperfections
mdb.models['Non-linear model'].keywordBlock.setValues(edited = 0)
mdb.models['Non-linear model'].keywordBlock.synchVersions(
    storeNodesAndElements=False)
mdb.models['Non-linear model'].keywordBlock.replace(31, """
** ----------------------------------------------------------------
**
** STEP: NBA
**
*IMPERFECTION, FILE= LBA, STEP=1
1, 0.4""")

# Create and submit job for non-linear analysis
mdb.Job(name='NBA', model='Non-linear model', description='', type=ANALYSIS,
    atTime=None, waitMinutes=0, waitHours=0, queue=None, memory=90,
    memoryUnits=PERCENTAGE, getMemoryFromAnalysis=True,
    explicitPrecision=SINGLE, nodalOutputPrecision=SINGLE, echoPrint=OFF,
    modelPrint=OFF, contactPrint=OFF, historyPrint=OFF, userSubroutine='',
    scratch='', resultsFormat=ODB, numThreadsPerMpiProcess=1,
    multiprocessingMode=DEFAULT, numCpus=1, numGPUs=0)
mdb.jobs['NBA'].submit(consistencyChecking=OFF)
```

K Input File: Single Tensile Element

```
from abaqus import *
from abaqusConstants import *
from caeModules import *
from driverUtils import executeOnCaeStartup
executeOnCaeStartup()

# Create a geometry
s = mdb.models['Model-1'].ConstrainedSketch(name='__profile__',
    sheetSize=200.0)
g, v, d, c = s.geometry, s.vertices, s.dimensions, s.constraints
s.setPrimaryObject(option=STANDALONE)
s.Line(point1=(0.0, 0.0), point2=(0.0, 100.0))
s.VerticalConstraint(entity=g[2], addUndoState=False)
s.Line(point1=(0.0, 100.0), point2=(100.0, 100.0))
s.HorizontalConstraint(entity=g[3], addUndoState=False)
s.PerpendicularConstraint(entity1=g[2], entity2=g[3], addUndoState=False)
s.Line(point1=(100.0, 100.0), point2=(100.0, 0.0))
s.VerticalConstraint(entity=g[4], addUndoState=False)
s.PerpendicularConstraint(entity1=g[3], entity2=g[4], addUndoState=False)
s.Line(point1=(100.0, 0.0), point2=(0.0, 0.0))
s.HorizontalConstraint(entity=g[5], addUndoState=False)
s.PerpendicularConstraint(entity1=g[4], entity2=g[5], addUndoState=False)
p = mdb.models['Model-1'].Part(name='Single tensile element',
    dimensionality=THREE_D, type=DEFORMABLE_BODY)
p = mdb.models['Model-1'].parts['Single tensile element']
p.BaseShell(sketch=s)
s.unsetPrimaryObject()

# Define material properties
mdb.models['Model-1'].Material(name='S355')
mdb.models['Model-1'].materials['S355'].Density(table=((7.8e-09, ), ))
mdb.models['Model-1'].materials['S355'].Elastic(table=((210000.0, 0.3), ))
mdb.models['Model-1'].materials['S355'].Plastic(scaleStress=None, table=((
    355.0, 0.0), (355.6, 0.0003), (361.2, 0.0153), (399.9, 0.0301), (438.2,
    0.0439), (469.2, 0.0578), (489.4, 0.0717), (504.5, 0.0846), (518.1,
    0.0985), (531.4, 0.1115), (544.6, 0.1244), (558.0, 0.1373), (571.5,
    0.1503)))
mdb.models['Model-1'].materials['S355'].plastic.RateDependent(table=((4795.23,
    4.07), ))

# Create a shell section
mdb.models['Model-1'].HomogeneousShellSection(name='Shell section',
    preIntegrate=OFF, material='S355', thicknessType=UNIFORM, thickness=4.0,
    thicknessField='', nodalThicknessField='', idealization=NO_IDEALIZATION,
    poissonDefinition=DEFAULT, thicknessModulus=None, temperature=GRADIENT,
    useDensity=OFF, integrationRule=SIMPSON, numIntPts=5)

# Assign section to the part
p = mdb.models['Model-1'].parts['Single tensile element']
f = p.faces
faces = f.getSequenceFromMask(mask=('[#1 ]', ), )
region = p.Set(faces=faces, name='Set-1')
p.SectionAssignment(region=region, sectionName='Shell section', offset=0.0,
    offsetType=MIDDLE_SURFACE, offsetField='',
    thicknessAssignment=FROM_SECTION)
```

```
# Create a root assembly
a = mdb.models['Model-1'].rootAssembly
a.DatumCsysByDefault(CARTESIAN)
p = mdb.models['Model-1'].parts['Single tensile element']
a.Instance(name='Single tensile element-1', part=p, dependent=OFF)

# Create dynamic implicit step
mdb.models['Model-1'].ImplicitDynamicsStep(name='DI', previous='Initial',
    timePeriod=10000.0, maxNumInc=100000000, initialInc=10.0, minInc=0.1,
    maxInc=10.0, nlgeom=ON)

# Create field output
mdb.models['Model-1'].fieldOutputRequests['F-Output-1'].setValues(variables=(
    'S', 'PE', 'PEEQ', 'PEMAG', 'LE', 'U', 'RF'), frequency=1)

# Apply loads and boundary conditions
a = mdb.models['Model-1'].rootAssembly
e1 = a.instances['Single tensile element-1'].edges
edges1 = e1.getSequenceFromMask(mask=('[#1 ]', ), )
region = a.Set(edges=edges1, name='Set-1')
mdb.models['Model-1'].EncastreBC(name='Bottom boundary',
    createStepName='Initial', region=region, localCsys=None)
edges1 = e1.getSequenceFromMask(mask=('[#4 ]', ), )
region = a.Set(edges=edges1, name='Set-2')
mdb.models['Model-1'].VelocityBC(name='Top boundary', createStepName='Initial',
    region=region, v1=0.0, v2=UNSET, v3=0.0, vr1=0.0, vr2=0.0, vr3=0.0,
    amplitude=UNSET, localCsys=None, distributionType=UNIFORM, fieldName='')
mdb.models['Model-1'].SmoothStepAmplitude(name='Smooth', timeSpan=STEP, data=((
    0.0, 0.0), (250.0, 1.0), (10000.0, 1.0)))
mdb.models['Model-1'].boundaryConditions['Top boundary'].setValuesInStep(
    stepName='DI', v2=0.001, amplitude='Smooth')

# Generate mesh
a = mdb.models['Model-1'].rootAssembly
partInstances =(a.instances['Single tensile element-1'], )
a.seedPartInstance(regions=partInstances, size=100.0, deviationFactor=0.1,
    minSizeFactor=0.1)
a.generateMesh(regions=partInstances)
elemType1 = mesh.ElemType(elemCode=S4R, elemLibrary=STANDARD,
    secondOrderAccuracy=OFF, hourglassControl=DEFAULT)
elemType2 = mesh.ElemType(elemCode=S3, elemLibrary=STANDARD)
f1 = a.instances['Single tensile element-1'].faces
faces1 = f1.getSequenceFromMask(mask=('[#1 ]', ), )
pickedRegions =(faces1, )
a.setElementType(regions=pickedRegions, elemTypes=(elemType1, elemType2))

# Create and submit job
mdb.Job(name='DI', model='Model-1', description='', type=ANALYSIS,
    atTime=None, waitMinutes=0, waitHours=0, queue=None, memory=90,
    memoryUnits=PERCENTAGE, getMemoryFromAnalysis=True,
    explicitPrecision=SINGLE, nodalOutputPrecision=SINGLE, echoPrint=OFF,
    modelPrint=OFF, contactPrint=OFF, historyPrint=OFF, userSubroutine='',
    scratch='', resultsFormat=ODB, numThreadsPerMpiProcess=1,
    multiprocessingMode=DEFAULT, numCpus=2, numDomains=4, numGPUs=0)
mdb.jobs['DI'].submit(consistencyChecking=OFF)
```

L Input File: Dynamic Analysis of Rod 1

```
from part import *
from material import *
from section import *
from assembly import *
from step import *
from load import *
from mesh import *
from job import *
from sketch import *
from visualization import *
import regionToolset

# Rename model
mdb.models.changeKey(fromName='Model-1', toName='Linear model')

# Specimen properties
ao=3.9          # original thickness
bk=44.0         # width of the clamping area
bo=20.0         # original width of the parallel length
Lcl=60.0        # length of clamped area
Ltot=250.0      # total length of specimen
r=12.0          # transition radius
force=100.0     # reference load value

# Create a constrained sketch
s = mdb.models['Linear model'].ConstrainedSketch(name='__profile__',
    sheetSize=200.0)
g, v, d, c = s.geometry, s.vertices, s.dimensions, s.constraints
s.setPrimaryObject(option=STANDALONE)
s.Line(point1=(0.0, 0.0), point2=(bk/2, 0.0))
s.HorizontalConstraint(entity=g[2], addUndoState=False)
s.Line(point1=(bk/2, 0.0), point2=(bk/2, -Lcl))
s.VerticalConstraint(entity=g[3], addUndoState=False)
s.Line(point1=(bk/2, -Lcl), point2=(bo/2, -Lcl))
s.HorizontalConstraint(entity=g[4], addUndoState=False)
s.Line(point1=(bo/2, -Lcl), point2=(bo/2, -Ltot/2))
s.VerticalConstraint(entity=g[5], addUndoState=False)
s.FilletByRadius(radius=r, curve1=g[4], nearPoint1=(bk/2-0.1,
    -Lcl-0.1), curve2=g[5], nearPoint2=(bo/2+0.1,
    -Lcl-0.1))
s.Line(point1=(bo/2, -Ltot/2), point2=(0.0, -Ltot/2))
s.HorizontalConstraint(entity=g[7], addUndoState=False)
s.Line(point1=(0.0, -Ltot/2), point2=(0.0, 0.0))
s.VerticalConstraint(entity=g[8], addUndoState=False)
s.setAsConstruction(objectList=(g[8], ))
s.setAsConstruction(objectList=(g[7], ))
s.copyMirror(mirrorLine=g[8], objectList=(g[2], g[3], g[4], g[5], g[6]))
s.copyMirror(mirrorLine=g[7], objectList=(g[5], g[6], g[4], g[3], g[2], g[9],
    g[10], g[11], g[13], g[12]))
p = mdb.models['Linear model'].Part(name='Tensile member', dimensionality=THREE_D,
    type=DEFORMABLE_BODY)
p = mdb.models['Linear model'].parts['Tensile member']
p.BaseShell(sketch=s)
s.unsetPrimaryObject()

# Create partition
f, e, d = p.faces, p.edges, p.datums
t = p.MakeSketchTransform(sketchPlane=f[0], sketchUpEdge=e[12],
    sketchPlaneSide=SIDE1, origin=(0.0, -Ltot/2, 0.0))
```

```
s = mdb.models['Linear model'].ConstrainedSketch(name='__profile__',
    sheetSize=500, gridSpacing=10, transform=t)
g, v, d1, c = s.geometry, s.vertices, s.dimensions, s.constraints
s.setPrimaryObject(option=SUPERIMPOSE)
p = mdb.models['Linear model'].parts['Tensile member']
p.projectReferencesOntoSketch(sketch=s, filter=COPLANAR_EDGES)
s.Line(point1=(-bk/2, Ltot/2-Lcl), point2=(bk/2, Ltot/2-Lcl))
s.HorizontalConstraint(entity=g[18], addUndoState=False)
s.PerpendicularConstraint(entity1=g[3], entity2=g[18], addUndoState=False)
s.Line(point1=(-bo/2, (Ltot/2-Lcl-r)), point2=(bo/2, (Ltot/2-Lcl-r)))
s.HorizontalConstraint(entity=g[19], addUndoState=False)
s.PerpendicularConstraint(entity1=g[4], entity2=g[19], addUndoState=False)
s.Line(point1=(-bo/2, -(Ltot/2-Lcl-r)), point2=(bo/2, -(Ltot/2-Lcl-r)))
s.HorizontalConstraint(entity=g[20], addUndoState=False)
s.PerpendicularConstraint(entity1=g[6], entity2=g[20], addUndoState=False)
s.Line(point1=(-bk/2, -(Ltot/2-Lcl)), point2=(bk/2, -(Ltot/2-Lcl)))
s.HorizontalConstraint(entity=g[21], addUndoState=False)
s.TangentConstraint(entity1=g[7], entity2=g[21], addUndoState=False)
p = mdb.models['Linear model'].parts['Tensile member']
f = p.faces
pickedFaces = f.getSequenceFromMask(mask=('[#1 ]', ), )
e, d1 = p.edges, p.datums
p.PartitionFaceBySketch(sketchUpEdge=e[12], faces=pickedFaces, sketch=s)
s.unsetPrimaryObject()

# Define material properties
mdb.models['Linear model'].Material(name='Steel')
mdb.models['Linear model'].materials['Steel'].Density(table=((7.8e-9, ), ))
mdb.models['Linear model'].materials['Steel'].Elastic(table=((205000.0, 0.3), ))

# Create a shell section
mdb.models['Linear model'].HomogeneousShellSection(name='Steel', preIntegrate=OFF,
    material='Steel', thicknessType=UNIFORM, thickness=ao, thicknessField='',
    nodalThicknessField='', idealization=NO_IDEALIZATION,
    poissonDefinition=DEFAULT, thicknessModulus=None, temperature=GRADIENT,
    useDensity=OFF, integrationRule=SIMPSON, numIntPts=5)

# Assign section to the part
p = mdb.models['Linear model'].parts['Tensile member']
f = p.faces
faces = f.getSequenceFromMask(mask=('[#1f ]', ), )
region = p.Set(faces=faces, name='Set-1')
p.SectionAssignment(region=region, sectionName='Steel', offset=0.0,
    offsetType=MIDDLE_SURFACE, offsetField='',
    thicknessAssignment=FROM_SECTION)

# Create a root assembly
a = mdb.models['Linear model'].rootAssembly
a.DatumCsysByDefault(CARTESIAN)
p = mdb.models['Linear model'].parts['Tensile member']
a.Instance(name='Tensile member-1', part=p, dependent=ON)

# Create a buckling step
mdb.models['Linear model'].BuckleStep(name='LBA', previous='Initial', numEigen=6, vectors=12)

# Apply loads and boundary conditions
f1 = a.instances['Tensile member-1'].faces
faces1 = f1.getSequenceFromMask(mask=('[#2 ]', ), )
region = a.Set(faces=faces1, name='Set-1')
mdb.models['Linear model'].DisplacementBC(name='Bottom boundary',
```

```
    createStepName='LBA', region=region, u1=0.0, u2=0.0, u3=0.0, ur1=0.0,
    ur2=0.0, ur3=0.0, amplitude=UNSET, buckleCase=PERTURBATION_AND_BUCKLING,
    fixed=OFF, distributionType=UNIFORM, fieldName='', localCsys=None)
faces1 = f1.getSequenceFromMask(mask=('[#1 ]', ), )
region = a.Set(faces=faces1, name='Set-2')
mdb.models['Linear model'].DisplacementBC(name='Top boundary',
    createStepName='LBA', region=region, u1=0.0, u2=UNSET, u3=0.0, ur1=0.0,
    ur2=0.0, ur3=0.0, amplitude=UNSET, buckleCase=PERTURBATION_AND_BUCKLING,
    fixed=OFF, distributionType=UNIFORM, fieldName='', localCsys=None)
s1 = a.instances['Tensile member-1'].edges
side1Edges1 = s1.getSequenceFromMask(mask=('[#c ]', ), )
region = a.Surface(side1Edges=side1Edges1, name='Surf-1')
mdb.models['Linear model'].ShellEdgeLoad(name='Load', createStepName='LBA',
    region=region, magnitude=force, distributionType=UNIFORM, field='',
    localCsys=None)

# Generate mesh
p.seedPart(size=5.0, deviationFactor=0.1, minSizeFactor=0.1)
p.generateMesh()

# Adding keyword for buckling shape
mdb.models['Linear model'].keywordBlock.synchVersions(storeNodesAndElements=False)
mdb.models['Linear model'].keywordBlock.insert(40, """
*NODE FILE, GLOBAL=YES, LAST MODE=1
U""")

# Create different sets for post-processing
v = p.vertices
verts = v.getSequenceFromMask(mask=('[#4 ]', ), )
p.Set(vertices=verts, name='Set-2')
n = p.nodes
nodes = n.getSequenceFromMask(mask=('[#5000 #0:10 #1c ]', ), )
p.Set(nodes=nodes, name='Set-3')
v, e, d, n = p.vertices, p.edges, p.datums, p.nodes
p.ReferencePoint(point=v[15])

# Create and submit job for linear buckling
mdb.Job(name='LBA', model='Linear model', description='', type=ANALYSIS, atTime=None,
        waitMinutes=0, waitHours=0, queue=None, memory=90, memoryUnits=PERCENTAGE,
        getMemoryFromAnalysis=True, explicitPrecision=SINGLE, nodalOutputPrecision=SINGLE,
        echoPrint=OFF, modelPrint=OFF, contactPrint=OFF, historyPrint=OFF, userSubroutine='',
        scratch='', resultsFormat=ODB, numThreadsPerMpiProcess=1, multiprocessingMode=DEFAULT,
        numCpus=1, numGPUs=0).submit(consistencyChecking=OFF)
mdb.jobs['LBA'].waitForCompletion()

# Create a new model for dynamic explicit analysis
mdb.Model(name='DE', objectToCopy=mdb.models['Linear model'])

# Define additional plasticity and CS-model parameters
mdb.models['DE'].materials['Steel'].Plastic(scaleStress=None, table=((410.9,
    0.0), (416.1, 0.0028), (417.7, 0.004), (419.2, 0.0052), (421.1, 0.0068), (
    439.5, 0.0172), (456.3, 0.0275), (470.5, 0.0378), (482.3, 0.0481), (492.5,
    0.0584), (502.3, 0.0691), (511.3, 0.0803), (519.0, 0.0908), (526.5,
    0.1012), (533.2, 0.1118), (539.5, 0.1224), (546.1, 0.1337), (548.3,
    0.1374)))
mdb.models['DE'].materials['Steel'].plastic.RateDependent(table=((1094,
    3.47), ))

# Create dynamic explicit step
mdb.models['DE'].ExplicitDynamicsStep(name='LBA', previous='Initial',
```

```
    maintainAttributes=True, timePeriod=0.05128, improvedDtMethod=ON)
mdb.models['DE'].steps.changeKey(fromName='LBA', toName='DE')

# Delete load and modify boundary conditions
del mdb.models['DE'].loads['Load']
del mdb.models['DE'].boundaryConditions['Top boundary']
del mdb.models['DE'].boundaryConditions['Bottom boundary']
a = mdb.models['DE'].rootAssembly
f1 = a.instances['Tensile member-1'].faces
faces1 = f1.getSequenceFromMask(mask=('[#1 ]', ), )
region = regionToolset.Region(faces=faces1)
mdb.models['DE'].VelocityBC(name='Top BC', createStepName='Initial',
    region=region, v1=0.0, v2=UNSET, v3=0.0, vr1=0.0, vr2=0.0, vr3=0.0,
    amplitude=UNSET, localCsys=None, distributionType=UNIFORM, fieldName='')
mdb.models['DE'].SmoothStepAmplitude(name='Smooth', timeSpan=STEP, data=((0.0,
    0.0), (0.001282, 1.0), (0.05128, 1.0)))
mdb.models['DE'].boundaryConditions['Top BC'].setValuesInStep(stepName='DE',
    v2=-195.0, amplitude='Smooth')
faces1 = f1.getSequenceFromMask(mask=('[#2 ]', ), )
region = regionToolset.Region(faces=faces1)
mdb.models['DE'].DisplacementBC(name='Bottom BC', createStepName='Initial',
    region=region, u1=SET, u2=SET, u3=SET, ur1=SET, ur2=SET, ur3=SET,
    amplitude=UNSET, distributionType=UNIFORM, fieldName='', localCsys=None)

# Specify history outputs
regionDef=mdb.models['DE'].rootAssembly.sets['Set-1']
mdb.models['DE'].historyOutputRequests['H-Output-1'].setValues(variables=(
    'RF2', ), numIntervals=800, region=regionDef, sectionPoints=DEFAULT,
    rebar=EXCLUDE)
regionDef=mdb.models['DE'].rootAssembly.allInstances['Tensile member-1'].sets['Set-2']
mdb.models['DE'].HistoryOutputRequest(name='H-Output-2', createStepName='DE',
    variables=('U2', ), numIntervals=800, region=regionDef,
    sectionPoints=DEFAULT, rebar=EXCLUDE)
regionDef=mdb.models['DE'].rootAssembly.allInstances['Tensile member-1'].sets['Set-3']
mdb.models['DE'].HistoryOutputRequest(name='H-Output-3', createStepName='DE',
    variables=('U3', ), numIntervals=800, region=regionDef,
    sectionPoints=DEFAULT, rebar=EXCLUDE)

# Introducing imperfections
mdb.models['DE'].keywordBlock.setValues(edited = 0)
mdb.models['DE'].keywordBlock.synchVersions(storeNodesAndElements=False)
mdb.models['DE'].keywordBlock.replace(42, """
** ----------------------------------------------------------------
**
** STEP: DE
**
*IMPERFECTION, FILE= LBA, STEP=1
1, 0.05""")

# Create and submit job for dynamic analyses
mdb.Job(name='DE', model='DE', description='', type=ANALYSIS, atTime=None,
    waitMinutes=0, waitHours=0, queue=None, memory=90, memoryUnits=PERCENTAGE,
    explicitPrecision=DOUBLE_PLUS_PACK, nodalOutputPrecision=SINGLE,
    echoPrint=OFF, modelPrint=OFF, contactPrint=OFF, historyPrint=OFF,
    userSubroutine='', scratch='', resultsFormat=ODB, numDomains=4,
    activateLoadBalancing=False, numThreadsPerMpiProcess=1,
    multiprocessingMode=DEFAULT, numCpus=4)
mdb.jobs['DE'].submit(consistencyChecking=OFF)
```

M Input File: Dynamic Analysis of Rod 2

```
from part import *
from material import *
from section import *
from assembly import *
from step import *
from load import *
from mesh import *
from job import *
from sketch import *
from visualization import *
import regionToolset

# Rename model
mdb.models.changeKey(fromName='Model-1', toName='Linear model')

# Specimen properties
ao=3.9          # original thickness
bk=44.0         # width of the clamping area
bo=20.0         # original width of the parallel length
Lcl=60.0        # lenght of clamped area
Ltot=380.0      # total length of specimen
r=12.0          # transition radius
force=100.0     # reference load value

# Create a constrained sketch
s = mdb.models['Linear model'].ConstrainedSketch(name='__profile__',
    sheetSize=200.0)
g, v, d, c = s.geometry, s.vertices, s.dimensions, s.constraints
s.setPrimaryObject(option=STANDALONE)
s.Line(point1=(0.0, 0.0), point2=(bk/2, 0.0))
s.HorizontalConstraint(entity=g[2], addUndoState=False)
s.Line(point1=(bk/2, 0.0), point2=(bk/2, -Lcl))
s.VerticalConstraint(entity=g[3], addUndoState=False)
s.Line(point1=(bk/2, -Lcl), point2=(bo/2, -Lcl))
s.HorizontalConstraint(entity=g[4], addUndoState=False)
s.Line(point1=(bo/2, -Lcl), point2=(bo/2, -Ltot/2))
s.VerticalConstraint(entity=g[5], addUndoState=False)
s.FilletByRadius(radius=r, curve1=g[4], nearPoint1=(bk/2-0.1,
    -Lcl-0.1), curve2=g[5], nearPoint2=(bo/2+0.1,
    -Lcl-0.1))
s.Line(point1=(bo/2, -Ltot/2), point2=(0.0, -Ltot/2))
s.HorizontalConstraint(entity=g[7], addUndoState=False)
s.Line(point1=(0.0, -Ltot/2), point2=(0.0, 0.0))
s.VerticalConstraint(entity=g[8], addUndoState=False)
s.setAsConstruction(objectList=(g[8], ))
s.setAsConstruction(objectList=(g[7], ))
s.copyMirror(mirrorLine=g[8], objectList=(g[2], g[3], g[4], g[5], g[6]))
s.copyMirror(mirrorLine=g[7], objectList=(g[5], g[6], g[4], g[3], g[2], g[9],
    g[10], g[11], g[13], g[12]))
p = mdb.models['Linear model'].Part(name='Tensile member', dimensionality=THREE_D,
    type=DEFORMABLE_BODY)
p = mdb.models['Linear model'].parts['Tensile member']
p.BaseShell(sketch=s)
s.unsetPrimaryObject()

# Create partition
f, e, d = p.faces, p.edges, p.datums
t = p.MakeSketchTransform(sketchPlane=f[0], sketchUpEdge=e[12],
    sketchPlaneSide=SIDE1, origin=(0.0, -Ltot/2, 0.0))
```

```
s = mdb.models['Linear model'].ConstrainedSketch(name='__profile__',
    sheetSize=500, gridSpacing=10, transform=t)
g, v, d1, c = s.geometry, s.vertices, s.dimensions, s.constraints
s.setPrimaryObject(option=SUPERIMPOSE)
p = mdb.models['Linear model'].parts['Tensile member']
p.projectReferencesOntoSketch(sketch=s, filter=COPLANAR_EDGES)
s.Line(point1=(-bk/2, Ltot/2-Lcl), point2=(bk/2, Ltot/2-Lcl))
s.HorizontalConstraint(entity=g[18], addUndoState=False)
s.PerpendicularConstraint(entity1=g[3], entity2=g[18], addUndoState=False)
s.Line(point1=(-bo/2, (Ltot/2-Lcl-r)), point2=(bo/2, (Ltot/2-Lcl-r)))
s.HorizontalConstraint(entity=g[19], addUndoState=False)
s.PerpendicularConstraint(entity1=g[4], entity2=g[19], addUndoState=False)
s.Line(point1=(-bo/2, -(Ltot/2-Lcl-r)), point2=(bo/2, -(Ltot/2-Lcl-r)))
s.HorizontalConstraint(entity=g[20], addUndoState=False)
s.PerpendicularConstraint(entity1=g[6], entity2=g[20], addUndoState=False)
s.Line(point1=(-bk/2, -(Ltot/2-Lcl)), point2=(bk/2, -(Ltot/2-Lcl)))
s.HorizontalConstraint(entity=g[21], addUndoState=False)
s.TangentConstraint(entity1=g[7], entity2=g[21], addUndoState=False)
p = mdb.models['Linear model'].parts['Tensile member']
f = p.faces
pickedFaces = f.getSequenceFromMask(mask=('[#1 ]', ), )
e, d1 = p.edges, p.datums
p.PartitionFaceBySketch(sketchUpEdge=e[12], faces=pickedFaces, sketch=s)
s.unsetPrimaryObject()

# Define material properties
mdb.models['Linear model'].Material(name='Steel')
mdb.models['Linear model'].materials['Steel'].Density(table=((7.8e-9, ), ))
mdb.models['Linear model'].materials['Steel'].Elastic(table=((205000.0, 0.3), ))

# Create a shell section
mdb.models['Linear model'].HomogeneousShellSection(name='Steel', preIntegrate=OFF,
    material='Steel', thicknessType=UNIFORM, thickness=ao, thicknessField='',
    nodalThicknessField='', idealization=NO_IDEALIZATION,
    poissonDefinition=DEFAULT, thicknessModulus=None, temperature=GRADIENT,
    useDensity=OFF, integrationRule=SIMPSON, numIntPts=5)

# Assign section to the part
p = mdb.models['Linear model'].parts['Tensile member']
f = p.faces
faces = f.getSequenceFromMask(mask=('[#1f ]', ), )
region = p.Set(faces=faces, name='Set-1')
p.SectionAssignment(region=region, sectionName='Steel', offset=0.0,
    offsetType=MIDDLE_SURFACE, offsetField='',
    thicknessAssignment=FROM_SECTION)

# Create a root assembly
a = mdb.models['Linear model'].rootAssembly
a.DatumCsysByDefault(CARTESIAN)
p = mdb.models['Linear model'].parts['Tensile member']
a.Instance(name='Tensile member-1', part=p, dependent=ON)

# Create a buckling step
mdb.models['Linear model'].BuckleStep(name='LBA', previous='Initial', numEigen=6, vectors=12)

# Apply loads and boundary conditions
f1 = a.instances['Tensile member-1'].faces
faces1 = f1.getSequenceFromMask(mask=('[#2 ]', ), )
region = a.Set(faces=faces1, name='Set-1')
mdb.models['Linear model'].DisplacementBC(name='Bottom boundary',
```

```
    createStepName='LBA', region=region, u1=0.0, u2=0.0, u3=0.0, ur1=0.0,
    ur2=0.0, ur3=0.0, amplitude=UNSET, buckleCase=PERTURBATION_AND_BUCKLING,
    fixed=OFF, distributionType=UNIFORM, fieldName='', localCsys=None)
faces1 = f1.getSequenceFromMask(mask=('[#1 ]', ), )
region = a.Set(faces=faces1, name='Set-2')
mdb.models['Linear model'].DisplacementBC(name='Top boundary',
    createStepName='LBA', region=region, u1=0.0, u2=UNSET, u3=0.0, ur1=0.0,
    ur2=0.0, ur3=0.0, amplitude=UNSET, buckleCase=PERTURBATION_AND_BUCKLING,
    fixed=OFF, distributionType=UNIFORM, fieldName='', localCsys=None)
s1 = a.instances['Tensile member-1'].edges
side1Edges1 = s1.getSequenceFromMask(mask=('[#c ]', ), )
region = a.Surface(side1Edges=side1Edges1, name='Surf-1')
mdb.models['Linear model'].ShellEdgeLoad(name='Load', createStepName='LBA',
    region=region, magnitude=force, distributionType=UNIFORM, field='',
    localCsys=None)

# Generate mesh
p.seedPart(size=5.0, deviationFactor=0.1, minSizeFactor=0.1)
p.generateMesh()

# Adding keyword for buckling shape
mdb.models['Linear model'].keywordBlock.synchVersions(storeNodesAndElements=False)
mdb.models['Linear model'].keywordBlock.insert(40, """
*NODE FILE, GLOBAL=YES, LAST MODE=1
U""")

# Create different sets for post-proccessing
v = p.vertices
verts = v.getSequenceFromMask(mask=('[#4 ]', ), )
p.Set(vertices=verts, name='Set-2')
n = p.nodes
nodes = n.getSequenceFromMask(mask=('[#5000 #0:12 #e0000000 ]', ), )
p.Set(nodes=nodes, name='Set-3')
v, e, d, n = p.vertices, p.edges, p.datums, p.nodes
p.ReferencePoint(point=v[15])

# Create and submit job for linear buckling
mdb.Job(name='LBA', model='Linear model', description='', type=ANALYSIS, atTime=None,
    waitMinutes=0, waitHours=0, queue=None, memory=90, memoryUnits=PERCENTAGE,
    getMemoryFromAnalysis=True, explicitPrecision=SINGLE, nodalOutputPrecision=SINGLE,
    echoPrint=OFF, modelPrint=OFF, contactPrint=OFF, historyPrint=OFF, userSubroutine='',
    scratch='', resultsFormat=ODB, numThreadsPerMpiProcess=1, multiprocessingMode=DEFAULT,
    numCpus=1, numGPUs=0).submit(consistencyChecking=OFF)
mdb.jobs['LBA'].waitForCompletion()

# Create a new model for dynamic explicit analysis
mdb.Model(name='DE', objectToCopy=mdb.models['Linear model'])

# Define additional plasticity and CS-model parameters
mdb.models['DE'].materials['Steel'].Plastic(scaleStress=None, table=((410.9,
    0.0), (416.1, 0.0028), (417.7, 0.004), (419.2, 0.0052), (421.1, 0.0068), (
    439.5, 0.0172), (456.3, 0.0275), (470.5, 0.0378), (482.3, 0.0481), (492.5,
    0.0584), (502.3, 0.0691), (511.3, 0.0803), (519.0, 0.0908), (526.5,
    0.1012), (533.2, 0.1118), (539.5, 0.1224), (546.1, 0.1337), (548.3,
    0.1374)))
mdb.models['DE'].materials['Steel'].plastic.RateDependent(table=((1094.0,
    3.47), ))

# Create dynamic explicit step
mdb.models['DE'].ExplicitDynamicsStep(name='LBA', previous='Initial',
```

```
    maintainAttributes=True, timePeriod=0.07692, improvedDtMethod=ON)
mdb.models['DE'].steps.changeKey(fromName='LBA', toName='DE')

# Delete load and modify boundary conditions
del mdb.models['DE'].loads['Load']
del mdb.models['DE'].boundaryConditions['Top boundary']
del mdb.models['DE'].boundaryConditions['Bottom boundary']
a = mdb.models['DE'].rootAssembly
f1 = a.instances['Tensile member-1'].faces
faces1 = f1.getSequenceFromMask(mask=('[#1 ]', ), )
region = regionToolset.Region(faces=faces1)
mdb.models['DE'].VelocityBC(name='Top BC', createStepName='Initial',
    region=region, v1=0.0, v2=UNSET, v3=0.0, vr1=0.0, vr2=0.0, vr3=0.0,
    amplitude=UNSET, localCsys=None, distributionType=UNIFORM, fieldName='')
mdb.models['DE'].SmoothStepAmplitude(name='Smooth', timeSpan=STEP, data=((0.0,
    0.0), (0.001923, 1.0), (0.07692, 1.0)))
mdb.models['DE'].boundaryConditions['Top BC'].setValuesInStep(stepName='DE',
    v2=-130.0, amplitude='Smooth')
faces1 = f1.getSequenceFromMask(mask=('[#2 ]', ), )
region = regionToolset.Region(faces=faces1)
mdb.models['DE'].DisplacementBC(name='Bottom BC', createStepName='Initial',
    region=region, u1=SET, u2=SET, u3=SET, ur1=SET, ur2=SET, ur3=SET,
    amplitude=UNSET, distributionType=UNIFORM, fieldName='', localCsys=None)

# Specify history outputs
regionDef=mdb.models['DE'].rootAssembly.sets['Set-1']
mdb.models['DE'].historyOutputRequests['H-Output-1'].setValues(variables=(
    'RF2', ), numIntervals=800, region=regionDef, sectionPoints=DEFAULT,
    rebar=EXCLUDE)
regionDef=mdb.models['DE'].rootAssembly.allInstances['Tensile member-1'].sets['Set-2']
mdb.models['DE'].HistoryOutputRequest(name='H-Output-2', createStepName='DE',
    variables=('U2', ), numIntervals=800, region=regionDef,
    sectionPoints=DEFAULT, rebar=EXCLUDE)
regionDef=mdb.models['DE'].rootAssembly.allInstances['Tensile member-1'].sets['Set-3']
mdb.models['DE'].HistoryOutputRequest(name='H-Output-3', createStepName='DE',
    variables=('U3', ), numIntervals=800, region=regionDef,
    sectionPoints=DEFAULT, rebar=EXCLUDE)

# Introducing imperfections
mdb.models['DE'].keywordBlock.setValues(edited = 0)
mdb.models['DE'].keywordBlock.synchVersions(storeNodesAndElements=False)
mdb.models['DE'].keywordBlock.replace(42, """
** ----------------------------------------------------------------
**
** STEP: DE
**
*IMPERFECTION, FILE= LBA, STEP=1
1, 0.3""")

# Create and submit job for dynamic analyses
mdb.Job(name='DE', model='DE', description='', type=ANALYSIS, atTime=None,
    waitMinutes=0, waitHours=0, queue=None, memory=90, memoryUnits=PERCENTAGE,
    explicitPrecision=DOUBLE_PLUS_PACK, nodalOutputPrecision=SINGLE,
    echoPrint=OFF, modelPrint=OFF, contactPrint=OFF, historyPrint=OFF,
    userSubroutine='', scratch='', resultsFormat=ODB, numDomains=4,
    activateLoadBalancing=False, numThreadsPerMpiProcess=1,
    multiprocessingMode=DEFAULT, numCpus=4)
mdb.jobs['DE'].submit(consistencyChecking=OFF)
```